# Rational Design of Semiconductors for Efficient Charge Transfer and Light Harvesting for Enhanced Photovoltaic and Sensing Applications

*A Dissertation Submitted to the*
*Indian Institute of Technology Guwahati*
*as Partial Fulfillment for the Degree of*

**DOCTOR of PHILOSOPHY**
***by***

**Mohammad Shaad Ansari**

**DEPARTMENT OF CHEMISTRY**
**INDIAN INSTITUTE OF TECHNOLOGY GUWAHATI**
**GUWAHATI, INDIA**
**FEBRUARY 2019**

# Rational Design of Semiconductors for Efficient Charge Transfer and Light Harvesting for Enhanced Photovoltaic and Sensing Applications

*A Dissertation Submitted to the*
*Indian Institute of Technology Guwahati*
*as Partial Fulfillment for the Degree of*

**DOCTOR of PHILOSOPHY**

***by***

**Mohammad Shaad Ansari**
**Roll No: 136122015**


**DEPARTMENT OF CHEMISTRY**
**INDIAN INSTITUTE OF TECHNOLOGY GUWAHATI**
**GUWAHATI – 781039, ASSAM, INDIA**
**FEBRUARY 2019**

## STATEMENT

I hereby declare that work incorporated in this thesis entitled, "**Rational Design of Semiconductors for Efficient Charge Transfer and Light Harvesting for Enhanced Photovoltaic and Sensing Applications"** is the outcome of research work carried out by me under the supervision of Prof. Mohammad Qureshi, at the Department of Chemistry, Indian Institute of Technology Guwahati, Guwahati, Assam, India.

Research material used in this thesis from any other sources, has been duly cited and acknowledged. The work is original and has not been submitted in part or full by me for any other degree or diploma to other Institute or University.

IIT Guwahati **Mohammad Shaad Ansari**

February 2019 Candidate

*Dr. Mohammad Qureshi*
*Professor*
*Department of Chemistry*
*Indian Institute of Technology Guwahati*
*Guwahati – 781036, India*
*Tel: +91 – 361 – 2582320; Fax: +91 – 361 – 2582349*
*Email: mq@iitg.ac.in*

## Certificate

This is to certify that the work included in this thesis entitled "**Rational Design of Semiconductors for Efficient Charge Transfer and Light Harvesting for Enhanced Photovoltaic and Sensing Applications**" by Mr. Mohammad Shaad Ansari, Department of Chemistry, Indian Institute of Technology Guwahati has been carried out under my supervision. I further certify that this work has not been submitted to any other University or Institution in part or full for the award of any degree or diploma.

IIT Guwahati
February 2019

**Dr. Mohammad Qureshi**
Thesis supervisor
Department of Chemistry
Indian Institute of Technology Guwahati
Guwahati – 781039, Assam, India

## ACKNOWLEDGEMENT

*"Never look back, Reminiscing on yesterday, Smile for the future, Tomorrow is a new day." Zayn Malik*

*First of all, I thank almighty Allah for giving me a great life, strength to chase my dreams, and being with me in all my failure and success!*

*My sincere gratitude towards all those people who have contributed directly and indirectly during my scientific journey is endless and cannot be fully express with words. I will try, however, taking into consideration my love for writing, this part may grow even longer than the thesis itself. Allow me for just briefly mentioning the most important people who actually made this thesis a reality and an unforgettable experience for me.*

*To begin with a deepest sense of gratitude, I wish to express my sincere thanks to my supervisor, Prof. Mohammad Qureshi who gave me an opportunity to work under his supervision. He is a source of inspiration and enthusiasm, and has always motivated me with his devotion, dedication, hard work, optimistic approach and eagerness to learn new things. I will never forget his endless support and encouragement throughout my research period. I learned a lot from his knowledge, experience, and philosophy of life which molded me into a good human being. His scientific discussions, keen observation, analytical ability, critical comments has nurtured my scientific skill and also inspired me to strive to be a good researcher. I have been fortunate enough as he gave me complete freedom to execute and explore new ideas and assisted me throughout this time when I needed help.*

*Besides my supervisor, I am highly indebted to my doctoral committee members, Dr. A. S. Achalkumar, Prof. Parameswar Krishnan Iyer, Dr. Chivukula V. Sastri and Prof. Aditya Narayan Panda for their periodic assessment of my research work and their valuable suggestions.*

*I sincerely thanks to my collaborators, Prof. Rajneesh Misra and Dr. Ramesh Maragani, IIT Indore, India, and Dr. Anamika Kalita, IIT Guwahati for their continuous help and support.*

*I would like to thank all faculty and staff members of Chemistry department. My sincere thanks to all staffs of Central Instruments Facility, for their help and guidance to several analytical instruments, required during my research work. I wish to express my sincere gratitude to IIT Guwahati for all the facilities and the Ministry of Human Resource Development (MHRD), India for the financial support.*

*I would like to thank all my past and present labmates Dipankar da, Tridip da, Anindya da, Avishek, Gaurangi, Tushar, Suhaib, Adit, Sourav, Manoj and Moite for their timely help, support and creating a pleasant and vibrant laboratory atmosphere. I especially thank to Tridip da for sharing his enormously broad knowledge and endless patience. You taught me all the basics, experiments and how to use almost all the instruments that we need. I also thanks to Avishek for being my excellent colleague cum friend, sharing his valuable ideas and assisting in most of my research work. In addition to all scientific*

*discussions and several hours spent in the labs, Tea breaks and hanging out with you guys specially Tushar are the essential part of my research life. I would like to thank Sonia Ma'am for her encouraging words and technical inputs during my research period. I would also like to thank present and past lab members of Organic Electronics Lab, Subbarao bhaiya, Asish bhaiya, Dipjyoti bhaiya, Anamika Ma'am, Adil bhai, Rahul, Indrani, Maimur, Ramesh ji, Ritesh, Biki, Anwesha and Rabindra for their timely help, suggestions and support.*

*I extend my sincere thanks to my friends Aamir, Farha, Lalit, Vikas, Yeshab, Late Sufiyan, Yusuf, Faizan, Zaid, Arshad, Naved, Anas bhai, Azhar, Ibrar bhai, Nishad, Zafar, Vasi, Masab, Khushboo, Halima, Anju, Nishat, Samiksha, Mohsin, Yashika, Saud, Kamran, Shahrukh, Shawez, Azeem bhai, Anzar, Sabera di, Randeep, Anushree, Gopi, Kamal, Raman, Arvin, Gattu, Mustakim, Anjali, Nehal, Dhirti, Afsana di, Suranjan, Hiranya, Minati, Ila, Biswajit, Rajkumar and other close friends for their constant unfailing support, their encouragement and all the help they extended whenever required.*

*My sincere thanks to Dr. Sarfaraz, Dr. Sameer Hussain and Mr. Mohammad Adil Afroz, for their brotherly caring nature, sharing all kinds of moments and helping to improve my thinking approach.*

*I sincerely express my gratitude towards entire fraternity from my school and university especially Late Mrs. Videja Sharma Ma'am, Mr. Ashok Sir, Mr. Ramgopal Sharma Sir, Mr. Pramod Sir, Dr. Mohammad Shahid Sir and Prof. Suhail Sabir Sir for imbibing good values and knowledge in me.*

*A special thanks to all my seniors and juniors from AMU, Palash da, Ajaz bhai, Sameer bhai, Akhtar bhai, Sahnawaz bhai, Wajid bhai, Kripa bhaiya, Zia bhai, Faheem bhai, Adil bhai, Kafeel bhai, Tasleem, Mehbub bhai, Maimur, Adil Rather, Tarique bhai, Akhter Alam, Munendra, Suhaib, Shavez, Nehal, Saghir, Tipu, Altaf, Tarik and Masud for giving me unforgettable moments and delightful experiences. I will specially miss the memorable moments shared with Sameer bhai, Adil bhai, Wajid bhai, Sabera di, Kafeel bhai, Akhtar bhai, Randeep and Suhaib during my stay at IIT Guwahati.*

*Finally, my Ph. D. endeavor could not have been completed without the endless love, support, tolerance and blessings from my family. I am fortunate and blessed enough to have such a caring and supportive parents; Mrs. Sabra Begam (who taught me the value of education) and Mr. Mohammad Nazim, it is because of their prayers, sacrifice and struggle, I am able to live my dream to complete my higher education from a prestigious institute. I am also grateful to my sisters (Almas, Late Mehnaz) and brothers (Abdul Kadir, Zaid, Zeeshan) for their eternal love, cooperation and emotional support which had immensely needed to complete this work.*

*Still many names are missing whose contribution and help is worth mentioning.*

*Shaad*

# TABLE OF CONTENTS

*Dedicated*

*To*

*My Grandparents*

*for*

*their Endless Love and Support*

| | |
|---|---|
| **Thesis Title:** | **Rational Design of Semiconductors for Efficient Charge Transfer and Light Harvesting for Enhanced Photovoltaic and Sensing Applications** |
| **Name of the Candidate**: | Mr. Mohammad Shaad Ansari |
| **Registration Number**: | 136122015 |
| **Thesis Supervisor**: | Prof. Mohammad Qureshi |
| **Department**: | Chemistry |
| **Institute**: | Indian Institute of Technology Guwahati, Assam – 781039, India. |

## Thesis Overview

### Chapter 1: Introduction and Literature Survey

Recent progress in rational design and synthesis of several semiconductors based on their morphologies, accountable for the improved charge transfer and light harvesting ability have been discussed in the present chapter. An overview on photovoltaic technology, basic concepts and working principle of dye-/ semiconductor quantum dot (QD) sensitized solar cells are briefly discussed. This chapter also includes a brief literature survey of current state of art scenario and challenges related to the rational design of semiconductors, utilized for photoanodic segment. Advantages of zinc oxide (ZnO) as a photoanodic material have been discussed over traditionally used titanium dioxide ($TiO_2$) to get the different morphological structures, to improve the charge carrier dynamics as well as light harvesting of the photoanodic material. With respect to present state of art, templating agents used for tuning the morphology have several drawbacks in terms of the high cost, difficult to remove and environmental unfriendly. Therefore, with low cost and environmentally benign, bio-mass derived templating agents are used for tuning the morphologies of semiconductors. A brief discussion related to the development of chemiresistor device, basic architecture and working principle for gas sensing are also included. This chapter is concluded with a brief literature survey related to ZnO based $NH_3$ gas sensing.

## Chapter 2: Experimental Section

Comprehensive routes for the synthesis and fabrication of materials and basic instrumentation techniques used for material characterization have been discussed in chapter **2**. This chapter also includes photoanode preparation, sensitization and characterization of the photovoltaic devices using the various instrumental techniques/methods. Photovoltaic parameters of devices are characterized using instrumental techniques such as Keithley 2400 (current–voltage characteristics), IQE–200 (incident photon-to-current efficiency, IPCE analyzer) and CHI 680D (electrochemical impedance spectroscopy, EIS measurements). This chapter is concluded with the fabrication of chemiresistor device and sensing assembly, utilized for detection of gas vapors. Sensing studies of chemiresistor device are characterized using Keithley 4200–SCS.

## Chapter 3: Morphological Tuning of Photo-booster g–$C_3N_4$ with Higher Surface Area and Better Charge Transfers for Enhanced Power Conversion Efficiency of Quantum Dot Sensitized Solar Cells

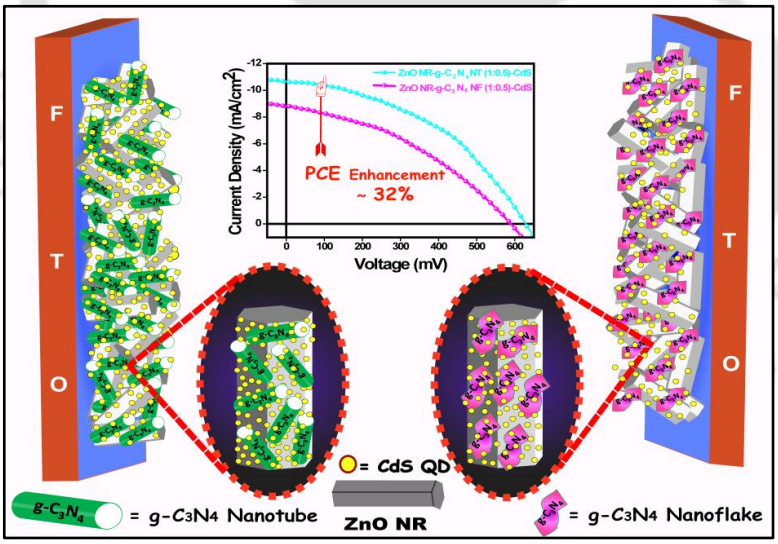


**Figure 1.** Schematic representation of comparative photovoltaic study of both morphological structures of g–$C_3N_4$ based solar devices. **[(Carbon 2017, 121, 90–105)]**

In this chapter, photo-booster effect of g-$C_3N_4$ Nanotubes (g-$C_3N_4$ NTs) on the photovoltaic properties is investigated using the composites having ZnO Nanorods (NRs) with different composition ratios, sensitized by CdS quantum dots. Enhanced performance is

attributed to the cumulative effects of this composite i.e., (i) a significant decrement of fluorescence intensity in steady state photoluminescence (PL), (ii) faster electron lifetime and good electron injection rate from dynamic PL, and (iii) sufficient loading of sensitizer at photoanodic scaffold for better harvesting of solar energy. An increase of ~ 32 % in power conversion efficiency (PCE, η) is observed in case of g-$C_3N_4$ NTs based device as compare to g-$C_3N_4$ Nanoflakes (g-$C_3N_4$ NFs). Increased PCE value is mainly due to (i) efficient separation and transportation of the photogenerated charge carriers along a one dimensional (1–D) path, resulting in shorter lifetime of charge carriers and (ii) high surface area which provides more active sites for loading of sensitizer particles, results in an improvement of light harvesting ability. Further, electrochemical impedance spectroscopic (EIS) analyses showed an efficient interfacial charge transfer by reducing the recombination processes i.e., the back transferring of photoexcited electron at electrode/electrolyte interface. Figure **1** depicts the Schematic representation of comparative photovoltaic study of both morphological structures of g-$C_3N_4$ based solar devices with optimized composites ratio. Morphological features of as-synthesized g-$C_3N_4$ structures and their utilization in photovoltaic study are depicted in the figure **2** and **3** respectively.

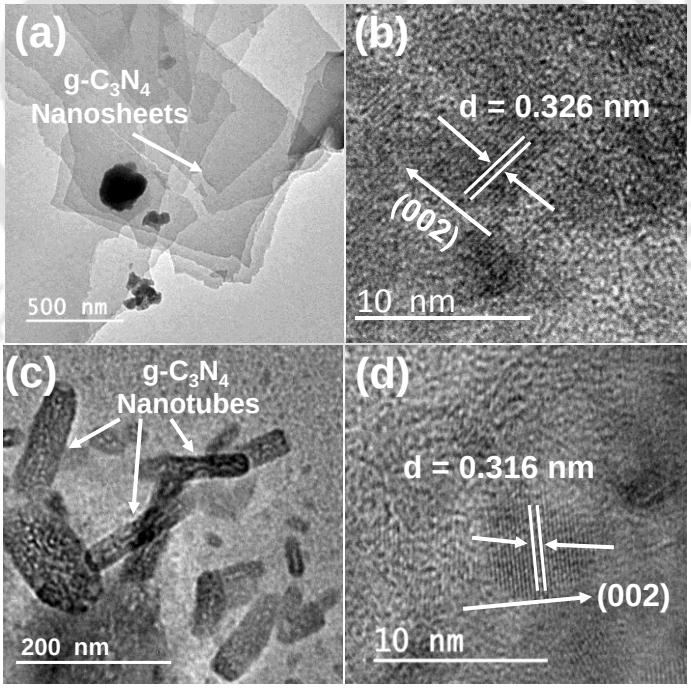


**Figure 2.** Transmission electron microscopy (TEM) images show the structural features of as-synthesised of g–$C_3N_4$ NFs [**(a)** and **(b)**] and g–$C_3N_4$ NFs [**(c)** and **(d)**].

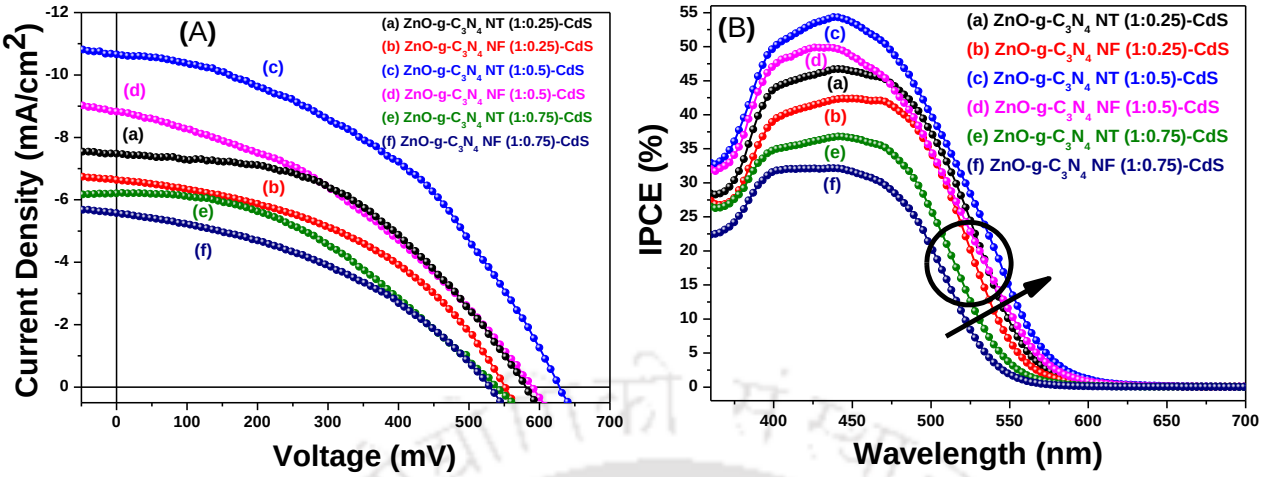


**Figure 3. (A)** Current density–Voltage (*J*–V) curves for all fabricated photovoltaic devices based on both morphology of g–$C_3N_4$ with different weight ratios namely: **(a)** ZnO NR–g–$C_3N_4$ NT (1:0.25)–CdS, **(b)** ZnO NR–g–$C_3N_4$ NF (1:0.25)–CdS, **(c)** ZnO NR–g–$C_3N_4$ NT (1:0.5)–CdS, **(d)** ZnO NR–g–$C_3N_4$ NF (1:0.5)–CdS, **(e)** ZnO NR–g–$C_3N_4$ NT (1:0.75)–CdS and **(f)** ZnO NR–g–$C_3N_4$ NF (1:0.75)–CdS. **(B)** Corresponding IPCE plots for the respective devices employing $S^{2-}/S_n^{2-}$ as the redox couple.

## Chapter 4: Combined Effect of *In-Situ* Grown p-type $CuSbS_2$ / n-type CdS Coupled with Hierarchical ZnO Nanodisks for Improved Photovoltaic Light Harvesting Efficiency

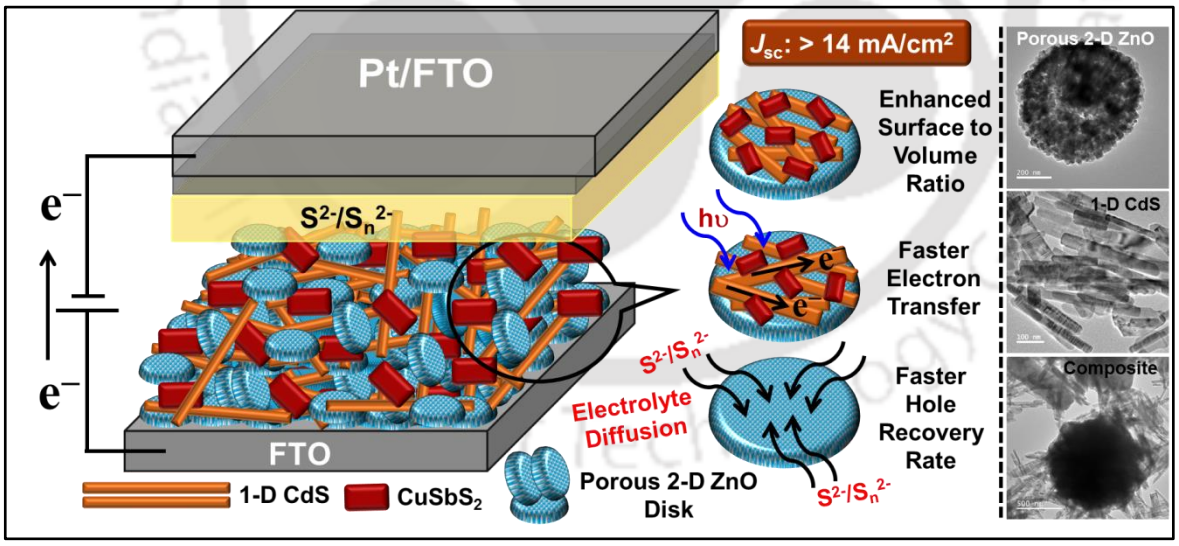


**Figure 4.** Schematic illustration of various features of photoanodic architecture based on 2–D porous ZnO disk structures, sensitized with 1–D CdS nanowires and $CuSbS_2$ nanobricks. **[(J. Power Sources, 2019, 425, 204–216)]**

This chapter demonstrates the synthesis of porous two dimensional (2–D) zinc oxide (ZnO) disk structures, using a biomass derived templating agent i.e., Xanthan gum. This

templating agent is mainly accountable to control the growth kinetics of high energy facets of wurtzite ZnO crystal structure and likely to obtain these disk structures. A comparative photovoltaic study of as-synthesized 2–D porous ZnO structures with respect to 1–D ZnO structures (in absence of xanthan gum) is carried out by co-sensitizing with *in-situ* grown 1–D CdS nanowires array and ternary metal chalcogenide viz. copper antimony sulfide ($CuSbS_2$). Superior photovoltaic performance (~ 45 % enhancement in efficiency) is obtained for CdS-$CuSbS_2$ co-sensitized with 2–D porous ZnO disks as compared to 1–D ZnO structures, owing to improved current density and fill factors. This enrichment is mainly attributed to large exposed surface active sites for optimum loading of light absorbing materials, better light scattering and improved hole recovery rate of sensitizers with the better penetration of redox shuttle. Moreover, crystal phase purity of $CuSbS_2$ (CAS) and p-n junction formed between $CuSbS_2$ and CdS also support the enhanced efficiency by facilitating the electron–hole separation and electron transportation.

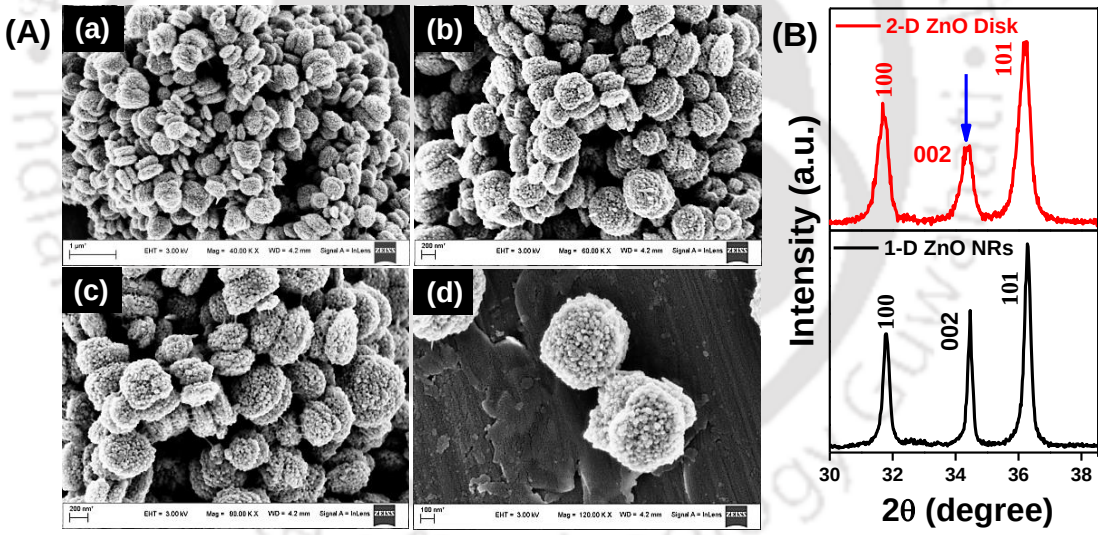


**Figure 5. (A)** Field emission scanning electron microscopy (FESEM) images show as-synthesized 2−D porous ZnO disk structures [traces **(a−d)**] at different magnifications. **(B)** Powder X-ray diffraction patterns for both ZnO heterostructures, synthesized under different reaction conditions showing intensity variation of the diffraction peaks.

Figure **4** depicts the schematic illustration of various features of photoanodic architecture based on 2–D porous ZnO disk structures, sensitized with *in-situ* 1–D CdS nanowires and $CuSbS_2$ nanobricks. Morphological features with powder x-ray diffraction (PXRD) analysis of as-synthesized 2–D porous ZnO structures and morphology dependent photovoltaic performances based on both ZnO structures are depicted in the figure **5** and **6** respectively.

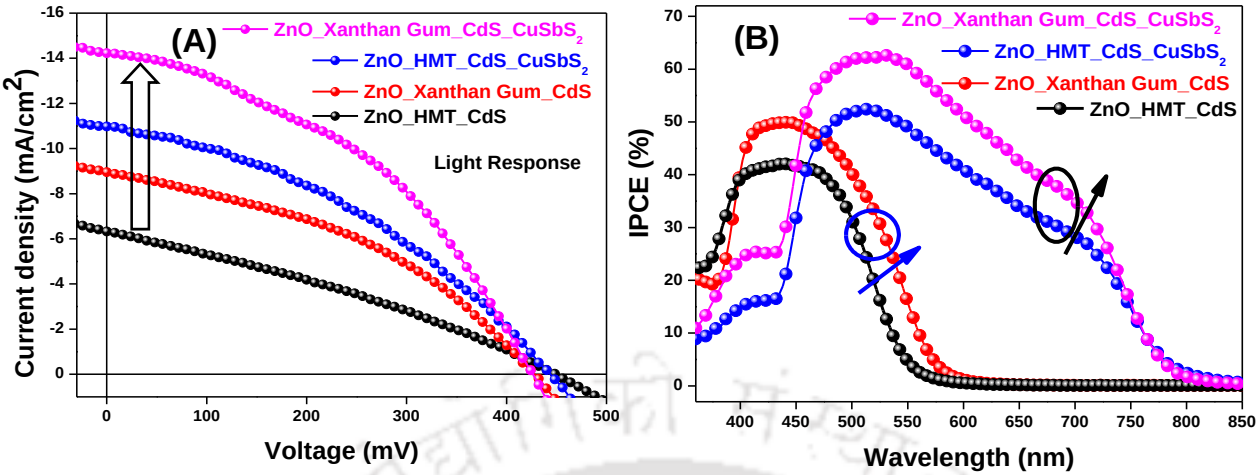


**Figure 6. (A)** Current density–Voltage (*J*–V) curves for as-fabricated photovoltaic devices based on both morphology of ZnO, sensitized with 1–D CdS and $CuSbS_2$ while **(B)** Corresponding IPCE plots for the respective devices employing $S^{2-}/S_n^{2-}$ as the redox couple.

## Chapter 5: Enhanced Photovoltaic Performance using Biomass derived nano 3–D ZnO Hierarchical Superstructures and a D–A type $C_S$–Symmetric triphenylamine linked bisthiazole

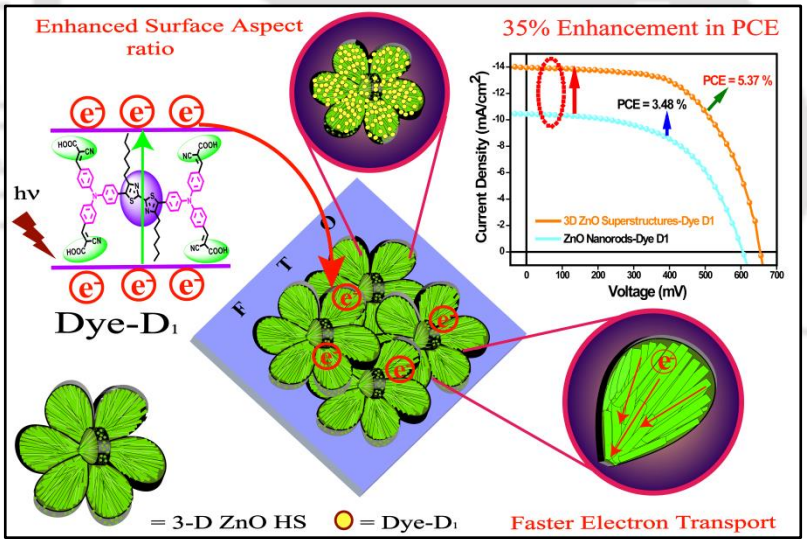


**Figure 7.** Schematic representation of 3–D hierarchical superstructures based photoanode showing the enhanced surface to volume ratio and fast charge transportation. **[(ACS Omega 2017, 2, 5981–5991; Electrochimica Acta 2018, 259, 262–275)]**

This chapter demonstrates a facile one step biomass assisted hydrothermal route for the controlled synthesis of three dimensional (3–D) Zinc oxide (ZnO) hierarchical superstructures

(HSs), assembled with compacted ZnO nanorods (NRs). Anionic polysaccharide "Polygalacturonic acid" is utilized as a crystal growth modifier for assembling the basic building blocks (ZnO NRs). Probable mechanism for the formation of superstructures through the interaction between the polysaccharide and ZnO growth units is discussed. Photovoltaic properties of as-synthesized 3–D ZnO HSs as compared to its basic structural unit i.e., ZnO NRs are investigated by sensitizing with a bisthiazole linked metal free donor-acceptor dye; **D1**. A substantial enhancement (~ 35%) in efficiency (η) for 3–D ZnO HSs based device (η ≈ 5.37 %) as compare to ZnO NRs (η ≈ 3.48 %) is being observed, mainly due to better charge separation and collection, owing to a superior electron transport ability of compacted building blocks, better light-scattering effect, higher BET surface area for sensitizer loading and efficient electron injection from dye **D1** to the ZnO. Electrochemical impedance spectroscopic (EIS) analysis is carried out to support a slower photogenerated electron–hole recombination rate and better charge transports in the 3–D ZnO HSs based photovoltaic device. Figure **7** shows the schematic representation 3–D hierarchical superstructures based photoanode, exhibiting the enhanced surface to volume ratio and fast charge transportation. Morphological characterizations of as-synthesized 3–D hierarchical ZnO superstructures and photovoltaic performances based on both morphological structures are depicted in the figure **8** and **9** respectively.

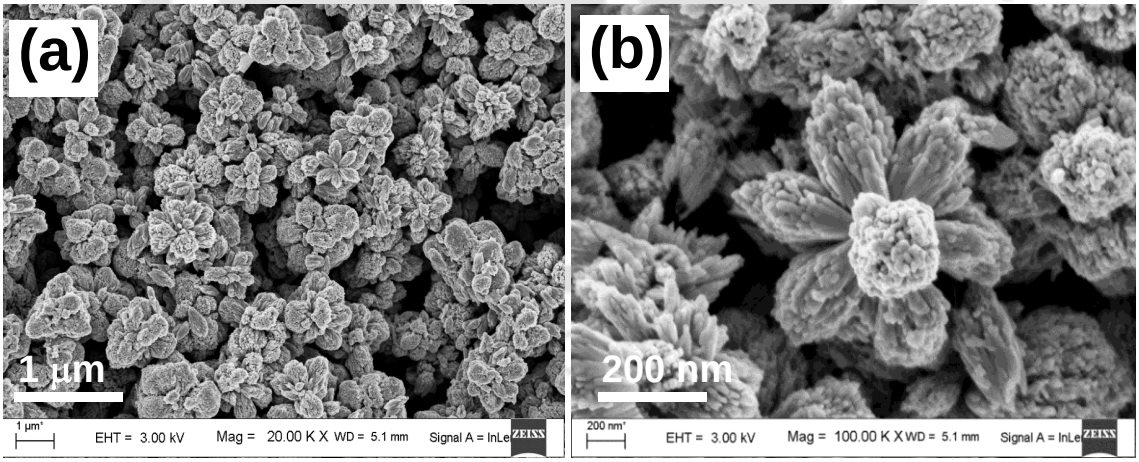


**Figure 8.** Traces **(a–b)** represent the FESEM images of as-synthesized 3–D ZnO hierarchical superstructures at different magnifications.

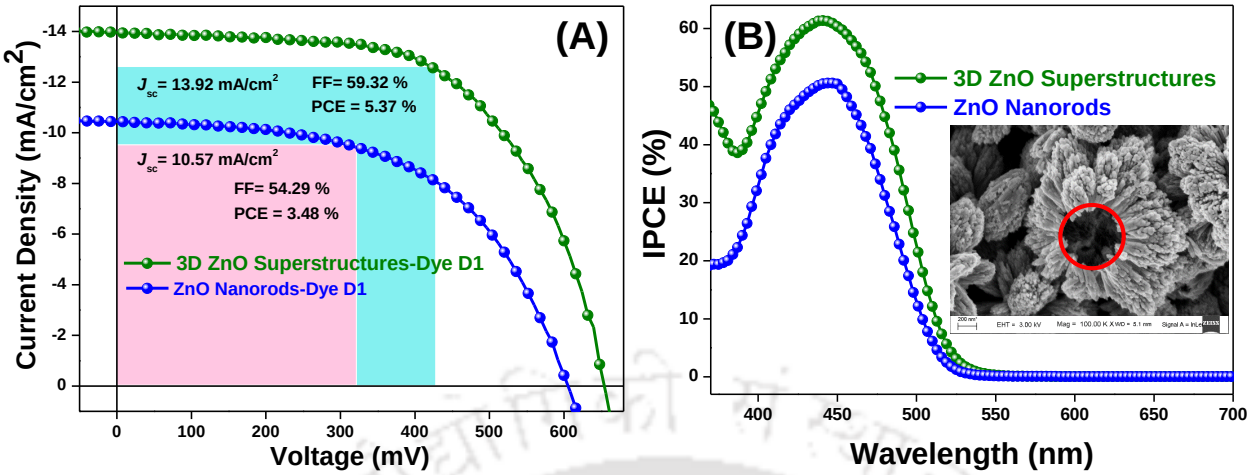


**Figure 9. (A)** Current density–Voltage (*J*–V) curve for as-fabricated photovoltaic devices based on both ZnO heterostructures. **(B)** Corresponding IPCE plot for the respective devices. Inset shows the porous and hollow nature of ZnO superstructures, helpful for the better infiltration of redox couple and efficient light scattering in the photovoltaic devices.

## Chapter 6: Multifunctional Hierarchical 3–D ZnO Superstructures Directly Grown over FTO glass substrates: Enhanced Photovoltaic and Selective Sensing Applications

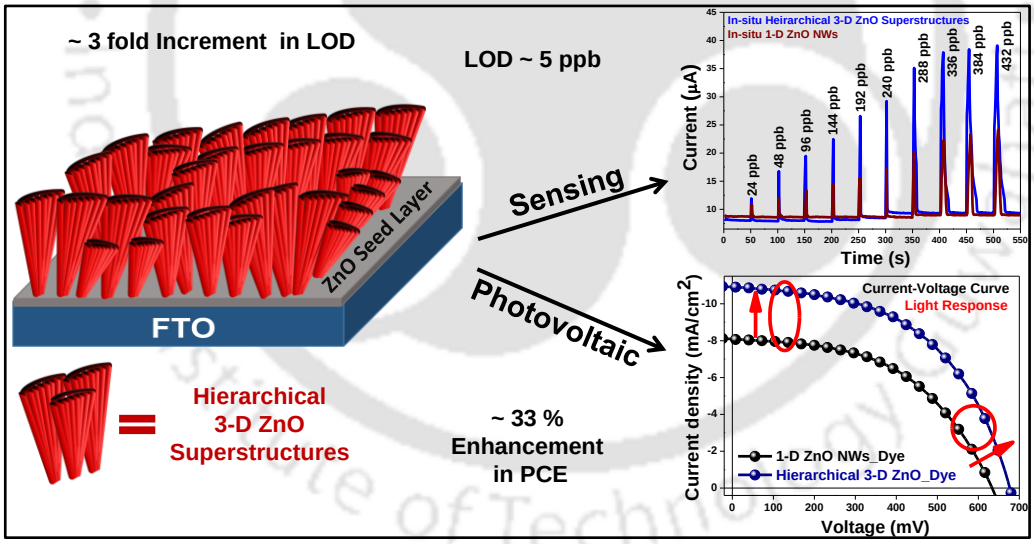


**Figure 10.** Schematic representation showing 3–D hierarchical superstructures based photoanode and its utilization for Photovoltaic and Gas sensing applications. **[(J. Mater. Chem. A 2018, 6, 15868–15887)]**

This Chapter presents the photovoltaic/sensing device which relies on electron transport; often suffer from the drawback of higher Ohmic contacts between the active materials and its collecting electrode. Designing and developing the chemiresistor device with low ohmic resistance would become more important when the vapor pressure of the compounds yield very

low concentrations of sensing elements. Here, an *in-situ* growth of hierarchical three dimensional Zinc oxide superstructures over conductive glass substrate i.e., fluorine doped tin oxide under controlled hydrothermal route has been reported for low Ohmic contact, thereby an efficient charge injection. An anionic polysaccharide "k-carrageenan" is employed for assisting the hetero epitaxial aggregated growth of 1–D nanocrystals. We have successfully demonstrated the applications of as-characterized multifunctional 3–D ZnO hierarchical structures in photovoltaic and selective chemical vapor sensing. A significant enrichment (~ 33 %) in power conversion efficiency (η) for hierarchical 3–D ZnO superstructures based photovoltaic device as compared to 1–D ZnO nanowires has been observed which is mainly due to the larger surface to volume ratio for sensitizer loading, better light-scattering effect, better charge separation and collection. Two terminal sensor devices have displayed high sensitivity and selectivity for $NH_3$ vapors with the limit of detection value of ~ 5 parts per billion (ppb) for 3–D ZnO hierarchical superstructures while ~ 17 ppb for 1–D ZnO NWs, which is very less as compared to maximum permissible limit i.e., 25 parts per million (ppm). Selectivity, recyclability, response/recovery time and sensitivity for primary, secondary and tertiary amines are studied for both the chemiresistor devices. Figure 10 illustrates the schematic representation of 3–D hierarchical superstructures based photoanode and its utilization for Photovoltaic and Gas sensing applications. Morphological features of *in-situ* grown 3–D hierarchical ZnO structures and photovoltaic performances are shown in the figure **11** and **12**. Gas sensing studies of both heterostructures of ZnO are depicted in figure **13** while sensing mechanism is illustrated in figure **14**.

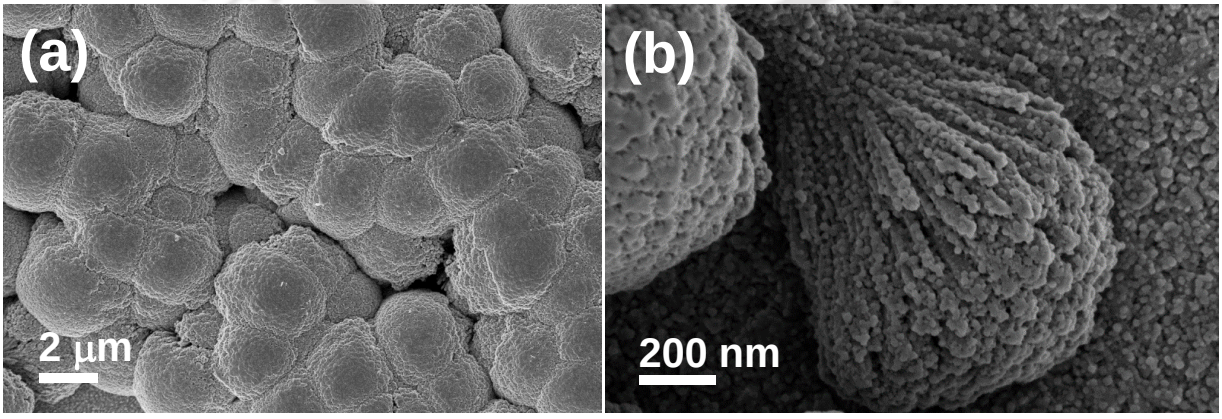


**Figure 11.** Traces **(a, b)** represent the Field emission scanning electron microscopy (FESEM) images of *in-situ* grown hierarchical 3–D ZnO superstructure of different regions at different magnifications.

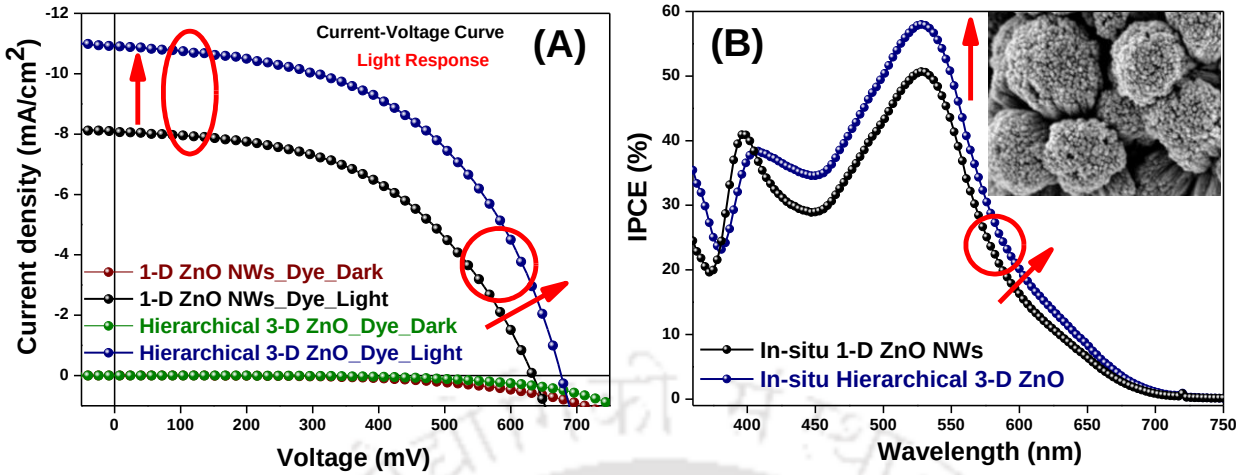


**Figure 12. (A)** Current density–voltage (*J*–V) curve for both *in-situ* grown ZnO heterostructure-based photovoltaic devices. **(B)** Corresponding IPCE plots for the respective devices. Inset of **(B)** shows the *in-situ* grown hierarchical 3–D ZnO superstructures, helpful for the effective light utilization by providing higher loading sites for sensitizer adsorption.

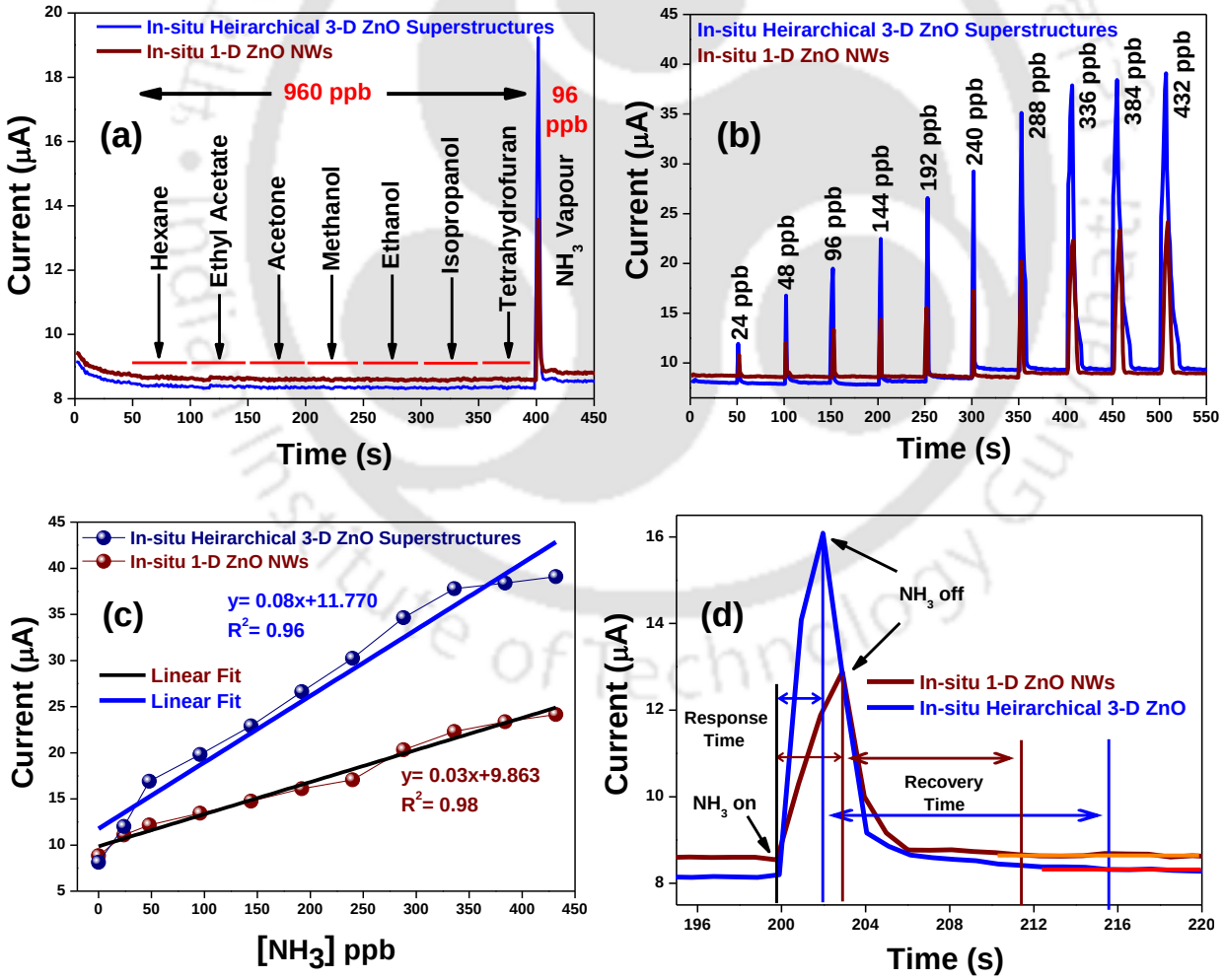

**Figure 13. (a)** Sensing response of the as-fabricated chemiresistor devices based on both *in-situ* grown ZnO heterostructures for various common organic solvents as well as $NH_3$ vapors at relative humidity of RH 49 %. **(b)** Sensing response for both devices towards various concentrations of $NH_3$ vapors (RH 48 %). **(c)** Calibration curve for calculating the limit of detection (LOD) of both chemiresistor devices as a function of $NH_3$ concentration. **(d)** Response and recovery time of the $NH_3$ sensing based on both devices (RH 48 %).

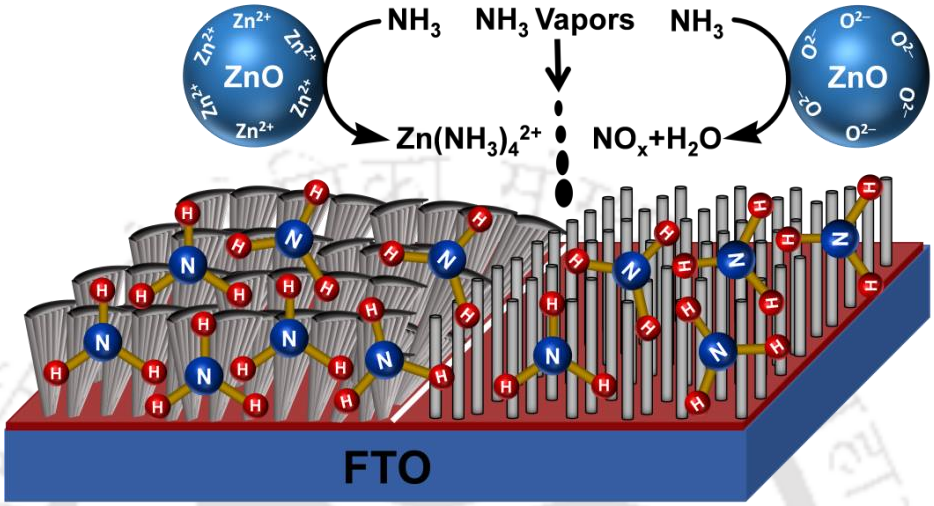


**Figure 14.** Schematic illustration represents the probable gas sensing mechanism.

## Conclusions and Thesis Overview

In conclusion, we have tuned the morphology of UV-Vis light responsive semiconducting materials using different synthetic strategies. Various biomass derived templating agents are explored to modify the structural features of ZnO. These different dimensional ZnO nanostructures are utilized to fabricate the hybrid photoanodes for dye-/ quantum dots sensitized solar cells. Numerous light absorbing materials are employed to construct the photoanodes of highly efficient photovoltaic devices. We have also developed highly selective and sensitive gas sensor device by using different morphological structures of ZnO.

# CHAPTER 1

## Introduction and Literature Survey

*This chapter deals with a comprehensive overview on photovoltaic and gas sensor technology. A brief literature survey of current state of art scenario and challenges allied to the rational design of zinc oxide (ZnO), utilized for photoanodic segment has been discussed. With respect to present state of art, templating agents used for tuning the morphology with their advantages and drawbacks have been discussed. A brief discussion correspond to the development of chemiresistor device, basic architecture and working principle for gas sensing are also included.*

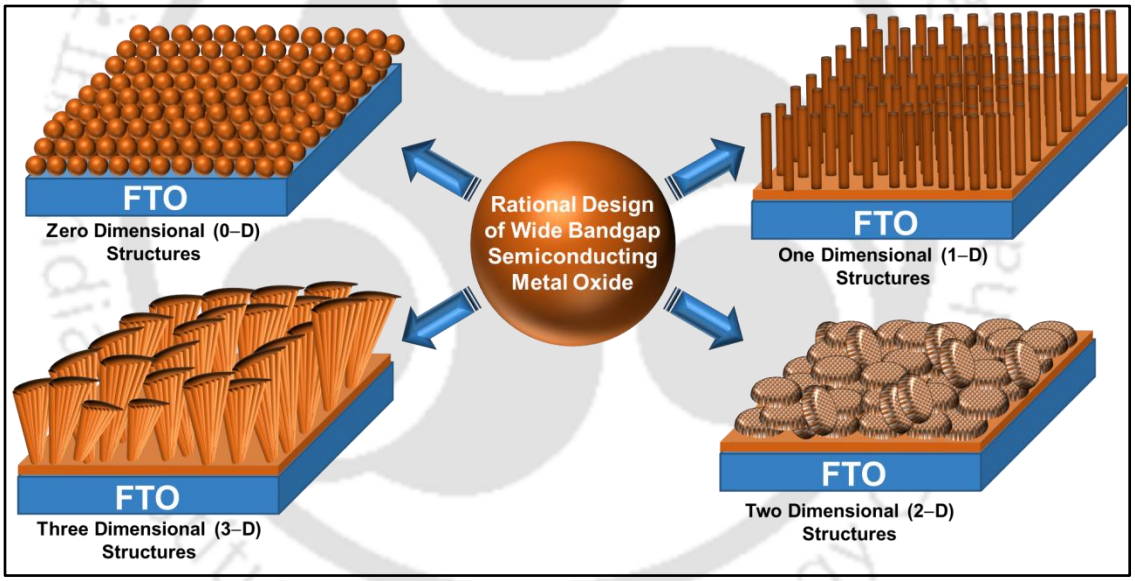

## 1.1 AN OVERVIEW ON PHOTOVOLTAIC TECHNOLOGY

In the 21st century, energy issue will become more projecting due to overconsumption of conventional energy resources.[1] So, solar energy is considered to be main energy resource to meet the desirable clean and abundant energy.[2] 'Photovoltaics' is a most viable technology to convert the solar energy into electrical energy, using the solar cell devices. Solar cells can be categorized into different types based on the generation of technology.[3] Single crystalline Si (c-Si) wafers based photovoltaics are the first generation solar cell, considered to be a leading technology in the commercial market with highest efficiency of about ~ 26.7 %.[4] Unfortunately, these solar cells are highly expensive in terms of their fabrication and long energy payback time, limit their utilization at large scale. To overcome these issues, second generation solar cells based on thinner polycrystalline layers have been emerged.[5] Amorphous Si (a-Si), CdTe, $Cu(InGa)Se_2$ (CIGS) or $Cu_2ZnSn(S/Se)_4$ (CZTS) have been utilized for fabrication of this generation solar cells, reaching highest efficiency of ~ 22.9 % for CIGS based Solar cells.[4] In spite of having economical in terms of their fabrication, thin films solar cells are still less efficient as compared to the first generation solar cells. With advancement of nanotechnology and material science, third generation solar cells have entered the photovoltaics arena to improve the efficiency of solar cells with minimum fabrication cost.[6] Dye-sensitized solar cells (DSSCs), Quantum dot sensitized solar cells (QDSSCs), Polymer solar cells, Perovskite solar cells are known as third generation solar cells. Fabrication of large area highly efficient, low-cost and lightweight solar cells is prime concern this category. Moreover, these solar cells are capable to meet the Shockley and Queisser theoretical upper limit of single junction solar cells.[7] Essentially, in 1991, O'Regan and M. Grätzel has introduced the concept of DSSCs, utilizing a mesoscopic $TiO_2$ layer along with electron injecting Ru based dye and achieved the efficiency of ~ 7.1 %.[8] Till now, several attempts have been made to improve the efficiency of DSSC and achieved the highest power conversion efficiency (PCE) up to ~ 13 %.[9] In general, mesoporous metal oxide layer is considered to be main component of device, helpful for enhancing the efficiency value with large-surface area for better loading of the dye molecules and improved charge transfer kinetics. QDSSC is the imitative form of DSSC with same working principle.[10] In QDSSC, narrow band gap semiconductor QDs are utilized as sensitizer rather organic dye in DSSC. As compared to organic dyes, QDs have the potential to improve the solar cell stability, and their special multi-electron generation character can enable the theoretically maximum efficiency to

be as high as 44%,[11] which is much higher than the DSSCs. Recently, Sargent group have achieved a record efficiency of about ~ 12.48 % for a PbS QDs based QDSSC.[12] With DSSC efficiencies exceeding 11 %, various companies and industrial research laboratories are engaged in development, manufacturing and commercialization of DSSC technology and products.[13, 14–15]

## 1.2 WORKING PRINCIPLE OF DSSC/QDSSC DEVICES

In general, DSSCs and QDSSCs are considered to be the electrochemical devices, consisting two electrodes, i.e., one photoanode and a cathode which act as a counter electrode. Redox electrolyte is injected between the electrodes to complete the photovoltaic device assembly. Basically, a DSSC/ QDSSC device has four main components which are metal oxide layer, sensitizer, redox couple and platinized FTO.

Working principle along with several electron transfer processes of a DSSC/ QDSSC device is depicted in figure **1.2.1**. Firstly, metal oxide layer is deposited on cleaned FTO substrate. Then, sensitizer particles are deposited onto the surface of metal oxide layer. A suitable redox electrolyte is infiltrated into metal oxide films for regeneration of sensitizer species. Sensitizer gets excited with incident solar irradiation, generates photoexcitons and injected them into conduction band (CB) of metal oxide layer, as shown in processes **1** and **2** of figure **1.2.1**. As injected photoexcitons gets diffused to metal oxide layer and collected at FTO substrate (process **3**), then go to external circuit.

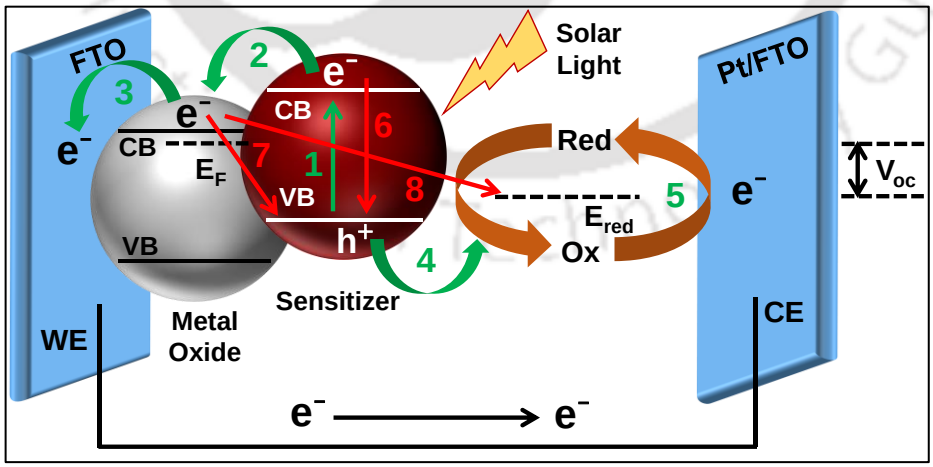


**Figure 1.2.1** Graphic representation related to working principle of a semiconductor-/dye-sensitized solar cell, having well matched energy levels of all components. Desired electron transfer and unwanted recombination processes of a solar device are displayed through green and red colored arrows.

In the meantime, oxidized sensitizer species are regenerated by hole transfer with the help of redox electrolyte, and redox electrolyte takes electron from platinized FTO to complete the electronic circuit (processes **4** and **5)**. For the better regeneration of the oxidized sensitizer species, redox potential of the electrolyte must be more positive than the highest occupied molecular orbital (HOMO) energy level of sensitizer particles.[16] In the QDSSC devices, redox electrolyte is also helpful for preventing photocorrosion by transferring the holes, created in the valence band of sensitizer species.[17] Oxidized redox couple is then reduced by taking electron from the counter electrode, while photoexcited electrons are migrated from photoanode to cathode by means of external circuit. Maximum output of open circuit voltage ($V_{oc}$) of a solar device is determined by the difference between the Fermi level ($E_F$) of the metal oxide and the redox potential of an electrolyte, represented in figure **1.2.1**.[18] For effective photoexcited electron injection, lowest unoccupied molecular orbital (LUMO) of organic dye has to be more positive than CB edge of the metal oxide. Organic dyes are attached to metal oxide layer with the help of anchoring groups such as –COOH, $–SO_3H$, $–PO_3H_2$, –OH *etc*. Electron injection process (process **2**) must be faster than the recombination process (process **6**) of the sensitizer for better kinetics of electron injection.[19–20] Generally, photoinduced electron injection from the dye molecules to metal oxide films are observed to be in range of femtosecond ($10^{-15}$ s) while recombination process of photoinduced electrons (relaxation process) is pragmatic in the range of $10^{-7}$ s.[21] So, electron injection efficiency ($\phi_{inj}$) is attained very close to unity in case of optimized DSSC devices. However, photoexcited electron injection process of a QDSSC device is found to be in the range of picosecond ($10^{-12}$ s) which is slower with respect to electron injection process of a DSSC device.[22–23] In QD sensitizers, time scales of direct band-to-band recombination and trap mediated recombination processes of photoexcited electrons vary in range of $10^{-11}$ to $10^{-6}$ s, mainly depend on specific semiconductor and nature of semiconductor surface.[22] Commonly used semiconductor QDs (II–VI) such as, CdS, CdSe, CdTe etc. demonstrate the recombination lifetimes in the range of $10^{-11}$–$10^{-9}$ s.[22] In some cases, recombination processes of semiconductor QDs dominate over the photoinduced electron injection and sensitizer regeneration processes, mainly related to creation of mid energy trap sites for recombination or back electron transfer at interface of semiconductor QDs and redox electrolyte.[24] Several efforts have been devoted to improve the electron injection rate of photoinduced electrons with minimal recombination processes.[25] Surface passivation of QDs is

beneficial for reducing the trap sites related recombinations whereas with size optimization of QDs (elevated CB offset), electron injection kinetics of a QDSSC device can be improved.[26–29] Timescale related to diffusion of photoexcited electrons into metal oxide layer is observed in the range of millisecond ($10^{-3}$ s).[30] During the diffusion, there is a possibility of photoexcited electrons recombination with the oxidized sensitizer species i.e., dye molecules or semiconductor QDs (process **7**) and the oxidized redox species in the electrolyte, adsorbed on the semiconductor surface (process **8)**.[31] Both the processes of electrons back transferring affect the regeneration process of sensitizer species i.e., process **4**. Fortunately, sensitizer regeneration processes are found to faster with time scale of $10^{-8}$ s for dye and $10^{-11}$ for QD as compared to recombination processes with time scale of micro to millisecond.[22, 24] However, with the slower transport of photoexcited electrons through the metal oxide scaffold layer, recombination processes become more feasible in real time devices. To reduce the recombination processes related to back transferring of electrons, a thin blocking layer of metal oxide is deposited on FTO substrate, inhibiting the contact formation between the redox electrolyte and FTO.[32–33] Moreover, a thin surface passivation layer of an appropriate material (e.g., MgO, $SiO_2$, $Al_2O_3$, $TiO_2$ etc.) is deposited onto metal oxide layer to minimize the trap sites for recombination processes.[34–35] Additionally, kinetics of photoexcited electron transport can be enhanced, using different morphologies of metal oxide.[36]

## 1.3 DEVELOPMENT OF PHOTOANODIC MATERIALS AND ARCHITECTURES

As per earlier discussion, light harvesting efficiency of a DSSC/QDSSC device gets limited due to happening of several recombination processes in the photoanodic segment. For development of highly efficient solar cell, it is essential to reduce the recombination processes by employing the functional materials having excellent optoelectronic properties. Since the discovery of DSSC, various wide band gap metal oxides such as ZnO,[37–38] $SnO_2$,[39–40] $Nb_2O_5$,[41–42] $SrTiO_3$[43] *etc.* have been utilized as the alternative photoanodic materials to conventionally used $TiO_2$. Amongst all, ZnO is considered to be a worthy candidate to be used as a photoanodic material, attributed to its unique physical and optoelectronic properties.[44–45] A comparative study of electronic and optical properties of ZnO and $TiO_2$ is summarized in table **1.3.1**.

**Table 1.3.1** Comparative study of wide band gap semiconducting material zinc oxide (ZnO) with conventionally used Titanium dioxide ($TiO_2$).

| Parameters | ZnO | $TiO_2$ | Ref. |
|---|---|---|---|
| **Crystal Structure** | Wurtzite | Anatase, Rutile | 46–48 |
| **Bandgap (eV)** | 3.2–3.4 | 3.0–3.2 | 46–49 |
| **Conduction Band Minimum (eV)** | − 4.36 | − 4.41 | 50 |
| **Electron Effective Mass** | 0.26 | 9 | 51 |
| **Electron Mobility ($cm^2 V^{-1}s^{-1}$)** | 130–200 | 0.1–4 | 46, 52 |
| **Effective Electron Diffusion Coefficient ($cm^2.s^{-1}$)** | $1.1\times10^{-4}$ | $4.3\times10^{-4}$ | 53 |
| **Static Dielectric Constant ($\varepsilon_{\perp,//}$)** | 9.26, 8.2 | 86, 170 | 54 |

From table **1.3.1**, more positive conduction band edge of ZnO is favorable for getting a high value of '$V_{oc}$' while higher electron mobility is helpful to get faster kinetics of photoexcited electron transport. Conductivity of ZnO can be further improved by Zn substitution with suitable metal atoms such as Al, Ga, and In.[55–57] Based on anisotropic growth behaviour and simple crystallization process,[58] ZnO structures can be tuned into numerous dimensions such as zero- (0–D), one- (1–D), two-dimensional (2–D) and three-dimensional (3–D) nanoarchitechtures. Optoelectronic properties of ZnO are strongly dependent on its morphology, size and crystallinity. Thus far, several morphologies of ZnO have been reported by using various synthetic methods and used in the photovoltaic application.[59–69] Hydrothermal route has some advantages over other synthetic route in terms of getting highly pure and crystalline product.

Figure **1.3.1** shows the as-synthesized ZnO morphologies which are utilized as a metal oxide scaffold for DSSC/QDDSC devices of present thesis work. Usually, ZnO nanoparticles (0–D) offer high specific surface area for better loading of sensitizer particles, helpful to improve the light harvesting efficiency of solar device. 0–D structures have drawback in term of having high population of trap sites for recombination of photoexcited electron and also follow the random pathway before collecting at FTO.[70] In general, 1–D ZnO nanostructures (nanowires and nanorods) have shown their importance as excellent transportation of photo-excited electrons but has limitations in terms of less exposed surface area for sensitizer loading, due to which the efficiency of solar device become very less.[71–72] ZnO nanodisks (2–D) have provided more interfacial area for promoting the better charge transfer kinetics at different interfaces. They also show large exposed surface area for sensitizer loading to enhance the light harvesting efficiency.[73]

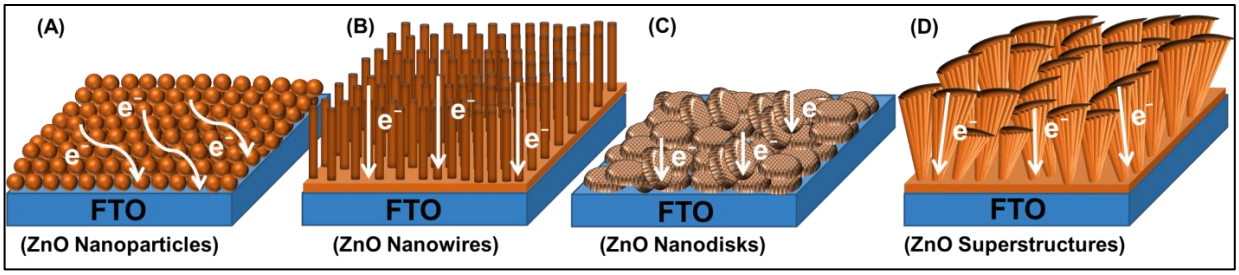


**Figure 1.3.1** Graphical illustration of different ZnO morphological structures such as **(A)** zero dimensional (0–D) ZnO nanoparticles, **(B)** one dimensional (1–D) nanowires, **(C)** two dimensional (2–D) nanodisks and three dimensional (3–D) superstructures, utilized for the fabrication of photoanodes. Different morphological structures are accountable for getting distinct photovoltaic properties based on charge transport, specific surface area and light scattering phenomenon.

Fabrication of 3–D hierarchical structure assembled with 1–D nanocrystal possess superior surface area for higher loading of light harvesting molecule, exceptional light scattering capability and faster transport of photogenerated electrons. Furthermore, porous nature of 2–D and 3–D structures is helpful for better infiltration of redox couple in the photovoltaic devices. In the recent trends, combinations of controlled shape micro/nanostructured materials are explored for the development of highly efficient DSSC/QDSSC devices. Various morphologies of ZnO are employed as an electron transporting material in DSSC devices to enhance the photovoltaic conversion efficiency, summarized in the table **1.3.2**. Conventional templating agents utilized to synthesize different ZnO structures, have several limitations like high cost, difficult to remove and environment unfriendly. Therefore, biomass derived templating agents can be used to tune the crystal growth behaviour of ZnO. Nature has wide range of materials which are used as the bio-templates to synthesize micro-and nano-scaled inorganic materials with numerous morphologies and more often these structures mimic the bio-template as a result of biomorphic mineralization process.[91] Various naturally abundant bio-species have been explored as templating agents in biomimetic synthetic protocols to fabricate the inorganic nanomaterials.[92–99] Subsequently, it is necessary to understand the growth mechanism for the development of new synthetic methodologies based on bio-templating route. It is believed that 3–D hierarchical structures are basically constructed through the nonclassical self-oriented attachment of nanocrystals,[100] in which high energy surfaces are eliminated by the epitaxial attachment of nanocrystals.

**Table 1.3.2** Tabular data is demonstrating the dependency of photovoltaic performance on different morphological structures of ZnO and its composites by fabricating DSSC devices.

| ZnO Structures | Sensitizer | $J_{sc}$ (mA.cm$^{-2}$) | $V_{oc}$ (mV) | FF (%) | η (%) | Ref. |
|---|---|---|---|---|---|---|
| Nanorods like structures | N719 | 23.2 | 620 | 57 | 8.2 | 60 |
| Hierarchical aggregates | N719 | 19.8 | 640 | 59 | 7.5 | 74 |
| Nanowires (NWs) arrays assembly | N719 | 15.3 | 780 | 59 | 7.0 | 61 |
| Commercial nanopowder | N719 | 18.1 | 621 | 58 | 6.6 | 75 |
| ZnO tetrapods/$SnO_2$ nanoparticles | N719 | 16.3 | 656 | 59 | 6.3 | 76 |
| ZnO aggregates/$TiO_2$ shell | N3 | 15.8 | 709 | 56 | 6.3 | 77 |
| Nanocrystalline aggregates | N3 | 21 | 660 | 44 | 6.1 | 78 |
| ZnO nanosheet | D149 | 18.0 | 530 | 63 | 6.1 | 59 |
| Oriented porous films | D149 | 12.2 | 690 | 65 | 5.6 | 79 |
| Nanoparticles/Hollow cavities | N719 | 15.7 | 563 | 62 | 5.5 | 80 |
| Nanoparticles | D102 | 17.4 | 630 | 48 | 5.4 | 62 |
| Hierarchical aggregates | N3 | 18.7 | 635 | 45 | 5.4 | 81 |
| Nanoparticles | CYC-B1 | 16.1 | 570 | 59 | 5.4 | 82 |
| Hierarchical aggregates | D205 | 12.2 | 653 | 67 | 5.3 | 83 |
| ZnO/$Nb_2O_5$ shell | N719 | 12.4 | 712 | 59 | 5.2 | 84 |
| Caterpillar like ZnO Array | N719 | 15.2 | 690 | 50 | 5.2 | 63 |
| ZnO Nanoparticles/Buffer layer | N719 | 11.8 | 670 | 64 | 5.0 | 85 |
| Tetrapod-like ZnO nanopowder | D149 | 12.4 | 607 | 65 | 4.9 | 64 |
| Nanosheet/Nanowires | N719 | 10.9 | 680 | 65 | 4.8 | 86 |
| Self-assembled nanostructures | N719 | 10.7 | 710 | 62 | 4.7 | 65 |
| Nanocones | N719 | 15 | 640 | 45 | 4.3 | 66 |
| ZnO Nanowires/Nanoparticles | N3 | 15.2 | 610 | 46 | 4.2 | 87 |
| Hierarchical NWs/Nanoporous layer | D419 | 12.3 | 570 | 58 | 4.1 | 88 |
| Mesoporous film | N719 | 11.8 | 650 | 52 | 4.0 | 89 |
| Rectangular Prism | N719 | 8.9 | 730 | 51 | 3.3 | 67 |
| Hierarchical Nanowires | N719 | 8.8 | 680 | 53 | 2.6 | 90 |
| Nanoflower | N719 | 5.5 | 650 | 53 | 1.9 | 68 |
| Nanotubes | N719 | 3.3 | 739 | 64 | 1.6 | 69 |

Although, usability of ZnO nanostructures as photoanodic layer in DSSC devices has significantly increased in last decade but the highest reported efficiency value (~ 8.2 %) is still very less as compared to conventional $TiO_2$ based DSSC device.[9] As-observed lower PCE value of ZnO based DSSC devices is accredited to following two factors – (i) slower injection of photoexcited electron from dye to CB of ZnO, owing to formation of electrically bound (electron–dye cation) pairs after dye excitation and (ii) instability and etching of ZnO layer because of lesser chemical stability in acidic environment of dye sensitization process and formation of ($Zn^{2+}$–dye) complexes.[101] These complexes [($Zn^{2+}$–dye) complexes] are unable to inject the photoexcited electrons from dye to metal oxide under solar light irradiation. Dye

concentration and loading time can reduce the probability of ($Zn^{2+}$–dye) complex formation.[102] Recently, various morphologies of ZnO with excellent electron transport property have also been explored to improve the photovoltaic performance of QDSSC devices. Semiconductor QDs have several advantages over the organic dye molecules such as tuning the optical properties based on QDs size,[103] larger extinction coefficients,[104] multiple exciton generation,[105] higher stability *etc*. Suitability of inorganic sensitizer based on their energy band edges and extinction co-efficient is believed to be very crucial to enrich the efficiency of solar devices. Binary metal sulfide based sensitizer materials have limitation in terms of getting high efficiency. So, ternary metal chalcogenides based on system I–V–$VI_2$, have gained significant attention as light absorber due to their suitable energy bandgap with high extinction co-efficient and plentiful availability of raw materials.[106] So far, various ternary metal chalcogenides such as $CuInS_2$, $AgInS_2$, $CuInSe_2$, $AgSbS_2$, $AgBiS_2$, $CuSbS_2$ and $CuSbSe_2$ etc. have been used as absorbers to improve the efficiency of solar devices.[107–111] Among these ternary metal chalcogenides, copper antimony sulfide ($CuSbS_2$) has been considered as an ideal solar absorbers due to its bandgap (1.5 eV), high extinction coefficient ($10^5$ $M^{-1}cm^{-1}$) and crystallization at lower temperature, showing spectroscopic limited maximum efficiency (SLME) of about 23 %.[112]

However, nanoparticles based photoanodes are not suitable to get a high PCE value of QDSSC devices, owing to blockage the mesopores during the QDs sensitization, resulting in poor penetration of redox electrolyte for efficient regeneration of oxidized QDs. For considering the factors of smooth diffusion of electrolyte and better electron transportation, 1–D ZnO nanostructures having open end are used and got a efficiency of about ~ 6.2 %.[113–114] However, photoanodes based on these 1–D structures are generally suffers with inadequate loading of sensitizer particles which limit the PCE value of QDSSC devices. So, combination of different nanostructures such as, double-layer ZnO nanorod–nanotetrapod,[115] ZnO nanoparticles–porous microspheres,[116] *etc*. based hybrid photoanodes are utilized to improve the loading of QDs, and achieved the PCE of more than 5 %. Hybrid photoanodic structure provides a possibility to utilize advantageous gains of different morphological structures in a single photoanode and notice further enhancement in light conversion efficiency of QDSSC devices. Various photoanodic architectures based on several morphologies of ZnO are demonstrated for enhanced photovoltaic performance of ZnO based QDDSC, display in Table **1.3.3**.

**Table 1.3.3** An overview related to different Photoanodic architectures based on ZnO morphologies, utilized for evaluating photovoltaic performance of semiconductor sensitized solar devices.

| Photoanodic Architecture | $J_{sc}$ (mA.cm$^{-2}$) | $V_{oc}$ (mV) | FF (%) | η (%) | Ref. |
|---|---|---|---|---|---|
| ZnO tetrapods/CdSe/ZnSe | 17.3 | 760 | 47 | 6.2 | 113 |
| ZnO nanorods/CdS/CdSe | 16.5 | 700 | 45 | 5.2 | 115 |
| ZnO microsphere/CdS/CdSe | 17.1 | 560 | 53 | 5.1 | 116 |
| ZnO nanoparticles/CdS/CdSe | 10.4 | 683 | 62 | 4.4 | 117 |
| ZnO nanowire array/CdS/CdSe | 17.3 | 627 | 38 | 4.1 | 118 |
| ZnO nanorods/nanosheets/CdS/CdSe | 10.7 | 610 | 50 | 3.2 | 114 |
| ZnO nanoparticles/CdS/$CuSbS_2$ | 15.6 | 470 | 43 | 3.2 | 119 |
| ZnO nanoparticles/CdS/$CuSbS_2$ | 14.7 | 490 | 44 | 3.1 | 120 |
| ZnO nanoparticles/CdS nanorods | 7.3 | 703 | 54 | 2.8 | 121 |
| ZnO nanosheets/CdS/CdSe | 19.3 | 490 | 28 | 2.6 | 122 |
| ZnO nanorods/g-$C_3N_4$/CdS | 11.1 | 650 | 34 | 2.4 | 123 |
| ZnO nanowires/mesospheres/CdS | 9.0 | 511 | 51 | 2.4 | 124 |
| ZnO hierarchical nanowires array/CdS | 7.3 | 700 | 31 | 1.6 | 125 |
| ZnO nanowires/$CuSbS_2$ | 5.9 | 491 | 56 | 1.6 | 41 |
| ZnO nanowires/CdS | 5.4 | 580 | 34 | 1.1 | 126 |
| ZnO nanoparticles/CdS/$CuSbS_2$ | 8.9 | 309 | 31 | 0.9 | 40 |

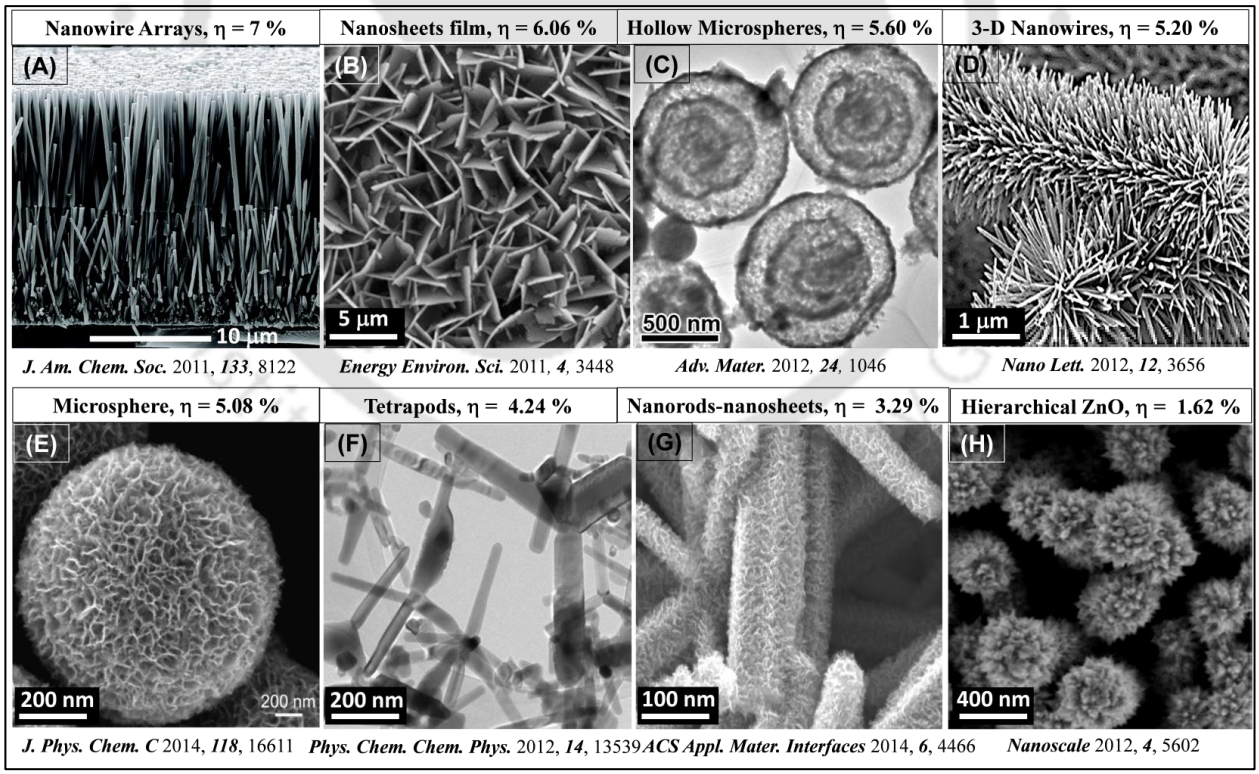


**Figure 1.3.2** Some examples related to utilization of different morphological structures of ZnO, as photoanodic scaffold in dye sensitized solar cells [traces **(A)**, **(B)**, **(C)** & **(D)**] and semiconductor sensitized solar cells [traces **(E)**, **(F)**, **(G)** & **(H)**].

Some examples of ZnO morphologies and their utilization to fabricate the photoanodes of DSSC devices [traces **(A)**, **(B)**, & **(C)**] and QDSSC devices [traces **(D)**, **(E)** & **(F)**] are depicted in figure **1.3.2**.

## 1.4 BASIC INTRODUCTION OF CHEMICAL SENSOR

In the past few decades, living standard of human beings has been improved with the continuous industrial revolution. With the development of several technologies, environmental safety issues become an alarming factor for human and living animals. However, industrialization needs the detection and monitoring of the released toxic pollutants and gases. Therefore, it is necessary to develop sensors which can easily monitor these toxic and inflammable gases at ambient conditions. Sensor is a transducer which can identifies the changes in a measurable quantity and converts it into corresponding output signal process-able by a data acquisition system. At the present time, sensors are generally used in most of the everyday operations like touch sensitive elevators buttons and dimming/brightening lamps by touching their base. Chemical sensors play an important role in the detection and monitoring of various toxic and harmful gases,[127] that are generated due to rapid industrialization, combustion of fuels and the use of agro-chemicals. Basically, a chemical sensor recognizes and is sensitive to the chemical composition of its surrounding environment. Sensing signals is directly correlated with type and concentration of analyte. In a biological system, receptor organs identify and transfer signals to the brain through sensory neurons. Likewise, in technological systems active sensing material acts as a receptor that responds to its environment by changing its inherent property. Transducer changes the physical information into electrical signals which is then transferring to data acquisition system i.e. a computer; behave similarly to the central nervous system of brain.

In 1991, International Union of Pure and Applied Chemistry (IUPAC) has been defined chemical sensor as chemical sensor is defined by as *"A chemical sensor is a device that transforms chemical information, ranging from concentration of a specific sample component to total composition analysis, into an analytically useful signal"*.[128] Chemical sensor can be classified into various types based on operating principle of transducer,[129] as shown in figure **1.4.1**.

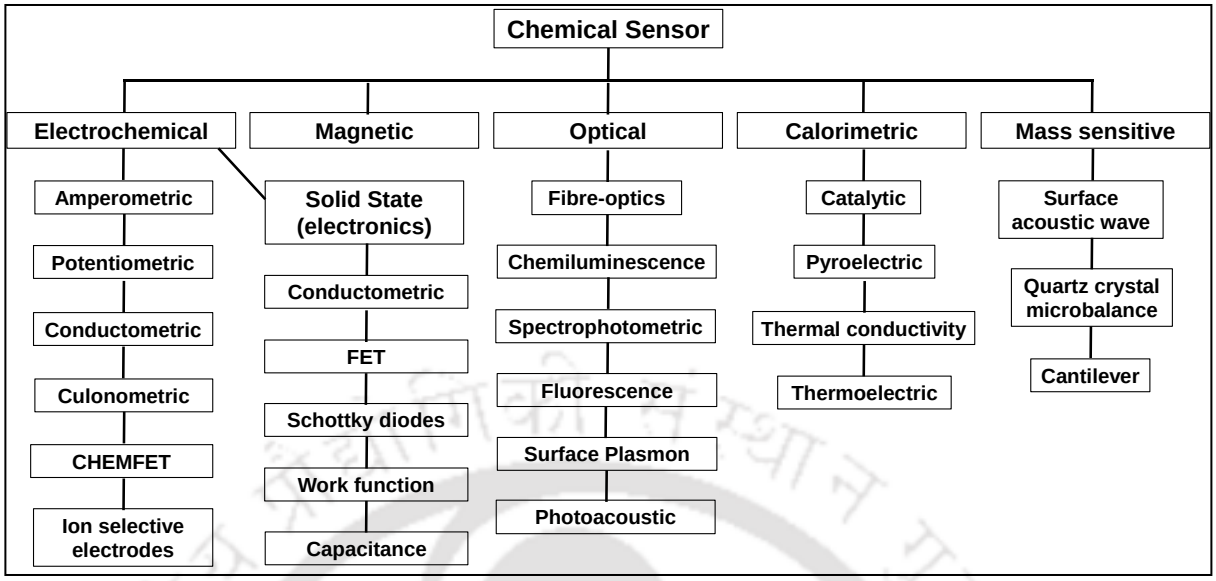


**Figure 1.4.1** Classification of chemical sensors based on operating principle of transducer.

Among the various volatile toxic gases, ammonia ($NH_3$) detection has been gained notable consideration due to its toxic and corrosive impact on the atmosphere and human health.[130–131] Ammonia has been extensively utilized in many applications such as agrochemicals, pharmaceuticals, organic dyes, synthetic fibers, and it can diffuse into the atmosphere and cause severe effects on human health as well as the environment.[132] Ammonium nitrate is usually found in many explosives and they release trace amounts of ammonia upon decomposition, the monitoring of which is very crucial in order to prevent lethal accidents. Therefore, it is necessary to develop a highly-sensitive room-temperature efficient $NH_3$ gas sensor. The exposure limit of $NH_3$ Vapors is 25 parts per million (ppm) for 8 h at the working sites, while the short-term exposure limit is 35 ppm for 15 min, as set by the Occupational Safety & Health Administration (OSHA).[133] Ammonia vapor sensors based on various conducting materials, potentiometric electrodes, infrared devices and metal oxides have been explored,[131, 133–134] and among them, metal oxide-based $NH_3$ sensors are commonly preferred due to their high sensitivity and low fabrication cost. In present work, ammonia vapors have been sensed by fabricating ZnO nanostructures based chemiresistor devices.

### 1.4.1 GAS SENSOR

Gas sensor is considered to be a subdivision of chemical sensor. It shows various applications like controlling the industrial processes and also monitoring the toxic gases released

into the atmosphere. So, there is always a necessity to develop a gas sensor which is selective to a particular gas. In general, working principle of a gas sensor should possess two main functions which are; identification of analyte species and translate physical senses to a sensor signal. Identification of analyte species happens as a result of adsorption or chemical interaction of analyte molecules with sensing materials. Translating sensor signals relate to material being used for analyte detection.

Generally, there are three main types of gas sensors; electrochemical, pellistor, and conductometric or chemiresistance sensors, are mainly available in market and produced at large scale.[135] In the present thesis, conductometric or chemiresistor device is used for detection of ammonia gas vapors. Based on the performance parameters, comparative studies of different types of gas sensor are summarized in table **1.4.1**.[136]

**Table 1.4.1** Comparative analysis of different types of gas sensors based on their performance parameters.

| **Parameter** | **Type of Gas Sensors** | | | | |
|---|---|---|---|---|---|
| | Semiconducting | Catalytic combustion | Electrochemical | Thermal conductive | Infrared absorption |
| **Sensitivity** | e | g | g | b | e |
| **Accuracy** | g | g | g | g | e |
| **Selectivity** | p | b | g | b | e |
| **Response Time** | e | g | p | g | p |
| **Stability** | g | g | b | g | g |
| **Durability** | g | g | p | g | e |
| **Maintenance** | e | e | g | g | p |
| **Cost** | e | e | g | g | p |
| **Suitability to portable instruments** | e | g | p | g | b |
| **e : excellent, g : good, p : poor, b : bad** | | | | | |

### 1.4.1.1 SEMICONDUTOR METAL OXIDES BASED CHEMIRESISTOR GAS SENSOR

Chemiresistor sensor devices based on semiconductor metal oxides are extensively utilized to detect toxic and inflammable gases, owing to their ease of operation and low cost. Generally, these devices notice changes in their electrical properties due to the gas–solid interaction.[137] Chemiresistor sensor (figure **1.4.2)** is working using similar principle as gas sensor, showing a change in resistance or conductance, upon exposure to the target analyte. Change in resistance of sensor device is mainly attributed to surface induced adsorption, desorption and oxidation reactions of the analyte molecules on the surface of sensing material,

resulting in changing the charge carrier concentration which act as source for changes in electrical resistance.[138] Semiconducting metal oxides based chemiresistor sensors show high sensitivity, faster response time, stability and low cost.

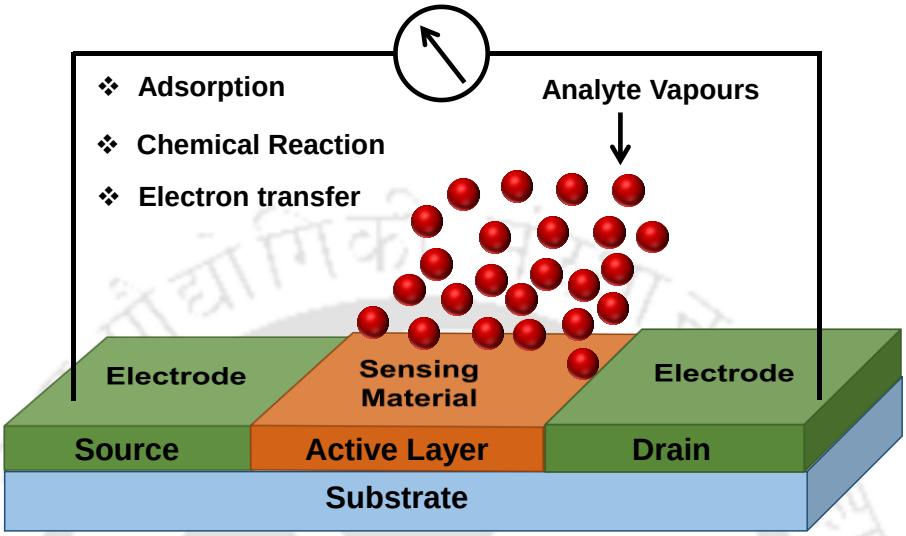


**Figure 1.4.2** Schematic illustration of a chemiresistor device, fabricated by sandwiching the sensing material between two electrodes act as source and drain respectively.

Performance of a chemiresistor device can be evaluated based on the parameters which are responsivity, selectivity, response/recovery times, reproducibility, repeatability and stability. Responsivity is most fundamental parameters, defined as a sensor output with the amount of analyte applied as input to sensing system. Selectivity of sensor is another parameter, described as showing sensing response to a particular analyte. Rapid response time ($t_{90}$), time taken by a sensor for responding from zero concentration to a change in concentration and fast recovery time ($t_{-90}$), time required for a sensor to reach to its initial point, are also important factors to decide the sensor applicability in different environments. Reproducibility and repeatability of the sensor device is crucial for real use application and also support to the reliability of sensor device. Stability of a sensor device is defined as no changes in sensing signal after a period of time, is considered to be another important parameter to decide the accuracy of sensor device.

Performance parameters of a chemiresistor sensor can be enhanced by controlling the crystallite phase, grain size, morphology, and by making heterojunction with several metal atoms or metal oxides. Morphology of sensing material can also affect the physicochemical properties by improving the sensing activity and thermochemical stability. Several morphologies of ZnO and its composites have been utilized for ammonia gas detection, are summarized in table **1.4.2**.

**Table 1.4.2** An overview of various ZnO morphologies and its composites used as active sensing materials for ammonia gas sensing application.

| Sensing Material Composition | Sensing Limit; Limit of detection (LOD) | Response Time (s) | Recovery Time (s) | Ref. |
|---|---|---|---|---|
| Au doped ZnO nanorods | 100 ppm | 22 | 57 | 139 |
| Reduced GO/ZnO NWs | 50 ppm | 50 | 250 | 140 |
| ZnO spherical nanostructures | 25 ppm | 20 | 25 | 141 |
| Ce doped ZnO | 25 ppm | 18 | 12 | 142 |
| Mn doped ZnO microspheres | 20 ppm | 4 | 10 | 143 |
| ZnO nanorod arrays | 20 ppm | 200 | 800 | 144 |
| Cu-doped ZnO nanorods | 10 ppm | 13 | 15 | 145 |
| Ag doped ZnO nanorod flower | 10 ppm | 13 | 20 | 146 |
| Ni-doped ZnO micro-discs | 10 ppm | 18 | 50 | 147 |
| Carbon nanotubes/ ZnO NWs | 4 ppm | 25 | 18 | 148 |
| ZnO hierarchical 3D-flower | 2 ppm | 45 | 17 | 149 |
| Au doped ZnO nanowires (NWs) | 0.5 ppm | 20 | 22 | 150 |
| Graphene oxide (GO)/ZnO NWs | 0.5 ppm | 2 | 36 | 151 |
| $Fe_2O_3$–ZnO nanocomposite | 0.4 ppm | 20 | 20 | 152 |
| Carbon nanotubes/ ZnO tetrapods | 0.2 ppm | 18 | 35 | 153 |

Figure **1.4.3** [traces **(a-f)**] shows some examples of ZnO morphologies which are employed as sensing material for detection of ammonia gas vapors.

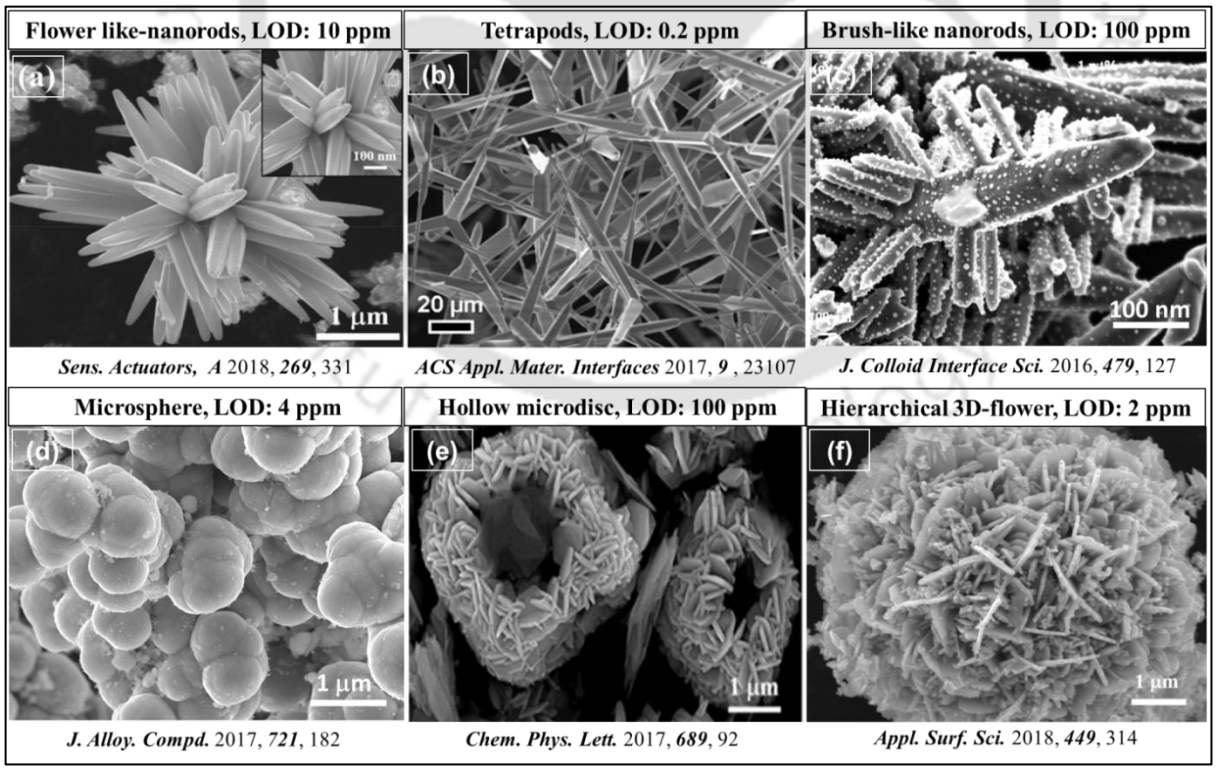


**Figure 1.4.3** Different morphologies of ZnO [traces **(a)**, **(b)**, **(c)**, **(d)**, **(e)** and **(f)**] employed as active sensing materials for ammonia gas sensing.

## 1.5 CONCLUSIONS AND OUTLOOK

Several attempts have been utilized to optimize the photoanodic architecture of photoanodes by using various morphologies of ZnO and their composites. Based on these efforts, ZnO based DSSC device has achieved highest efficiency of about ~ 8.2 % while ~ 6.2 % for QDSSC device. Therefore, further progress is required for ZnO based photovoltaic devices for their commercialization. Accordingly, several approaches can be incorporated to enhance the performance of ZnO based photovoltaic devices. Light harvesting efficiency of ZnO based photoanodes can be improved by using the light scattering materials and sensitizer with broad absorption profile. Efficient charge separation and transfer in photoanodic segment can be accomplished by utilizing core-shell structures and blocking layers. All these approaches are promising for construction of highly efficient photoanodes for better energy conversion. However, it is still difficult to optimize and incorporate these essential attributes in a single photoanode for enriching the light harnessing ability. So, execution of several other methods is highly needed for fabrication of efficient photoanodic architecture which brings a new hope for improving the sensitized photovoltaic technology.

## 1.6 MOTIVATION AND OBJECTIVES OF THE PRESENT WORK

Due to having high electron mobility, ease of crystallization and anisotropic crystal growth behaviour, ZnO is believed to be a virtuous candidate for using as a photoanodic material in DSSC and QDSSC devices. Additionally, appropriate energy band positions of ZnO can easily make composites with well-matched semiconductor metal oxide, helpful for improving light harvesting ability as well as charge transfer kinetics of photoanode. Based on these intrinsic properties, we have anticipated to further enhancement in the solar light conversion capability of ZnO based dye as well as semiconductor quantum dot sensitized solar cell devices. The objectives of the present thesis work are as follows:

- Rational design and development of different morphologies of ultraviolet (UV) and visible (Vis) light absorbing semiconductor materials
- Fabrication of different photoanodic architectures by employing the various morphologies of ZnO, synthesized using biomass derived templating agents
- Utilizing several light absorbing materials for ZnO based DSSC and QDDSC devices according to well–matched energy band positions for better charge injection

- Measurement of morphology dependent photovoltaic performance parameters of as-fabricated dye/quantum dot sensitized solar devices
- Study the kinetics of photoexcited electron transfer and recombination processes for better understanding of photovoltaic properties
- Fabrication of chemiresistor devices using different morphologies of ZnO and evaluate the sensing performance for ammonia gas sensing

## 1.7 REFERENCES


(1) *IPCC Panel Reports on Climate Change and Biodiversity*, April 2002.

(2) R. Gross, M. Leach and A. Baven, *Environ. Int.*, 2003, **29**, 105–122.

(3) D. M. Bagnall and M. Boreland, *Energy Policy*, 2008, **36**, 4390–4396.

(4) M. A. Green, Y. Hishikawa, E. D. Dunlop, D. H. Levi, J. H. Ebinger, M. Yoshita and A. W. Y. Ho-Baillie, *Prog. Photovolt: Res. Appl.*, 2019, **27**, 3–12.

(5) A. Shah, P. Torres, R. Tscharner, N. Wyrsch and H. Keppner, *Science*, 1999, **285**, 692–698.

(6) M. R. Kim and D. Ma, *J. Phys. Chem. Lett.*, 2015, **6**, 85–99.

(7) W. Shockley and H. J. Queisser, *J. Appl. Phys.*, 1961, **32**, 510.

(8) B. O'Regan and M. Grätzel, *Nature*, 1991, **353**, 737–740.

(9) S. Mathew, A. Yella, P. Gao, R. Humphry-Baker, B. F. E. Curchod, N. Ashari-Astani, I. Tavernelli, U. Rothlisberger, M. K. Nazeeruddin and M. Grätzel, *Nat. Chem.*, 2014, **6**, 242–247.

(10) P. V. Kamat, *J. Phys. Chem. Lett.*, 2013, **4**, 908–918.

(11) J. E. Randy, C. B. Matthew, C. J. Justin, Y. Pingrong, I. M. Olga, J. N. Arthur, S. Andrew and L. E. Alexander, *Nano Lett.*, 2005, **5**, 865–871.

(12) J. Xu, O. Voznyy, M. Liu, A. R. Kirmani, G. Walters, R. Munir, M. Abdelsamie, A. H. Proppe, A. Sarkar, F. P. G. de Arquer, M. Wei, B. Sun, M. Liu, O. Ouellette, R. Quintero-Bermudez, J. Li, J. Fan, L. Quan, P. Todorovic, H. Tan, S. Hoogland, S. O. Kelley, M. Stefik, A. Amassian and E. H. Sargent, *Nat. Nanotechnol.*, 2018, **13**, 456–462.

(13) J. B. Baxter, *J. Vac. Sci. Technol., A*, 2012, **30**, 020801.

(14) J. Goldstein, I. Yakupov and B. Breen, *Sol. Energy Mater. Sol. Cells*, 2010, **94**, 638–641.

(15) Y. Chiba, A. Islam, K. Kakutani, R. Komiya, N. Koide and L. Han, 15th International Photovoltaic Science and Engineering Conference, Shanghai, October 2005, 665–666.

(16) M. K. Kashif, M. Nippe, N. W. Duffy, C. M. Forsyth, C. J. Chang, J. R. Long, L. Spiccia and U. Bach, *Angew. Chem. Int. Ed.*, 2013, **52**, 5527–5531.

(17) I. Mora-Seró, S. Giménez, F. Fabregat-Santiago, R. Gómez, Q. Shen, T. Toyoda and J. Bisquert, *Acc. Chem. Res*, 2009, **42**, 1848–1857.

(18) A. Hagfeldt, G. Boschloo, L. Sun, L. Kloo and H. Pettersson, *Chem. Rev.*, 2010, **110**, 6595–6663.

(19) G. Ramakrishna, D. A. Jose, D. K. Kumar, A. Das, D. K. Palit and H. N. Ghosh, *J. Phys. Chem. B*, 2005, **109**, 15445–15453.

(20) G. Benko, J. Kallioinen, J. E. I. Korppi-Tommola, A. P. Yartsev and V. Sundstrom, *J. Am. Chem. Soc.*, 2002, **124**, 489–493.

(21) S. A. Haque, E. Palomares, B. M. Cho, A. N. M. Green, N. Hirata, D. R. Klug and J. R. Durrant, *J. Am. Chem. Soc.*, 2005, **127**, 3456–3462.

(22) G. Hodes, *J. Phys. Chem. C*, 2008, **112**, 17778–17787.

(23) J. E. Evans, K. W. Springer and J. Z. Zhang, *J. Chem. Phys.*, 1994, **101**, 6222.

(24) I. Hod, V. González-Pedro, Z. Tachan, F. Fabregat-Santiago, I. Mora-Seró, J. Bisquert and A. Zaban, *J. Phys. Chem. Lett.*, 2011, **2**, 3032–3035.

(25) K. Zhao, Z. Pan and X. Zhong, *J. Phys. Chem. Lett.*, 2016, **7**, 406–417.

(26) P. V. Kamat, *Acc. Chem. Res.*, 2012, **45**, 1906–1915.

(27) I. Robel, V. Subramanian, M. Kuno and P. V. Kamat, *J. Am. Chem. Soc.*, 2006, **128**, 2385–2393.

(28) P. Santra and P. V. Kamat, *J. Am. Chem. Soc.*, 2013, **135**, 877–885.

(29) E. Barea, M. Shalom, S. Giménez, I. Hod, I. Mora-Seró, A. Zaban and J. Bisquert, *J. Am. Chem. Soc.*, 2010, **132**, 6834–6839.

(30) B. O'Regan, J. Moser, M. Anderson and M. Grätzel, *J. Phys. Chem.*, **1990**, *94*, 8720–8726.

(31) J. Bisquert, D. Cahen, G. Hodes, S. Ruhle and A. Zaban, *J. Phys. Chem. B*, 2004, **108**, 8106–8118.

(32) L. Kavan and M. Grätzel, *Electrochim. Acta*, 1995, **40**, 643–652.

(33) S. Ito, P. Liska, P. Comte, R. L. Charvet, P. Pechy, U. Bach, L. Schmidt-Mende, S. M. Zakeeruddin, A. Kay, M. K. Nazeeruddin, M. Grätzel, *Chem. Commun.*, 2005, **0**, 4351–4353.

(34) S. Chappel, S.-G. Chen and A. Zaban, *Langmuir*, 2002, **18**, 3336–3342.

(35) A. Kay and M. Grätzel, *Chem. Mater.*, 2002, **14**, 2930–2935.

(36) I. Concina and A. Vomiero, *Small*, 2015, **11**, 1744–1774.

(37) H. Rensmo, K. Keis, H. Lindström, S. Södergren, A. Solbrand, A. Hagfeldt, S.-E. Lindquist, L. N. Wang and M. Muhammed, *J. Phys. Chem. B*, 1997, **101**, 2598–2601.

(38) K. S. Leschkies, R. Divakar, J. Basu, E. Enache-Pommer, J. E. Boercker, C. B. Carter, U. R. Kortshagen, D. J. Norris and E. S. Aydil, *Nano Lett.*, 2007, **7**, 1793–1806.

(39) H. J. Snaith and C. Ducati, *Nano Lett.*, 2010, **10**, 1259–1265.

(40) Md. A. Hossain, J. R. Jennings, Z. Y. Koh and Q. Wang, *ACS Nano*, 2011, **5**, 3172–3181.

(41) K. Sayama, H. Sugihara and H. Arakawa, *Chem. Mater.*, 1998, **10**, 3825–3832.

(42) J. H. Kang, Y. Myung, J. W. Choi, D. M. Jang, C. W. Lee, J. Park and E. H. Cha, *J. Mater. Chem.*, 2012, **22**, 8413–8419.

(43) S. Burnside, J.-E. Moser, K. Brooks, M. Grätzel and D. Cahen, *J. Phys. Chem. B*, 1999, **103**, 9328–9332.

(44) M. H. Huang, S. Mao, H. Feick, H. Yan, Y. Wu, H. Kind, E. Weber, R. Russo and P. Yang, *Science*, 2001, **292**, 1897–1899.

(45) F. Xu and L. Sun, *Energy Environ. Sci.*, 2011, **4**, 818–841.

(46) Ü. Özgür, Ya. I. Alivov, C. Liu, A. Teke, M. A. Reshchikov, S. Doğan, V. Avrutin, S.-J. Cho and H. Morkoç, *J. Appl. Phys.*, 2005, **98**, 041301.

(47) U. Diebold, *Surf. Sci. Rep.*, 2003, **48**, 53–229.

(48) D. O. Scanlon, C. W. Dunnill, J. Buckeridge, S. A. Shevlin, A. J. Logsdail, S. M. Woodley, C. R. A. Catlow, M. J. Powell, R. G. Palgrave, I. P. Parkin, G. W. Watson, T. W. Keal, P. S. A. Walsh and A. A. Sokol, *Nat. Mater.*, 2013, **12**, 798–801.

(49) S. F. Matar, G. Campet and M. A. Subramanian, *Prog. Solid State Chem.*, 2011, **39**, 70–95.

(50) K. Tvrdy, P. A. Frantsuzov and P. V. Kamat, *Proc. Natl. Acad. Sci. USA.*, 2011, **108**, 29–34.

(51) G. Oskam, Z. Hu, R. L. Penn, N. Pesika and P. C. Searson, *Phys. Rev. E*, 2002, **66**, 011403.

(52) H. Tang, K. Prasad, R. Sanjinès, P. E. Schmid and F. Lévy, *J. Appl. Phys.*, 1994, **75**, 2042.

(53) P. Tiwana, P. Docampo, M. B. Johnston, H. J. Snaith and L. M. Herz, *ACS Nano*, 2011, **5**, 5158–5166.

(54) K. F. Young and H. P. R. Frederikse, *J. Phys. Chem. Ref. Data*, 1973, **2**, 313.

(55) G.-D. Yuan, W.-J. Zhang, J.-S. Jie, X. Fan, J.-X. Tang, I. Shafiq, Z.-Z. Ye, C.-S. Lee and S.-T. Lee, *Adv. Mater.*, 2008, **20**, 168–173.

(56) C. X. Xu, X. W. Sun and B. J. Chen, *Appl. Phys. Lett.*, 2004, **84**, 1540.

(57) R.-C. Wang, C.-P. Liu, J.-L. Huang and S.-J. Chen, *Appl. Phys. Lett.*, 2006, **88**, 023111.

(58) N. S. Ramgir, I. S. Mulla and V. K. Pillai, *J. Phys. Chem. B*, 2006, **110**, 3995–4001.

(59) C. Y. Lin, Y. H. Lai, H. W. Chen, J. G. Chen, C. W. Kung, R. Vittal and K. C. Ho, *Energy Environ. Sci.*, 2011, **4**, 3448–3455.

(60) Y. Xie, X. Zhou, H. Mi, J. Ma, J. Yang and J. Cheng, *Appl. Surf. Sci.*, 2018, **434**, 1144–1152.

(61) C. Xu, J. Wu, U. V. Desai and D. Gao, *J. Am. Chem. Soc.*, 2011, **133**, 8122–8125.

(62) S. B. Ambade, R. S. Mane, S.-H. Han, S.-H. Lee, M.-M. Sung and O.-S. Joo, *J. Photochem. Photobiol., A*, 2011, **222**, 366–369.

(63) M. McCune, W. Zhang and Y. Deng, *Nano Lett.*, 2012, **12**, 3656−3662.

(64) W. H. Chiu, C. H. Lee, H. M. Cheng, H. F. Lin, S. C. Liao, J. M. Wu and W. F. Hsieh, *Energy Environ. Sci.*, 2009, **2**, 694–698.

(65) A. Ranga Rao and V. Dutta, *Nanotechnology*, 2008, **19**, 445712.

(66) J. Chang, R. Ahmed, H. Wang, H. Liu, R. Li, P. Wang and E. R. Waclawik, *J. Phys. Chem. C*, 2013, **117**, 13836–13844.

(67) F. A. Al-Agela, M. S. Akhtarb, H. Alshammaric, A. Alshammaria and S. A. Khand, *Mater. Lett.*, 2015, **147**, 119–122.

(68) C. Y. Jiang, X. W. Sun, G. Q. Lo, D. L. Kwong and J. X. Wang, *Appl Phys Lett.*, 2007, **90**, 263501.

(69) A. B. F. Martinson, J. W. Elam, J. T. Hupp and M. J. Pellin, *Nano Lett.*, **2007**, *7*, 2183–2187.

(70) M. Law, L. E. Greene, J. C. Johnson, R. Saykally and P. Yang, *Nat. Mater.*, 2005, **4**, 455–459.

(71) H.-Y. Chen, D.-B. Kuang and C.-Y. Su, *J. Mater. Chem.*, 2012, **22**, 15475–15489.

(72) Q. Zhang, C. S. Dandeneau, X. Zhou and G. Cao, *Adv. Mater.*, 2009, **21**, 4087–4108.

(73) Y. Chen, L. Zhang, L. Ning, C. Zhang, H. Zhao, B. Liu and H. Yang, *Chem. Eng. J.*, 2015, **264**, 557–564.

(74) N. Memarian, I. Concina, A. Braga, S. M. Rozati, A. Vomiero and G. Sberveglieri, *Angew. Chem., Int. Ed.*, 2011, **50**, 12321–12325.

(75) M. Saito and S. Fujihara, *Energy Environ. Sci.*, 2008, **1**, 280–283.

(76) W. Chen, Y. Qiu, Y. Zhong, K. S. Wong and S. Yang, *J. Phys. Chem. A*, 2010, **114**, 3127–3138.

(77) K. Park, Q. Zhang, B. B. Garcia, X. Zhou, Y.-H. Jeong and G. Cao, *Adv. Mater.*, 2010, **22**, 2329–2332.

(78) Q. Zhang, C. S. Dandeneau, S. Candelaria, D. Liu, B. B. Garcia, X. Zhou, Y.-H. Jeong and G. Cao, *Chem. Mater.*, 2010, **22**, 2427–2433.

(79) T. Yoshida, J. B. Zhang, D. Komatsu, S. Sawatani, H. Minoura, T. Pauporte, D. Lincot, T. Oekermann, D. Schlettwein, H. Tada, D. Wohrle, K. Funabiki, M. Matsui, H. Miura and H. Yanagi, *Adv. Funct. Mater.*, 2009, **19**, 17–43.

(80) X. Sheng, Y. Zhao, J. Zhai, L. Jiang and D. Zhu, *Appl. Phys. A: Mater. Sci. Process.*, 2007, **87**, 715–719.

(81) Q. F. Zhang, T. R. Chou, B. Russo, S. A. Jenekhe and G. Z. Cao, *Angew. Chem., Int. Ed.*, 2008, **47**, 2402–2406.

(82) C. P. Lee, C. Y. Chou, C. Y. Chen, M. H. Yeh, L. Y. Lin, R. Vittal, C. G. Wu and K. C. Ho, *J. Power Sources*, 2014, **246**, 1–9.

(83) H.-M. Cheng and W.-F. Hsieh, *Energy Environ. Sci.*, 2010, **3**, 442–447.

(84) S. Ueno and S. Fujihara, *Electrochim. Acta*, 2011, **56**, 2906–2913.

(85) M. W. Pfau, A. Kunzmann, D. Segets, W. Peukert, G. G. Wallace, D. L. Officer, T. Clark, R. D. Costa and D. M. Guldi, *J. Mater. Chem. A*, 2017, **5**, 7516–7522.

(86) F. Xu, M. Dai, Y. N. Lu and L. T. Sun, *J. Phys. Chem. C*, 2010, **114**, 2776–2782.

(87) S. Yodyingyong, Q. F. Zhang, K. Park, C. S. Dandeneau, X. Y. Zhou, D. Triampo and G. Z. Cao, *Appl. Phys. Lett.*, 2010, **96**, 073115.

(88) V.-M. Guérin and T. Pauporté, *Energy Environ. Sci*., 2011, **4**, 2971–2979.

(89) G. Pérez-Hernández, A. Vega-Poot, I. Pérez-Juárez, J. M. Camacho, O. Arés, V. Rejón, J. L. Peña and G. Oskam, *Sol. Energy Mater. Sol. Cells.*, 2012, **100**, 21–26.

(90) S. H. Ko, D. Lee, H. W. Kang, K. H. Nam, J. Y. Yeo, S. J. Hong, C. P. Grigoropoulos and H. J. Sung, *Nano Lett.*, 2011, **11**, 666–671.

(91) A.-W. Xu, Y. Ma and H. Cölfen, *J. Mater. Chem.*, 2007, **17**, 415–449.

(92) D. Yang, L. Qi and J. Ma, *Adv. Mater.*, 2002, **14**, 1543–1546.

(93) S. R. Hall, H. Bolger and S. Mann, *Chem. Commun.*, 2003, **0**, 2784–2785.

(94) J. Huang, X. Wang and Z. L. Wang, *Nano Lett.*, 2006, **6**, 2325–2331.

(95) J. He, T. Kunitake and A. Nakao, *Chem. Mater.*, 2003, **15**, 4401–4406.

(96) J. Yin, Q. Lu, Z. Yu, J. Wang, H. Pang and F. Gao, *Cryst. Growth Des.*, 2010, **10**, 40–43.

(97) R. N. McMillan, C. D. Paavola, J. Howard, S. L. Chan, N. J. Zaluzec and J. D. Trent, *Nat. Mater.*, 2002, **1**, 247–252.

(98) Y.-H. Tseng, H.-Y. Lin, M.-H. Liu, Y.-F. Chen and C.-Y. Mou, *J. Phys. Chem. C*, 2009, **113**, 18053–18061.

(99) F. Waltz, G. Wismann, J. Lippke, A. M. Schneider, H.-C. Schwarz, A. Feldhoff, S. Eiden and P. Behrens, *Cryst. Growth Des.*, 2012, **12**, 3066–3075.

(100) S. Sotiropoulou, Y. Sierra-Sastre, S. S. Mark and C. A. Batt, *Chem. Mater.*, 2008, **20**, 821–834.

(101) T. Horiuchi, H. Miura, K. Sumioka and S. Uchida, *J. Am. Chem. Soc*., 2004, **126**, 12218–12219.

(102) K. Keis, J. Lindgren, S. E. Lindquist and A. Hagfeldt, *Langmuir*, 2000, **16**, 4688–4694.

(103) C. A. Leatherdale, W. K. Woo, F. V. Mikulec and M. G. Bawendi, *J. Phys. Chem. B*, 2002, **106**, 7619–7622.

(104) W. W. Yu, L. Qu, W. Guo and X. Peng, *Chem. Mater.*, **2003**, *15*, 2854–2860.

(105) M. T. Trinh, A. J. Houtepen, J. M. Schins, T. Hanrath, J. Piris, W. Knulst, A. P. L. M. Goossens and L. D. A. Siebbeles, *Nano Lett.*, **2008**, *8*, 1713–1718.

(106) X. Guo, Q. Tan, S. Liu, D. Qin, Y. Mo, L. Hou, A. Liu, H. Wu and Y. Ma, *Nano Energy*, 2018, **46**, 150–157.

(107) K. Ramasamy, H. Sims, W. H. Butler and A. Gupta, *J. Am. Chem. Soc.*, 2014, **136**, 1587–1598.

(108) Y. M. Tang, P. Wang, J. H. Yun, R. Amal and Y. H. Nq, *J. Mater. Chem. A*, 2015, **3**, 15876–15881.

(109) J. H. Han, Z. F. Liu, K. Y. Guo, J. Ya, Y. F. Zhao, X. Q. Zhang, T. T. Hong and J. Q. Liu, *ACS Appl. Mater. Interfaces*, 2014, **6**, 17119–17125.

(110) Y. R. Ho and M. W. Lee, *Electrochem. Commun.*, 2013, **26**, 48–51.

(111) P. C. Huang, W. C. Yang and M. W. Lee, *J. Phys. Chem. C*, 2013, **117**, 18308–18314.

(112) B. Yang, L. Wang, J. Han, Y. Zhou, H. Song, S. Chen, J. Zhong, L. Lv, D. Niu and J. Tang, *Chem. Mater.*, 2014, **26**, 3135–3143.

(113) K. Yan, L. Zhang, J. Qiu, Y. Qiu, Z. Zhu, J. Wang and S. Yang, *J. Am. Chem. Soc.*, 2013, **135**, 9531–9539.

(114) J. Tian, E. Uchaker, Q. Zhang and G. Cao. *ACS Appl. Mater. Interfaces*, 2014, **6**, 4466–4472.

(115) Z. Zhu, J. Qiu, K. Yan and S. Yang, *ACS Appl. Mater. Interfaces*, 2013, **5**, 4000–4005.

(116) J. Tian, L. Lv, X. Wang, C. Fei, X. Liu, Z. Zhao, Y. Wang and G. Cao, *J. Phys. Chem. C*, 2014, **118**, 16611−16617.

(117) C. Li, L. Yang, J. Xiao, Y.-C. Wu, M. Søndergaard, Y. Luo, D. Li, Q. Meng and B. B. Iversen, *Phys. Chem. Chem. Phys.*, 2013, **15**, 8710–8715.

(118) M. Seol, H. Kim, Y. Taka and K. Yong, *Chem. Commun.*, 2010, **46**, 5521−5523.

(119) S. Banu, S. J. Ahn, S. K. Ahn, K. Yoon and A. Cho, *Sol. Energy Mater. Sol. Cells*, 2016, **151**, 14–23.

(120) W. Septina, S. Ikeda, Y. Iga, T. Harada and M. Matsumura, *Thin Solid Films*, 2014, **550**, 700–704.

(121) D. Barpuzary and M. Qureshi, *ACS Appl. Mater. Interfaces*, 2013, **5**, 11673−11682.

(122) Q. Hou, L. Zhu, H. Chen, H. Liu and W. Li, *Electrochim. Acta*, 2013, **94**, 72−79.

(123) T. R. Chetia, M. S. Ansari and M. Qureshi, *J. Mater. Chem. A*, 2016, **4**, 5528−5541.

(124) T. R. Chetia, D. Barpuzary and M. Qureshi, *Phys. Chem. Chem. Phys.*, 2014, **16**, 9625–9633.

(125) X.-Y. Chen, T. Ling and X.-W. Du, *Nanoscale*, 2012, **4**, 5602−5607.

(126) C.-Z. Yao, B.-H. Wei, L.-X. Meng, H. Li, Q.-J. Gong, H. Sun, H.-X. Ma and X.-H. Hu, *J. Power Sources*, 2012, **207**, 222–228.

(127) R. Kumar, O. Al-Dossary, G. Kumar and A. Umar, *Nano-Micro Lett.*, 2015, **7**, 97–120.

(128) A. Hulanicki, S. Glab and F. Ingman, *Pure Appl. Chem.*, 1991, **63**, 1247–1250.

(129) G. S. Korotchenkov, *Chemical Sensors: Comprehensive Sensors Technologies.* Solid-state Devices: Momentum Press; 2011.

(130) M. Appl, Wiley-VCH, New York, USA, 1999.

(131) C. Cannilla, G. Bonura, F. Frusteri, D. Spadaro, S. Trocinoc and G. Neri, *J. Mater. Chem. C*, 2014, **2**, 5778–5786.

(132) K. Wetchakun, T. Samerjai, N. Tamaekong, C. Liewhiran, C. Siriwong, V. Kruefu, A. Wisitsoraat, A. Tuantranont and S. Phanichphant, *Sens. Actuators, B*, 2011, **160**, 580–591.

(133) T. Grady, T. Butler, B. D. MacCraith, D. Diamond and M. A. McKervey, *Analyst*, 1997, **122**, 803–806.

(134) X. J. Huang and Y. K. Choi, *Sens. Actuators, B*, 2007, **122**, 659–671.

(135) A. Mandelis and C. Christofides, *Physics, chemistry and technology of solid state gas sensor devices*: John Wiley & Sons; 1993.

(136) G. Korotcenkov, *Mater. Sci. Eng., B*, 2007, **139**, 1–23.

(137) Q. Meng, F. Zhang, Y. Zang, D. Huang, Y. Zou, J. Liu, G. Zhao, Z. Wang, D. Ji, C. Di, W. Hu and D. Zhu, *J. Mater. Chem. C*, 2014, **2**, 1264–1269.

(138) G. F. Fine, L. M. Cavanagh, A. Afonja and R. Binions, *Sensors*, 2010, **10**, 5469–5502.

(139) K. Shingange, Z. P. Tshabalala, O. M. Ntwaeaborwa, D. E. Motaung and G. H. Mhlongo, *J. Colloid Interface Sci.*, 2016, **479**, 127–138.

(140) T. Wang, Z. Sun, D Huang, Z. Yang, Q. Ji, N. Hu, G. Yin, D. He, H. Wei and Y. Zhang, *Sens. Actuators, B*, 2017, **252**, 284–294.

(141) G. K. Mani and J. B. B. Rayappan, *Sens. Actuators, B*, 2013, **183**, 459–466.

(142) M. R. Prasada, M. Harisa and M. Sridharan, *Sens. Actuators, B*, 2018, **269**, 435–443.

(143) R. S. Ganesh, E. Durgadevi, M. Navaneethan, V. L. Patil, S. Ponnusamy, C. Muthamizhchelvan, S. Kawasaki, P. S. Patil, Y. Hayakawa, *J. Alloy. Compd.*, 2017, **721**, 182–190.

(144) J. X. Wang, X. W. Sun, Y. Yang, H. Huang, Y. C. Lee, O. K. Tan and L. Vayssieres, *Nanotechnology*, 2006, **17**, 4995.

(145) R. S. Ganesh, E. Durgadevi, M. Navaneethan, V. L. Patil, S. Ponnusamy, C. Muthamizhchelvan, S. Kawasaki, P. S. Patil and Y. Hayakawa, *Sens. Actuators, A*, 2018, **269**, 331–341.

(146) R. S. Ganesh, M. Navaneethan, V. L. Patil, S. Ponnusamy, C. Muthamizhchelvan, S. Kawasaki, P. S. Patil and Y. Hayakawa, *Sens. Actuators, B*, 2018, **255**, 672–683.

(147) R. S. Ganesh, E. Durgadevi, M. Navaneethan, V. L. Patil, S. Ponnusamy, C. Muthamizhchelvan, S. Kawasaki, P. S. Patil and Y. Hayakawa, *Chem. Phys. Lett.*, 2017, **689**, 92–99.

(148) O. Lupan, F. Schütt, V. Postica, D. Smazna, Y. K. Mishra and R. Adelung, *Sci. Rep.*, 2017, **7**, 14715.

(149) R. S. Ganesh, G. K. Mani, R. Elayaraja, E. Durgadevi, M. Navaneethan, S. Ponnusamy, K. Tsuchiya, C. Muthamizhchelvan and Y. Hayakawa, *Appl. Surf. Sci.*, 2018, **449**, 314–321.

(150) A. N. A. Anasthasiya, R. K. Kampara, P. K. Rai and B. G. Jeyaprakash, *Appl. Surf. Sci.*, 2018, **449**, 244–249.

(151) A. N. A. Anasthasiya, R. K. Kampara, P. K. Rai and B. G. Jeyaprakash, *Sens. Actuators, B*, 2018, **255**, 1064–1071.

(152) H. Tang, M. Yan, H. Zhang, S. Li, X. Ma, M. Wang, D. Yang, *Sens. Actuators, B*, 2006, **114**, 910–915.

(153) F. Schütt, V. Postica, R. Adelung and O. Lupan, *ACS Appl. Mater. Interfaces*, 2017, **9**, 23107–23118.

# CHAPTER 2

## Experimental Section

*This chapter discusses the general synthetic methodologies utilized for preparation of materials, basic instrumental techniques for materials characterization, fabrication of semiconductor metal chalcogenide-/ dye-sensitized solar cells highlighting the ZnO based photoanode preparation. Fabrication of two-terminal chemiresistor devices has been also mentioned in this chapter.*

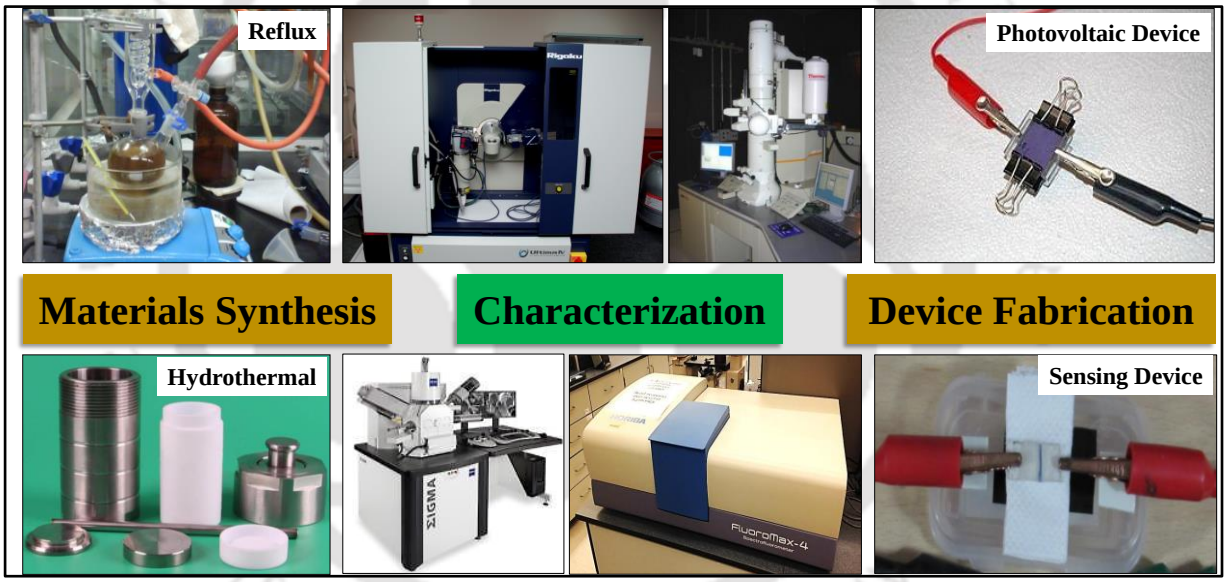

## 2.1 INTRODUCTION

Zinc oxide (ZnO) has been extensively utilized as a photoanodic material in the present thesis due to its unique features such as large exciton binding energy, high carrier mobility and anisotropic growth pattern.[1–2] Growth behaviour of different morphological structures is greatly affected by synthetic methodologies and the internal structure of a given crystal. Structure directing agents are mainly responsible for the rational design and development of nanostructure morphologies. Several biomass derived templating agents are used for tuning the morphology of ZnO structure in the subsequent chapters. Various steps involved in the synthesis and fabrication of quantum dot sensitized solar cell (QDSSC) and dye sensitized solar cell (DSSC) are described. Photovoltaic performance parameters and characterization techniques of a solar device are discussed in detail. Fabrication and performance parameters of two terminal chemiresistor device for vapor phase sensing are also included in this chapter.

## 2.2 EXPERIMENTAL METODS

### 2.2.1 MATERIALS AND REAGENTS USED

Chemicals and reagents used in all synthetic protocols are of analytical grade and used without further purification. Melamine, Xanthan gum, polygalacturonic acid, k-carrageenan, 2-methoxy ethanol, zinc nitrate hexahydrate, sodium sulfide, antimony trichloride (anhydrous), cupric chloride (anhydrous), oleylamine, octadecene, oleic acid, nafion perfluorinated resin solution (5 wt % in lower aliphatic alcohols and water), chloroplatinic acid, lithium iodide, 1-butyl 3-methyl imidazolium iodide, guanidinium thiocyanate, valeronitrile and fluorine doped tin oxide (FTO) coated glass substrates (sheet resistance 13–15 $\Omega/cm^2$) are procured from Sigma Aldrich. Zinc acetate dehydrate, zinc chloride, sodium hydroxide, ammonium hydroxide, hexamethylenetetramine, cadmium nitrate hexahydrate, ethylene diamine, thiourea, sulphur powder, potassium chloride, tert-butyl alcohol, ethyl acetate, methanol, 2-propanol, acetone, tetrahydrofuran, nitrobenzene, methylamine, diethyl amine, triethyl amine, diethyl triamine and hexane are purchased from Merck. Ethanolamine, terpineol, ethocel, 4-tert-butylpyridine are procured from Himedia. Ethanol and PTFE syringe filter are purchased from TMEDA, USA and Axiva Sichem Biotech, India respectively. Reagents used during synthesis of dye D1 are mentioned in synthetic protocol. Dye, di-tetrabutylammonium cis-bis-(isothiocyanato)bis (2,20-

bipyridyl-4,40-dicarboxylato)ruthenium(II) is procured from Dyesol, Australia. Milli-Q water (18.2 MΩ $cm^{-2}$) is used for all the synthesis protocol.

### 2.2.2 CHARACTERIZATION OF AS-SYNTHESIZED MATERIALS, PHOTOVOLTAIC AND CHEMIRESISTOR DEVICES

All synthesized materials and as-fabricated photovoltaic/chemiresistor devices are characterized using various analytical techniques. Instrumental tools used in the present studies involve:

(1) Crystal phase purity of all materials are investigated by Powder X-ray diffraction (PXRD) analyses using Bruker D2 PHASER X-ray diffractometer with Cu–Kα X-ray generator (λ = 1.54 Å), operating voltage of 30 kV and current 30 kA, and Rigaku RINT 2500 TTRAX-III, with Cu–Kα (λ = 1.54 Å) X-ray source.

(2) Morphological analyses of as-synthesized materials are conducted by field emission scanning electron microscopic (FESEM) analysis using a Zeiss (Gemini) instrument, recorded at the voltages of 3 kV−10 kV.

(3) Structural features of all materials are analyzed by transmission electron microscopy (TEM) measurements, performed on a JEOL JEM 2100 microscope having an operating voltage of 200 kV.

(4) Elemental and compositional analyses of pristine and composite materials are demonstrated by performing energy-dispersive X-ray spectroscopy (EDS) analysis using INCA, Oxford instruments.

(5) Optical properties of the bare and sensitized photoanodic materials are examined by diffuse reflectance UV-Visible spectra (DRS) using a JASCO Model V−650 spectrophotometer equipped with a 150 mm integrating sphere and $BaSO_4$ as an internal standard.

(6) Excited state charge transfer in bare as well as composite materials is investigated by performing steady state photoluminescence (PL) measurements using a Horiba−Jobin Yvon Fluoromax 4C spectrophotometer.

(7) Kinetics and injection rate of excited charge carriers are analyzed by time-resolved photoluminescence (TRPL) measurements performing on LifeSpec II Edinburgh

instrument, having a lamp with frequency 5MHz and Nd:YAG lasers of different excitation wavelengths.

(8) Surface area of as-synthesized ZnO structures are estimated by Brunauer–Emmett–Teller (BET) surface area analysis using Beckman–Coulter SA 3100 $N_2$ adsorption apparatus. All samples are degassed at 150 °C for 4 h prior to surface area analysis.

(9) Fourier transformed infrared spectroscopy (FT–IR) analysis is performed using a Perkin Elmer FT–IR instrument.

(10) Phase composition of all materials is analyzed by micro–Raman spectroscopy, using a LabRam HR800, Jobin Yvon at an excitation of 514 nm.

(11) NMR spectra of as-synthesized sensitizer molecule are recorded in a Bruker Avance (III) 400 MHz instrument using $CDCl_3$ as solvent for $^1H$ NMR (400 MHz) or $^{13}C$ NMR (100 MHz). Chemical shifts (δ) are reported in ppm and coupling constants (J) are given in Hz.

(12) Bruker-Daltonics micrOTOF-Q II mass spectrometer is used for recording HRMS spectra of as-synthesized sensitizer molecule.

(13) Electrochemical analysis of as-synthesized sensitizer molecule is performed by cyclic Voltammetry (CV), recorded using the saturated calomel electrode (SCE) [reference electrode], glassy carbon [working electrode] and Pt wire [counter electrode] at 100 mV $s^{-1}$ scan rate on a CHI620D electrochemical workstation. A 0.1 M solution of tetrabutylammonium hexafluorophosphate in $CH_2Cl_2$ is used as supporting electrolyte. The reduction and oxidation peaks are calibrated using the ferrocene/ferrocenium ion ($Fc/Fc^+$) system. Here, the $Fc/Fc^+$ couple exhibited $E° = 0.38$ V versus SCE.

(14) Thin films are deposited through spin coating method, using SPIN–150 spin coater.

(15) Thickness of photoanodic film is measured by using Veeco Dektak 150 surface profilometer.

(16) Photovoltaic performances of all solar cells are demonstrated by using a Keithley 2400 sourcemeter in the dark. Newport ORIEL Sol3A solar simulator having AM 1.5G artificial solar simulator of power 100 mW/$cm^2$ is used for solar light illumination. Before illumination it is calibrated with a standard Si photovoltaic cell.

(17) A Newport ORIEL IQE–200 instrument fitted with a 250 W quartz tungsten halogen lamp is utilized to measure the incident photon to current conversion efficiency (IPCE) of solar device. Tungsten halogen lamp is calibrated by standard Si and Ge diodes.

(18) Electrochemical impedance spectroscopic (EIS) analyses of the devices are performed using an electrochemical work station provided by CH instruments model CHI680E, Inc., Austin, TX.

(19) All the sensing measurements are carried out by using a Keithley 4200–SCS under ambient conditions.

### 2.2.3 STEPS INVOLVED FOR THE FABRICATION OF A QDSSC AND DSSC

#### (A) PHOTOANODE PREPARATION

(1) Firstly, as-synthesized photoanodic powder sample is weight and then ultra-sonicated in ethanol for 30 min to reduce the particles agglomeration, as shown in digital images **(1)** and **(2)** of figure **2.2.1**. Now, a homogeneous paste of ultrasonicated sample is made by using terpineol and binder material; ethocel in a mortar pestle. This step is depicted in digital image **(3)** of figure **2.2.1**.

(2) For all photovoltaic studies, Conductive glass substrate i.e., Fluorine doped Tin Oxide (FTO) coated glass substrate is utilized as electrode material. FTO substrate is first cut into specific dimension [(2×2) $cm^2$, 2 slides for 1 cell)], washed properly using soap solution, acetone, and isopropanol, and then ozonized for 15 min. Active area of device is fixed by masking with a scotch tape, as shown in image **(4)** of figure **2.2.1**.

(3) A thin film of as-prepared homogenous paste is deposited over masked FTO glass substrate using doctor blade technique and dried in a hot air oven at 90 ºC for 30 min. Scotch tape is then removed and the metal oxide films are calcined at 450 ºC in a muffle furnace to remove the organic impurities of binder. Metal oxide coated FTO substrate is thus obtained, display in digital picture **(5)** of figure **2.2.1**.

(4) Now, these metal oxide films are sensitized with sensitizer particles such as semiconductor quantum dots (QDs) or organic dye molecule. For example, CdS QDs sensitized ZnO film as a photoanode is shown in image **(6)** of figure **2.2.1**.

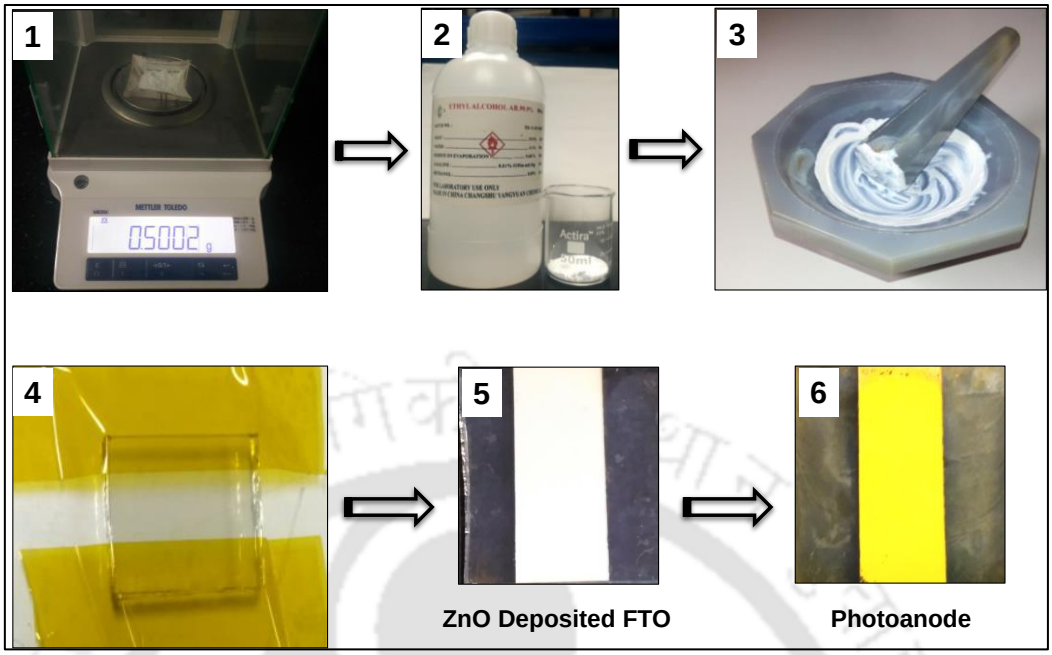


**Figure 2.2.1** Illustrative representation of various steps involved in the fabrication of photoanode.

## (B) SENSITIZATION OF PHOTOANODES

(1) Successive ionic layer adsorption and reaction (SILAR) method is employed for sensitization of CdS QDs, as shown in scheme **2.2.1**.

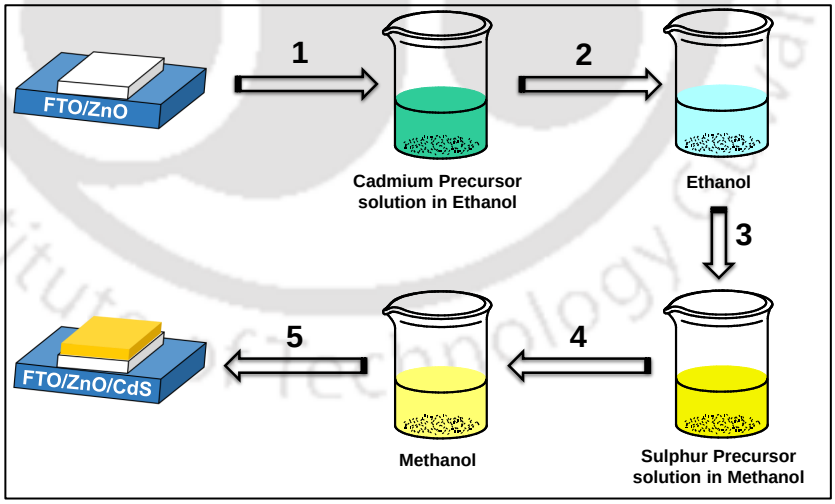


**Scheme 2.2.1** Graphic related to CdS quantum dots sensitization over ZnO deposited FTO glass substrate using SILAR method.

In SILAR method, firstly ZnO deposited FTO substrate is dipped into a 0.5 M ethanolic solution of $Cd(NO_3)_2$. $4H_2O$ for 2 min, rinsed with ethanol, and dried under hot air blow, as

depict in step **1** and **2** of scheme **2.2.1**. After that, this substrate is dipped into a 0.5 M $Na_2S$ solution in methanol for 2 min, rinsed with methanol and dried under hot air blow, as depict in step **3** and **4** of scheme **2.2.1**. Amount of CdS loading onto the ZnO layer is controlled by the number of repeated SILAR cycles.

(2) Copper antimony sulfide ($CuSbS_2$) is deposited over FTO/ZnO/CdS photoanode using spin coating method by making ink using ethylene glycol and nafion resin. Schematic illustration related to $CuSbS_2$ sensitization is shown in scheme **2.2.2**.

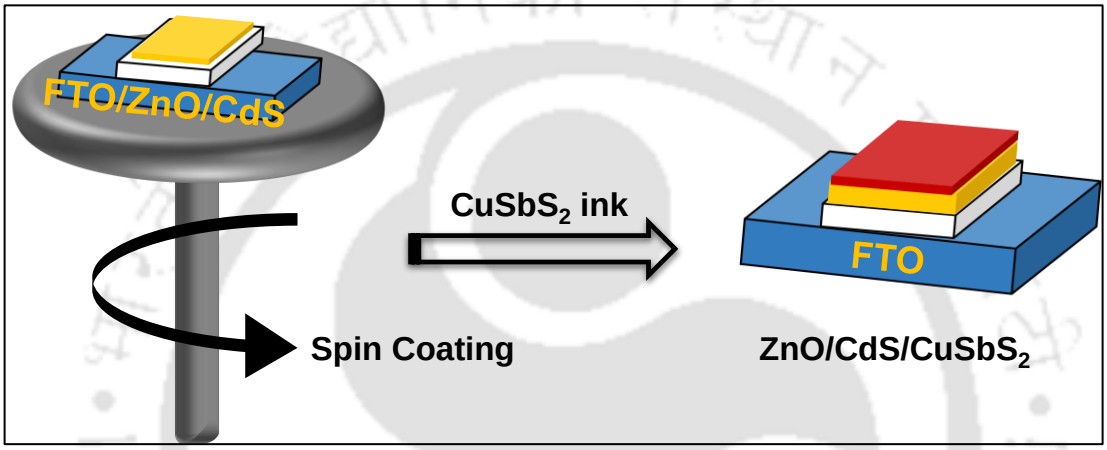


**Scheme 2.2.2** Schematic representation of copper antimony sulfide deposition over FTO/ZnO/CdS photoanode using spin coating method.

(3) For dye (D1 and N719 dyes) sensitization, as-fabricated ZnO photoanodes are dipped into dye solution (0.3 mM) for 3 h. Sensitized photoanodes are removed from dye solution, rinsed with same solvent and dried, represent graphically in scheme **2.2.3**.

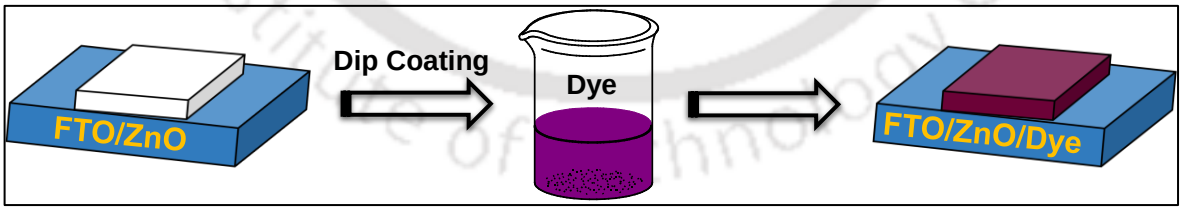


**Scheme 2.2.3** Graphical depiction of dye loading over FTO/ZnO photoanode using dip coating method.

## (C) COUNTER ELECTRODE PREPARATION

Platinum (Pt) counter electrodes are prepared through spin coating of a chloroplatinic acid solution (in isopropanol) on a cleaned ozonized FTO glass substrate, followed by the calcination at 450 °C for 30 min in a muffle furnace and cooled down to room temperature

naturally. Figure **2.2.2** shows the pictorial representation for fabrication of counter electrode, illustrating a digital image of $H_2PtCl_6$ solution and platinized FTO glass substrate.

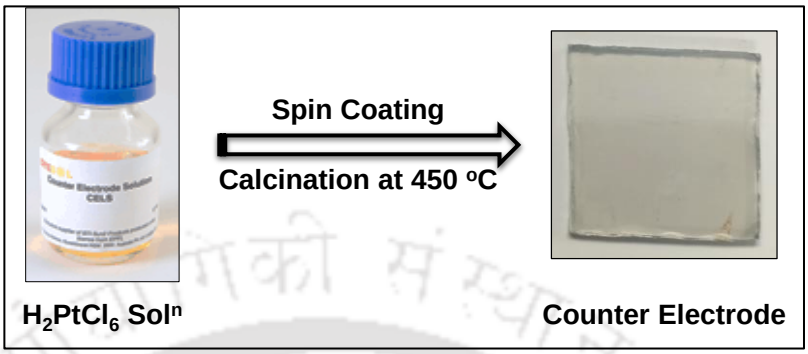


**Figure 2.2.2** Pictographic representation related to platinum deposition over FTO glass substrate to construct the counter electrode.

### (D) ASSEMBLING OF PHOTOVOLTAIC DEVICE

Finally, a photovoltaic device is fabricated by sandwiching the as-prepared photoanode and counter electrode. Redox electrolyte solution is then injected between sandwiched electrodes to complete the photovoltaic device assembly. Now, device is ready for photovoltaic measurement, display in figure **2.2.3**.

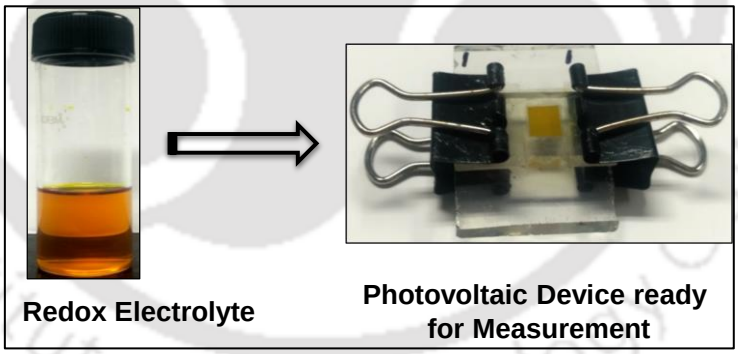


**Figure 2.2.3** Digital images related to redox electrolyte solution and as-fabricated photovoltaic devices in our laboratory.

### 2.2.4 ESTIMATION OF SOLAR CELL PERFORMANCE

(1) As-fabricated photovoltaic device is connected to Keithley 2400 SourceMeter using connecting cables.

(2) In dark condition, dark current values are measured by sweeping the voltage in the range of –1 V to +1 V across the photovoltaic device.

(3) After that, simulated solar light is irradiated onto the photovoltaic device and sweeping the voltage like step 2. This step has been repeated for 5 times to check the consistency of extracted parameters.

(4) Current *vs.* Voltage (*I*–V) graphs of the device is plotted by taking current values as abscissa and voltage as ordinate.

(5) Values of all photovoltaic performance parameters such as current density ($J_{sc}$), open circuit voltage ($V_{oc}$), Fill Factor (FF), maximum power output ($P_{max}$) and Power Conversion Efficiency (PCE, η) are estimated the (*I*–V) plot. Short-circuit current density ($J_{sc}$) is mentioned for all photovoltaic devices in all chapters rather short circuit current ($I_{sc}$) in order to allow comparison between devices whose dimensions may vary.

$$J_{sc} = \frac{I_{sc}}{Active\ area}$$

## 2.2.5 SOLAR CELL PERFORMANCE PARAMETERS

Efficiency of a photovoltaic device is sensitive to differences in both the power and the spectrum of the incident light. For better comparison, performance parameters of solar device is characterized at different laboratories all over the world, a simulated solar spectrum of air mass 1.5 G (AM 1.5 G) corresponding to a Zenith angle (φ) 42° is used as the standard to test their efficiency. Air Mass is the path length through which incident light takes shortest possible path length to strike on earth surface. Air Mass also quantifies the reduction in the power of light as it passes through the atmosphere and is absorbed by air and dust. Mathematically, air mass is expressed as: ($AM = 1/cos\varphi$). Zenith angle (φ) is the angle of elevation of the sun and is shown schematically in figure **2.2.4 (A)**.

Performance parameters of a photovoltaic device are estimated from its corresponding photocurrent–voltage (*I*–V) curve. A schematic representation of the Photocurrent-voltage (*I*–V) curve of a photovoltaic device is shown in figure **2.2.4 (A)**, gives the information about behaviour of a photovoltaic device with the irradiation of light, shifting the *I*–V curve down into the fourth quadrant where power is extracted from the diode.

Short-circuit current ($I_{sc}$) is the current flowing through the solar cell when the voltage across the solar cell is zero, obtained due to the generation and collection of light-generated charge carriers. Short-circuit current increases with light intensity due to generation of more flux of photoexcited electrons. In order to eliminate the area dependence of solar cells, short-circuit

current is expressed in terms of short-circuit current density ($J_{sc}$, in mA.cm$^{-2}$). Open–circuit voltage ($V_{oc}$) is the maximum voltage output from a photovoltaic device when current across the solar device is zero. Since $V_{oc}$ corresponds to the amount of forward bias on the solar cell, it measures the amount of recombination in the device. $V_{oc}$ depends on the saturation current and the light-generated current of a solar device.

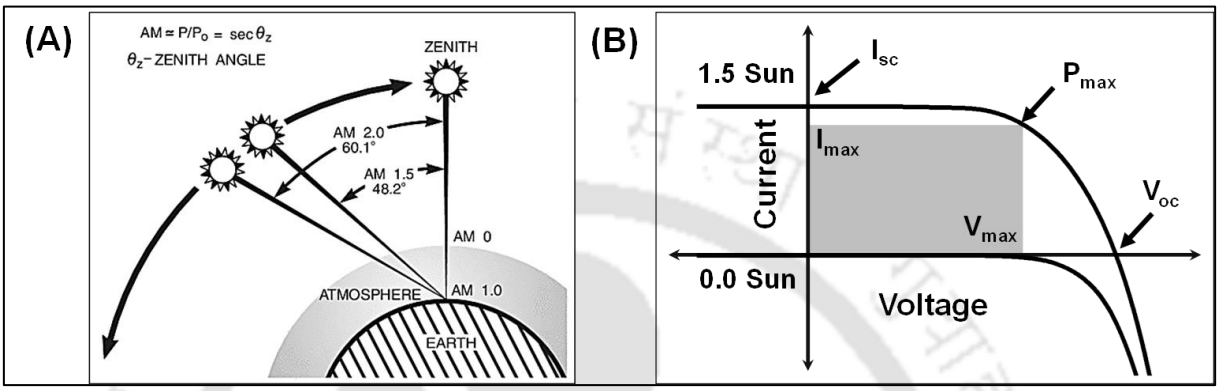


**Figure 2.2.4 (A)** Path length of solar irradiation in units of Air Mass, changes with the zenith angle (φ); (source: https://www.newport.com). **(B)** Graphic represents the current–voltage (*I*–V) curve of a photovoltaic device in dark condition as well as under AM 1.5 G simulated solar irradiation.

Fill factor (FF) is defined as the ratio of the maximum power output from a solar cell to the product of $V_{oc}$ and $J_{sc}$. It determines the maximum power ($P_{max}$) coming from a solar device. Graphically, FF is measured as the squareness of (*I*–V) curve and is also the area of the largest fitted rectangle in the (*I*–V) curve, as shown in figure **2.2.4 (B)**. Fill factor (FF) can be expressed as:

$$FF = \frac{P_{max}}{J_{sc} \times V_{oc}}$$

Where, $P_{max}$ is the maximum power output of the solar cell, attained from the product of maximum photocurrent and photovoltage output. Overall solar-to-electrical energy conversion efficiency or power conversion efficiency, PCE (η) of a solar cell is calculated from the following relation;

$$\eta = \frac{J_{sc} \times V_{oc} \times FF}{P_{in}}$$

Incident photon-to-current conversion efficiency (IPCE) is considered an essential measurement to evaluate the performance of a photovoltaic device. IPCE corresponds to the photocurrent density produced in the external circuit under monochromatic illumination of the cell divided by the photon flux that strikes the cell. It can be expressed as;

$$\mathbf{IPCE} = \mathbf{1240} \times \frac{\boldsymbol{J_{sc}}}{\boldsymbol{\lambda} \times \mathbf{P_{in}}(\boldsymbol{\lambda})}$$

### 2.2.6 ELECTROCHEMICAL IMPEDANCE SPECTROSCOPY (EIS) ANALYSIS

Electrochemical impedance spectroscopy (EIS) is a crucial technique for explaining the kinetics of interfacial charge transfer along with the numerous recombination processes, arising from the electrochemical reactions occurring at various interfaces of the solar device. Figure **2.2.5 (A)** display the schematic of the cross-section of a QDSSC/DSSC device, exhibiting the different solid/liquid interfaces, i.e., ZnO/sensitizer(S)/electrolyte and counter electrode (CE)/electrolyte respectively. EIS analyses for all devices are performed in dark conditions within the frequency range of 0.1 Hz to 100 kHz by employing a bias equivalent to open circuit voltage ($V_{oc}$), shows as Nyquist and Bode phase plots in figure **2.2.5 (B)** and **(D)**. Nyquist plot has two semicircles, one in the medium frequency region while another one in the higher frequency region. The semicircle in the medium frequency region denotes the charge-transfer process occur at the working electrode/electrolyte interface, while the smaller semicircle in the higher frequency region is related to electrochemical processes happen at the interface of counter electrode/electrolyte.[3] The diameter of the right semicircle ($R_k$) primarily contributed from electron recombination resistance and is partly due to the transport resistance.[4] Higher value of $R_k$ implies larger recombination resistance at the working electrode/ electrolyte interfaces. The interpretation of the EIS measurements is carried out by fitting the impedance data to an equivalent electrical circuit, represent in trace **(C)** of figure **2.2.5**. From the inset of trace **(B)** of figure **2.2.5**, Nyquist plot can also give information about the impedance of the Nernst diffusion of redox species ($R_D$) in the electrolyte. However the semicircle associated with the Nernst diffusion process appears at low-frequency ($10^{-1}$ to $10^{-2}$ Hz) which needs a longer time for complete analysis. In order to eliminate the detrimental effects related to slow evaporation of volatile solvent of the redox electrolyte, EIS data recording time for the fabricated devices is limited to a couple of minutes per cell and frequency range of $10^5$ to $10^{-1}$ Hz is selected for acquisition of data. Therefore, we have focused on electrochemical processed happen at working electrode/electrolyte interfaces and counter electrode/electrolyte interfaces. From the inset of trace **(B)**, Nyquist plot shows all possible three semicircles for better understanding of charge transfer processes. The value of $R_s$ signifies the sheet resistance of the FTO substrate in the device while $R_k$ and $R_D$ represent diameter of the respective semicircles. Maximum peak

frequency of the second semicircle ($f_{max}$) is correlated with the rate of recombination of electrons ($k_{eff}$) at the Working electrode/Electrolyte interfaces.

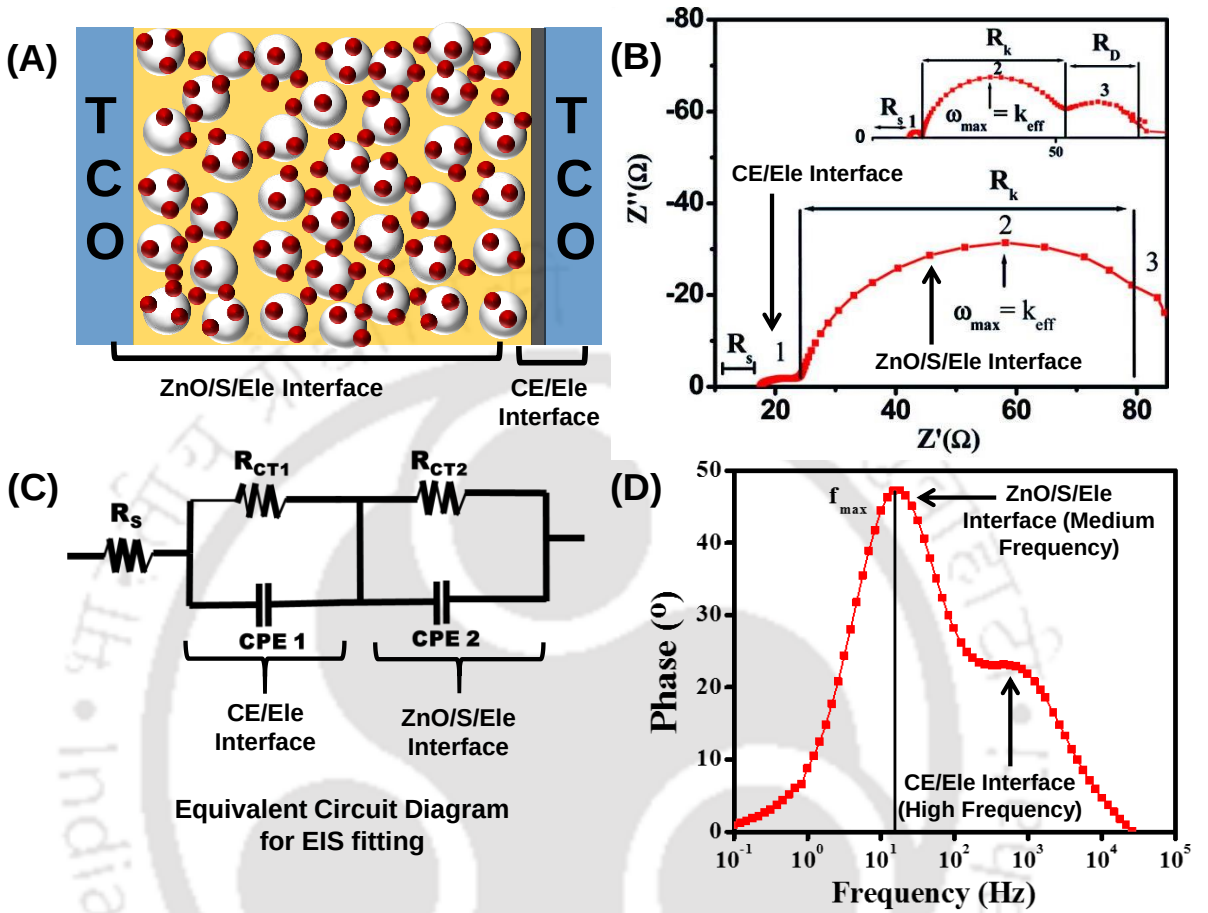


**Figure 2.2.5 (A)** Graphical representation related to cross-sectional view of a QDSSC/ DSSC device, exhibiting the different solid-liquid interfaces such as ZnO/sensitizer(S)/electrolyte and counter electrode (CE)/electrolyte respectively. **(B)** Depicts the Nyquist plot for a QDSSC/ DSSC device. Inset of same plot shows the Nyquist plot having all three semicircles, observed at different interfaces of a photovoltaic device such as **(1)** charge transfer process at CE/Electrolyte interface **(2)** Charge transfer process at working electrode/Electrolyte interface and **(3)** Nernst diffusion of the electrolyte in the photoanode. [Nyquist plot of inset **(B)** is taken from reference 4]. **(C)** Represents the equivalent circuit diagram used to fit the EIS data; having abbreviations $R_s$, sheet resistance; $R_{ct1}$ & $R_{ct2}$, charge-transfer resistance of the counter electrode and working electrode; CPE1 & CPE2, constant-phase element of the counter electrode and working electrode respectively. **(D)** Shows the Bode Phase plot for a QDSSC/ DSSC device.

Trace **(D)** of figure **2.2.5** represents the Bode phase plot of a photovoltaic device. Two different peaks corresponding to two diode interfaces of the device are noticed in different frequency regions. Photoinduced electron lifetimes ($\tau_e$) of a solar cell can be estimated from the maximum peak frequency ($f_{max}$) in the mid-frequency region. We have estimated the values of $\tau_e$ by using the following **equation**.[5]

$$\tau_e = \frac{1}{2\pi f_{max}}$$

Larger ($\tau_e$) value of a solar device validates the minimized recombination processes, occur due to the back transfer of photoinduced electrons to the electrolyte at the working electrode/electrolyte interfaces. Moreover, higher '$\tau_e$' value is also indicated that the photoinjected electrons spent more time in the photoanodic film before collecting at the FTO substrate. Therefore, there is an enrichment of photoinduced electron density in the photoanodic segment, helpful to improve the $J_{sc}$ value and efficiency of a solar device.

### 2.2.7 FABRICATION OF TWO-TERMINAL CHEMIRESISTOR DEVICE FOR VAPOR PHASE SENSING

Scheme **2.2.4** illustrates the schematic representation related to step by step fabrication of sensor device. Firstly, FTO glass substrate is patterned using zinc dust and conc. HCl to make the active sensing area (channel) of about 0.10 $cm^2$ [1 mm length (L) and 10 mm width (W)]. Sensing materials are deposited on active sensing area and create a schottky barrier with conductive FTO. Chemiresistor device having FTO on both sides, act as source and drain. Now, sensing device is ready for all kinds of electrical measurements related to vapor phase sensing.

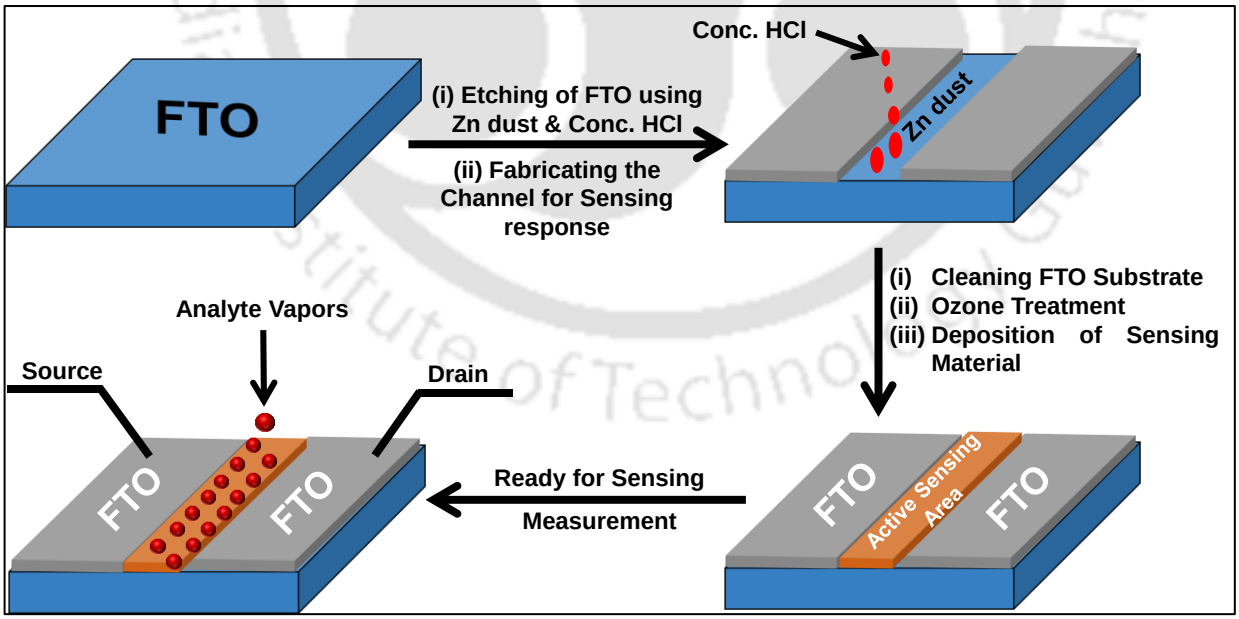


**Scheme 2.2.4** Schematic illustration of the step by step fabrication of two terminal chemiresistor devices for vapor phase sensing.

### 2.2.8 GAS SENSING ASSEMBLY

After fabrication of chemiresistor device, all gas sensing experiments are performed at room temperature with specific relative humidity level. Schematic illustration of whole gas sensing assembly is presented in Scheme **2.2.5**.

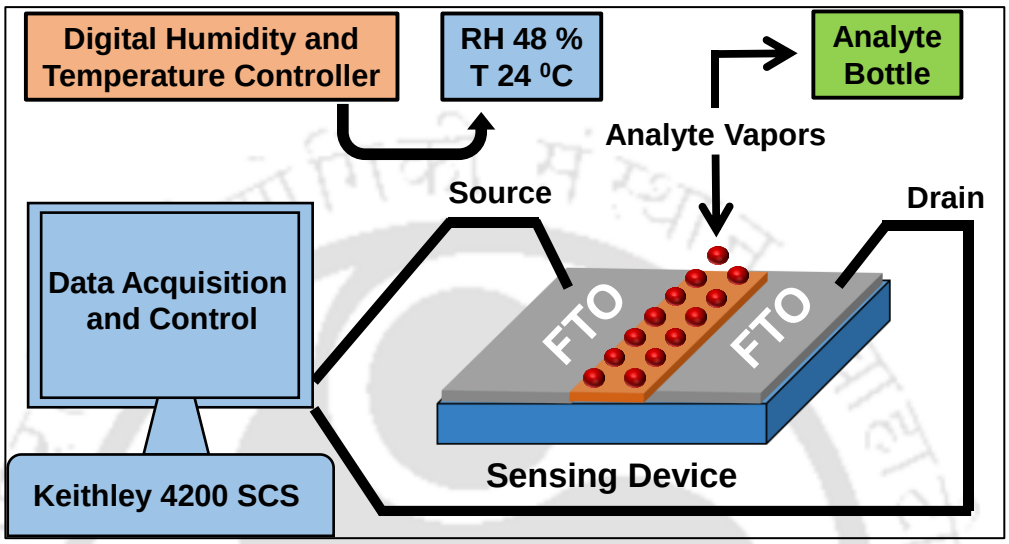


**Scheme 2.2.5** Schematic drawing related to experimental set-up for $NH_3$ gas sensing assembly.

### 2.2.9 GAS SENSING PERFORMANCE PARAMETERS

Performance of a chemiresistor device for gas sensing is evaluated on the basis of parameters; (1) limit of detection (LOD) and (2) response-recovery time. LOD of a sensing device is defined as the minimum amount of analyte concentration that can be detected by sensing device. For the quantitative estimation as LOD value, calibration curve is plotted as the maximum current intensity response as a function of different concentration of analyte vapors, represent in figure **2.2.6 (A)**. Afterward, this curve is fitted linearly and calculates the slope (S) for a sensing device with considerable correlation coefficient ($R^2$) value. LOD is calculated by using the mathematical expression viz., **LOD = 3σ/S**, where 'σ' is the relative standard deviation of the current response of sensor device in the absence of analyte vapors and 'S' is the slope of the calibration curve.[6] Sensing device having lesser LOD value is reflected to be more sensitive and mainly depends on the better interaction of analyte vapors to sensing material, enhanced diffusion and efficient electron transportation. Response and recovery time is considered to be the essential parameter for determining the efficient usability of a vapor phase sensor device. Response time of a sensing device is the time required to change the 90 % of the current

response after exposing the analyte vapor on the device while recovery time is the time elapsed in changing the 90 % of the current response to reach the original position after the turning off the analyte vapor.

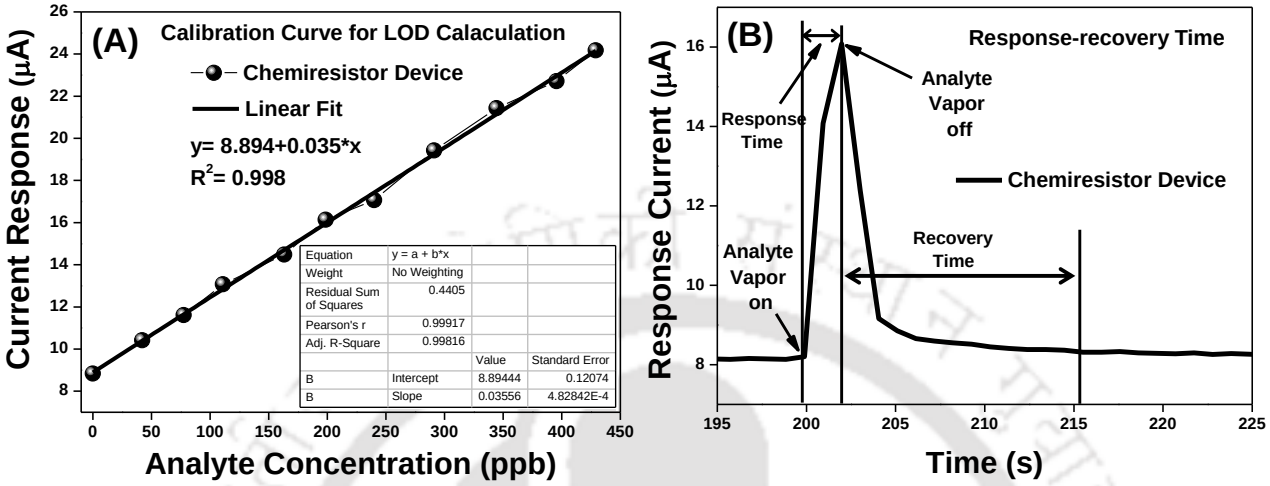


**Figure 2.2.6 (A)** Represents the Calibration curve for calculating the limit of detection (LOD) value for a chemiresistor device as a function of analyte concentration. **(B)** Exhibits the response and recovery time of the gas sensing of a chemiresistor device.

Trace **(B)** of figure **2.2.6** shows the response and recovery time for a sensing device. However, sensing device revealing lower response/recovery time is found to be highly sensitive. Lower response and recovery times of a sensing device are highly suitable for the rapid detection of analyte vapors.

## 2.3 REFERENCES


(1) F. Xu and L. Sun, *Energy Environ. Sci.*, 2011, **4**, 818–841.

(2) N. S. Ramgir, I. S. Mulla and V. K. Pillai, *J. Phys. Chem. B*, 2006, **110**, 3995–4001.

(3) S. Phadke, A. D. Pasquier and D. P. Birnie, *J. Phys. Chem. C*, 2011, **115**, 18342–18347.

(4) V. D. Dao, L. L. Larina, Q. C. Tran, V. T. Bui, V. T. Nguyen, T. D. Pham, I. M. A. Mohamede, N. A. M. Barakate and B. T. Huyc, *Carbon*, 2017, **116**, 294–302.

(5) R. Kern, R. Sastrawan, J. Ferber, R. Stangl and J. Luther, *Electrochim. Acta*, 2002, **47**, 4213–4225.

(6) A. H. Malik, S. Hussain, A. Kalita and P. K. Iyer, *ACS Appl. Mater. Interfaces*, 2015, **7**, 26968–26976.

# CHAPTER 3

## Morphological Tuning of Photo-booster g–$C_3N_4$ with Higher Surface Area and Better Charge Transfers for Enhanced Power Conversion Efficiency of Quantum Dot Sensitized Solar Cells

*This chapter explains the photo-booster effect of graphitic carbon nitride ($g-C_3N_4$ NTs) in the photovoltaic devices, fabricated using the composites having ZnO Nanorods (ZnO NRs) An increase of ~ 32 % in power conversion efficiency (PCE, η) is observed in case of $g-C_3N_4$ NTs based optimized device as compare to $g-C_3N_4$ Nanoflakes ($g-C_3N_4$ NFs).*

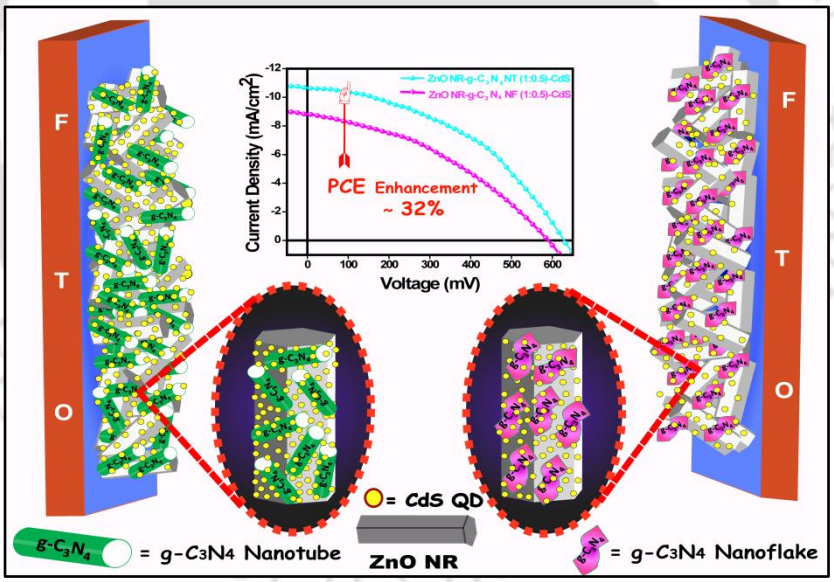


***Ansari, et al., Carbon* 2017, *121*, 90–105.**

## 3.1 INTRODUCTION

Numerous ultraviolet (UV) or visible light responsive materials have been utilized to harvest the solar energy using photovoltaic devices.[1–2] Due to unique electronic and optical properties, graphitic carbon nitride (g-$C_3N_4$) is likely to be a promising metal free, visible light active polymeric organic semiconductor for solar energy conversion.[3–4] g-$C_3N_4$ has various advantages like low cost, high physicochemical and thermal stability with the limitation of having high recombination rate of photogenerated electron–hole pairs, which inhibit its beneficial effects in photovoltaic performances.[5–7] Radiative recombination rate of photogenerated electron–hole pairs of g-$C_3N_4$ can be minimized by making heterojunction with the semiconducting materials like metal oxides and metal sulfides with well-matched energy band positions.[8–12] To get better performance of g-$C_3N_4$, it is important to optimize the material by modifying morphology, optical, and electronic properties via nanocasting, doping and coupling with other semiconductors.[13–14] It is known that bulk structure of g-$C_3N_4$ confines the benefits of its usability in energy conversion due to having less number of active sites and high recombination rate of photogenerated electron–hole pair. Therefore, several groups have been successfully synthesized the various morphological structures of g-$C_3N_4$ such as nanosheets, nanoparticles, nanoribbon, nanobelts, nanorods, nanotubes and hollow mesoporous spheres, resolving the drawbacks related to usability of g-$C_3N_4$.[15–20] However, tuning the morphology of bulk g-$C_3N_4$ is a very challenging job due to its layered structure, produced during the polycondensation process. Usually, tubular nanostructures have been given special attention due to their unique properties such as efficiently transfer the photogenerated electrons along one dimensional (1–D) path and having open-end mesoporous morphology which provides more surface area for loading of sensitizer particles, to improve the photovoltaic performance of solar device.[21–23] g-$C_3N_4$ nanotubes (NTs) have been prepared via using self-assembly of fibrous structures, chemical vapor deposition and templating methods.[24–28] These synthetic methods have some disadvantages such as high fabricating cost, using of harsh chemicals as templates and operation complexity which limits the industrial scale synthesis of g-$C_3N_4$ NTs. In this chapter, g-$C_3N_4$ NTs are synthesized through rolling of ultrasonically exfoliated g-$C_3N_4$ nanoflakes (NFs),[29] by generating a thermal gradient between outer and inner surfaces of g-$C_3N_4$ NFs. To the best of our knowledge, beneficial effects of photo-booster g-$C_3N_4$ NTs have not


Part of this chapter has been published in **Carbon 2017, 121, 90–105**.

been explored in photovoltaic application.[30–31] Subsequently, comparative photovoltaic study based on both structures of g-$C_3N_4$ are carried out by making the composites having zinc oxide nanorods (ZnO NRs) with different composition ratios and sensitized with CdS QDs. Furthermore, we have also done the photovoltaic dependent comparative study for both morphologies of ZnO i.e., ZnO NRs and ZnO NPs.

## 3.2 EXPERIMENTAL METHODS

### 3.2.1 SYNTHESIS OF BULK g–$C_3N_4$

Synthesis of bulk g-$C_3N_4$ from melamine mainly involved high temperature polycondensation process via the elimination of ammonia.[32] In a typical synthesis process, 2 g of melamine was taken in a mortar pestle and ground it for about 10 min. Grounded sample was first put into hot air oven at 120 $^{o}$C for about 2 h and then put into an alumina crucible with a cover and placed in a muffle furnace for heat treatment.

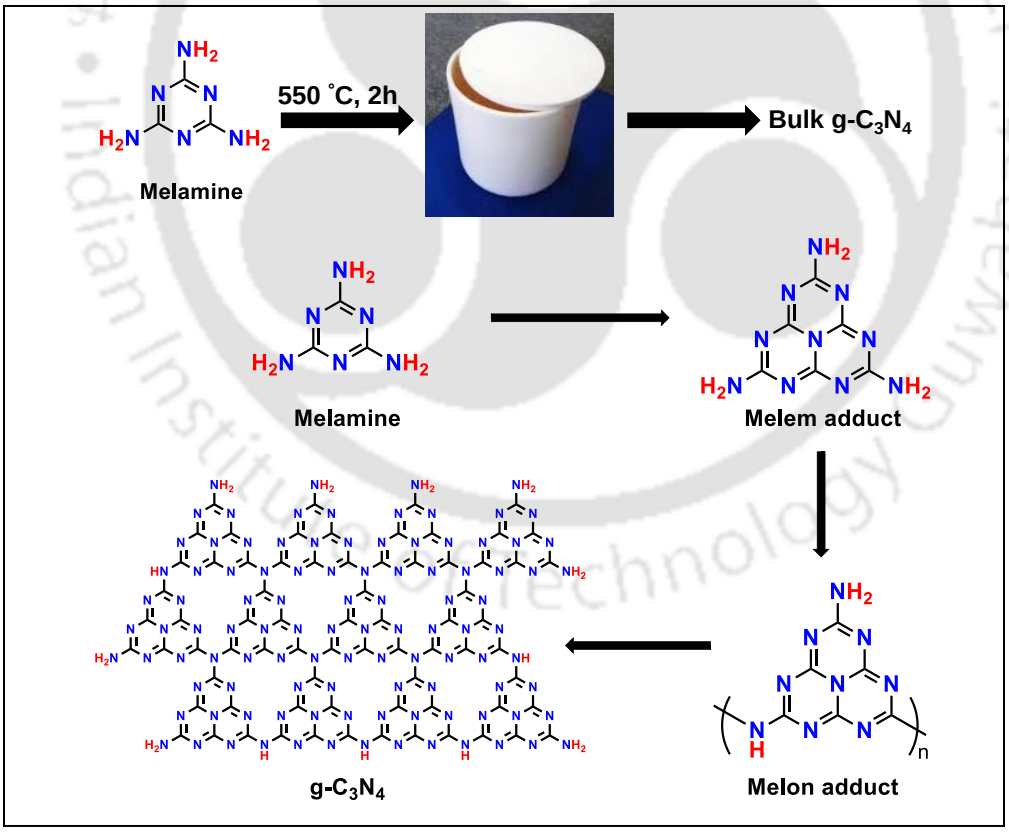


**Scheme 3.2.1** Synthetic protocol and reaction pathway illustrate the formation of bulk g–$C_3N_4$ via polycondensation of Melamine.


Part of this chapter has been published in **Carbon 2017, 121, 90–105**.

The furnace temperature was raised upto 550 $^oC$ at a heating ramp of 10 $^oC$ $min^{-1}$ and maintained for 2 h. After cooling to room temperature, the product was taken out and again ground into fine powers in an agate mortar. Briefly, the synthesis of bulk g-$C_3N_4$ from melamine illustrated in scheme **3.2.1** and also showed the involved different reaction steps. First step of the reaction started with condensation of the precursors i.e., melamine into melem-adduct at approximately 390 $^oC$. After that melem-adduct is converted into melon-adduct by the elimination of ammonia in next step. Finally, melon-adduct was converted into polymeric structure of graphitic carbon nitride (g-$C_3N_4$) through further condensation process.

### 3.2.2 SYNTHESIS OF g–$C_3N_4$ NANOFLAKES (NFs) AND NANOTUBES (NTs)

g-$C_3N_4$ nanoflakes (NFs) are synthesised through the ultrasonic exfoliation of bulk g-$C_3N_4$. g-$C_3N_4$ NTs were prepared through a simple and facile method i.e., rolling of NFs by means of thermal gradient.[29] In this synthetic protocol, first we exfoliated as-synthesised bulk g-$C_3N_4$ in water through ultrasonic treatment of about 1 h. After exfoliating, sample was collected through centrifugation and dried it at 80 $^oC$ for the complete removal of water, followed by the heating at 400 $^oC$ for 30 min to increase the distance between the layers. Now, g-$C_3N_4$ NFs powder from 400 $^oC$ was swiftly transferred to 500 mL cold water to get it quenched. Due to thermal stress at surface of g-$C_3N_4$ NFs, shrinkage of flakes started and formed rolled g-$C_3N_4$ NTs. Finally, g-$C_3N_4$ NTs sample was obtained by centrifugation followed via drying process. Detailed explanation of the mechanistic formation is mentioned in later section.

### 3.2.3 SYNTHESIS OF ZINC OXIDE NANORODS (ZnO NRs)

ZnO nanorods (ZnO NRs) were synthesized by following a previously used synthetic protocol.[31] 10 mmol of zinc nitrate hexahydrate (2.97 g) was dissolved in 50 mL of Milli-Q water with constant stirring. Then, equimolar amount of hexamine was added into the reaction mixture and the solution is heated at a temperature of 90 $^oC$ for 4 h with constant stirring. After cooling down to the room temperature, the resultant precipitate was centrifuged and purified by washing with water and ethanol several times. As obtained product was dried in a hot air oven at 75 $^oC$ for 4 h and then calcined it at 480 $^oC$ for 2 h to get final product.


Part of this chapter has been published in **Carbon 2017, 121, 90–105**.

### 3.2.4 SYNTHESIS OF ZnO NANOPARTICLES (NPs)

ZnO nanoparticles (NPs) were synthesized by adopting earlier reported synthetic route.[33] In this synthetic procedure, 40 mmol of $ZnCl_2$ (1.1 g) was dissolved in 40 mL of Milli-Q water and heated upto a temperature of 90 °C with constant stirring. An aqueous solution of sodium hydroxide (5 M, 3.2 mL) was added slowly into the reaction mixture with constant stirring at the same temperature for another 30 min. The reaction mixture was allowed to cool down to room temperature and the precipitate was separated out by discarding the supernatant liquid. For purification, this precipitate was washed with distilled water several times and dispersed in iso-propanol in an ultrasonic bath for 10 min at room temperature. The solution was centrifuged and dried in a hot air oven at 70 $^oC$ for 6 h. Finally, ZnO NPs were obtained via calcination at 450 °C for 1 h in a muffle furnace.

### 3.2.5 PREPARATION OF ZnO NR-g-$C_3N_4$ NF AND ZnO NR-g-$C_3N_4$ NT COMPOSITES

ZnO NR based composites of g-$C_3N_4$ NF and g-$C_3N_4$ NT were prepared by ultra-sonication treatment of both the components. In detail, an appropriate amount of as-synthesized g-$C_3N_4$ NF or g-$C_3N_4$ NT was dispersed in ethanol under ultrasonic treatment for 30 min. Now, a specific amount (according to weight ratio) of ZnO NRs was added into solution and continued the ultrasonic treatment for another 15 min. Finally, these solutions were placed inside a hot air oven to evaporate the solvent to obtain the composites which are ZnO NR-g-$C_3N_4$ NF or ZnO NR-g-$C_3N_4$ NT. A series of composites based on their morphologies were prepared by following same approach with different weight ratios of g-$C_3N_4$ to ZnO NR (0.25:1, 0.5:1, 0.75:1, 1:1 and 1:2). ZnO NPs based composites having different composite weight ratio of g-$C_3N_4$ NFs and g-$C_3N_4$ NTs were synthesized using the similar synthetic route, utilized for making the ZnO NRs based composites.

### 3.2.6 FABRICATION OF PHOTOANODES AND DEVICES

Photoanodes based on ZnO NR-g-$C_3N_4$ NF or ZnO NR-g-$C_3N_4$ NT composites were fabricated by making a homogeneous paste of the composite powders. For preparation of the paste, appropriate amounts of terpineol and ethanolic ethyl cellulose solution were added to the powders as binder materials and ground well in an agate mortar. As prepared homogenous paste was deposited on a cleaned conductive glass substrate i.e. FTO by using doctor blade method and dried in a hot air oven at 80 °C for 1 h. After cooling down to room temperature, all the films


Part of this chapter has been published in **Carbon 2017, 121, 90–105**.

were calcined at 400 °C for 30 min to remove the organic impurities. Thickness of the photoanodic films were measured by surface profilometer and found to be in the range of 8–10 μm. Photoanodes were sensitized with CdS QDs via successive ionic layer adsorption and reaction (SILAR) technique. Hereafter, the fabricated photoanode was represented as ZnO NR-g-$C_3N_4$ NF-CdS or ZnO NR-g-$C_3N_4$ NT-CdS. Photovoltaic devices were fabricated by sandwiching the photoanodes and counter electrodes. Polymeric tape was used as a spacer between the electrodes. A solution of Sulfide/polysulfide ($S^{2-}/S_n^{2-}$) in methanol and water mixture was used as an electrolyte for all the solar devices. Similarly, photoanodes of ZnO NPs based composites of g-$C_3N_4$ NFs and g-$C_3N_4$ NTs were fabricated by using similar procedure used for photoanodes of ZnO NRs based composites. Pt counter electrode was prepared by spin coating a solution of chloroplatinic acid (5 mM in isopropanol) on a cleaned FTO substrate followed by calcination at 450°C for 30 min in a muffle furnace and cooled down to room temperature. Sulfide/polysulfide ($S^{2-}/S_n^{2-}$) electrolyte was prepared by dissolving 0.5 M $Na_2S$, 2 M Sulfur powder and 0.2 M KCl in a solvent mixture of methanol-water (7:3, v/v). The active area for all fabricated devices was fixed and found to be 0.16 $cm^2$. Before the photovoltaic measurements, the fabricated devices were kept under dark condition for 24 h. ZnO NPs-based photoanodes were fabricated by following the same procedure used for fabrication of ZnO NRs based photoanodes.

## 3.3 RESULTS AND DISCUSSIONS

### 3.3.1 POWDER X-RAY DIFFRACTION ANALYSIS

Powder X-ray diffraction (PXRD) patterns have been taken to analyse the phase purity and crystal structure of all the synthesised pristine as well as their composite materials, as shown in figure **3.3.1**. Trace **(a)** shows PXRD pattern of ZnO NRs which is defined to be hexagonal wurtzite phase with (100), (002), (101), (102), (110), (103), (112) and (201) crystal planes and the space group symmetry is $P6_3mc$, according to the JCPDS Card No. 36-1451. There is no impurity peak detected in PXRD pattern which confirms the purity of synthesised material. Traces **(b)** and **(c)** depict the PXRD patterns of g-$C_3N_4$ NFs and g-$C_3N_4$ NTs. From the PXRD pattern of g-$C_3N_4$ NFs [trace **(b)**], two broad diffraction peaks are observed at $2\theta \approx 13.20°$ and 27.22° corresponding to the *d*-spacing values of 0.714 nm and 0.326 nm, which are indexed to (100) and (002) crystal plane in JCPDS 87-1526, as similar to the graphitic material.[34] Weak diffraction peak at $2\theta \approx 13.2°$ relates to characteristic in-plane structural motif i.e., repeating


Part of this chapter has been published in **Carbon 2017, 121, 90–105**.

pattern of tri-*s*-triazine units while strong diffraction peak at 2θ ≈ 27.22° indicates the staking of conjugated double bonds which resembles with the graphitic material. In the PXRD pattern of tubular structure [trace **(c)**], we observed a single diffraction peak at around 2θ ≈ 27.57° related to (002) crystal plane with an interlayer distance of d = 0.316 nm.

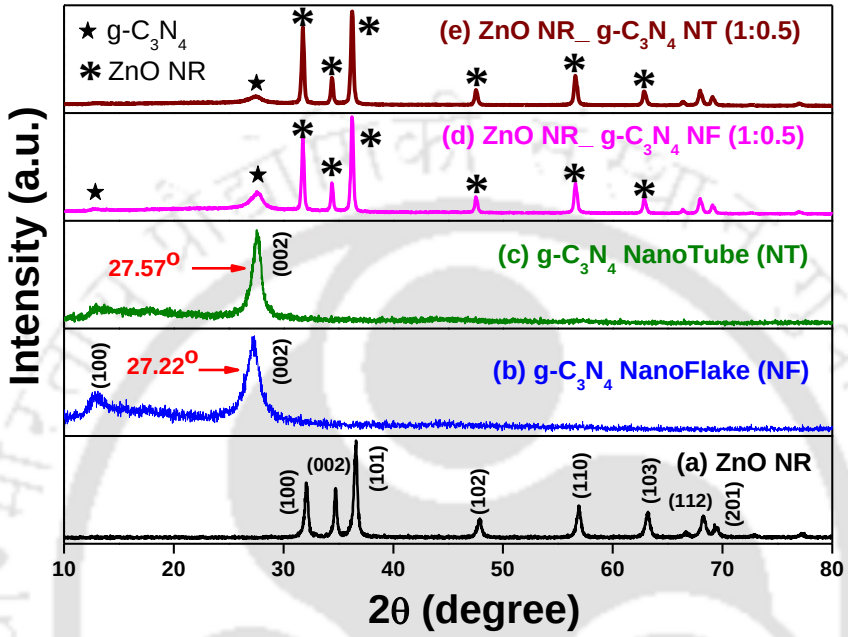


**Figure 3.3.1** Powder X-ray diffraction (PXRD) patterns of all the synthesized products; **(a)** ZnO NRs, **(b)** g–$C_3N_4$ NF, **(c)** g–$C_3N_4$ NT, **(d)** ZnO NR–g–$C_3N_4$ NFs (1:0.5) and **(e)** ZnO NR–g–$C_3N_4$ NTs (1:0.5) respectively.

Weaker diffraction peak at around 2θ ≈ 13.2° is almost disappeared for the g-$C_3N_4$ NTs and the diffraction intensity of the (002) plane gets weakened, demonstrating that the population of layered structural units are decreased. During the morphological transformation, (002) diffraction peak is slightly shifted towards a higher diffraction angle from 27.22° to 27.57° and interlayer distance decreases from 0.326 to 0.316 nm.[3] Consequently, there is an improvement in the interlayer staking of nanotubes due to decrement in the interlayer distance. Traces **(d)** and **(e)** are the PXRD patterns for composite materials of ZnO NRs with both the morphologies of g-$C_3N_4$ viz. ZnO NRs-g-$C_3N_4$ NFs (1:0.5) and ZnO NRs-g-$C_3N_4$ NTs (1:0.5) respectively. Crystal structures of both the components i.e., ZnO as well as g-$C_3N_4$ are retained in the diffraction patterns which confirmed the formation of respective composite samples.


Part of this chapter has been published in **Carbon 2017, 121, 90–105**.

### 3.3.2 MATERIAL MORPHOLOGY

Surface morphologies and textural modifications of as-synthesized pristine as well as their composites materials are investigated by performing Field emission scanning electron microscopy (FESEM) and Transmission electron microscopy (TEM) analysis. In the figure **3.3.2**, FESEM images **(a)** and **(b)** depict the morphological features of as-synthesized hexagon shaped ZnO NRs at lower and higher magnification and the size distribution of as-synthesized ZnO NRs appears to be in range of 400–600 nm.

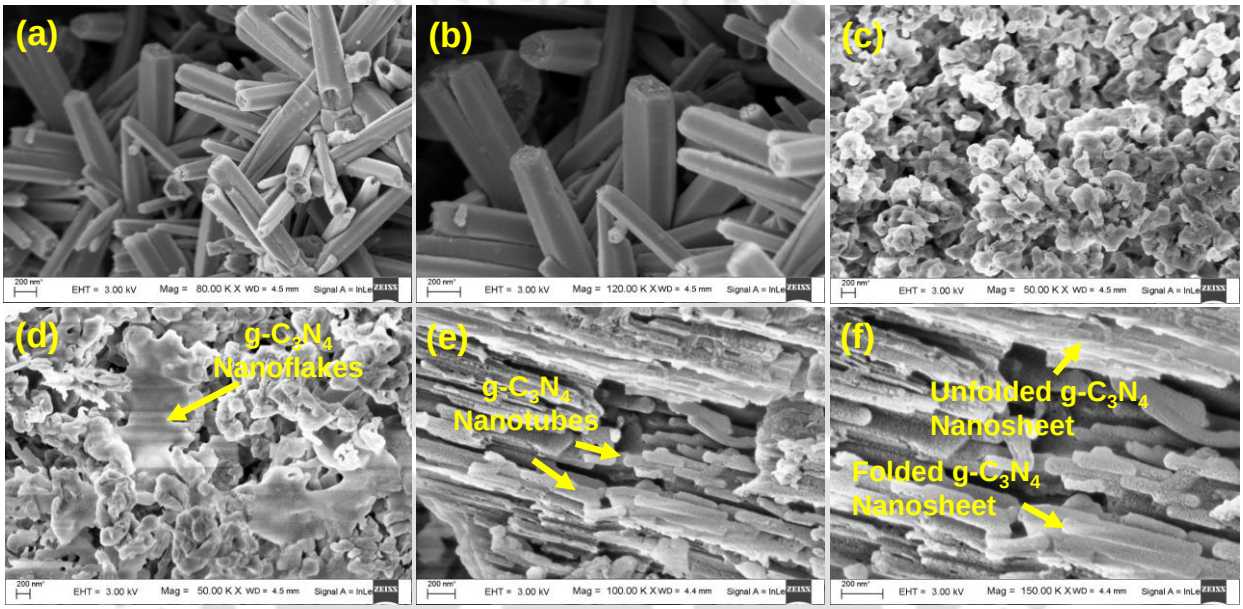


**Figure 3.3.2** Field emission scanning electron microscopy (FESEM) images show as synthesized hexagonal ZnO nanorods (NRs) [traces **(a)** and **(b)**], g–$C_3N_4$ nanoflakes (NFs) [traces **(c)** and **(d)**] and g–$C_3N_4$ nanotubes (NTs) [traces **(e)** and **(f)**] at different magnifications.

FESEM images **(c)** and **(d)** show the surface morphology of nanostructured g-$C_3N_4$ (dispersed in ethanol and exfoliated through ultrasonication) at different magnifications and exhibit flake-like layered structures. From FESEM image **(d)**, estimated size distribution of most of the g-$C_3N_4$ NFs are in the submicron range. Morphological features of texturally modified g-$C_3N_4$ NTs is demonstrating in FESEM images **(e)** and **(f)** of figure **3.3.2**. Due to random size distribution of as fabricated g-$C_3N_4$ NTs, it is difficult to calculate the exact dimensions of g-$C_3N_4$ NTs. It is proposed that as-synthesised g-$C_3N_4$ NFs are utilised to construct the g-$C_3N_4$ NTs through temperature gradient morphological transformation. Plausible mechanism for the formation of g-$C_3N_4$ NTs is the folding (rolling) of nanoflakes and to modulate themselves into the tubular structures by virtue of minimizing the total surface energy. Therefore, with the assistance of this


Part of this chapter has been published in **Carbon 2017, 121, 90–105**.

physical changes, tube-like g-$C_3N_4$ structures are efficiently formed by the rolling of g-$C_3N_4$ NFs, which can be further supported by the presence of some unfolded (unrolled) flakes around the nanotubes, as seen in FESEM images **(e)** and **(f)** of figure **3.3.2**.

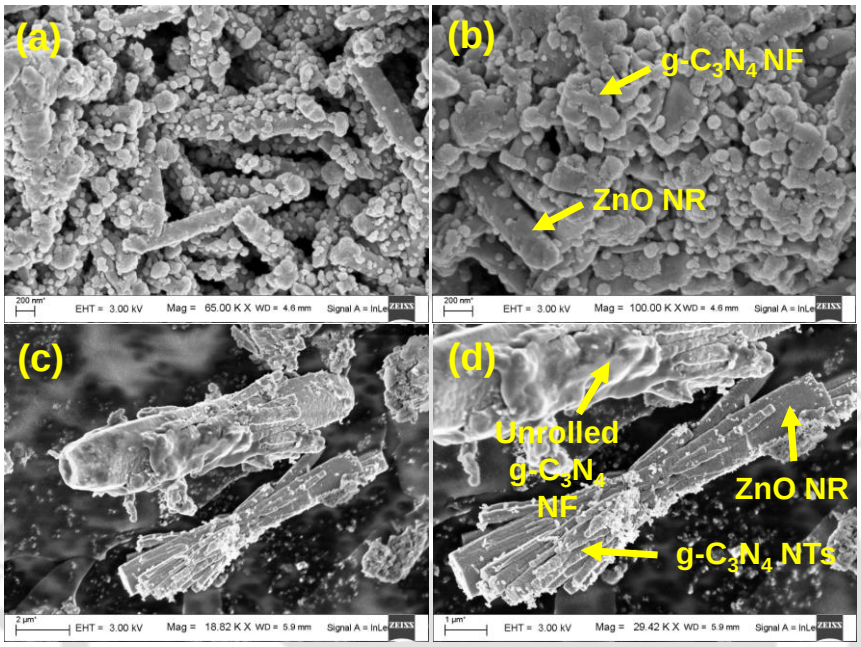


**Figure 3.3.3** Field emission scanning electron microscopy (FESEM) images show the features of as prepared ZnO NR–g–$C_3N_4$ NFs composite [traces **(a)** and **(b)**] and ZnO NR–g–$C_3N_4$ NTs composite [traces **(c)** and **(d)**] at various magnifications.

FESEM images **(a)** & **(b)** of figure **3.3.3** are portraying morphological features of as-prepared ZnO NR-g-$C_3N_4$ NF (weight ratio, 1:0.5) while images **(c)** & **(d)** are showing the morphology of ZnO NR-g-$C_3N_4$ NT based composite (weight ratio, 1:0.5) at different magnifications. In case of g-$C_3N_4$ NF based composite [FESEM images **(a)** & **(b)**], g-$C_3N_4$ NFs are well embedded around ZnO NRs, possibly due to unfolding and exfoliation of nanoflakes by means of ultrasonic treatment, used for making composites material. Moreover, other probable reason for the embedding process of nanoflakes around nanorods is the electronic interaction between polar wurtzite ZnO crystals and delocalized π-electrons as well as non-bonding electrons in the g-$C_3N_4$ nanoflakes which is later confirmed by FT–IR analysis. In other composite material viz. ZnO NR-g-$C_3N_4$ NT, ZnO NRs are well covered from folded nanoflakes i.e., g-$C_3N_4$ NTs along with some unfolded NFs, as shown in FESEM image **(c)** and **(d)** of figure **3.3.3**. From the FESEM images **(b)** and **(d)** of figure **3.3.3**, a number of undecorated ZnO NRs in both composites are observed, which are favourable for efficient photoexcited electron injection


Part of this chapter has been published in **Carbon 2017, 121, 90–105**.

by optimum loading of sensitizer particles i.e., CdS QDs on the photoanodic film. Charge transfer pathways of g-$C_3N_4$ to CdS QDs and to ZnO are advocated the photoexcited electron injection, described comprehensively in later section.

For further corroboration of structural features of as-prepared pristine materials, we have performed TEM analysis. In figure **3.3.4**, TEM image **(a)** illustrates the presence of layered structures (nanosheets) of as-synthesised g-$C_3N_4$ NFs at different magnifications. Trace **(b)** represents the selected area electron diffraction (SAED) pattern for g-$C_3N_4$ NFs which is showing a diffused diffraction ring corresponds to (002) crystal plane, implies an amorphous nature of the material. In the high resolution transmission electron microscopy (HRTEM) image [trace **(c)**], well distinct lattice fringes with the interplanar d-spacing value is calculated to be ~ 0.326 nm with respect to (002) lattice planes of g-$C_3N_4$ NFs.

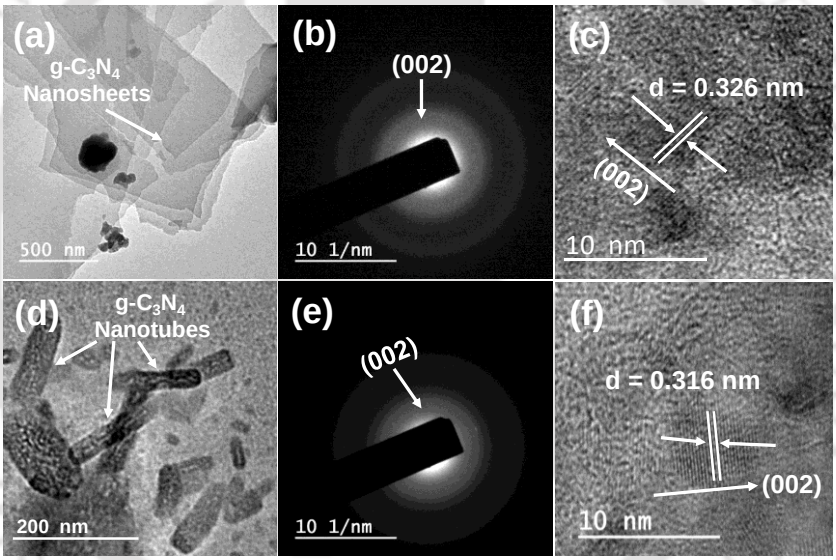


**Figure 3.3.4** Transmission electron microscopy (TEM) images **(a)** shows the features of as-synthesised g–$C_3N_4$ nanoflakes (NFs) while traces **(b)** and **(c)** display selected area electron diffraction (SAED) pattern and high resolution transmission electron microscopy (HRTEM) image of the g–$C_3N_4$ NFs. TEM images **(d)** shows the features of as-synthesised g–$C_3N_4$ nanotubes (NTs) while traces **(e)** and **(f)** display SAED pattern and HRTEM image of as prepared g–$C_3N_4$ NTs.

In figure **3.3.4**, TEM images **(d)** displays the presence of a large number of folded along with some unfolded g-$C_3N_4$ NFs which indicates the successful fabrication of g-$C_3N_4$ NTs. Hollow nature of g-$C_3N_4$ is confirmed by presence of an opening at end [trace **(d)**], which is beneficial to improve the light utilising harvesting efficiency, results generate the more number of photoexcitons which improves the current output from the device. Sizes of as fabricated g-$C_3N_4$ NTs are not uniform due to different degree of rolling of g-$C_3N_4$ NFs during the quenching


Part of this chapter has been published in **Carbon 2017, 121, 90–105**.

process so that the size of individual nanotube cannot be controlled. TEM image **(e)** denotes SAED pattern for g-$C_3N_4$ NTs. In case of g-$C_3N_4$ NTs, intensity of diffused diffraction ring corresponds to (002) crystal plane is weakened, suggesting the decrement in layered structure population. HRTEM image **(f)** related to g-$C_3N_4$ NTs reveals well-defined lattice fringes with the interplanar d-spacing value of ~ 0.316 nm, assign to (002) lattice planes of g-$C_3N_4$ NTs. During the textural modification of g-$C_3N_4$ NFs, diffraction peak corresponding to (002) crystal plane shifts toward the high 2θ value which suggests the decreasing interplanar d-spacing value and this observation is consistent with previously discussed PXRD analysis.

### 3.3.3 FORMATION MECHANISM FOR TUBULAR STRUCTURES OF g–$C_3N_4$

Based on all the considerations related to textural modification in the morphology section, the probable mechanism for the fabrication of tubular structures of g-$C_3N_4$ NFs i.e., g-$C_3N_4$ NTs is enlightened in scheme **3.3.1**. In the current preparation system, g-$C_3N_4$ NTs are formed by simply folding (rolling) of g-$C_3N_4$ NFs based on sudden hot-cool condition which generates a temperature gradient throughout the nanoflakes.

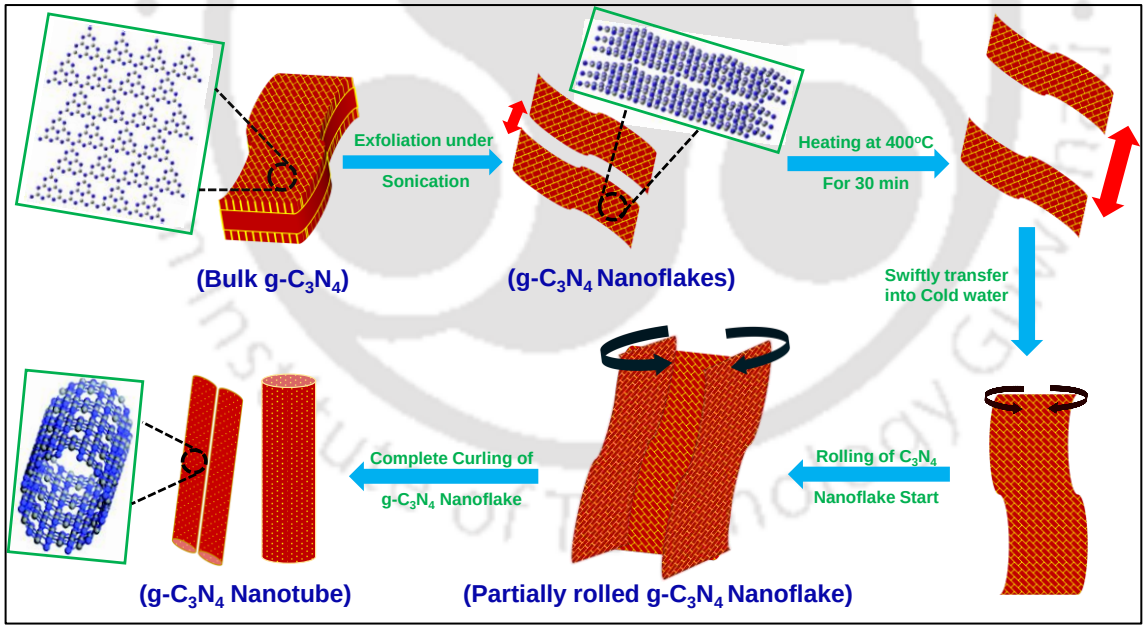


**Scheme 3.3.1** Schematic illustration represents probable mechanism for the formation of g–$C_3N_4$ nanotubes (g–$C_3N_4$ NTs) from bulk g-$C_3N_4$.

A key advantage of this synthetic protocol is using of cold water as a medium rather harsh chemical templates for this transformation. In detail, firstly as prepared bulk g-$C_3N_4$ is dispersed in water and exfoliates it through ultrasonication treatment for 30 min and produces

two dimensional (2–D) fibrous structures i.e., flakes. After sonication, sample is collected after centrifuging and drying. As dried sample i.e., g-$C_3N_4$ NFs went through further heat treatment at 400 $^oC$, results in increment in interlayer distance between the nanoflakes. After that, these flakes are swiftly transferred into the cold water. In the sudden hot-cold process, a temperature gradient is generated, due to which the outer cooling rate of nanoflakes is higher than the inner surface cooling rate. Consequently, a thermal stress is generated throughout the nanoflakes. As a result, stretching of inner surface of nanoflakes started while outer surface gets compressed; therefore the curling of nanoflakes happened. Finally, these nanoflakes are modified into tubular structures. Tubular structures of g-$C_3N_4$ show higher specific surface area as compared to nanoflakes due to the presence of opening ends, as can be seen from TEM image. Thus, nanotubes provide more active sites for loading of sensitizer particles, responsible to upsurge the flux of photoinduced electrons and these charge carriers are associated to generate more photocurrent of solar device. During the textural modification, electronic structure of surface is changed due to formation of polar surface sites which may also improve the device efficiency.

### 3.3.4 ENERGY DISPERSIVE X-RAY SPECTROSCOPIC ANALYSIS

To further confirm the elemental distribution and composition in g-$C_3N_4$ NTs and its composite i.e., ZnO NR-g-$C_3N_4$ NTs having weight ratio (1:0.5), selected area elemental mapping is carried out by energy dispersive X-ray (EDX) spectroscopic technique, as depicted in the figure **3.3.5 (A)** and **(B)** respectively. Homogeneous distribution of all the elements i.e., Carbon (C), Nitrogen (N) in case of g-$C_3N_4$ NTs while Carbon (C), Nitrogen (N), Zinc (Zn) and Oxygen (O) in case of composite are observed from the EDX mappings. This observation confirms the purity of successfully synthesized materials viz. pristine g-$C_3N_4$ NTs as well as its composite material. EDX pattern in figure **3.3.5 (A)** shows the elemental compositions (wt %) contained in the bare g-$C_3N_4$ NTs. It displays that nanotubes contain a weight ratio of carbon to nitrogen 3.18:3.99, which is very close to expected ratio of bulk g-$C_3N_4$.

Elemental compositions (wt %) for the composite material having weight ratio, 1:0.5 display in figure **3.3.5 (B)**. we found that the nitrogen content in the composite material become low due to the more thermo-dynamical stability of carbon and separate nitrogen molecules. Aluminum (Al) peak is also observed in the EDX pattern of g-$C_3N_4$ NTs because of the background aluminum foil, used for samples preparation.


Part of this chapter has been published in **Carbon 2017, 121, 90–105**.

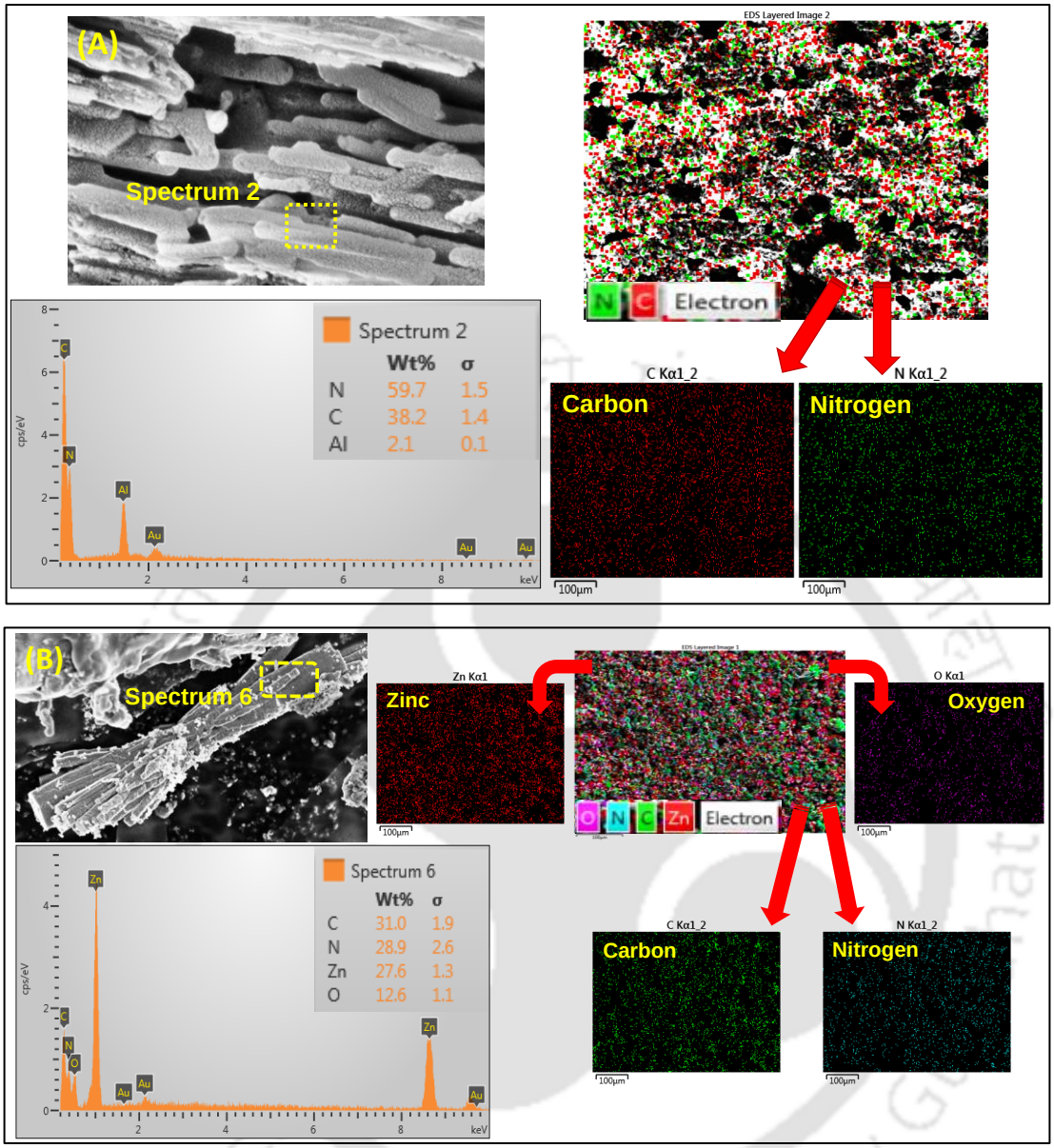


**Figure 3.3.5** Energy-dispersive X-ray (EDX) spectroscopy map and pattern of as-synthesized g–$C_3N_4$ nanotubes (NTs) [**(A)**] and (ZnO NR–g–$C_3N_4$ NTs) composite with weight ratio (1:0.5) [**(B)**] respectively.

### 3.3.5 BET SURFACE AREA ANALYSIS

Figure **3.3.6** depicts $N_2$ adsorption and desorption isotherms and Barrett-Joyner-Halenda (BJH) pore size distribution plot (inset) for as-synthesized g-$C_3N_4$ NFs (blue line) and g-$C_3N_4$ NTs (olive line) respectively. High surface area with porosity of any photoanodic material is the key attribute to be used in the photovoltaic devices in order to get high photovoltaic performance. Appearance of a hysteresis loop in the adsorption-desorption isotherm indicates the mesoporous nature of the samples. Both pristine materials show type IV isotherms with H3


Part of this chapter has been published in **Carbon 2017, 121, 90–105**.

hysteresis loops. Observed BET surface area values for g-$C_3N_4$ NFs and g-$C_3N_4$ NTs are estimated to be 29 $m^2g^{-1}$ and 43 $m^2g^{-1}$ respectively. Value of BET surface area for g-$C_3N_4$ NTs is found to be higher than g-$C_3N_4$ NFs which offers more active sites for sensitizer loading, leading to a better loading in Nanotubes compared to Nanoflakes.

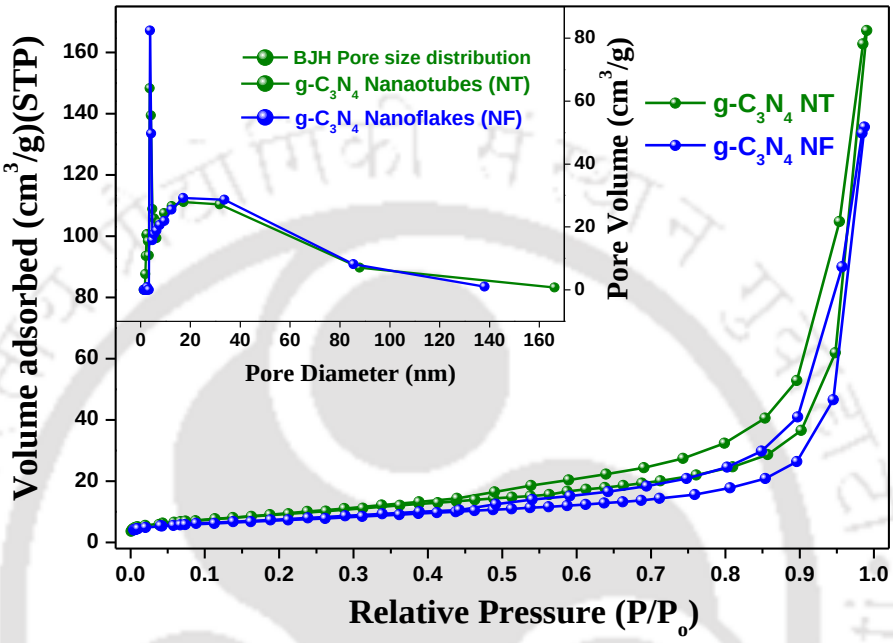


**Figure 3.3.6** Nitrogen adsorption–desorption isotherms and Barrett-Joyner-Halenda (BJH) pore size distribution plot (inset) for as synthesized g–$C_3N_4$ NFs (blue line) and g–$C_3N_4$ NTs (olive line) respectively.

From the pore-size distribution curves it is found that both the materials are showing similar porous behaviour and demonstrate a narrow peak centered at 3.6 nm, which may be due to the releasing of $NH_3$ during the polycondensation of melamine. The broad pore size distribution peak for both sample reveals at range of 10–35 nm, possibly due to existence of inter void spaces in both nanostructures.

### 3.3.6 UV–VISIBLE DIFFUSE REFLECTANCE SPECTRA

Figure **3.3.7 (A)** shows the normalized UV–visible (UV–Vis) absorption spectra all material, have recorded by fabricating thin films in the wavelength range of 350–800 nm, using a glass substrate as a reference and digital photos of all thin films displayed in same spectra. From figure **3.3.7 (A)**, absorption edges of as synthesized g-$C_3N_4$ NFs, g-$C_3N_4$ NTs and ZnO NRs are observed to be at ~ 454 nm, ~ 435 nm and ~ 395 nm respectively, corresponding to the band gap of ~ 2.73 eV, ~ 2.85 eV and ~ 3.13 eV. We observed a blue shift in the absorption profile of g-


Part of this chapter has been published in **Carbon 2017, 121, 90–105**.

$C_3N_4$ NTs with respect to g-$C_3N_4$ NFs, clearly seen in enlarged spectra of figure **3.3.7 (A)** inset. Hypsochromic shift in the absorption edge of g-$C_3N_4$ NTs is mainly because of the strong quantum confinement effects induced by decreased size of nanoscale tubes.[35]

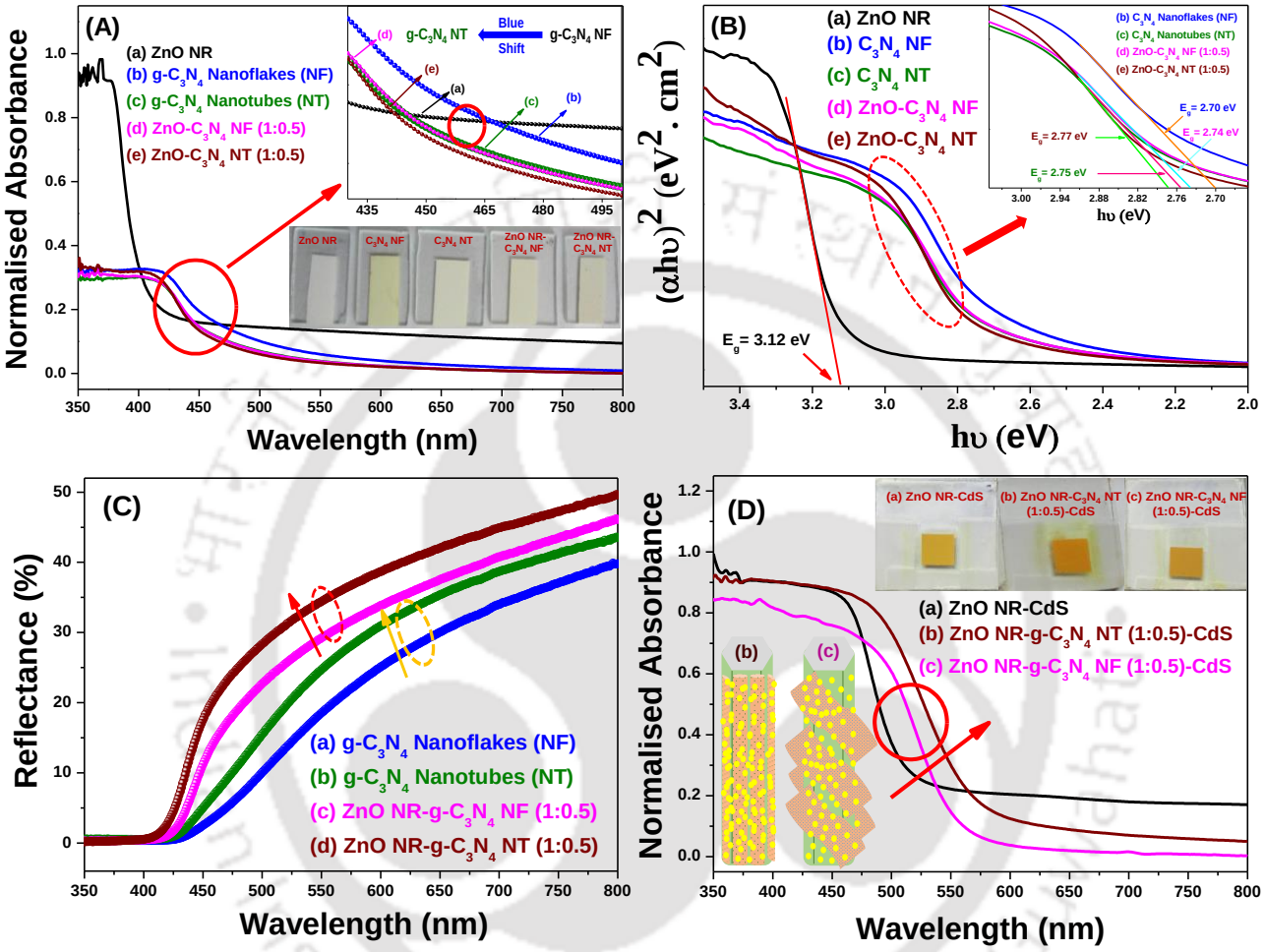


**Figure 3.3.7 (A)** Diffuse reflectance UV–visible (UV–Vis) absorption profiles for all the synthesized bare products and their composites namely; traces **(a)** pure ZnO nanorods (NRs), **(b)** g–$C_3N_4$ nanoflakes (NFs), **(c)** g–$C_3N_4$ nanotubes(NTs), **(d)** ZnO NR–g–$C_3N_4$ NF composite and **(e)** ZnO NR–g–$C_3N_4$ NT composite with weight ratio (1:0.5) respectively. Inset of figure **(A)** consists the enlarge portion of same spectra which indicates the possible blue shift in case of g–$C_3N_4$ NTs with respect to g–$C_3N_4$ NFs and digital photographs of as fabricated thin films of same materials. **(B)** Optical band gap energies for both the morphology of g–$C_3N_4$ and their composites, calculated from the Tauc plots. Inset of figure **(B)** shows magnify spectra of selected portion for better comparisons. **(C)** Diffused reflectance spectra of both morphology of g–$C_3N_4$ with their composites [weight ratio (1:0.5)] based films of comparable thickness. **(D)** Diffuse reflectance UV–Vis absorption spectra of CdS QDs sensitized composites based on both morphology of g–$C_3N_4$ [weight ratio (1:0.5)] as well as with bare ZnO NRs. Inset of figure **(D)** contains schematic illustration for the loading of CdS QDs on both the composites along with digital photographs for the same.


Part of this chapter has been published in **Carbon 2017, 121, 90–105**.

More perfect packing and electronic coupling may be other possible reason for this blue shift. In spite of having limitation in terms of visible light absorption, g-$C_3N_4$ NTs based device showed the superior performance because of its high specific surface area for sensitizer loading. We also observed similar trend for both morphology based composites. There is a distinct blue shift in absorption edges for both morphology based composites as compared to their parent materials, as shown in enlarge absorption spectra [inset to figure **3.3.7 (A)**]. This outcome suggests a possible electronic interaction between g-$C_3N_4$ and ZnO NRs due to the charge migration from g-$C_3N_4$ to ZnO. Figure **3.3.7 (B)** denotes a plot for estimation of optical band gap energy ($E_g$) from the tangent of corresponding Tauc plot of bare and composite materials. Inset to it shows the enlarged form of same plots (selected with red circled) for all samples. We get similar trend from Tauc plot as observed in UV−Vis spectra. From Tauc plot, estimated band gap energies for g-$C_3N_4$ NFs, g-$C_3N_4$ NTs and ZnO NRs are found to be ~ 2.72 eV, ~ 2.78 eV and ~ 3.12 eV respectively which are in good agreement with observed values from absorption spectra. An apparent blue shift in the absorption profile of g-$C_3N_4$ NTs relative to g-$C_3N_4$ NFs is also well supported with the shift of ~ 0.06 eV in the estimated band gap energies. Blue shift in the absorption profile of composites is also consistent with the band gap values, obtained from Tauc plots.

Reflectance measurements are performed for all the photoanode films of comparable thickness based on **(a)** g-$C_3N_4$ NFs, **(b)** g-$C_3N_4$ NTs, **(c)** ZnO NR-g-$C_3N_4$ NFs and **(d)** ZnO NR-g-$C_3N_4$ NTs deposited on glass substrates to investigate the light scattering effects as shown in figure **3.3.7 (C)**. We observed higher reflectance value in case of g-$C_3N_4$ NTs as compare to g-$C_3N_4$ NFs which suggests more utilization of incident light and enhanced the repeated excitation process of sensitizer molecules in tubular structures. Tubular nature of g-$C_3N_4$ NTs is probable reason for superior light scattering which is not in case of g-$C_3N_4$ NFs. ZnO NR-g-$C_3N_4$ NTs composite based photoanodic film exhibits higher reflectance in the wavelength range of 420−800 nm than that of ZnO NR-g-$C_3N_4$ NFs composite based film. Better light harvesting ability of g-$C_3N_4$ NTs and ZnO NR-g-$C_3N_4$ NTs composite is because of confinement of light which increases the stay of the incident light through multiple reflections within the photoanodic film. This confirms role of light scattering effect in enhanced photovoltaic performance of ZnO NR-g-$C_3N_4$ NTs composite based devices.


Part of this chapter has been published in **Carbon 2017, 121, 90–105**.

Figure **3.3.7 (D)** depicts normalized UV–Vis absorption profiles of CdS QDs sensitized photoanodes fabricated with pristine ZnO NR (Black line), ZnO NR-g-$C_3N_4$ NFs [magenta line, (1:0.5)] and ZnO NR-g-$C_3N_4$ NTs [wine red line, (1:0.5)] respectively. Absorption range for all the photoanodes are observed to be in region (350–800 nm). Note that we have carried out the same number of SILAR cycles for sensitization of all the photoanodes, as similar in device fabrication. We have noted a red shift in absorption edges for both composites with respect to bare ZnO NRs based photoanode film which is due to more loading sites provide by g-$C_3N_4$ for successive growth of CdS QDs. A gradual increase in absorbance for the ZnO NR-g-$C_3N_4$ NTs composite based photoanode as compared to the ZnO NR-g-$C_3N_4$ NFs composite based photoanode is attributed to the higher specific surface area of g-$C_3N_4$ NTs. Therefore, g-$C_3N_4$ NTs offer more active sites for sensitizer loading so the observations are in accordance with higher loading of sensitizer molecules in case of ZnO NR-g-$C_3N_4$ NTs composite based photoanode as compare to ZnO NR-g-$C_3N_4$ NFs based photoanode. After anchoring the more amounts of CdS QDs, light harvesting ability of photoanode gets improve and boost the efficacy value of photovoltaic device.

### 3.3.7 STEADY STATE AND TIME RESOLVED PHOTOLUMINESCENCE ANALYSES

Figure **3.3.8 (A)** shows the steady state photoluminescence (PL) spectra for **(a)** g-$C_3N_4$ NFs, **(b)** g-$C_3N_4$ NTs and their composites with different weight ratios of ZnO NR to g-$C_3N_4$, viz. ZnO NR-g-$C_3N_4$ NFs [1:0.5 (orange line)], ZnO NR-g-$C_3N_4$ NFs [1:0.25 (magenta line), ZnO NR-g-$C_3N_4$ NTs [1:0.5 (pink line)] and ZnO NR- g-$C_3N_4$ NTs [1:0.25 (wine red line)], recorded at an excitation wavelength of 360 nm which is correspond to g-$C_3N_4$. From steady state PL spectra, a strong PL emission peak has occurred at around 460 nm correspond to as-synthesized g-$C_3N_4$ NFs which is due to radiative recombination of excitons or photogenerated ($e^-$ – $h^+$) pairs. PL spectra show a gradual static quenching of PL intensity for the tubular structures of g-$C_3N_4$ as compare to g-$C_3N_4$ NFs which signifies an inhibited recombination of ($e^-$ – $h^+$) pairs and facilitated charge separation, later confirmed by TRPL study. This observation confirms efficient transportation of photoexcited charge carriers at the g-$C_3N_4$ NTs surface. Observed changes in emission characteristics of both structure of g-$C_3N_4$ are well supported by digital images, as shown in inset of figure **3.3.8 (A)**. In case of composite materials, PL intensity decreases with respect to their parent material due to the proposed photo-generated charge


Part of this chapter has been published in **Carbon 2017, 121, 90–105**.

transfer phenomenon at the interface of g-$C_3N_4$ structures and ZnO NRs. This statement is advocated the possibility of photogenerated charge injection from the g-$C_3N_4$ (CB edge ~ – 3.62 eV) to the ZnO NRs (CB edge ~ – 4.24 eV).

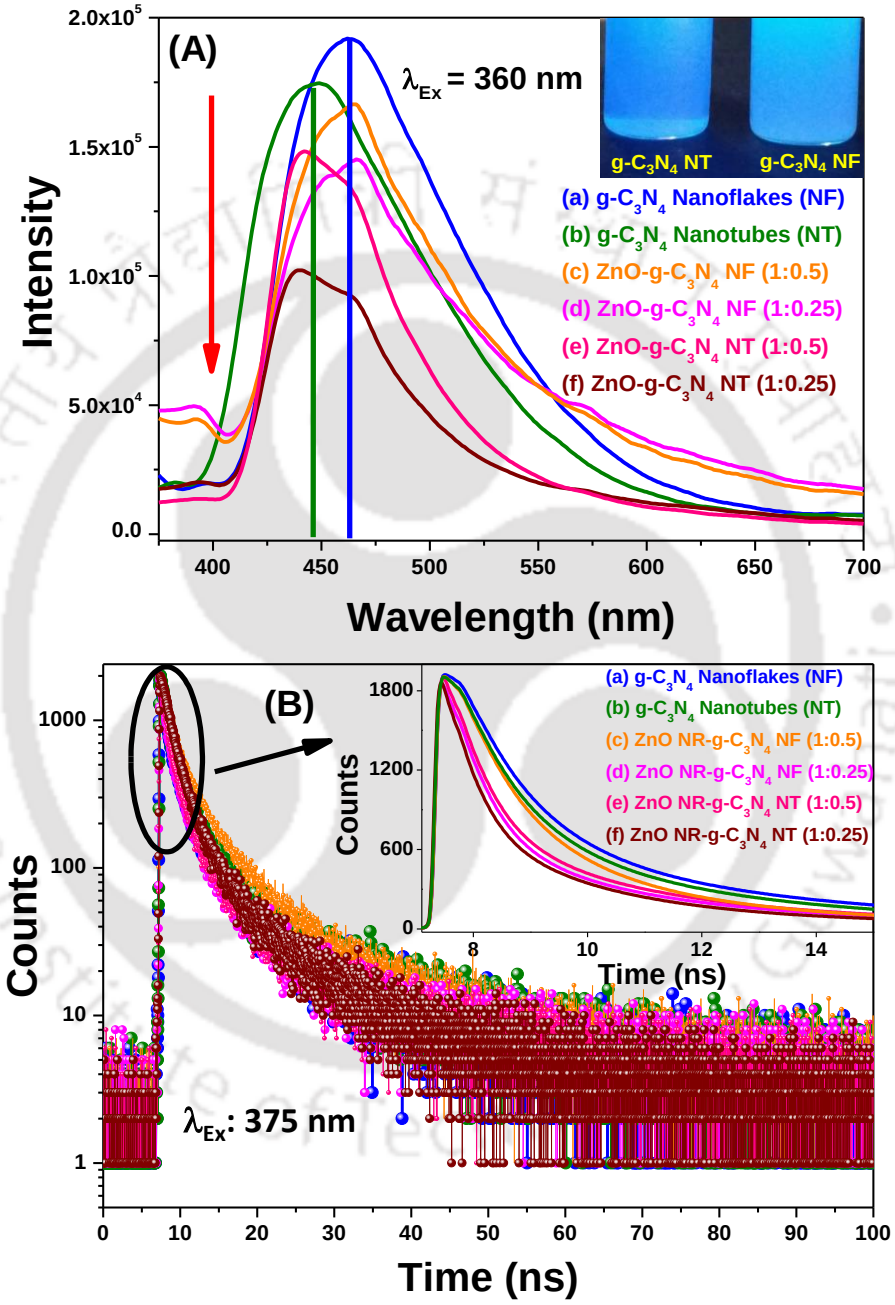


**Figure 3.3.8** Traces **(A)** & **(B)** display Steady state and Dynamic photoluminescence (PL) spectra for as-synthesised pristine materials and their composites namely **(a)** g–$C_3N_4$ NF, **(b)** g–$C_3N_4$ NTs, **(c)** ZnO NR–g–$C_3N_4$ NF (1:0.5), **(d)** ZnO NR–g–$C_3N_4$ NF (1:0.25), **(e)** ZnO NR–g–$C_3N_4$ NT (1:0.5) and **(f)** ZnO NR–g–$C_3N_4$ NT (1:0.25) respectively.


Part of this chapter has been published in **Carbon 2017, 121, 90–105**.

There is a slight red shift in the peaks of nanoflakes based composites, probably due to delocalization of photogenerated charges in composites while the composite based on nanotubes get blue shifted as compare to bare nanotubes, owing to localization of photogenerated charges at ZnO NRs in composites. As the substantial decrement in amount of g-$C_3N_4$ for composites materials, we have noticed a regular quenching of PL intensities of the composites. Increase in the weight ratios of g-$C_3N_4$ to ZnO NR in the composite i.e., from (0.25:1) to (0.5:1), population of bare or unbounded g-$C_3N_4$ structures become more resulting in the inhibited charge injection of the photogenerated charges from g-$C_3N_4$ to ZnO NRs. To gain further insights into the excited state interaction between g-$C_3N_4$ and ZnO NRs, and also charge transport kinetics in the composites, time resolved photoluminescence (TRPL) measurements are carried out for bare as well as composite materials as shown in figure **3.3.8 (B)**, using a 375 nm diode laser excitation source. PL decay traces are fitted with a tri-exponential function using fast software provided by Edinburgh instruments to calculate the exciton lifetime values. Observed multi-exponential decay patterns reveal processes that are involved during the decay of emissive excitons. The values of fitting parameter ($\chi^2$) and detailed spectroscopic results such as, exciton lifetimes ($\tau_1$, $\tau_2$, $\tau_3$), pre-exponential factors ($\alpha_1$, $\alpha_2$, $\alpha_3$), average exciton lifetimes ($<\tau>$) etc. are summarized in the table **3.3.1**. The average lifetime values are derived from **equation (1)**: [36]

$$<\tau>=\frac{\alpha_1\tau_1^2+\alpha_2\tau_2^2+\alpha_3\tau_3^2}{\alpha_1\tau_1+\alpha_2\tau_2+\alpha_3\tau_3} \qquad (1)$$

**Table 3.3.1.** Calculated parameters such as fitting parameter ($\chi^{2)}$, exciton lifetimes ($\tau_1$, $\tau_2$, $\tau_3$) (ns), pre-exponential factors ($\alpha_1$, $\alpha_2$, $\alpha_3$) (%), average exciton lifetimes ($<\tau>$) (ns) for bare as well as their composite materials and electron injection rate constants ($k_{einj}$) ($S^{-1}$) for all composite materials are summarized in the following table:

| Samples | $\chi^2$ | $\tau_1$ | $\tau_2$ | $\tau_3$ | $\alpha_1$ | $\alpha_2$ | $\alpha_2$ | $<\tau>$ (ns) | $k_{einj}$ ($s^{-1}$) |
|---|---|---|---|---|---|---|---|---|---|
| **g-$C_3N_4$ NF** | 1.090 | 0.586 | 2.778 | 14.036 | 25.30 | 47.63 | 27.07 | 14.03 | ------ |
| **g-$C_3N_4$ NT** | 1.071 | 0.585 | 2.807 | 15.340 | 22.49 | 48.86 | 28.65 | 13.20 | ------ |
| **(1:0.5) NF** | **1.078** | **1.185** | **4.463** | **18.540** | **31.36** | **48.91** | **19.73** | **12.53** | **$0.08\times10^8$** |
| **(1:0.5) NT** | **1.044** | **0.431** | **2.266** | **12.296** | **21.73** | **50.61** | **27.65** | **9.57** | **$0.28\times10^8$** |
| **(1:0.25) NF** | 1.057 | 0.448 | 2.273 | 12.633 | 21.44 | 51.25 | 27.31 | 9.81 | $0.30\times10^8$ |
| **(1:0.25) NT** | 1.004 | 0.938 | 2.530 | 11.257 | 27.13 | 49.57 | 23.30 | 7.86 | $0.51\times10^8$ |


Part of this chapter has been published in **Carbon 2017, 121, 90–105**.

From the Table **3.3.1**, average exciton lifetime of g-$C_3N_4$ NTs is observed to be faster as compare to g-$C_3N_4$ NFs, suggesting the efficient charge separation. A gradual decrement in exciton lifetimes is noticed for all the composites as compared to their bare material which confirms the feasible photoexcited electron transfer from g-$C_3N_4$ to ZnO NR, results inhibit the recombination process of g-$C_3N_4$. However, as substantial reduction in the amount of g-$C_3N_4$ for composites materials, we have noticed the continuous decrement in exciton lifetime for composites namely; ZnO NR-g-$C_3N_4$ NTs [1:0.25 (wine red spectrum)] and ZnO NR-g-$C_3N_4$ NFs [1:0.25 (magenta spectrum)], as evident from figure **3.3.8 (B)**. Calculated <τ> values are found to be ~ 7.86 ns (for 1:0.25 NTs) and ~ 9.81 ns (for 1:0.25 NFs) which are significantly lower than the average exciton lifetimes estimated for other composites and pure materials which are ~ 9.57 ns (for 1:0.5 NTs), ~ 12.53 ns ( for 1:0.5 NFs), ~ 14.03 ns (for g-$C_3N_4$ NFs) and ~ 13.20 ns (for g-$C_3N_4$ NTs) respectively. This observation confirms a strong excited state electronic interaction between g-$C_3N_4$ and ZnO NRs in the both type of composites. Lower values of average exciton life times observed for the g-$C_3N_4$ NT based composites are also indicative of faster photogenerated electron injection from g-$C_3N_4$ NTs to ZnO NR. Rate constants of electron injection ($k_{einj}$) from g-$C_3N_4$ to ZnO NRs is calculated from **equation (2)** and listed in table **3.3.1**: [36]

$$\boldsymbol{k_{einj} = \frac{1}{<\tau>_{composite}} - \frac{1}{<\tau>_{g-C_3N_4}}} \qquad (2)$$

From table **3.3.1**, the $k_{einj}$ values for the composites (1:0.25 NTs) and (1:0.25 NFs) are found to be $0.51 \times 10^8$ $s^{-1}$ and $0.30 \times 10^8$ $s^{-1}$, which are significantly higher than the other composites which are $0.28 \times 10^8$ $s^{-1}$ for (1:50 NTs) and $0.08 \times 10^8$ $s^{-1}$ for (1:0.50 NFs). These observations advocate a faster charge injection dynamics in both the composites having weight ratios (1:0.25). As the weight ratio of g-$C_3N_4$ increases in composites from (1:0.25) to (1:0.5), population of excitons undergoing radiative decay are higher, resulting in a slower charge injection dynamics from g-$C_3N_4$ to ZnO NR. Therefore, photogenerated charge transfer resulting in a stronger interaction of polar wurtzite ZnO NRs and delocalized π-electrons as well as non-bonding electrons in the g-$C_3N_4$. Although we observed a faster charge injection rate in case of composites having weight ratio (1:0.25, ZnO NR to g-$C_3N_4$ NTs), the efficacy value is more for


Part of this chapter has been published in **Carbon 2017, 121, 90–105**.

composite having weight ratio (1:0.5, ZnO NR to g-$C_3N_4$ NTs), probably due to allocation of sufficient active sites for optimum loading of CdS QDs.

### 3.3.8 FOURIER TRANSFORM INFRARED (FT–IR) SPECTRA

Figure **3.3.9** shows FT–IR spectra for **(a)** bare ZnO NRs, **(b)** g-$C_3N_4$ NFs, **(c)** g-$C_3N_4$ NTs, **(d)** ZnO NR-g-$C_3N_4$ NF and **(e)** ZnO NR-g-$C_3N_4$ NT. In the FT–IR spectrum of pristine material such as ZnO NRs trace **(a)**, dominating a peak centered at 531 $cm^{-1}$ corresponding to –Zn–O stretching vibration mode.[37] In trace **(b)**, g-$C_3N_4$ NF revealed a characteristics peak at 810 $cm^{-1}$ which corresponds to bending modes of s-triazine repeating units of g-$C_3N_4$.[38] Various strong peaks are observed in the region of 1200–1650 $cm^{-1}$, which relate to the typical stretching modes of C–N heterocycles. IR bands centered at 1236 $cm^{-1}$, 1315 $cm^{-1}$ and 1406 $cm^{-1}$ are corresponding to –C–N stretching vibration modes while the IR peaks centered at 1575 $cm^{-1}$ and 1640 $cm^{-1}$ are assigned to –C═N stretching vibrations.[39] Broad peaks present at 3000–3300 $cm^{-1}$ are associated with –N–H stretching. However, there is no IR band at 2200 $cm^{-1}$, related to –C≡N stretching vibration which means both pristine materials have continuity in their inorganic network structure.

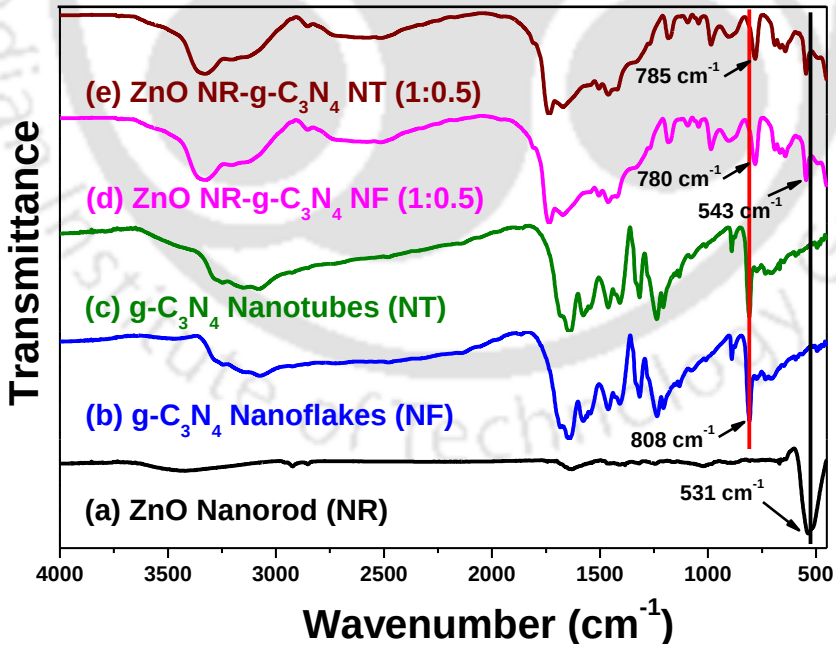


**Figure 3.3.9** FT–IR spectra of **(a)** bare ZnO NRs, **(b)** g–$C_3N_4$ NFs, **(c)** g–$C_3N_4$ NTs, **(d)** ZnO NR–g–$C_3N_4$ NF (1:0.5) and **(e)** ZnO NR–g–$C_3N_4$ NT (1:0.5) respectively.


Part of this chapter has been published in **Carbon 2017, 121, 90–105**.

FT–IR spectrum of g-$C_3N_4$ NTs appears to be similar to that of g-$C_3N_4$ NFs, suggesting that g-$C_3N_4$ NTs retained the same chemical structure as g-$C_3N_4$ NFs have. All the characteristic peaks of g-$C_3N_4$ and ZnO NR can be seen clearly in the spectra of composites, as shown in traces **(d)** & **(e)** respectively. In the spectra of composite materials, it is observed that characteristics peak of g-$C_3N_4$ i.e., s-triazine unit is shifted towards the lower wavenumber, revealing the bond strength of –C–N is weakened owing to ensure an electronic interaction between g-$C_3N_4$ and ZnO NR. This electronic interaction has a great significance to interfacial transfer of charge carriers and also to induce a synergetic effect between g-$C_3N_4$ and ZnO NRs in the composite material.

### 3.3.9 PHOTOVOLTAIC MEASUREMENTS OF SOLAR CELLS

To understand the effects of different morphologies of g-$C_3N_4$ in terms of light harvesting and charge transfer ability of as prepared (ZnO NR-g-$C_3N_4$) composites, we have constructed the CdS QDs sensitized photovoltaic devices and systematically analysed the photovoltaic performance parameters by using platinized FTO as a counter electrode. Figure **3.3.10 (A)** demonstrates current density–voltage (*J*–V) curves for all composite based devices, having different weight ratios of ZnO NRs to g-$C_3N_4$. Photovoltaic performance parameters for all devices such as, short circuit current density ($J_{sc}$), open circuit voltage ($V_{oc}$), fill factor (FF) and the overall power conversion efficiency (PCE, η) are summarized in table **3.3.2**. From table **3.3.2**, it is clear that PCE values for all devices based on composite (ZnO NR-g-$C_3N_4$ NTs) are superior to that of (ZnO NR-g-$C_3N_4$ NFs) which confirm supremacy of the tubular structures of g-$C_3N_4$ by means of improved light harvesting as well as better charge transfer ability. For devices having weight ratio (1:0.25, ZnO NR to g-$C_3N_4$), all photovoltaic parameters i.e., $J_{sc}$, $V_{oc}$, FF and η are found to be inferior as compare to all devices with (1:0.5, ZnO NR to g-$C_3N_4$) composite ratio. Although composite ratio (1:0.25, ZnO NR to g-$C_3N_4$) has a faster charge injection rate (in TRPL analysis) but efficiency value is less due to having lesser surface active sites for loading of CdS QDs. For devices having weight ratio (1:0.75, ZnO NR to g-$C_3N_4$), efficacy value further decreases with respect to composite (1:0.5) based devices, possibly due to an increased amount of g-$C_3N_4$ in composites, leads to non-uniform loading of CdS QDs. Usually, composites having more content of g-$C_3N_4$ should offer more adsorption sites for loading of CdS QDs, but with the repeated deposition cycles, the QDs tend to agglomerate due to


Part of this chapter has been published in **Carbon 2017, 121, 90–105**.

anchoring of bigger QDs which is not in case of composite (1:0.5) based photoanodes. Thus, optimized weight ratio of composite i.e., (1:0.5, ZnO NR to g-$C_3N_4$) based devices showed the maximum PCE as compare to other composites based devices. For optimum weight ratio (1:0.5), all performance parameters i.e., $J_{sc}$ (mAcm$^{-2}$), $V_{oc}$ (mV), FF (%) and PCE, η (%) for g-$C_3N_4$ NTs based devices are superior as compare to g-$C_3N_4$ NFs, values are found to be ≈ 10.88, ≈ 628, ≈ 43.21, ≈ 2.90 (for g-$C_3N_4$ NTs based device) while ≈ 8.87, ≈ 590, ≈ 37.50, ≈ 2.0 for g-$C_3N_4$ NFs based devices respectively.

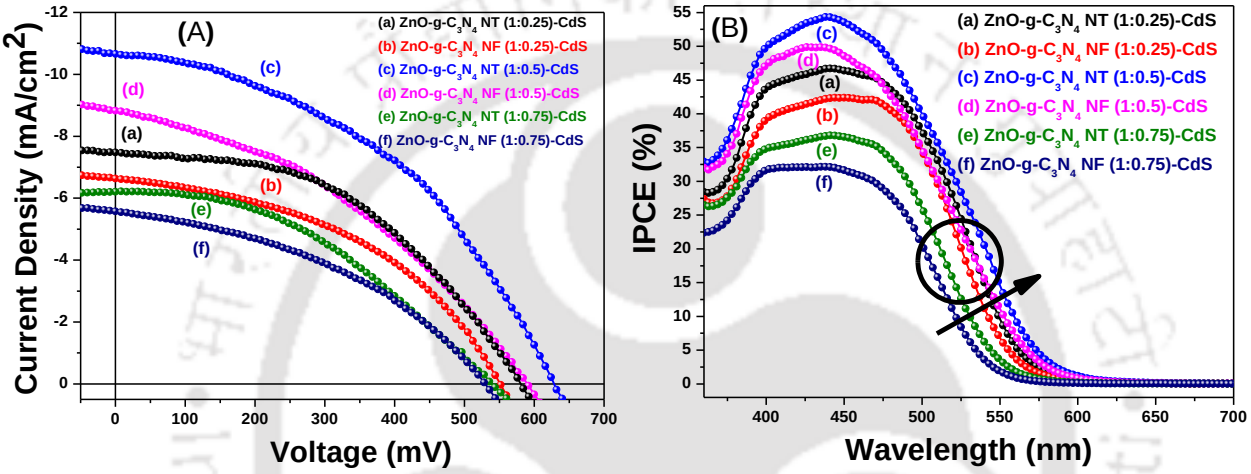


**Figure 3.3.10 (A)** Current density–Voltage (*J*–V) curves for all fabricated photovoltaic devices based on both morphology of g–$C_3N_4$ with different weight ratios namely: **(a)** ZnO NR–g–$C_3N_4$ NT (1:0.25)–CdS, **(b)** ZnO NR–g–$C_3N_4$ NF (1:0.25)–CdS, **(c)** ZnO NR–g–$C_3N_4$ NT (1:0.5)–CdS, **(d)** ZnO NR–g–$C_3N_4$ NF (1:0.5)–CdS, **(e)** ZnO NR–g–$C_3N_4$ NT (1:0.75)–CdS and **(f)** ZnO NR–g–$C_3N_4$ NF (1:0.75)–CdS and **(B)** Corresponding IPCE plots for the respective devices employing $S^{2-}/S_n^{2-}$ as the redox couple.

**Table 3.3.2** Short-circuit current density ($J_{sc}$), open-circuit voltage ($V_{oc}$), fill factor (FF), and power conversion efficiency (η) for the fabricated solar cells incorporating different photoanodes.

| **Device Composition (ZnO NR-g-$C_3N_4$)** | **$J_{sc}$ (mAcm$^{-2}$)** | **$V_{oc}$ (mV)** | **FF (%)** | **PCE (η %)[a]** | **IPCE (%)** |
|---|---|---|---|---|---|
| (a) NT (1:0.25)-CdS | 7.52 | 581 | 46.28 | 2.02 | 46 |
| (b) NF (1:0.25)-CdS | 6.72 | 554 | 43.33 | 1.61 | 42 |
| **(c) NT (1:0.50)-CdS** | **10.88** | **628** | **43.21** | **2.90** | **54** |
| **(d) NF (1:0.50)-CdS** | **8.87** | **590** | **37.50** | **2.01** | **49** |
| (e) NT (1:0.75)-CdS | 6.26 | 538 | 40.90 | 1.37 | 37 |
| (f) NF (1:0.75)-CdS | 5.65 | 529 | 39.45 | 1.17 | 32 |

[a]PCE value for the best performed device out of 5 identical devices.


Part of this chapter has been published in **Carbon 2017, 121, 90–105**.

Enhancement in $J_{sc}$ value is a good agreement with the occurrence of higher loading sites for sensitizer deposition, offered by mesoporous tubular structures of g-$C_3N_4$. Therefore, flux of photoinduced electron injection may increase due to better electronic interaction between g-$C_3N_4$ NTs and ZnO NR in the optimized composite (1:0.5). We observe highest $V_{oc}$ value (≈ 628 mV) for the best performed device, is a clear indication of better separation of photogenerated electron–hole pair and interfacial charge injection. This statement also supports the minimum reverse tunneling probability i.e., back transferring of photoinduced electron at the electrode-electrolyte interface. We have performed electrochemical impedance spectroscopic analyses for better understanding of recombination processes which are discussed later. After sensitization of optimum device, sufficient pores are available in the photoanodic film for better functioning of electrolyte, responsible for effective regeneration of the sensitizer particles. We have also noticed that there is significant enhancement in the fill factor value for (1:0.5) g-$C_3N_4$ NTs based device, about ≈ 43.21 % while for (1:0.5) g-$C_3N_4$ NFs based device, it is ≈ 37.50 %. This observation endorses the better electron transport within the device, results minimizing the unfavorable recombination processes and improves the performance of device.

Figure **3.3.10 (B)** demonstrates corresponding incident photon-to-current conversion efficiency (IPCE) plots for all the devices. Devices with optimum content of g-$C_3N_4$ [(1:0.5), device **c** & **d**] showed better light harvesting ability as an accordance with their $J_{sc}$ value, attributed to optimal sites offered by g-$C_3N_4$ for CdS QDs loading. Therefore, composite (1:0.5) based devices exhibited IPCE of about ~ 54 % (for g-$C_3N_4$ NTs based device) while about ~ 49 % (for g-$C_3N_4$ NFs based device) in the wavelength range of 360–560 nm. The substantial increment in the IPCE value for g-$C_3N_4$ NTs based device is due to higher loading of CdS QDs attributed to the hollow mesoporous nature of tubular g-$C_3N_4$ nano architectures. As observed IPCE plots are follow the similar increasing trend as we noticed for $J_{sc}$ values from (*J*–V) curves for the devices [i.e., **(f)**< **(e)**< **(b)**< **(a)**< **(d)**< **(c)**]. For devices having composite (1:0.75) [**(e)** & **(f)**], minimum IPCE values are noticed because of high recombination rate of photogenerated electrons which may be due to non-uniform loading of CdS QDs and also clogging the available pores in photoanodic film which limits the better functioning of redox couple. Observed lower IPCE value for (1:0.25) composite based devices suggest the inadequate loading of CdS QDs, which limits the light harvesting ability as well as performance of devices. Higher IPCE values for g-$C_3N_4$ NTs based devices [**(c)**, **(a)** & **(e)**] observed at longer wavelengths, signify the


Part of this chapter has been published in **Carbon 2017, 121, 90–105**.

enhanced light scattering ability, expected due to hollow mesoporous nature of g-$C_3N_4$ NTs. So, considerable increment in IPCE value for device **(c)** as compare to device **(d)** is a result of higher flux of photo-generated electrons due to the optimum CdS QDs loading and light scattering effect of g-$C_3N_4$ NTs. Hence, higher photovoltaic boosting ability of g-$C_3N_4$ NTs is confirmed from enhanced light harvesting by their composite material as compare to g-$C_3N_4$ NFs based composites.

### 3.3.10 ELECTROCHEMCIAL IMPEDANCE SPECTROSCOPY ANALYSIS

Further, to investigate the beneficial effects of g-$C_3N_4$ NTs in terms of electron transport and charge recombination kinetics, electrochemical impedance spectroscopy (EIS) analyses are carried out for all devices under the dark conditions in a frequency range from 0.1 Hz to 100 kHz at an external bias equivalent to open circuit voltage, as shown in figure **3.3.11 (A)** & **(B)**. EIS analysis of a QDSSC mainly explain the charge transfer and recombination processes, taking place at various interfaces of device such as at counter electrode/electrolyte interface in the high-frequency region (1–100 kHz), at the ZnO/QD/electrolyte interface in the mid-frequency region (0.1–1 kHz), and the diffusion of electrolyte in the low frequency region (0.1–0.01 Hz).[40] Figure **3.3.11 (A)** shows the Nyquist plots recorded under dark condition at the applied bias equivalent to the open-circuit voltages in the frequency range from 0.1 Hz to 100 kHz. All the Nyquist plots comprise of two semicircles, one in the medium frequency region while another one in the higher frequency region. The diameter of the right semicircle ($R_k$) mainly corresponds to charge transfer resistance ($R_{ct}$).[40] From figure **3.3.11 (A)**, as can be seen that diameter of semicircle ($R_k$) at medium frequency region is significantly higher for best performed device **(c)** [1:0.5, ZnO NR-g-$C_3N_4$ NTs] as compare to device **(d)** [1:0.5, ZnO NR- g-$C_3N_4$ NFs]. This observation supports our claim of faster and better charge transport in case of g-$C_3N_4$ NTs, resulting in a reduced recombination process by inhibiting the back transfer probability of photoinduced electron at the ZnO NR/electrolyte or ZnO NR/CdS/electrolyte interfaces. Increasing trend of $R_{ct}$ based on $R_k$ for all devices is: **(f)** < **(e)** < **(b)** < **(a)** < **(d)** < **(c)** which is in good agreement with observed trend of $V_{oc}$ values in *J*–V curve. So, enhanced $V_{oc}$ value in the device **(c)** is essentially due to efficient charge transport along 1–D path and better interfacial electron injection while in case of device **(d)** a random pathway of electrons at interfacial transport. Like $V_{oc}$, Fill factor (FF) is also


Part of this chapter has been published in **Carbon 2017, 121, 90–105**.

correlated with $R_{ct}$ and value of FF improve as increases the Rct of device, which is seen in the device **(c)** with the highest fill factor of ~ 43.21 %.

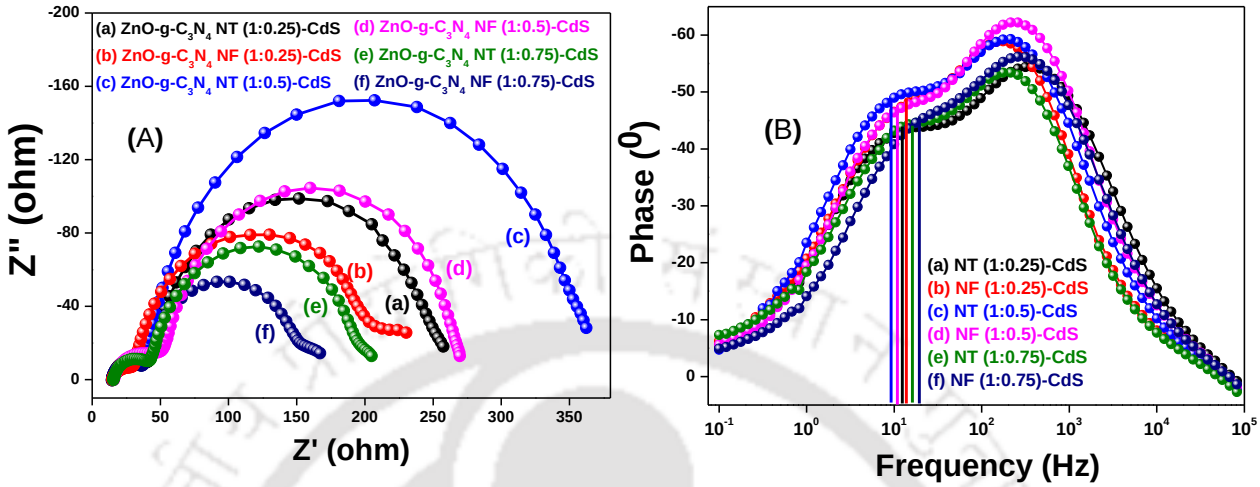


**Figure 3.3.11 (A)** Nyquist plots for all the fabricated photovoltaic devices of both morphologies of g–$C_3N_4$ based composites with different weight ratios of ZnO NR and g–$C_3N_4$ in dark at open-circuit voltage and in a frequency range from 0.1 Hz to 100 kHz. **(B)** Bode phase plots for all the respective devices.

**Table 3.3.3** Characteristic peak frequencies in the medium frequency region ($f_{max}$) and calculated values of photoinduced electron lifetimes ($\tau_e$) in all the devices.

| **Device Composition (ZnO NR-g-$C_3N_4$)** | **$f_{max}$ (Hz)** | **$\tau_e$ (ms)** |
|---|---|---|
| (a) NT (1:0.25)-CdS | 12.80 | 12.44 |
| (b) NF (1:0.25)-CdS | 14.60 | 10.99 |
| **(c) NT (1:0.50)-CdS** | **9.80** | **16.24** |
| **(d) NF (1:0.50)-CdS** | **12.15** | **13.10** |
| (e) NT (1:0.75)-CdS | 17.29 | 9.20 |
| (f) NF (1:0.75)-CdS | 19.37 | 8.22 |

Corresponding Bode phase plots for all the fabricated devices are depicted in figure **3.3.11 (B)**. In the Bode plots, observed two distinct peaks corresponds to two diode interfaces of the devices. Photoinduced electron lifetimes ($\tau_e$) can be estimated from characteristics maximum peak frequency ($f_{max}$) in the mid-frequency region. We have calculated the values of $\tau_e$ (listed in table **3.3.3**) by using the **equation (3)**:[41]

$$\tau_e = \frac{1}{2\pi f_{max}} \qquad (3)$$


Part of this chapter has been published in **Carbon 2017, 121, 90–105**.

From table **3.3.3**, maximum peak frequencies for optimized g-$C_3N_4$ NTs and g-$C_3N_4$ NFs based photoanodes are found to be present at ~ 9.80 Hz and ~ 12.15 Hz respectively and the corresponding $\tau_e$ value for same devices are calculated and found to be ~ 16.24 ms and ~ 13.10 ms. Higher $\tau_e$ values for g-$C_3N_4$ NTs based device confirms the minimized recombination processes, occurred due to back transferring of photoinduced electron to the electrolyte at the working electrode/electrolyte interfaces. This observation has also suggested that the photogenerated electrons stay more time in the photoanodic film, results increase the diffusion length of electrons in photoanodic film before getting collect at FTO. So, there is an enhancement of photoinduced electron density in CB of ZnO NRs, leads to the upsurge of $J_{sc}$ value, contributed to get the higher efficacy value of device. It is observed that the lower values of ($\tau_e$) as well as PCE ($\eta$) for composites with higher content of g-$C_3N_4$, i.e., [(1:0.75), device **(e)** and device **(f)**] reflects an inhibited photoinduced electron injection from CdS QDs to ZnO NRs. Subsequently, CB level of g-$C_3N_4$ is energetically well above the CB level of CdS QDs, so the photoinduced electrons are expected to tunnel from CdS QDs to ZnO NRs making g-$C_3$ $N_4$ as a partial energy barrier for interfacial charge transfer. Similar trend has been observed i.e., lower $\tau_e$ as well as efficiency values for composites [(1:0.25), device **(a)** and device **(b)**], possibly due to an inadequate loading of CdS QDs, as low content of g-$C_3N_4$ which results generate the less number of photoinduced electron.

For better understanding of charge transfers based on their band alignments, we proposed possible routes for charge separation and transfer between g-$C_3N_4$ and ZnO NR under visible light irradiation, as shown in scheme **3.3.2**. From scheme **3.3.2**, we have seen that a type–II band alignment present between ZnO and g-$C_3N_4$ due to suitable band structure of g-$C_3N_4$ and ZnO NR. Conduction band (CB) position of g-$C_3N_4$ (–3.62 eV) is more positive to that of CdS (–4.05 eV) and ZnO NR (–4.24 eV). Hence back transfer of photoinduced electrons from ZnO NR to the CdS QDs and g-$C_3N_4$ is an energetically unfavorable process. Therefore, g-$C_3N_4$ layer on ZnO NRs acts as both block layer and effective light absorption layer which effectively promote the electron transport by retarding the backward recombination of electrons from ZnO and electrolyte which results in enhancement of the performance of solar device. It is notable that sensitization of CdS QDs in the photoanodes leads to the probability of deposition on both the scaffolds, i.e., g-$C_3N_4$ and ZnO NRs; so, two routes are possible for charge transfer processes in the devices.


Part of this chapter has been published in **Carbon 2017, 121, 90–105**.

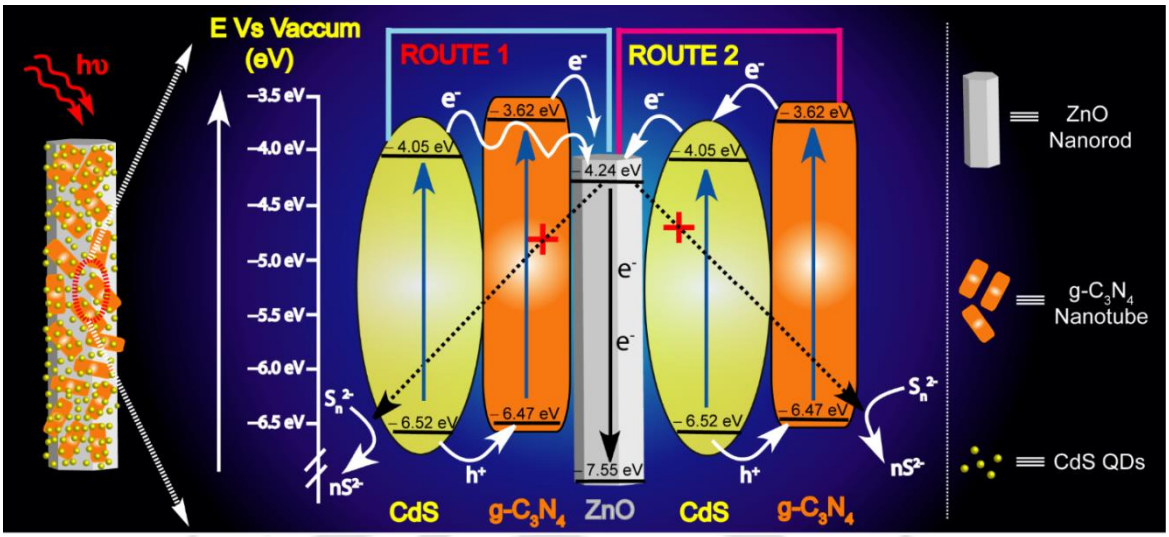


**Scheme 3.3.2** Schematic representation relates to possible routes for charge separation and transfer between CdS, g–$C_3N_4$ and ZnO NR under visible light irradiation.

The charge transfer **route (1)** occurred when CdS QDs are mainly adsorbed on the g-$C_3N_4$ while **route (2)** shows the deposition of CdS QDs on bare surface of ZnO NRs. When the weight ratio of g-$C_3N_4$ increases in the composite, the CdS QDs are adsorbed mainly on the g-$C_3N_4$ due to presence of minimal bare ZnO surfaces. Probability of charge transfer according to **route (1)** is increased in this condition where electron injection from CdS to ZnO is hindered by the g-$C_3N_4$ resulting in a decrease in the photoinduced electron density in the photoanode. However, the tunnelling possibility of photoexcited electrons from CdS QDs to ZnO NRs across the g-$C_3N_4$ barrier cannot be nullified; as the CB level of CdS QDs is energetically well above the CB level of ZnO. We found that with the optimum weight ratio of g-$C_3N_4$ to composites, i.e., [(1:0.5), device **(c)** & **(d)**], the charge transfer **route (2)** overcome the other **route (1)** and hence increases the photoexcited electron density in the photoanode. The maximum electron lifetime (~ 16.24 ms) observed for the best performed device **(c)** is symptomatic of increased photoinduced electron density which leads to obtain higher values of $V_{oc}$ ~ 628 mV, $J_{sc}$ ~ 10.88 mA $cm^{-2}$ and η ~ 2.90 %.

### 3.3.11 MORPHOLOGY DEPENDENT PHOTOVOLTAIC MEASUREMENTS

To corroborate the effect of g-$C_3N_4$ morphology on ZnO NR and ZnO NP based devices, we have performed photovoltaic measurements using CdS QD as a sensitizer. As seen from current density–voltage (*J*–V) curves [figure **3.3.12 (A)**], devices with g-$C_3N_4$ NT show the better performance as compared to g-$C_3N_4$ NF based devices. From table **3.3.4**, ZnO NR based


Part of this chapter has been published in **Carbon 2017, 121, 90–105**.

devices with g-$C_3N_4$ NT composite (1:0.5) show enhanced photovoltaic activity than ZnO NP based devices as ZnO NR shows stronger synergic effect between g-$C_3N_4$ NT and ZnO NR. ZnO NR provides minimum population of grain boundary induced trap sites and a longer diffusion length of photogenerated electrons as a result lesser recombination of photogenerated electrons yields a better photovoltaic performance as compared to ZnO NP based devices.

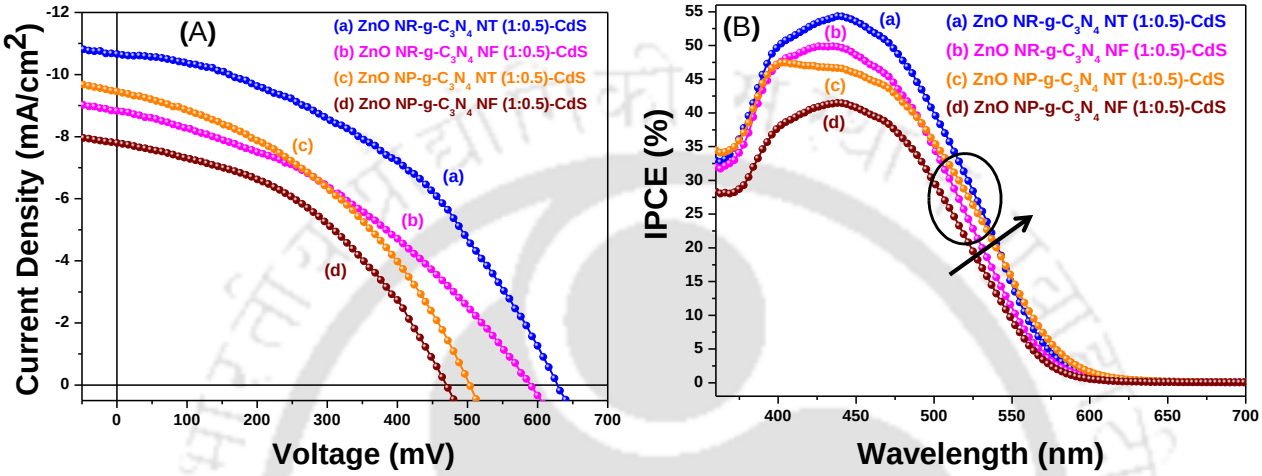


**Figure 3.3.12 (A)** Current density–Voltage (*J*–V) curve and **(B)** Corresponding IPCE spectra for composite photoanodes which are **(a)** ZnO NR–$C_3N_4$ NT (1:0.5), **(b)** ZnO NR–$C_3N_4$ NF (1:0.5), **(c)** ZnO NP–$C_3N_4$ NT (1:0.5) and (d) ZnO NP–$C_3N_4$ NF (1:0.5) respectively.

**Table 3.3.4** Short-circuit current density ($J_{sc}$), open-circuit voltage ($V_{oc}$), fill factor (FF), and power conversion efficiency (η) for the fabricated solar cells incorporating different photoanodes.

| **Devices Composition** | **$J_{sc}$ (mAcm$^{-2}$)** | **$V_{oc}$ (mV)** | **FF (%)** | **PCE (η %)[a]** | **IPCE (%)** |
|---|---|---|---|---|---|
| **(a) ZnO NR-g-$C_3N_4$ NT (1:0.5)-CdS** | **10.88** | **628** | **43.21** | **2.90** | **54** |
| (b) ZnO NR-g-$C_3N_4$ NF (1:0.5)-CdS | 8.87 | 590 | 37.50 | 2.01 | 49 |
| **(c) ZnO NP-g-$C_3N_4$ NT (1:0.5)-CdS** | **9.47** | **504** | **40.05** | **1.92** | **47** |
| (d) ZnO NP-g-$C_3N_4$ NF (1:0.5)-CdS | 7.88 | 472 | 42.04 | 1.56 | 41 |

[a]PCE value for the best performed device out of 5 identical devices.

Figure **3.3.12 (B)** shows the incident photon-to-current conversion efficiency (IPCE) spectra for all the composite photoanodes. It is observed that the photoanodes composed of ZnO NR showed higher IPCE as compared to ZnO NP for both the g-$C_3N_4$ morphologies owing to stronger synergic effect between ZnO NR and g-$C_3N_4$. Higher IPCE in case of g-$C_3N_4$ NT resulted from a better dye loading owing to the higher surface area furnished by g-$C_3N_4$ NT. Overall photovoltaic performances for all the devices are summarized in table **3.3.4**.


Part of this chapter has been published in **Carbon 2017, 121, 90–105**.

### 3.3.12 STABILITY OF PHOTOVOLTAIC DEVICES

Operational photo-stability of solar devices is essential for the practical application. All photovoltaic performance parameters with respect to time have been studied, under the solar irradiation (AM 1.5 G, 100 mWcm$^{-2}$) at ambient conditions without sealing of devices, as shown in figure **3.3.13**.

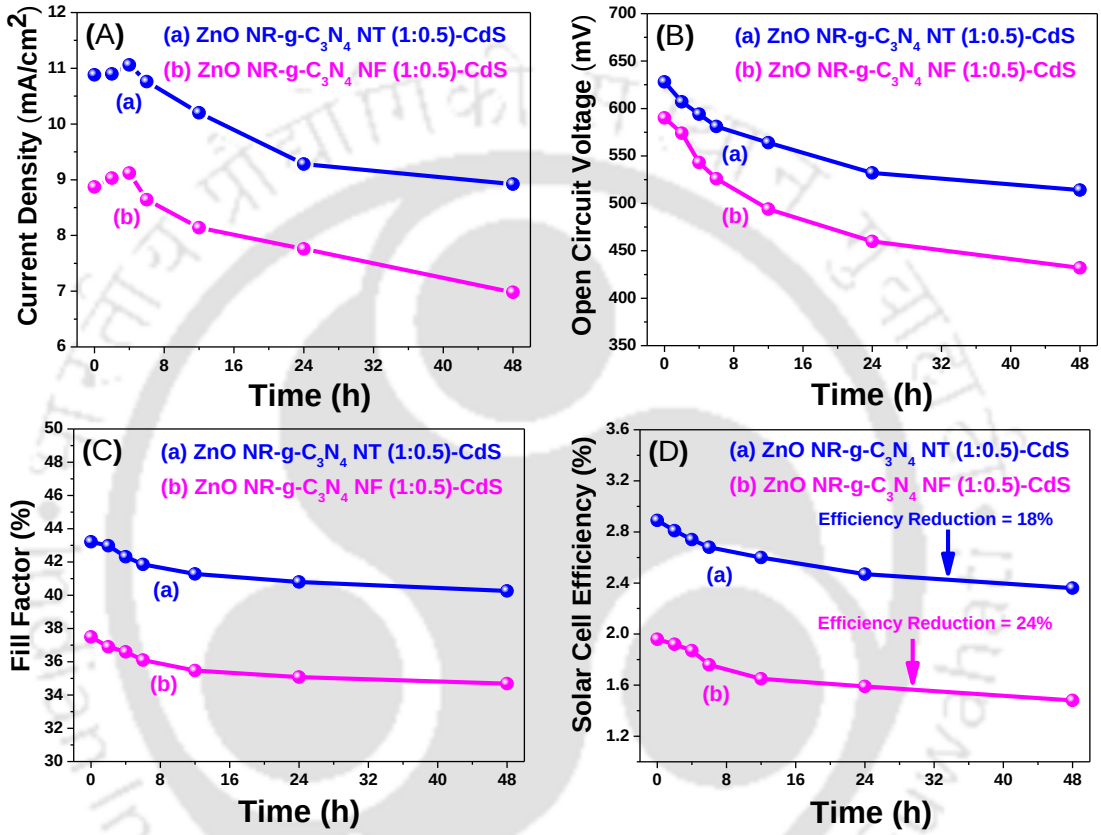


**Figure 3.3.13** Traces **(A)**, **(B)**, **(C)** and **(D)** display the changing of different photovoltaic parameters such as current density (mA/cm$^2$), open circuit voltage (mV), fill factor (%) and efficiency value (%) with respect to time to evaluate the stability of the best performing photovoltaic devices based on different morphologies of g–$C_3N_4$.

Values for $J_{sc}$, $V_{oc}$, FF, and η are recorded over a period of 48 h. Photo-current for both the devices increases substantially during the first 4 h owing to better penetration of $S^{2-}/S_n^{2-}$ electrolyte through the photoanodic film, after that $J_{sc}$ value decreases continually. Other parameters such as open circuit voltage and fill factor are constantly decreases as prolong irradiation, due to the corrosion of counter electrode as adsorption of sulfide/polysulfide redox couple, results in reduced hole recovery rate of the electrolyte. Efficacy value (η) for g-$C_3N_4$ NFs based photoanode decline much faster than g-$C_3N_4$ NTs based photoanode. Thus, there is a ~ 24


Part of this chapter has been published in **Carbon 2017, 121, 90–105**.

% reduction in efficiency for g-$C_3N_4$ NFs based device while ~ 18 % efficiency get reduced for g-$C_3N_4$ NTs based device after the 48 h duration. Based on the observations, we conclude that devices based on g-$C_3N_4$ NTs are more stable as compare to g-$C_3N_4$ NFs based devices.

## 3.4 CONCLUSIONS

In summary, we have utilized nanotubular structures of photo-booster g-$C_3N_4$ to improve the efficiency of a quantum dots sensitized solar cell (QDSSC). g-$C_3N_4$ NTs are synthesized through morphological transformation of as-exfoliated g-$C_3N_4$ NFs. Photo-booster effect of g-$C_3N_4$ NTs have investigated using the composites having ZnO nanorods (ZnO NRs) and sensitized with CdS QDs. There is a ~ 32 % enhancement in power conversion efficiency (PCE, η) for the devices fabricated with composite ZnO NR-g-$C_3N_4$ NTs [$\eta \approx 2.9$ %, for an optimized weight ratio of 1:0.5] as compared to composite ZnO NR-g-$C_3N_4$ NFs based device [$\eta \approx 2.0$ %, for same weight ratio (1:0.5)]. Enhanced photovoltaics is mainly due to (i) efficient separation and transportation of the photogenerated charge carriers along a one dimensional (1–D) pathway, resulting in faster lifetime of the charge carriers and (ii) high surface area for the loading of sensitizer particles, results in an improvement of light harvesting ability of devices. From electrochemical impedance spectroscopy (EIS) studies, as obtained higher recombination resistance and photoexcited electron lifetime in case of g-$C_3N_4$ NTs based devices are indicative of efficient separation and transfer of photogenerated electrons by reducing the recombination processes i.e., the back transferring of photoexcited electron at electrode/electrolyte interface.

## 3.5 REFERENCES

(1) X. X. Xu, C. Randorn, P. Efstathiou and J. T. S. Irvine, *Nat. Mater.*, 2012, **11**, 595–598.

(2) A. Hagfeldt, G. Boschloo, L. C. Sun, L. Klo and H. Pettersson, *Chem. Rev.*, 2010, **110**, 6595–6663.

(3) X. C. Wang, K. Maeda, A. Thomas, K. Takanabe, G. Xin, J. M. Carlsson, K. Domen and M. Antonietti, *Nat. Mater.*, 2009, **8**, 76–80.

(4) X. C. Wang, K. Maeda, X. Chen, K. Takanabe, K. Domen, Y. Hou, X. Fu and M. Antonietti, *J. Am. Chem. Soc.*, 2009, **131**, 1680–1681.

(5) Y. Wang, X. C. Wang and M. Antonietti, *Angew Chem Int. Ed.*, 2012, **51**, 68–89.


Part of this chapter has been published in **Carbon 2017, 121, 90–105**.

(6) J. J. Zhu, P. Xiao, H. L. Li and S. A. C. Carabineiro, *ACS Appl. Mater. Interfaces*, 2014, **6**, 16449–16465.

(7) S. W. Cao and J. G. Yu, *J. Phys. Chem. Lett.*, 2014, **5**, 2101–2107.

(8) J. W. Zhou, M. Zhang and Y. F. Zhu, *Phys. Chem. Chem. Phys.*, 2014, **16**, 17627–17633.

(9) L. Y. Huang, H. Xu, Y. Li, H. Li, X. Cheng, J. Xia, Y. Xu and G. Cai, *Dalton Trans.*, 2013, **42**, 8606–8616.

(10) L. Ge, F. Zuo, J. Liu, Q. Ma, C. Wang, D. Sun, L. Bartels and P. Feng, *J. Phys. Chem. C*, 2012, **116**, 13708–13714.

(11) C. Pan, J. Xu, Y. Wang, D. Li and Y. Zhu, *Adv. Funct. Mater.*, 2012, **22**,1518–1524.

(12) X. Liu, N. Chen, Y. Li, D. Deng, X. Xing and Y. Wang, *Sci. Rep.*, 2016, **6**, 1–17.

(13) J. S. Zhang, X. F. Chen, K. Takanabe, K. Maeda, K. Domen, J. D. Epping, X. Fu, M. Antonietti and X. Wang, *Angew Chem Int. Ed.*, 2010, **49**, 441–444.

(14) X. F. Chen, J. S. Zhang, X. Z. Fu, M. Antonietti and X. C. Wang, *J. Am. Chem. Soc.*, 2009, **131**, 11658–11659.

(15) S. B. Yang, Y. J. Gong, J. S. Zhang, L. Zhan, L. L. Ma, Z. Y. Fang, R. Vajtai, X. Wang and P. M. Ajayan, *Adv. Mater.*, 2013, **25**, 2452–2456.

(16) D. D. Zheng, C. Y. Pang, Y. X. Liu and X. C. Wang, *Chem. Commun.*, 2015, **51**, 9706–9709.

(17) D. D. Zheng, C. J. Huang and X. C. Wang, *Nanoscale*, 2015, **7**, 465–470.

(18) X. J. Bai, L. Wang, R. L. Zong and Y. F. Zhu, *J. Phys. Chem. C*, 2013, **117**, 9952–9961.

(19) M. Shalom, S. Inal, C. Fettkenhauer, D. Neher and M. Antonietti, *J. Am. Chem. Soc.*, 2013, **135**, 7118–7121.

(20) J. H. Sun, J. S. Zhang, M. W. Zhang, M. Antonietti, X. Z. Fu and X. C. Wang, *Nat. Commun.*, 2012, **3**, 1139–1146.

(21) K. P. Gong, F. Du, Z. H. Xia, M. Durstock and L. M. Dai, *Science*, 2009, **323**, 760–764.

(22) S. Iijima, *Nature*, 1991, **354**, 56–58.

(23) J. Gracia and P. Kroll, *J. Mater. Chem.*, 2009, **19**, 3020–3026.


Part of this chapter has been published in **Carbon 2017, 121, 90–105**.

(24) Q. X. Guo, Y. Xie, X. J. Wang, S. Y. Zhang, T. Hou and S. C. Lv, *Chem. Commun.*, 2004, **1**, 26–27.

(25) C. Cao, F. Huang, C. Cao, Jie. Li and H. Zhu, *Chem. Mater.*, 2004, **16**, 5213–5215.

(26) S.-W. Bian, Z. Ma and W.-G. Song, *J. Phys. Chem. C*, 2009, **113**, 8668–8672.

(27) J. Gao, Y. Zhou, Z. S. Li, S. C. Yan, N. Y. Wang and Z. G. Zou, *Nanoscale*, 2012, **4**, 3687–3692.

(28) J. W. Lee, R. Viswan, Y. J. Choi, Y. Lee, S. Y. Kim, J. Cho, Y. Jo and J. K. Kang, *Adv. Funct. Mater.*, 2014, **19**, 2213–2218.

(29) Z. X. Zeng, K. X. Li, L. S. Yan, Y. H. Dai, H. Q. Guo, M. X. Huo and Y. Guo, *RSC Adv.*, 2014, **4**, 59513–59518.

(30) J. Xu, G. Wang, J. Fan, B. Liu, S. Cao and J. Yu, *J. Power Sources*, 20015, **274**, 77–84.

(31) T. R. Chetia, M. S. Ansari and M. Qureshi, *J. Mater. Chem. A*, 2016, **4**, 5528–5541.

(32) S. Martha, A. Nashim and K. M. Parida, *J. Mater. Chem. A*, 2013, **1**, 7816–7824.

(33) A. Becheri, M. Durr, P. Lo. Nostro and P. Baglioni, *J. Nanopart. Res.*, 2008, **10**, 679–689.

(34) S. C. Yan, Z. S. Li and Z. G. Zou, *Langmuir*, 2010, **26**, 3894–3901.

(35) F. Dong, M. Y. Ou, Y. K. Jiang, S. Guo and Z. B. Wu, *Ind. Eng. Chem. Res.*, 2014, **53**, 2318–2330.

(36) A. Kongkanand, K. Tvrdy, K. Takechi, M. Kuno and P. V. Kamat, *J. Am. Chem. Soc.*, 2008, **130**, 4007–4015.

(37) M. D. R. Peralta, U. Pal and R. S. Zeferino, *ACS Appl. Mater. Interfaces*, 2012, **4**, 4807–4816.

(38) S. C. Yan, Z. S. Li and Z. G. Zou, *Langmuir*, 2009, **25**, 10397–10401.

(39) Q. J. Xiang, J. G. Yu and M. Jaroniec, *J. Phys. Chem. C*, 2011, **115**, 7355–7363.

(40) S. Phadke, A. Du Pasquier and D. P. Birnie, *J. Phys. Chem. C*, 2011, **115**, 18342–18347.

(41) R. Kern, R. Sastrawan, J. Ferber, R. Stangl and J. Luther, *Electrochim. Acta*, 2002, **47**, 4213–4225.

# CHAPTER 4

# Combined Effect of *In-Situ* Grown p-type $CuSbS_2$ / n-type CdS Coupled with Hierarchical ZnO Nano-Disks for Improved Photovoltaic Light Harvesting Efficiency

*This chapter elucidates the synthesis of porous two dimensional (2−D) zinc oxide (ZnO) disk structures, using a biomass derived templating agent i.e., Xanthan gum. Comparative photovoltaic study of as-synthesized 2−D porous ZnO structures with respect to 1−D ZnO structures is carried out by co-sensitizing with in-situ grown 1−D CdS nanowires array and ternary metal chalcogenide viz. copper antimony sulfide ($CuSbS_2$) nanobricks.*

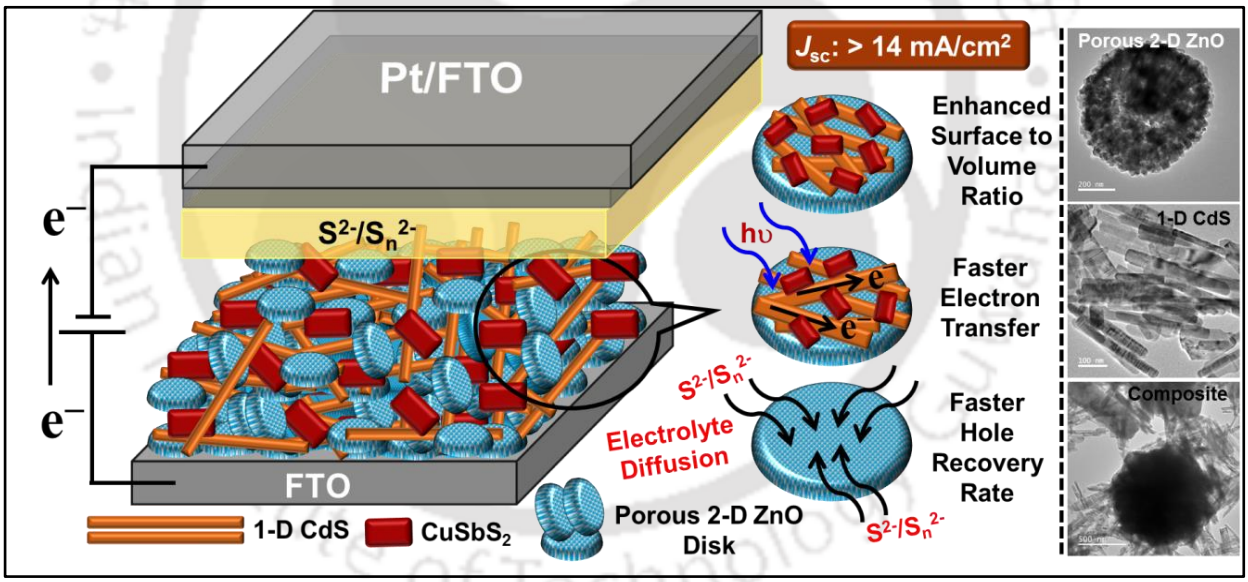


***Ansari, et al., J. Power Sources* 2019, *425*, 204–216.**

## 4.1 INTRODUCTION

The expedition to design and develop the nanostructure materials can be considered to be the next generation research to improve the efficiency of photovoltaic devices.[1] Optoelectronic properties of nanostructured semiconductors are not only affect with their size but also to their morphologies.[2–3] So, morphology controlled synthesis of nanostructured semiconductors has attracted large research interest. Due to having limitation in terms of less surface area, efficiency of one dimensional (1–D) nanostructures based solar devices becomes very less.[4] Therefore, two dimensional (2–D) structures with large surface area and remarkable optoelectronic properties have been considered the suitable metal oxide scaffolds to facilitate the photovoltaic application.[5–8] Accordingly, templating agents or additives have been utilized to control the crystal growth kinetics of high energy polar facets to obtain the exposed zinc oxide (ZnO) structures.[9–11] Templating agents are selectively adsorbed on these high energy polar facets and changed the growth pattern of ZnO crystal.[12] However, biomass derived templating agents have various benefits over the harsh chemical additives in terms of easy removal, economical and being environmental friendly.[13–17] Therefore, we have utilized the biomass derived templating agent, 'Xanthan gum' to tune the crystal growth pattern of ZnO.

Earlier, various metal sulfides (such as CdS, CdSe, PbS, CuS and $Sb_2S_3$ etc.) have been utilized as promising sensitizer materials to enrich the efficiency of solar devices.[18–22] In general, binary metal sulfide sensitizer materials are cost-effective, abundant and easily processable, with limitation of getting high efficiency.[22] Therefore, ternary and quaternary metal sulfides have been utilized to overcome this issue, owing to their excellent light harvesting efficiency and ideal band gap values.[23] Ternary metal chalcogenide; copper antimony sulfide ($CuSbS_2$) has been considered as an ideal solar absorbers due to its low optical bandgap of 1.5 eV, high extinction coefficient of $10^5$ $M^{-1}cm^{-1}$, and showing spectroscopic limited maximum efficiency (SLME) of about 23 %.[24] Several synthesis methods such as thermal evaporation, thermal diffusion, spray pyrolysis, electrodeposition, solvothermal, chalcogenization and hot-injection have been utilized to synthesize the phase and crystal pure $CuSbS_2$.[25–28] Solution processing method is more effective for maintaining the stoichiometric Cu/Sb ratio according to amounts of their precursors, to get pure $CuSbS_2$. In this chapter, we have synthesized two dimensional (2–D) porous ZnO disk structures, using a biomass derived templating agent i.e., Xanthan gum. Natural and water


Part of this chapter has been published in **J. Power Sources 2019, 425, 204-216**.

soluble biopolymer "Xanthan gum" is utilized as a crystal growth modifier which is easily take out from plant cell walls, chemical structure is shown in figure **4.1.1**. This templating agent is mainly responsible to control the growth kinetics of high energy facets of wurtzite ZnO crystal structure to obtain disk structures. A comparative photovoltaic study of as-synthesized 2–D porous ZnO structures with respect to 1–D ZnO structures (in absence of xanthan gum) is carried out by co-sensitizing with *in-situ* grown 1–D CdS nanowires array and ternary metal chalcogenide viz. copper antimony sulfide ($CuSbS_2$).

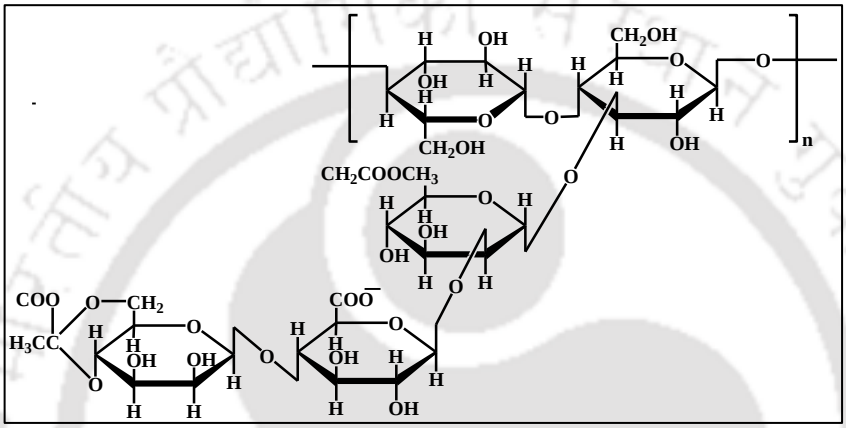

**Figure 4.1.1** Chemical structure of biomass derived templating agent "Xanthan gum".

## 4.2 EXPERIMENTAL METHODS

### 4.2.1 SYNTHESIS OF POROUS 2–D ZnO DISK

In this synthetic protocol, 25 mg of biomass derived templating agent i.e., xanthan gum (chemical structure; figure **4.1.1**) was dissolved in 25 mL of Milli-Q water with constant stirring to get a clear solution. 1 mmol of zinc nitrate hexahydrate (0.297 g) was then added in same solution. Due to interaction of templating agent and inorganic metal salt, viscidity of the above solution gets increased with continuous stirring. After that, 1 mmol of hexamine (0.14 g) was added into the solution under constant stirring. Now, this resulting solution was transferred into round bottom flask and refluxed for overnight. After cooling, resultant precipitate was centrifuged and washed with Milli-Q water and ethanol for three times to remove the unreacted residues, followed by drying in a hot air oven at 80 °C. Final powder sample was obtained by calcination at 500 °C for 2 h in a muffle furnace. For comparing the influence of templating agent, similar controlled reaction was also carried out in absence of xanthan gum and obtained the 1–D ZnO structures.

 Part of this chapter has been published in **J. Power Sources 2019, 425, 204-216**.

### 4.2.2 SYNTHESIS OF COPPER ANTIMONY SULFIDE NANOBRICKS

Phase stable copper antimony sulfide ($CuSbS_2$) nanobricks were synthesized by employing the reported synthetic protocol.[28] In brief, stoichiometric amount (1: 1: 3) of all three precursors i.e., cupric chloride, antimony trichloride and thiourea were dissolved in 10 ml of solvent mixture, consisting the oleylamine, octadecene and oleic acid (4.25 mL: 4.25 mL: 1.5 mL), followed by backfilling with nitrogen gas for 1 h at 80 °C. After that, temperature of reaction mixture was increased to 240 °C under $N_2$ atmosphere and maintained at this temperature for 1 h. After completion, the reaction mixture was cooled down and dispersed in a mixture of n-hexane and ethanol. This dispersion was centrifuged three times at 10000 rpm for 5 min. The resultant precipitate was dried at 60 °C to get powder sample. Final product was obtained after calcination at 350 °C for 1 h under $N_2$ atmosphere for further characterizations.

### 4.2.3 FABRICATION OF PHOTOANODES AND DEVICES

Firstly, ZnO seed layer was deposited on cleaned FTO substrates through spin coating of seed solution, dissolving 0.20 g of zinc acetate and 55 µL of ethanolamine in 3.0 mL of 2-methoxyethanol under constant stirring for 6 h. A consistent paste based on both structures of ZnO were prepared by using terpineol and ethocel (15 wt %), and deposited it over the ZnO seeded FTO glass substrates via doctor blade method. After that these photoanodic films were calcined at 450 °C for 30 min to remove the organic impurities. Thickness of as-deposited ZnO film was measured and found to be in range of ~ 9–13 µm. Now, photoanodic films were ready for sensitizer deposition. *In-situ* growth of 1–D CdS nanowires over ZnO deposited FTO substrate was carried out using the solvothermal reaction route. In this method, 1 mmol of cadmium nitrate $Cd(NO_3)_2 \cdot 4H_2O$ and 3 mmol of thiourea were dissolved in ethylene diamine to get the clear solution. This solution was poured into Teflon vessel and ZnO deposited FTO substrates were placed vertically to bottom of Teflon vessel. Now, Teflon autoclave was sealed properly and maintained at 160 °C for 6 h. After completion, photoanodic films were rinsed with Milli-Q water and ethanol, and dried at 70 °C. Now, as-synthesized $CuSbS_2$ (CAS) was deposited on ZnO/CdS by repeated cycle of spin coating of CAS ink at 2000 RPM for 45 s. CAS ink was prepared by dispersing of as-synthesized CAS in ethanol under ultrasonication and mixed with ethylene glycol and nafion. After each spin coating cycle, films were thermally treated at 200 °C under inert atmosphere. Instant thermal treatment improved the crystallinity


Part of this chapter has been published in **J. Power Sources 2019, 425, 204-216**.

and smoothening of the surface without formation of any other phases. Finally, photoanodic films were calcined at 350 °C for 30 min in presence of $N_2$ atmosphere to get crystal phase stable absorber film.

Devices were assembled by sandwiching the photoanodes and counter electrodes. Chloroplatinic acid solution (in propanol) was used to fabricate the counter electrode via spin coating on a cleaned FTO substrate, followed by calcination at 450 °C for 30 min in muffle furnace. Redox electrolyte ($S^{2-}/S_n^{2-}$) was introduced between both the electrodes. Electrolyte solution was prepared by following the earlier reported method.[29] Active area for all devices was fixed and found to be 0.16 $cm^2$. Prior to photovoltaic measurements, the fabricated devices were stored under dark condition.

## 4.3 RESULTS AND DISCUSSIONS

### 4.3.1 POWDER X-RAY DIFFRACTION ANALYSIS

From figure **4.3.1**, diffractogram of all co-sensitized photoanodes entailed the different crystals plane (marked in wine red color) such as (100), (002), (101), (102), (110), (103), (200), (112), and (201) related to wurtzite type hexagonal ZnO, as per JSPDS file 36-1451. In figure **4.3.1 (a)** & **(b)**, different diffraction patterns have been noted for both heterostructures of ZnO synthesized under different reaction conditions, suggesting the differential growth behaviour of ZnO crystals. Consequently, we have noticed the significant changes in the intensities ratio of (002) and (101) crystal planes in both the ZnO structures. Moreover, intensity of preferred crystal growth plane gets decreased in presence of templating agent xanthan gum, marked by black arrow in trace **(b)** of figure **4.3.1**. We have observed the lesser value of intensities ratio for (101/002) crystal planes in ZnO structures (synthesized in presence of xanthan gum), symptomatic of diminished crystal growth along c-axis which leads to formation of 2–D ZnO disk like structures with high exposed surface area for better loading of light absorber, as shown in scheme **4.3.1**. However, in absence of bio-template, 1–D ZnO structures along c-axis are formed. It is obvious that without any additives or templating agents, ZnO always prefers to grow along the c-axis and having less exposed surface area which limits the loading of sensitizer particles and efficiency of solar device. Morphological features of both ZnO structures are illustrated in Field emission scanning electron microscopy (FESEM) and Transmission electron microscopy (TEM) analysis sections.

 Part of this chapter has been published in **J. Power Sources 2019, 425, 204-216**.

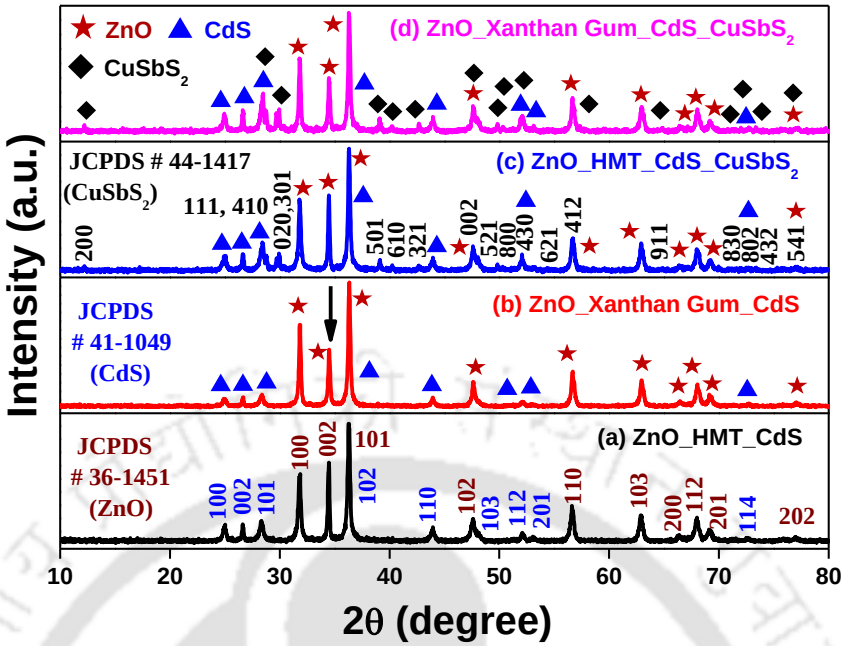


**Figure 4.3.1** Powder X-ray diffraction (PXRD) patterns of all sensitized photoanodes, fabricated as thin films on glass substrate.

All diffractogram (figure **4.3.1)** are showed the presence of crystals planes (marked in blue color) such as (100), (002), (101), (102), (110), (103), (112), (201) and (114) correspond to hexagonal CdS (JSPDS file 41-1049), revealing the successful loading of CdS nanostructures on ZnO without having any kind of crystalline impurities, represent in scheme **4.3.1**. Phase stability of ternary or quaternary chalcogenides is very critical to obtain. Solution processing method has been utilized to synthesize the pure phase of ternary chalcogenide under control reaction condition. Diffraction peaks of co-sensitized photoanodes (trace **(c)** and **(d)** of figure **4.3.1**) are index-able to (200), (111), (410), (020), (301), (501), (610), (321), (002), (521), (800), (430), (621), (412), (911), (830), (802), (432) and (541) crystal planes (marked in black color), correspond to chalcostibite phase of orthorhombic $CuSbS_2$ with lattice constants (a = 14.50 Å, b = 6.019 Å and c = 3.796 Å) as per JCPDS file 44-1417. No diffraction peaks have been noticed for binary as well as ternary metal chalcogenides impurities such as CuS, $Cu_2S$, $Sb_2S_3$, $Cu_{12}Sb_4S_{13}$ and $Cu_3SbS_4$ etc., inferring the phase stability of chalcostibite $CuSbS_2$ in both co-sensitized photoanodes. All photoanodes [traces **(a–d)** of figure **4.3.1**] show the retention of crystal structure of individual components such as ZnO, CdS and $CuSbS_2$, revealing that all materials are crystalline pure with stable phase even after co-sensitization.


Part of this chapter has been published in **J. Power Sources 2019, 425, 204-216**.

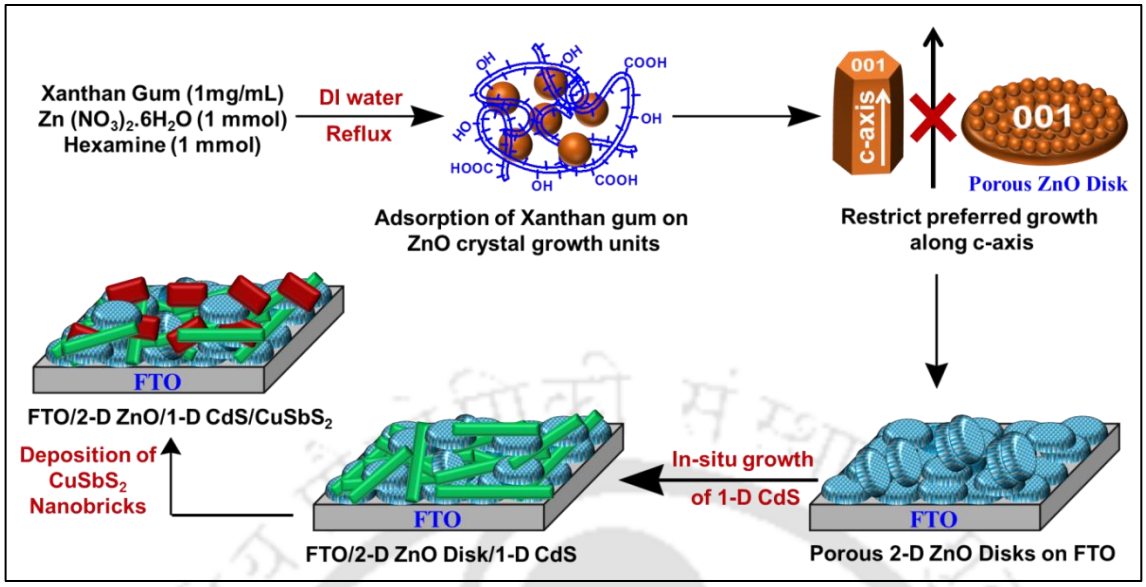


**Scheme 4.3.1** Schematic representation related to crystal growth of porous 2–D ZnO disks and photoanode fabrication.

### 4.3.2 MATERIAL MORPHOLOGY

Morphological features of both ZnO structures, synthesized under controlled reaction conditions are investigated by performing Field emission scanning electron microscopy (FESEM) and Transmission electron microscopy (TEM) analysis. FESEM image **(a)** of figure **4.3.2** exhibits the microstructural features of as-synthesized porous 2–D ZnO disk structures. Average size of 2–D ZnO structures is found to be in the sub-micron range. Distinct porous nature of 2–D ZnO structures is more prominent through FESEM image, present as inset of figure **4.3.2 (a)** and further analyzed by TEM analysis. 2–D porous ZnO structures are formed due to selective adsorption of biotemplate, xanthan gum on ZnO (001) crystal plane, responsible to restrict the preferred growth of ZnO crystal along these high energy (001) polar facets, as displays in scheme **4.3.1**. However, large exposed area of 2–D ZnO offers higher active sites for better loading of light absorbing materials while porous nature of similar structures helps in better functioning of redox electrolyte, resulting in enriching the light harvesting efficiency and hole recovery of oxidized sensitizer particles. Consequently, photovoltaic performance parameters such as current density ($J_{sc}$) and fill factor values will get improved. FESEM images **(b)** and **(c)** are representing the top and cross section views of porous 2–D ZnO structures after photoanode fabrication using doctor blade technique. Retaining the morphology of these structures demonstrates the structural stability of porous 2–D ZnO structures. This outcome

corroborates the beneficial role of these structures to achieve the superior photovoltaic performances of porous 2–D ZnO structures based solar devices.

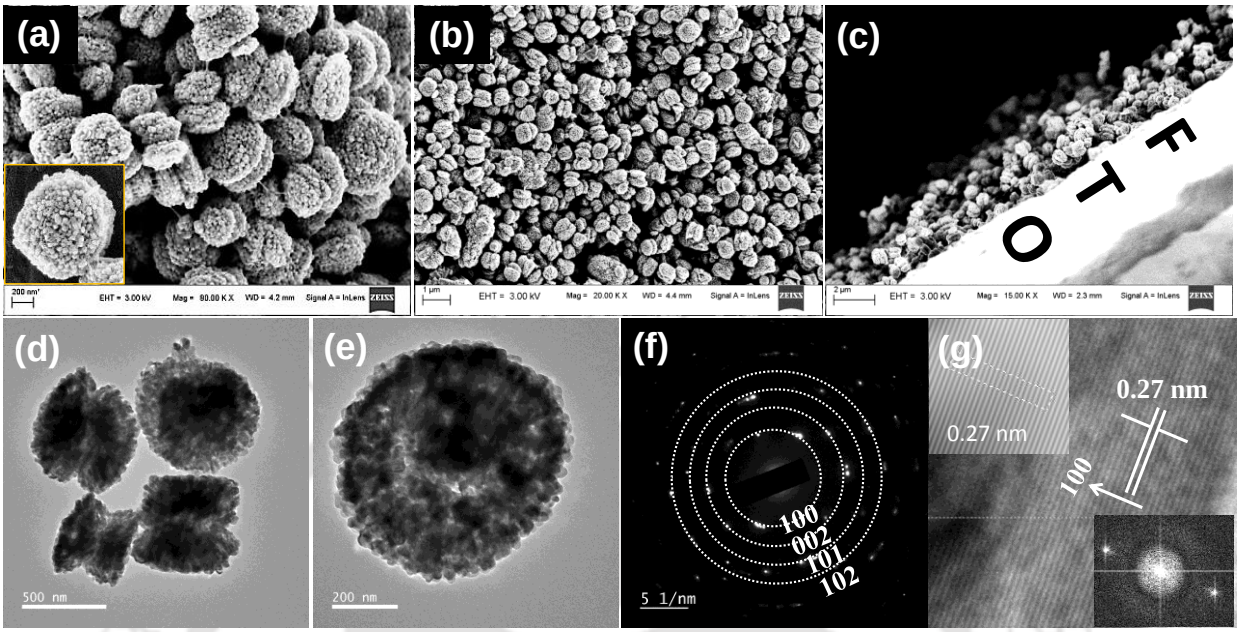


**Figure 4.3.2** Field emission scanning electron microscopy (FESEM) image **(a)** illustrates the morphological features of as-synthesized 2–D porous ZnO disk structures while FESEM images **(b)** and **(c)** show the top and cross sectional views of similar structures after photoanode fabrication. Transmission electron microscopy (TEM) images **(d-e)** depict the microstructural features of as-synthesized 2–D porous ZnO disk structures at different magnifications. Image **(f)** represents the selected area electron diffraction (SAED) pattern while trace **(g)** shows the high resolution transmission electron microscopy (HRTEM) image of the 2–D porous ZnO disk structure. Inset of trace **(g)** depicts the Inverse fast Fourier transform (IFFT) for the image **(f)** with corresponding fast Fourier transform (FFT) image.

Additionally, structural features of as-synthesized 2–D ZnO structures are confirmed by performing the transmission electron microscopy (TEM) analysis. From figure **4.3.2**, TEM images **(d)** and **(e)** show single as well as stacked porous flat disk like structures, similar to FESEM. The average dimensions of as-synthesized porous 2–D ZnO disk have been found to be in the range of ~ 600–1000 nm, appeared as similar as in FESEM analysis. Staking of these disk structures seems to be closely allied to each other which may be helpful for improved transportation of the photogenerated electrons by reducing the recombination sites between these structures. TEM image **(e)** illustrates the selective area electron diffraction (SAED) pattern for porous 2–D ZnO structures, revealing the polycrystalline nature of these structures based on their diffraction rings pattern. Based on different crystal planes, this pattern reveals the wurtzite hexagonal crystal structure of these structures which is well consistent with the PXRD analysis. High resolution TEM (HRTEM) image **(g)** of 2–D ZnO structures displays the well distinct


Part of this chapter has been published in **J. Power Sources 2019, 425, 204-216**.

lattice fringes, having interplanar distance of about ~ 0.27 nm corresponds to (100) crystal planes which is calculated by performing the inverse fast Fourier transform (IFFT) analysis.

Surface morphology of the material obtained in the absence of biotemplate; xanthan gum has been also analyzed by FESEM analysis and depicting in figure **4.3.3**. From the figure **4.3.3**, FESEM images **(a)** and **(b)** display the morphological features of as-synthesized ZnO sample at different magnifications. In absence of biotemplate, 1–D nanorods (NRs) of having different particle sizes are obtained, specifies the anisotropic crystal growth along longitudinal c-axis.

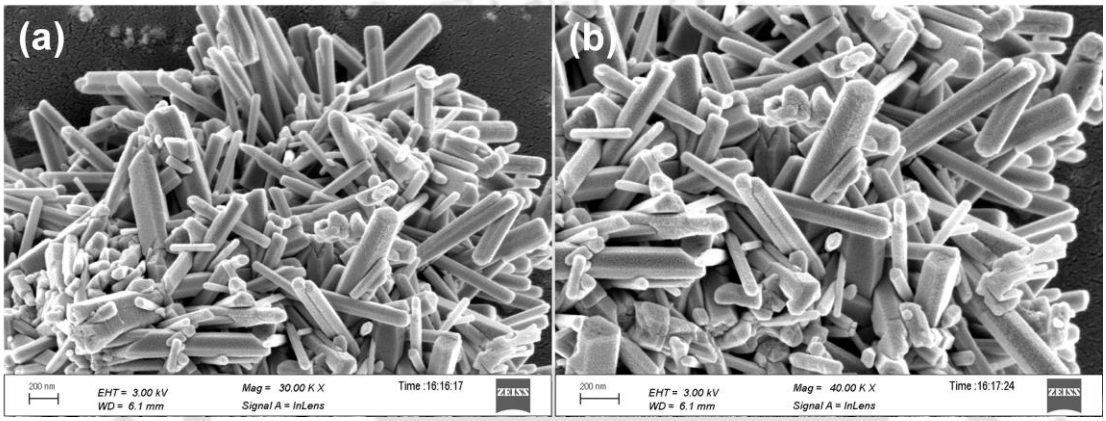


**Figure 4.3.3** Field emission scanning electron microscopy (FESEM) images **(a–b)** show the morphological features of 1–D ZnO structures, synthesized in absence of templating agent.

Further, we have also performed the FESEM and TEM analysis for exploration of morphological features of light absorbers such as *in-situ* deposited CdS and as-synthesized $CuSbS_2$, depicted in figure **4.3.4** and **4.3.5**.

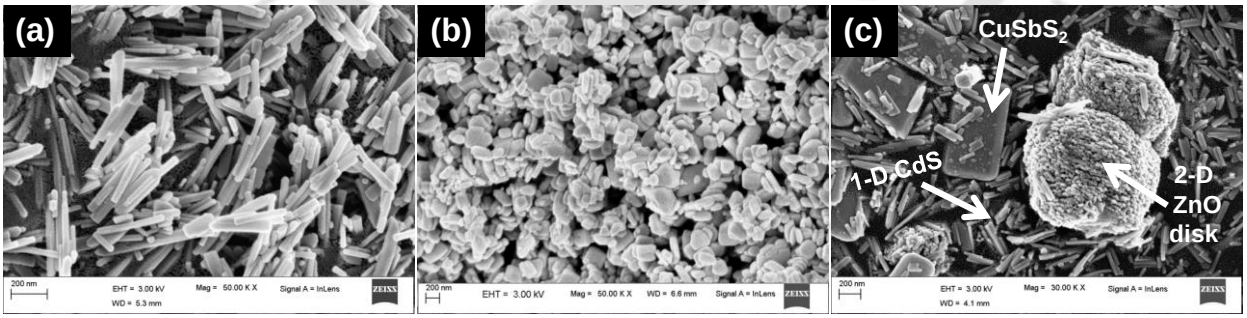


**Figure 4.3.4** Field emission scanning electron microscopy (FESEM) images **(a-c)** show the morphological features of *in-situ* grown 1–D CdS, $CuSbS_2$ and co-sensitized composite structures.

FESEM image **(a)** represents the successive *in-situ* growth of 1–D CdS nanostructures onto ZnO heterostructures deposited FTO substrates, facilitating the efficient transportation of photogenerated electrons. Image **(b)** characterizes the morphological features of as-synthesized $CuSbS_2$, exhibiting nanobricks kinds of structures. FESEM image **(c)** shows the morphological

 Part of this chapter has been published in **J. Power Sources 2019, 425, 204-216**.

features of composite material and confirms the retaining of features of individual components i.e., 2–D ZnO disk, 1–D CdS and $CuSbS_2$ nanobricks.

From the figure **4.3.5**, TEM image **(a)** represents the *in-situ* formation of 1–D CdS nanowires, having diameter and length in the range of ~ 30–50 nm and ~ 400–500 nm respectively.

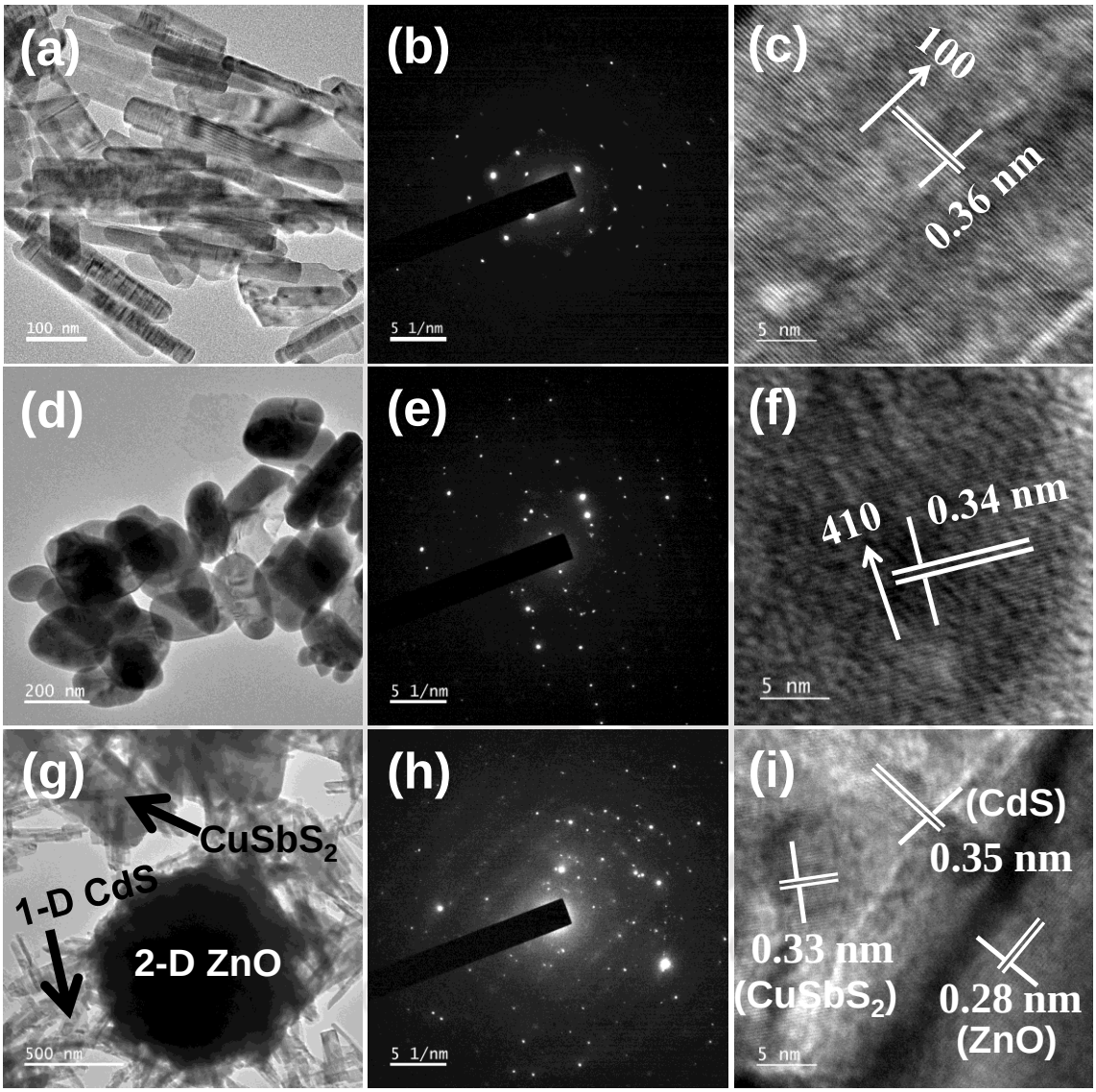


**Figure 4.3.5** Transmission electron microscopy (TEM) images **(a)**, **(d)** and **(g)** show the structural features of *in-situ* grown 1–D CdS, $CuSbS_2$ and co-sensitized composite structures at different magnifications. Trace **(b)** represents the selected area electron diffraction (SAED) pattern whereas trace **(c)** depicts the high resolution transmission electron microscopy (HRTEM) image of *in-situ* grown 1–D CdS structures. Trace **(e)** shows the SAED pattern while trace **(f)** illustrates the HRTEM image of as-synthesized $CuSbS_2$. Trace **(h)** represents the SAED pattern and trace **(i)** shows the HRTEM image of co-sensitized composite material.


Part of this chapter has been published in **J. Power Sources 2019, 425, 204-216**.

*In-situ* grown 1–D structures offers a lower interfacial resistance for charge transfers which supports better transportation of the photogenerated electrons, owing to follow the uni-directional pathway for the transfer, limiting the chances of electron trapping and recombining at defect sites. TEM image **(b)** shows the dotted SAED diffraction pattern for 1–D CdS structures, divulging the crystalline nature of these structures. TEM image **(c)** depicts the HRTEM image of similar structures, having the well-defined lattice fringes with the interplanar distance of about ~ 0.36 nm related to (100) crystal planes. TEM image **(d)** exhibits the structural feature of as-synthesized $CuSbS_2$, showing nano-brick like structures. Average dimensions of nanobricks structure have been found to be ~ 100 nm in diameter while ~ 200 nm in length respectively. Polycrystalline nature of orthorhombic $CuSbS_2$ has been supported by dotted SAED diffraction pattern, as shown in TEM image **(e)**. HRTEM image **(f)** of $CuSbS_2$ nanobricks entails the presence of distinct lattice fringes with the interplanar distance of about ~ 0.34 nm which corresponds to (410) crystal planes. After co-sensitization with both 1–D CdS and $CuSbS_2$ nanobricks of porous 2–D ZnO based photoanode, structural features of individual components have been investigated by TEM analysis, as illustrated in TEM image **(g)**. All the components such as porous 2–D ZnO disk, 1–D CdS and $CuSbS_2$ nanobricks retain their structures even after complete device fabrication which inferred the mechanical stability of all structures. TEM image **(h)** depicts a dotted SAED diffraction pattern for composite structures, disclosing the highly crystalline nature of these structures. TEM image **(i)** represents the HRTEM image of composite material, exhibiting the presence of three different kinds of lattice fringes based on their individual components. Accordingly, we have noticed three different interplanar distances; ~ 0.28 nm, ~ 0.35 nm and ~ 0.33 nm, corresponding to ZnO, CdS and $CuSbS_2$ respectively.

### 4.3.3 TEM ELEMENTAL MAPPING AND ENERGY DISPERSIVE X-RAY SPECTROSCOPIC ANALYSES

To verify the elemental distribution and compositional homogeneity of all elements in composite material, elemental mapping in TEM analysis and FESEM-energy dispersive X-ray (EDX) spectroscopic technique are performed and showing in figure **4.3.6** and **4.3.7**. Homogenous distribution of all elements such as Zinc, cadmium, copper, oxygen, antimony and sulfur has been clearly seen in complete elemental mapping image **(b)** of figure **4.3.6**. Elemental


Part of this chapter has been published in **J. Power Sources 2019, 425, 204-216**.

scanning images **(i-vi)** validate the presence of all elements, indicative of successfully loading of both light absorbing materials onto porous 2–D ZnO disk structures in composite sample.

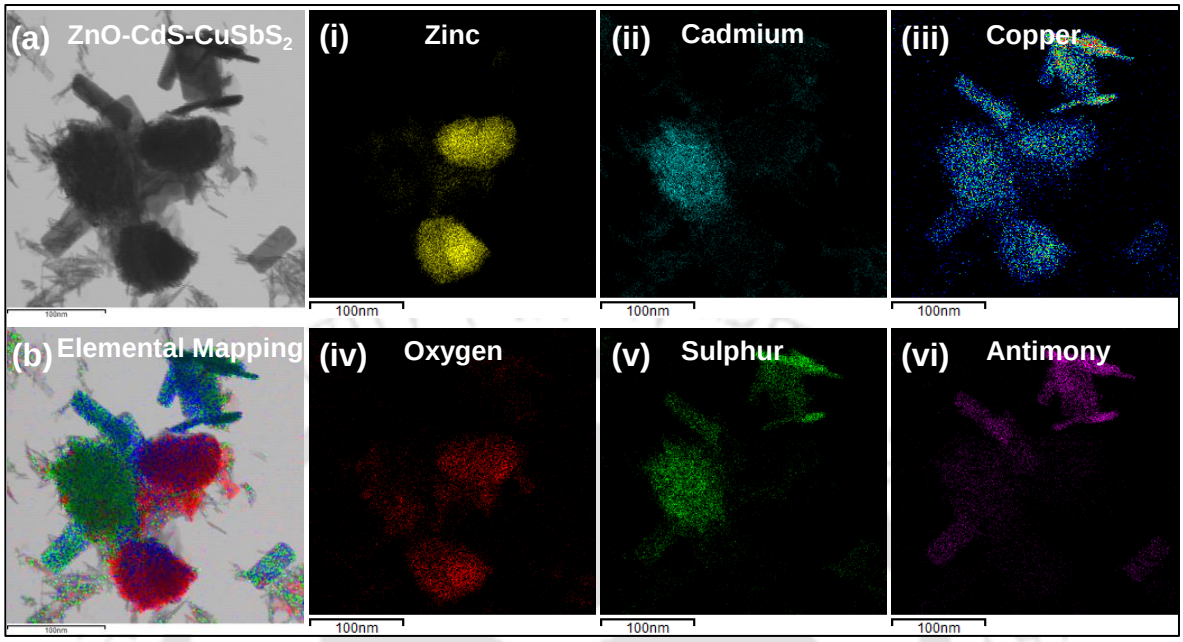


**Figure 4.3.6** Scanning Transmission electron microscopy (STEM) displays the mapping of 1–D CdS/ $CuSbS_2$ co-sensitized 2–D porous ZnO based composite material. STEM image **(b)** show the complete elemental scanning with homogeneous elemental distribution while images **(i-vi)** exhibit the individual elemental distribution of Zn, Cd, Cu, O, S and Sb respectively.

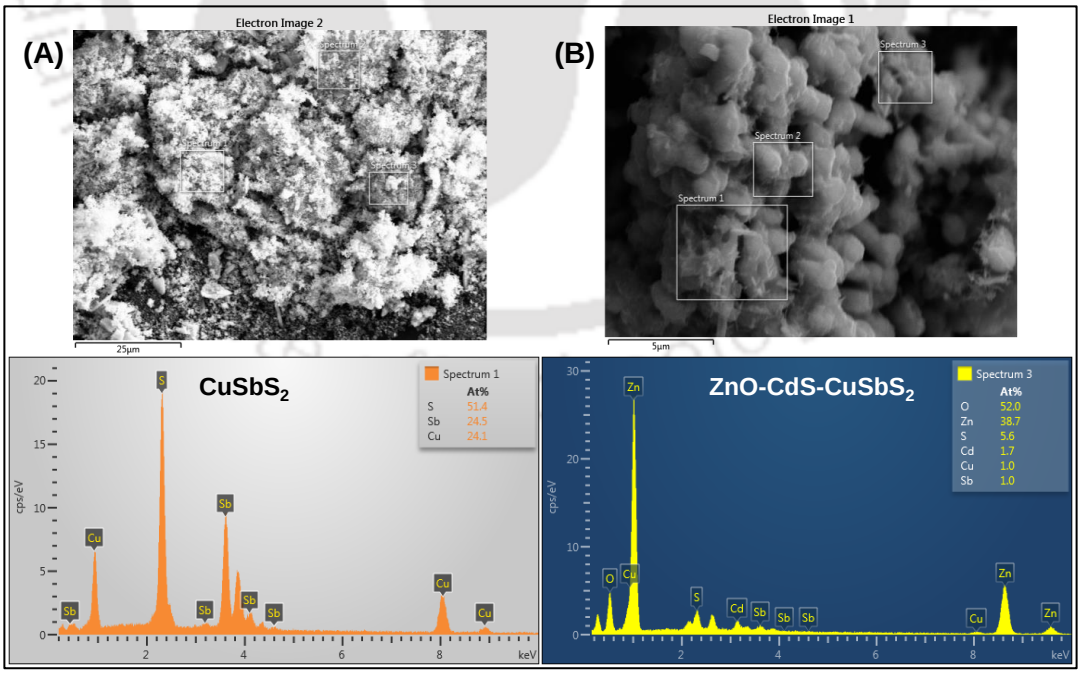


**Figure 4.3.7** Traces **(A)** and **(B)** show energy-dispersive X-ray (EDX) spectroscopy patterns of as-synthesized $CuSbS_2$ nanobricks and co-sensitized composite material respectively.


Part of this chapter has been published in **J. Power Sources 2019, 425, 204-216**.

Elemental composition of bare and composite materials has been analyzed by FESEM-EDX analysis, presenting in the figure **4.3.7**. EDX pattern of figure **4.3.7 (A)** represents the chemical composition (in at %) of as-synthesized bare $CuSbS_2$, showing the atomic ratio of all elements; Cu:Sb:S of about1.0:1.01:2.13 which is very close to expected stoichiometric value of 1:1:2. In general, deviation from this stoichiometric value would lead to formation of various defect sites related to binary and other phases of ternary metal chalcogenides. Therefore, as-synthesized $CuSbS_2$ is pure having stable chalcostibite phase and can be utilized as a proficient light absorber material. Chemical compositions (at %) of the composite material, having both light absorbers also evaluated and displayed in figure **4.3.7 (B)** and we found that all elements are present according to their compositional ratio.

### 4.3.4 UV–VISIBLE DIFFUSE REFLECTANCE SPECTRA

Optical behaviour of as-synthesized pristine and co-sensitized materials based photoanodes are analyzed by performing UV−visible (UV−Vis) diffused reflectance spectra, recorded in the wavelength range of 325–855 nm as presented in figure **4.3.8 (A-C)** respectively. In the figure **4.3.8 (A)**, absorption onset values of both ZnO structures i.e., porous 2–D disk and 1–D NR structures, synthesized under controlled reaction conditions are observed to be at ~ 406 nm and ~ 388 nm, correspond to the energy band gap of ~ 3.05 eV and ~ 3.19 eV respectively. A significant red shift (~ 18 nm) has been noticed in absorption profile of 2–D ZnO structures (synthesized using xanthan gum) with respect to 1–D ZnO which is mainly related to bigger size of porous disk structures. Moreover, optical band gap values of both ZnO structures are calculated based on their Tauc's plots, where $(\alpha h\upsilon)^2$ was plotted against the photon energy ($h\upsilon$), presented in figure **4.3.8 (B)**. From the Tauc's plots, estimated optical band gap values of porous 2–D ZnO structure and 1–D ZnO structures are observed to be ~ 3.12 eV and ~ 3.26 eV respectively, and these obtained values are seemed to be well in accordance to the values noted in absorption spectra. As obtained red shift in the absorption profile of 2–D ZnO structures as compared to 1–D ZnO structures is well supportive with the shift in the calculated band gap energies from Tauc's plots. The information of absorption profile and extinction co-efficient regarding visible light absorbing materials are very crucial for their specific application. Therefore, binary and ternary metal chalcogenides have been utilized as sensitizer materials to enrich the light harvesting efficiency of semiconductor sensitized photovoltaic device.


Part of this chapter has been published in **J. Power Sources 2019, 425, 204-216**.

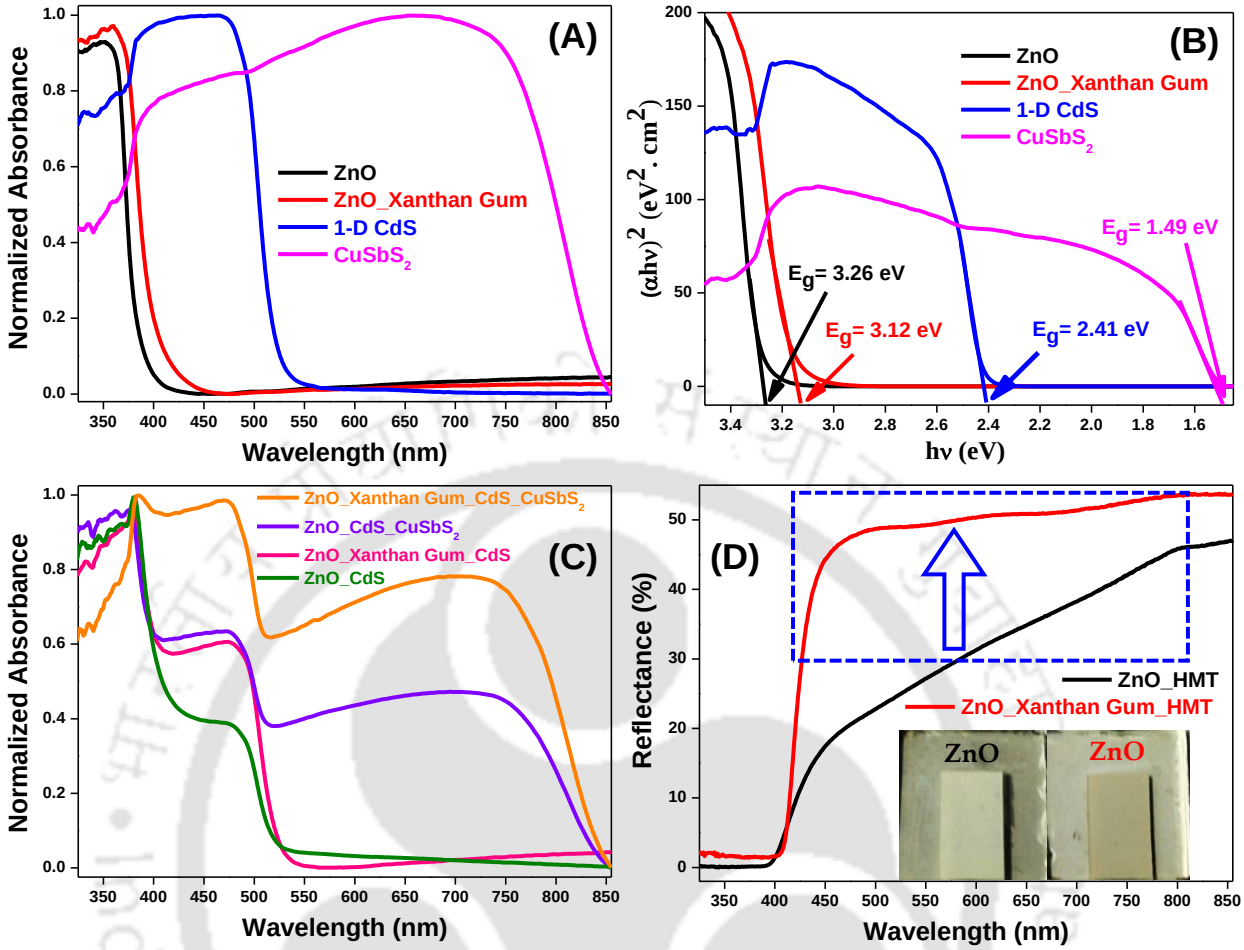


**Figure 4.3.8** Traces **(A)** and **(B)** display the Normalized UV–visible (UV–Vis) absorption spectra and Tauc's plots for as-synthesized pristine materials. Traces **(C)** shows Normalized UV–visible absorption spectra of sensitized photoanodes while trace **(D)** represents the diffuse reflectance spectra of both ZnO heterostructures [porous 2–D ZnO structure (red line) and 1–D ZnO structure (black line)] while inset of same figure shows the digital photographs of both ZnO heterostructures.

We have grown *in-situ* 1–D CdS nanostructures over both ZnO structures based photoanodes by means of controlled hydrothermal reaction. In the figure **4.3.8 (A)**, absorption onset value of *in-situ* deposited 1–D CdS nanostructures is noticed at ~ 528 nm, corresponds to the energy band gap of ~ 2.34 eV. As observed band gap value of 1–D CdS is well consistent with estimated optical band gap energy (~ 2.41 eV) from Tauc's plot, illustrated in figure **4.3.8 (B)**. From figure **4.3.8 (A)**, absorption onset of as-synthesized $CuSbS_2$ is found to be at ~ 844 nm related to energy band gap of ~ 1.47 eV, exhibiting the broad absorption profile from ultraviolet to near infra–red region. Optical band gap of as-synthesized $CuSbS_2$ has been estimated using Tauc's plot [figure


Part of this chapter has been published in **J. Power Sources 2019, 425, 204-216**.

**4.3.8 (B)**] and value is found to be ~ 1.49 eV, showing consistency with value observed in absorption profile.

Figure **4.3.8 (C)** shows the optical profile of sensitized photoanodes, fabricated using both structures of ZnO and measured in wavelength range of 325–855 nm against blank FTO as a reference. In case of only CdS sensitized photoanodes based on porous 2–D ZnO Structures (pink line) and 1–D structures (olive line), absorption profiles are noticed in the range of ~ 325–530 nm, infer the effective growth of 1–D CdS onto the photoanodic scaffolds. In general, nanocrystalline CdS structures absorb photon energy in the region 380-540 nm, validating the observations made in earlier statement. We have also noticed a substantial improvement in the absorption profile at higher wavelength region in case of CdS sensitized porous 2–D ZnO based photoanode with respect to CdS sensitized 1–D ZnO based photoanode, attributed to large exposed surface active sites for higher growth of 1–D CdS nanostructures. Furthermore, CdS/$CuSbS_2$ co-sensitized photoanodes [2–D ZnO Structures (orange line) and 1–D structures (purple line) in figure **4.3.8 (C)**] exhibit the broad absorption profiles, having three different absorption humps related to characteristics absorption profile of individual components such as ZnO, CdS and $CuSbS_2$. We have noted a significant red shift in case of porous 2–D ZnO based co-sensitized photoanode as compared to 1–D ZnO based co-sensitized photoanode, due to presence of large exposed surface area in porous disk structures which provided more active sites for loading of sensitizer particles. As a result, higher influx of photoexcitons will generate and contribute to enrich the light harvesting efficiency of photoanode.

Due to having porous nature and submicron particle size, 2–D ZnO disk structure can be effectively utilized as light scattering material. Light scattering phenomenon is employed to improve the light harvesting efficiency of photoanodic scaffold by confining the incident light which increases the path length of incident light through multiple internal reflections. UV–Vis reflectance measurement is carried out to probe the light scattering effect in both structures of ZnO by fabricating the photoanodic films on FTO glass substrate having similar film thickness, displaying in the figure **4.3.8 (D)**. From figure **4.3.8 (D)**, higher reflectance value in the wavelength region of 430–850 nm has been observed in case of porous 2–D ZnO structure (~ 50 %) with respect to 1–D ZnO structure (~ 34 %), suggesting the better utilization of incident light by means of scattering processes which are helpful for improving the repeated excitation

 Part of this chapter has been published in **J. Power Sources 2019, 425, 204-216**.

processes of sensitizer molecules on the photoanodic film of 2–D ZnO disk structures. Consequently, higher influx of photo-exciton is generated by means of multiple excitations of sensitizer particles, helpful to improve current density and efficiency of the solar device. Therefore, enhanced light harvesting ability of porous 2–D ZnO structure based photoanode will demonstrate an essential role to improve the photovoltaic performance of porous 2–D ZnO structure based solar devices.

### 4.3.5 BET SURFACE AREA ANALYSIS

Surface area of both ZnO structures, synthesized under different reaction conditions are investigated using $N_2$ adsorption and desorption isotherms, as shown in figure **4.3.9**. Porosity of both ZnO structures has been analyzed by using Barrett-Joyner-Halenda (BJH) pore size distribution plot, displaying as inset of figure **4.3.9**.

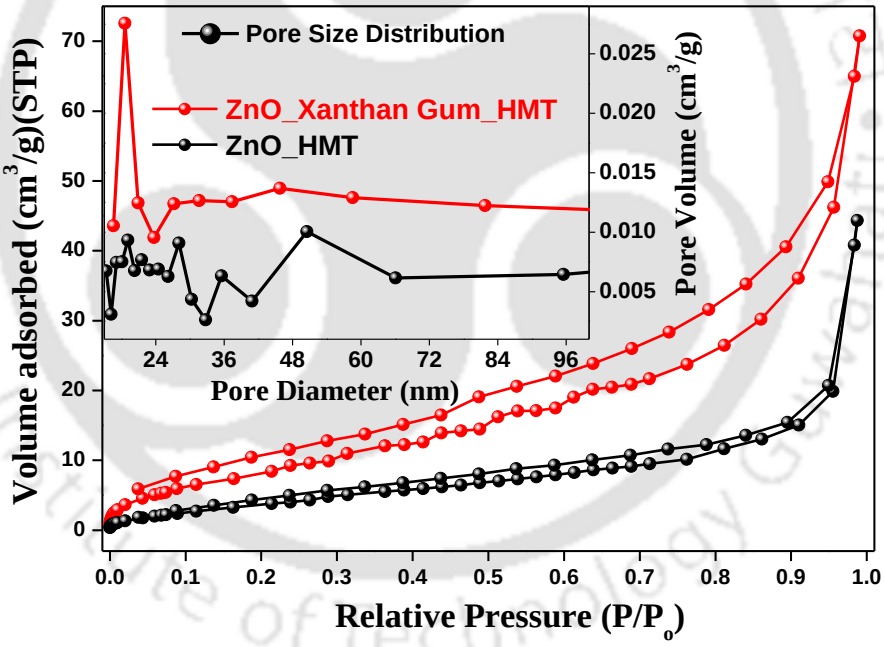


**Figure 4.3.9** Nitrogen adsorption–desorption isotherm for both structures of ZnO, synthesized under different reaction conditions. Inset of same figure shows the Barrett-Joyner-Halenda (BJH) pore size distribution plots of same materials.

From the adsorption-desorption isotherm, we have noted the type IV isotherms having H3 hysteresis loops for both the ZnO structures, revealing the mesoporous nature of as-synthesized ZnO Structures. Based on these isotherms, BET surface area for both ZnO Structures, porous 2–D ZnO (synthesized in presence of xanthan gum) and 1–D ZnO structures have been


Part of this chapter has been published in **J. Power Sources 2019, 425, 204-216**.

calculated which were found to be 28 $m^2g^{-1}$ and 17 $m^2g^{-1}$ respectively. As observed large exposed BET surface area of porous 2–D ZnO structures is responsible to provide higher surface active sites for deposition of sensitizer particles. Consequently, better loading of sensitizer particles is advocating the enhanced light harvesting ability of porous 2–D ZnO structures based photoanodic film. In the Barrett-Joyner-Halenda (BJH) pore size distribution plot, we have observed a sharp peak for porous 2–D ZnO structures (synthesized in presence of xanthan gum) in the range of the ~10–20 nm, demonstrating the pore size distribution in case of 2–D ZnO disk structures. Porous nature of disk structures are helpful for accomplishing the better hole recovery rate of oxidized species in photoanodic scaffold, resulting in improved charge transfer by reducing the recombination processes taken place at working electrode-electrolyte interface. Moreover, no prominent peak has been noted in pore size distribution plot for ZnO structures synthesized in absence of xanthan gum, advocating the no pores formation in case of 1–D ZnO structures.

### 4.3.6 RAMAN SPECTRA

Figure **4.3.10 (A)** and **(B)** represent the room temperature Raman spectra of pristine as well as sensitized materials, fabricated as thin films and measured at an excitation source of 514 nm. From figure **4.3.10 (A)**, Raman spectrum of ZnO structures [synthesized in absence of templating agent, traces **(a)**] shows two raman peaks, observed at 106 $cm^{-1}$and 437 $cm^{-1}$ which are labeled to $E_2$ (low) and $E_2$ (high) modes, considered to be signature Raman active modes related to wurtzite phase of hexagonal ZnO lattice.[30] Subsequently, similar Raman actives modes have also noted in case of 2–D ZnO disk structures [traces **(b)**]. It is clearly seen that both Raman peaks of 2–D ZnO disk structures gets blue shifted as compared to 1–D ZnO NR structures, attributed to defects and internal strains related to different growth directions. Additionally, blue shift in the characteristics $E_2$ (High) mode may also be due to optical phonon confinement and phonon localization, owing to defects or impurities in the nanostructures. In general, different morphological structures are formed based on their dissimilar growth patterns, due to which lattice defects are created as anisotropic internal strains corresponding to different growth directions of crystal structure.


Part of this chapter has been published in **J. Power Sources 2019, 425, 204-216**.

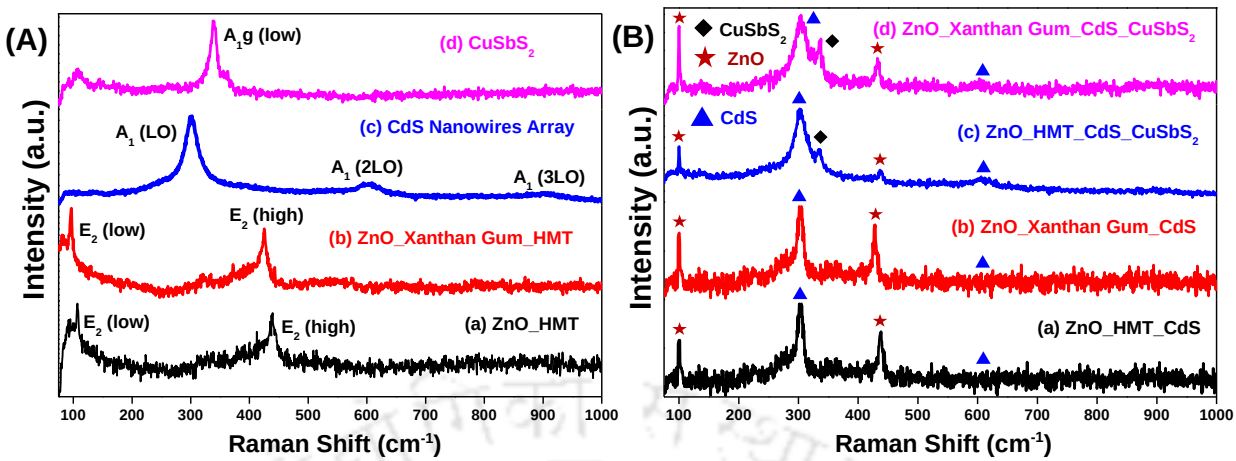


**Figure 4.3.10** Traces **(A)** and **(B)** depict the room temperature micro Raman spectra of the as-synthesized bare as well as sensitized photoanodic materials, excited at wavelength of 514 nm.

Trace **(c)** of figure **4.3.10 (A)** depicts the Raman spectrum of *in-situ* grown 1–D CdS nanostructures, exhibiting the three characteristic Raman peaks centered at 301, 603, and 906 $cm^{-1}$ which are assigned to first, second and third-order longitudinal optical phonon modes [($A_1$ (LO), $A_1$ (2LO) and $A_1$(3LO)] respectively. Intense Raman peak is noticed at 301 $cm^{-1}$ is considered as a signature peak for thermodynamically stable wurtzite phase of hexagonal CdS nanostructures having P63*mc* space group.[31] This observation reflects the formation of impurities free highly crystalline 1–D CdS nanostructures, helpful for improving the transport kinetics of photoexcited electrons.

Raman spectrum of as-synthesized $CuSbS_2$ is representing in trace **(d)** of figure **4.3.10 (A)**, showing an intense raman peak at 336 $cm^{-1}$ which is assign to the characteristic phononic vibrations [$A_1$g (low) mode] of chalcostibite phase of orthorhombic $CuSbS_2$ (Pnma space group) which is well matched with the RRUFF database (RRUFFID:R060262).[32] We have also noted a weaker Raman peak at 106 $cm^{-1}$, along with signature intense peak (336 $cm^{-1}$) demonstrating the chalcostibite phase. No raman modes related to binary chalcogenides ($Sb_2S_3$, CuS) and other stoichiometries of copper antimony sulfides ($Cu_3SbS_3$, $Cu_3SbS_4$ and $Cu_{12}Sb_4S_{13}$,) are observed in raman spectrum of $CuSbS_2$, revealing the crystal phase purity of $CuSbS_2$ and validating the observations of powder X-ray diffraction (XRD) measurements. In figure **4.3.10 (B)**, Raman spectra of sensitized photoanodes exhibit the various Raman active modes related to their individual components i.e., ZnO, CdS and $CuSbS_2$, confirming the retention of phase purity and crystal structures of all the components.


Part of this chapter has been published in **J. Power Sources 2019, 425, 204-216**.

### 4.3.7 PHOTOVOLTAIC MEASUREMENTS OF SOLAR CELLS

To demonstrate $CuSbS_2$ nanostructures as the potential photo-booster, photovoltaic measurements have been carried out by fabricating the semiconductor co-sensitized photovoltaic devices based on both morphological structures of ZnO, with platinized FTO as counter electrode and $S^{2-}/S_n^{2-}$ as redox shuttle under AM 1.5 G irradiation with intensity of 100 mW $cm^{-2}$. Photovoltaic performance parameters such as short circuit current density ($J_{sc}$), open circuit voltage ($V_{oc}$), fill factor (FF) and the overall power conversion efficiency (PCE, η) for all devices are estimated from current density–voltage (*J*–V) curves, showed in figure **4.3.11 (A)** and obtained value are represented in table **4.3.1**. From *J*–V curves, it is clear that solar devices based on porous 2–D ZnO disk structures are superior with respect to 1–D ZnO NR structures based solar devices, attributed to better light harvesting efficiency and hole regeneration capability, leading to enrich the efficiency values. In previous explanation, it is verified that the 2–D ZnO disk structures offered large exposed surface area for better growth of sensitizer particles, helpful for upsurging the flux of photoexcited electron generation which may lead to improve the injection and collection efficiency of photoanode. Moreover, improved light harvesting efficiency of 2–D ZnO disk structures based devices is ascribed to more confining of incident light based on multiple scattering processes. From table **4.3.1**, we have noted the enhanced fill factor (FF) values for 2–D ZnO disk structures based solar devices as contrast to 1–D ZnO structures based solar devices, credited to highly porous nature of disk structures which is beneficial for efficient infiltration of redox shuttle, resulting in effective regeneration of the sensitizer particles. Based on these observations, porous 2–D ZnO disk based metal chalcogenides sensitized photovoltaic devices are considered to be champion devices in both the cases (only CdS or co-sensitized devices). Therefore, calculated values of all photovoltaic parameters such as $J_{sc}$ ($mAcm^{-2}$), $V_{oc}$ (mV), FF (%) and PCE, η (%) of co-sensitized 2–D ZnO disk based solar device are found to be ≈ 14.24, ≈ 428, ≈ 42.46, ≈ 2.64 while ≈ 11.13, ≈ 442, ≈ 36.72, ≈ 1.82 for co-sensitized 1–D ZnO structures based solar device. As obtained high $J_{sc}$ value in 2–D ZnO disk based device validates the statements related to higher exposed surface area for enhanced sensitizer loading and porous nature for better functioning of redox shuttle. Moreover, as-observed $J_{sc}$ value also encourages the efficient loading and utilization of promising photo-booster $CuSbS_2$.

 Part of this chapter has been published in **J. Power Sources 2019, 425, 204-216**.

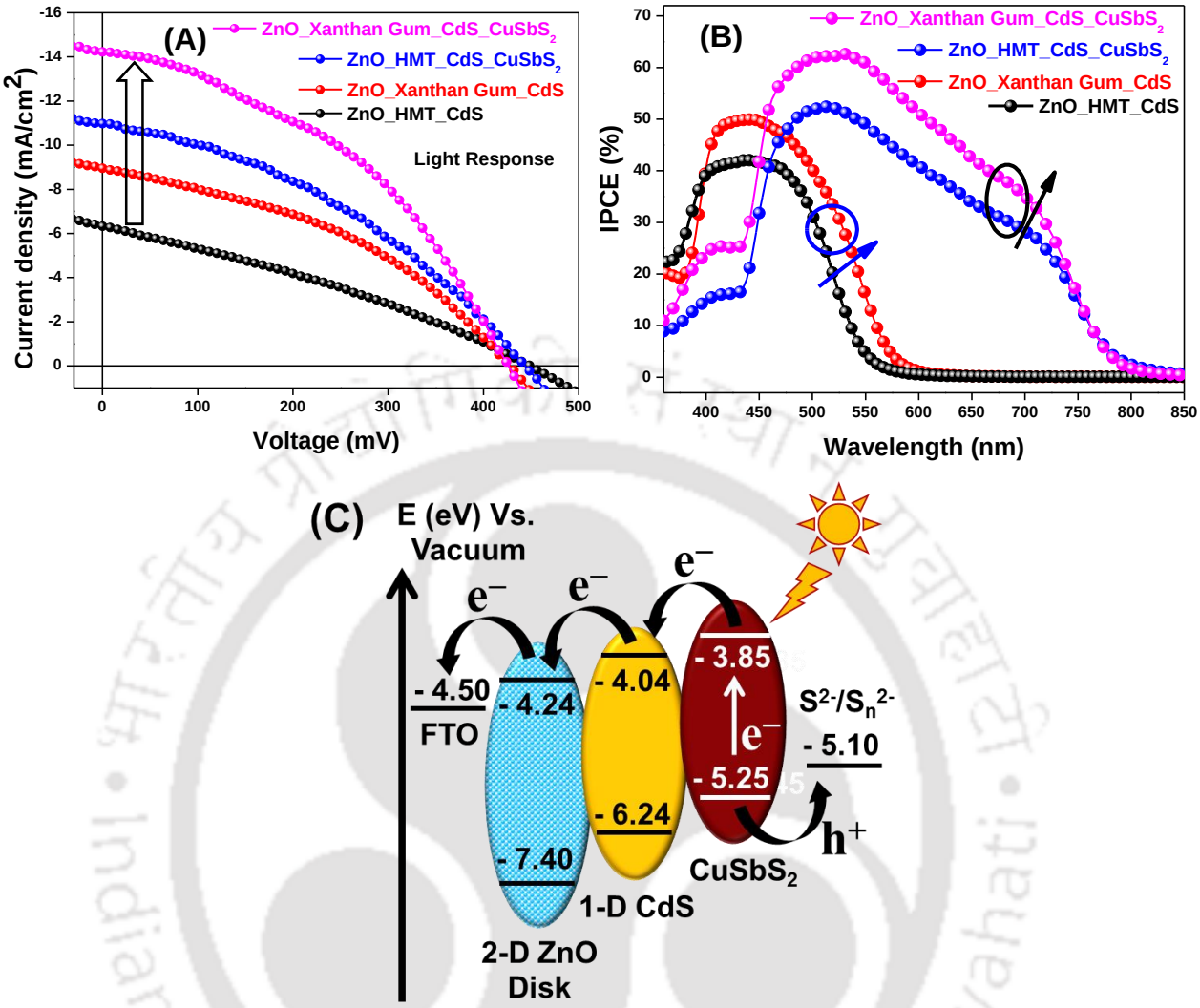


**Figure 4.3.11 (A)** Current density–Voltage (*J*–V) curve for 1–D CdS/$CuSbS_2$ co-sensitized photovoltaic devices based on both ZnO heterostructures. **(B)** Corresponding IPCE plot for the respective devices. **(C)** Schematic representation shows the efficient electron transportation in co-sensitized photoanodes based on their energy band positions (Energy band values of all the materials are taken from the reference 24 and 29).

**Table 4.3.1** Short-circuit current density ($J_{sc}$), open-circuit voltage ($V_{oc}$), fill factor (FF), power conversion efficiency (η) and incident photon to current conversion efficiency (IPCE) for as-fabricated photovoltaic devices based on both ZnO heterostructures.

| Photovoltaic Device | $J_{sc}$ (mA $cm^{-2}$) | $V_{oc}$ (mV) | FF (%) | PCE (η, %)[a] | $IPCE_{max}$ (%) |
|---|---|---|---|---|---|
| **ZnO_HMT_CdS** | 6.49 | 452 | 31.53 | 0.95 | 42.43 |
| **ZnO_Xanthan Gum_CdS** | **9.19** | **430** | **39.85** | **1.58** | **49.83** |
| **ZnO_HMT_CdS_$CuSbS_2$** | 11.13 | 442 | 36.72 | 1.82 | 53.26 |
| **ZnO_Xanthan Gum_CdS_$CuSbS_2$** | **14.24** | **428** | **42.46** | **2.64** | **62.46** |

[a]PCE value for the best performed device out of 5 identical devices.


Part of this chapter has been published in **J. Power Sources 2019, 425, 204-216**.

Charge separation and transfer processes are facilitated in 2–D ZnO disk structures due to exposed (001) polar facets. It is known that wurtzite crystal structure of ZnO possesses the regular alternate arrangement of positive Zn–terminated (001) surface and negative O–terminated (–001) surface which means each layer consists all positive $Zn^{2+}$ ions or all negative $O^{2-}$ ions in the (001) direction. Therefore, an internal electric field is generated, due to which photogenerated electrons and holes migrate to positive polar Zn–ZnO (001) and negative polar O–ZnO (–001) surfaces, respectively. Efficient charge separation between these polar (001) and (–001) surfaces can effectively minimize the possibility of recombination of photogenerated electrons and holes, resulting in improving the charge collection efficiency which in turn enriching the efficiency of photovoltaic device. In spite of having respectable $J_{sc}$ value, photovoltaic performance of $CuSbS_2$ based device is limited at present, owing to lesser $V_{oc}$ and FF values due to happening of bulk recombinations related to surface defects and theoretically predicted cliff-type conduction band offset between $CuSbS_2$ and CdS. Smaller $V_{oc}$ and FF values are also the result of reduced carrier diffusion length and high interfacial resistance of charge carriers.

Schematic representation of the possible charge transfer pathways in the CdS/$CuSbS_2$ co-sensitized photoanode is displayed in figure **4.3.11 (C)**. Based on the nature of metal chalcogenides, p–n heterojunction is formed between p–type $CuSbS_2$ and n–type CdS which promotes the separation of photoexcited electron–hole pair due to establishment of electric field between p–type and n–type absorber materials, shows the potential applicability of $CuSbS_2$ for use in electronic devices. *In-situ* growth of 1–D CdS layer between ZnO and $CuSbS_2$ not only facilitates an efficient photoexcited electron transfer through uni-directional pathway but also suppress the recombinations due to back transferring of photoexcited electrons at electrode-electrolyte interfaces. From **4.3.11 (C)**, we have noticed that the conduction band edge of the $CuSbS_2$ (− 3.85 eV) is found to be more positive than that of CdS (− 4.04 eV) whereas valence-band edge position of CdS (−6.41 eV) is found to be more negative than that of $CuSbS_2$ (−5.25 eV).[24, 29] Thus, type–II staggered heterojunction is formed between $CuSbS_2$ and CdS which is facilitating efficient electrons-holes separation, resulting in reduced recombination of photoexcited electrons-holes, which is necessary for high efficiency solar cell.


Part of this chapter has been published in **J. Power Sources 2019, 425, 204-216**.

For further demonstration of the photo-boosting effect of $CuSbS_2$, incident photon-to-current conversion efficiency (IPCE) analysis of all devices are performed in the wavelength range of 360–850 nm, showed in figure **4.3.11 (B)**. We have noticed higher IPCE values for solar devices based on porous 2–D ZnO disk structures as compared to 1–D ZnO NR structures based solar devices, owing to enhanced loading of sensitizer particles, better separation and transportation of photogenerated electrons-holes and reduced recombination processes. Moreover, similar increasing trends of IPCE values are observed for respective devices as $J_{sc}$ values in the *J*–V curve. IPCE plots of only CdS sensitized solar devices (marked in black and red symbol line) infer the efficacious *in-situ* growth of 1–D CdS nanostructures whereas co-sensitized devices based on both structures of ZnO show the broad IPCE plots, extended to near IR region which divulge the successful loading of both sensitizer species i.e., 1–D CdS and $CuSbS_2$. As observed IPCE plots have the covenant with the absorption profiles of individual components, presented in figure **4.3.8 (A)**. Therefore, IPCE values for co-sensitized 2–D and 1–D ZnO structures based devices are found to be ~ 62.46 % and ~ 53.26 % respectively. As-obtained lower IPCE value for 1–D ZnO structures based devices is ascribed to poor sensitizer loading due to lesser surface area, reducing the light harvesting ability. It is evident from 1–D CdS and $CuSbS_2$ co-sensitized IPCE spectra, quantum efficiency values for both ZnO structures based devices are gradually decreases from 550 nm to the onset wavelength of $CuSbS_2$. This gradual decrement of IPCE values at longer wavelength region can be accredited to short minority carrier diffusion length, poor carrier collection efficiency and domination of carrier recombination based on surface defect states. Additionally, in case of porous 2–D ZnO structure based devices, we noticed the shifting of IPCE spectra towards longer wavelength region [marked as circles in figure **4.3.11 (B)**] which is mainly related to effective light scattering processes due to which sensitizer particles are repetitively excited and enriching the light harvesting efficiency of photoanode. Subsequently, porous nature of ZnO disk structures encourage the better infiltration of redox shuttle in the photoanodic segment for faster hole recovery rate of oxidized sensitizer, helpful to improve the photovoltaic performance of solar devices.


Part of this chapter has been published in **J. Power Sources 2019, 425, 204-216**.

### 4.3.8 ELECTROCHEMCIAL IMPEDANCE SPECTROSCOPY ANALYSIS

Electrochemical impedance spectroscopy (EIS) analysis is performed to monitor the charge transport and recombination kinetics of all photovoltaic devices, measured by applying an external bias equivalent to open circuit voltage ($V_{oc}$) in the frequency range of 0.1 Hz to 100 kHz under dark condition, as presented in figure **4.3.12 (A)** and **(B)**. In general, EIS of a solar device elucidates the charge transfer and recombinations phenomenon occurring at different interfaces of photovoltaic devices such as at working electrode (ZnO−sensitizer)/electrolyte interface in the frequency range of 0.1 Hz to 1 kHz, at counter electrode (platinized FTO)/electrolyte interface in the frequency range of 1−100 kHz and the diffusion of redox shuttle in the frequency range of 0.1 Hz to 0.01 Hz. Figure **4.3.12 (A)** exhibits the Nyquist plot of as-fabricated solar devices, measured in the frequency range from 0.1 Hz to 100 kHz by employing an external bias equivalent to $V_{oc}$ under dark condition. Nyquist plots of all devices are showing two semicircles, one in the frequency range of 0.1−1 kHz due to the charge transfers and recombination processes happening at the working electrode/electrolyte interface while another one in the frequency range of 1−100 kHz the higher frequency region related to charge transfers and recombination processes arising at the counter electrode/electrolyte interface. The diameter of the semicircle ($R_k$) noticed in the frequency region of 0.1−1 kHz, is mainly associated to the recombination resistance due to charge transfer at working electrode/electrolyte interface.[33–34] Subsequently, we observed that diameter of semicircle is large in case of co-sensitized 1−D ZnO structures based solar device [marked as blue in figure **4.3.12 (A)**] contrary to 2−D ZnO structures based device [marked as magenta in figure **4.3.12 (A)**], suggesting the improved and faster charge transport phenomenon. For better understanding of transport and recombination kinetics, Nyquist plots are fitted by considering an equivalent electrical circuit [inset of figure **4.3.12 (A)**] having different electrical components, accountable for happening of different electrochemical processes at various interfaces of the solar device. Consequently, as-obtained fitted parameters of Nyquist plots are summarized in table **4.3.2**. From Table **4.3.2**, we have noted a lower series resistance ($R_s$) values for semiconductor sensitized 1−D ZnO structures based devices with respect to 2−D ZnO based devices, boosting the photogenerated electrons collection at the FTO substrate and contributing improve the current outcome from the device. Fitting components such as $R_{ct1}$ and CPE1 are yielded after fitting of the smaller semicircle in all devices which is linked with the

recombination resistance due to charge transfer and capacitance occurred at the surface of platinized FTO and the electrolyte interface.

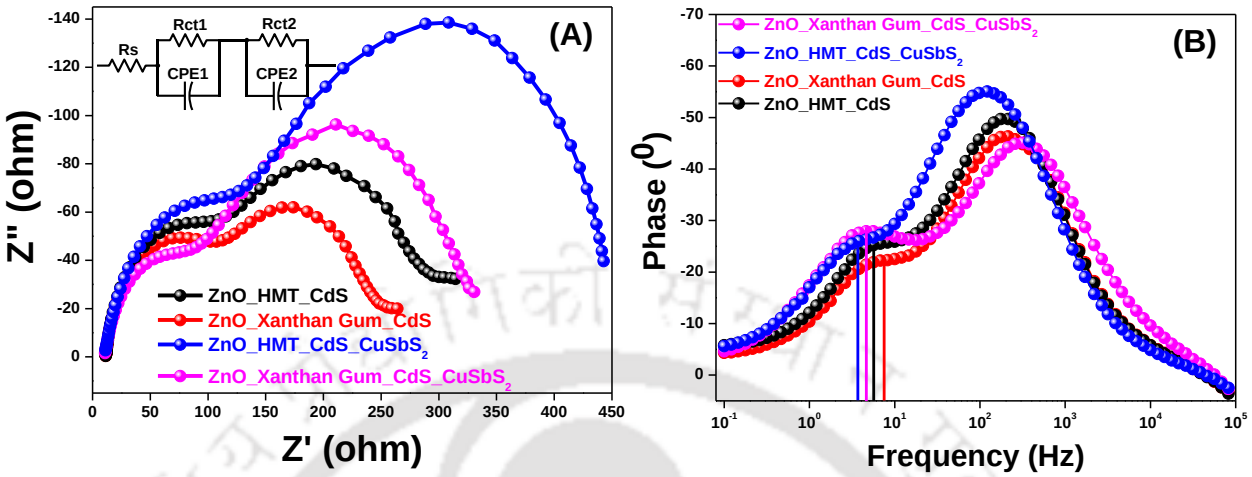


**Figure 4.3.12 (A)** Nyquist plot for as-fabricated semiconductor sensitized photovoltaic devices based on both morphological structures of ZnO. Inset of same plot shows the equivalent circuit diagram, used for fitting the EIS data, having abbreviations; $R_s$, sheet resistance; $R_{ct1}$ & $R_{ct2}$ , charge-transfer resistance of the counter electrode and working electrode; CPE1 & CPE2, constant-phase element of the counter electrode and working electrode respectively. **(B)** Bode phase plot for all semiconductor sensitized photovoltaic devices.

**Table 4.3.2** Fitted parameters such as series resistance ($R_s$), recombination resistance of the counter electrode and working electrode ($R_{ct1}$ & $R_{ct2}$), maximum peak frequency ($f_{max}$) and electron lifetime ($\tau_e$) for all devices based on different ZnO structures.

| Photovoltaic Device | $R_s$ (ohm) | $R_{ct1}$ (ohm) | $R_{ct2}$ (ohm) | $f_{max}$ (Hz) | $\tau_e$ (ms) |
|---|---|---|---|---|---|
| **ZnO_HMT_CdS** | 12.09 | 92.68 | 179.90 | 5.66 | 28.13 |
| **ZnO_Xanthan Gum_CdS** | 12.34 | 87.10 | 141.10 | 7.57 | 21.03 |
| **ZnO_HMT_CdS_$CuSbS_2$** | 11.24 | 109.50 | 302.20 | 3.69 | 43.15 |
| **ZnO_Xanthan Gum_CdS_$CuSbS_2$** | 11.29 | 77.18 | 216.10 | 4.57 | 34.85 |

From table **4.3.2**, we have found the higher recombination resistance ($R_{ct1}$) values for 1–D structures based devices, promoting the better separation of electrons–holes and transportation of electrons. For fitting the bigger semicircle of all devices, fitted components $R_{ct2}$ and CPE2 have been utilized which are related to recombination resistance and capacitance happened at the working electrode/electrolyte interface. In the table **4.3.2**, we found the higher $R_{ct2}$ value in case of co-sensitized 1–D ZnO structures based device as contrast to 2–D ZnO structures based device, assisting the better charge separation and transportation, due to which recombination processes gets reduced by inhibiting the back transferring of photoexcited


Part of this chapter has been published in **J. Power Sources 2019, 425, 204-216**.

electron at working electrode/electrolyte interface. Subsequently, improved charge separation and transfer in co-sensitized device (ZnO/CdS/$CuSbS_2$) is mainly related to formation of type–II staggered heterojunction between p–type $CuSbS_2$ and n–type CdS, which is favorable for electron separation and transportation processes.

Bode phase plots related to respective devices are displayed in figure **4.3.12 (B)**. We have noticed two dissimilar peaks correspond to electrochemical phenomenon happened at two different interfaces of the device. For further studying the trap states induced recombination processes, we have calculated the photoinduced electron lifetimes ($\tau_e$) from characteristics maximum peak frequency ($f_{max}$) in the frequency region of 0.1 Hz to 1 kHz, using the **equation (1)** [35] and summarized in table **4.3.2**.

$$\tau_e = \frac{1}{2\pi f_{max}} \qquad (1)$$

In table **4.3.2**, maximum peak frequencies ($f_{max}$) for the 1–D ZnO/CdS, 2–D ZnO disk/CdS, 1–D ZnO/CdS/$CuSbS_2$ and 2–D ZnO disk/CdS/$CuSbS_2$ based photovoltaic device are found to be at 5.66 Hz, 7.57 Hz, 3.69 Hz and 4.57 Hz respectively. Corresponding $\tau_e$ value for all devices are estimated and found to be ~ 28.13 ms, ~ 21.03 ms, ~ 43.15 ms and ~ 34.85 ms. As-obtained higher value of $\tau_e$ for co-sensitized 1–D ZnO structure based solar device confirms the presence of reduced recombination processes, happened due to back transferring of photoexcited electrons to the redox electrolyte at the ZnO–sensitizers/electrolyte interfaces. Inspite of having high $\tau_e$ and $R_k$ values, photovoltaic efficiency in case of 1–D ZnO structures based solar devices are found to be low, owing to poor light harvesting efficiency of photoanodes, related to lesser active surface area for loading of sensitizer particles. On the other hand, it is noticed that despite having the lower $\tau_e$ and $R_k$ values in 2–D ZnO disk based device, the photovoltaic efficiency of same device is high, attributed to improve light harvesting efficiency of photoanodes corresponds to large exposed surface area, offered more active sites for better loading of sensitizer materials and better light scattering. Moreover, due to highly porous nature of 2–D ZnO disk structures, redox electrolyte can easily infiltrate into photoanodic film and enhance the hole recovery rate of sensitizers, reflecting in better fill factor and efficiency values of solar devices. Thus, device based on porous 2–D ZnO disk structures is superior as compared to 1–D

ZnO NRs structures and exhibited the higher values of photovoltaic parameters such as $J_{sc}$ ~ 14.24 mAcm$^{-2}$, $V_{oc}$ ~ 428 mV, FF ~ 42.46 % and η ~ 2.64 % .

### 4.3.9 STABILITY OF PHOTOVOLTAIC DEVICES

For real-world application, photo- and environmental stability of as-fabricated photovoltaic devices is a crucial parameter to evaluate. Photovoltaic performance parameters such as $J_{sc}$, $V_{oc}$, FF and η of best performed solar device are examined with respect to different time interval, under the artificial solar irradiation (AM 1.5 G, 100 mWcm$^{-2}$).

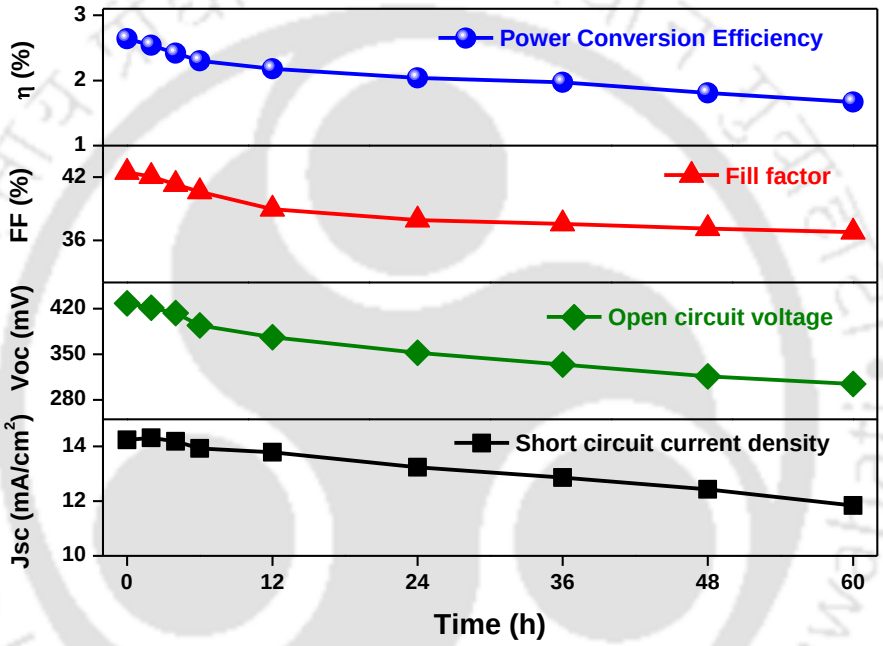


**Figure 4.3.13** Variation in the values of different photovoltaic parameters such as $J_{sc}$ (mA cm$^{-2}$), $V_{oc}$ (mV), FF (%) and η (%) with respect to time to demonstrate the stability of the best performing photovoltaic device based on porous 2–D ZnO disk structures.

Photovoltaic devices are stored at ambient conditions without proper sealing of device throughout the measurement time period. Changes in the value of all photovoltaic parameters of solar device are recorded over a time period of 60 h, as shown in figure **4.3.13**. Photocurrent of the device is seemed to increases gradually during few hours and then become steady, attributed to the better infiltration of $S^{2-}/S_n^{2-}$ redox electrolyte through the photoanodic film. After some time, $J_{sc}$ values start to decrease due to evaporation and leakage of redox electrolyte. Other parameters such as open circuit voltage and fill factor are also showed steady nature in early few hours and then constantly decreases as prolong irradiation. Thus, there is a ~ 34 % reduction in


Part of this chapter has been published in **J. Power Sources 2019, 425, 204-216**.

efficiency for porous 2–D ZnO disk structures based device after storing to 60 h. On the basis of these observations, we accomplish that semiconductor sensitized solar device is believed to be quite stable in the beginning of few hours but show the continual decrement in photovoltaic performances with increased time.

## 4.4 CONCLUSIONS

In brief, porous two dimensional (2–D) zinc oxide (ZnO) disk like structures are synthesized using a biomass derived templating agent i.e., Xanthan gum, mainly responsible to regulate the growth kinetics of high energy facets of wurtzite ZnO crystal structure. As-synthesized both ZnO structures are well characterized by using several analytical techniques. We have performed the morphology dependent comparative photovoltaic study based on both structures i.e., porous 2–D ZnO disk structures and 1–D ZnO NR structures based photovoltaic devices, co-sensitizing with *in-situ* grown 1–D CdS nanowires array and $CuSbS_2$ nanobricks. Superior photovoltaic performance (~ 45 % enhancement in PCE) is noticed for CdS-$CuSbS_2$ co-sensitized porous 2–D ZnO disks based photovoltaic device as compared to 1–D ZnO NR structures. This enrichment is mainly attributed to high exposed surface active sites for optimum loading of light absorbing materials, better light scattering and improved hole recovery rate of sensitizers with the better penetration of redox shuttle. Moreover, crystal phase purity of $CuSbS_2$ and p–n junction formed between $CuSbS_2$ and CdS also support the enhanced efficiency by facilitating the electron–hole separation and electron transportation. Presented work highlights the appealing optoelectronic properties of defect free chalcostibite $CuSbS_2$ to improve the $CuSbS_2$ based photovoltaic technology. Thus, pure $CuSbS_2$ is believed to be considered as a promising light absorber candidate for their future application.

## 4.5 REFERENCES

(1) M. C. Beard, J. M. Luther and A. J. Nozik, *Nat. Nanotechnol.*, 2014, **9**, 951–954.

(2) S. Lee, J. C. Flanagan, B. Lee, T. Hwang, J. Kim, B. Gil, M. Shim and B. Park, *ACS Appl. Mater. Interfaces*, 2017, **9**, 31931−31939.

(3) Y. Nie, Z. Wang, J. Wang, F. Bao, J. Zhang, Y. Ma, T.-K. Sham and X. Sun, *J. Phys. Chem. C*, 2017, **121**, 26076–26085.

(4) K. S. Leschkies, R. Divakar, J. Basu, E. E. Pommer, J. E. Boercker, C. B. Carter, U. R. Kortshagen, D. J. Norris and E. S. Aydil, *Nano Lett.*, 2007, **7**, 1793–1798.

(5) Y. Qiu, W. Chen and S. Yang, *J. Mater. Chem.*, 2010, **20**, 1001–1006.

(6) H. Chen, W. Li, H. Liu and L. Zhu, *Electrochem. Commun.*, 2011, **13**, 331–334.

(7) F. Xu, M. Dai, Y. Lu and L. Sun, *J. Phys. Chem. C*, 2010, **114**, 2776–2782.

(8) M. Fu, J. Zhou, Q. Xiao, B. Li, R. Zong, W. Chen and J. Zhang, *Adv. Mater.*, 2006, **18**, 1001–1004.

(9) K. L. Meagley and S. P. Garcia, *Cryst. Growth Des.*, 2011, **12**, 707−713.

(10) M. K. Kavitha, H. John and P. Gopinath, *Mater. Res. Bull.*, 2014, **49**, 132−137.

(11) T. R. Chetia, M. S. Ansari and M. Qureshi, *ACS Appl. Mater. Interfaces*, 2015, **7**, 13266–13279.

(12) C. Tang, M. J. S. Spencer and A. S. Barnard, *Phys. Chem. Chem. Phys.*, 2014, **16**, 22139–22144.

(13) S. Sotiropoulou, Y. Sierra-Sastre, S. S. Mark and C. A. Batt, *Chem. Mater.*, 2008, **20**, 821–834.

(14) H. Zhou, T. Fan and D. Zhang, *Chem. Sus Chem.*, 2011, **4**, 1344–1387.

(15) Y. H. Tseng, H. Y. Lin, M. H. Liu, Y. F. Chen and C. Y. Mou, *J. Phys. Chem. C*, 2009, **113**, 18053–18061.

(16) F. Waltz, G. Wismann, J. Lippke, A. M. Schneider, H. C. Schwarz, A. Feldhoff, S. Eiden and P. Behrens, *Cryst. Growth Des.*, 2012, **12**, 3066–3075.

(17) J. Yin, Q. Lu, Z. Yu, J. Wang, H. Pang and F. Gao, *Cryst. Growth Des.*, 2010, **10**, 40–43.

(18) L. Li, X. Yang, J. Gao, H. Tian, J. Zhao, A. Hagfeldt and L. Sun, *J. Am. Chem. Soc.*, 2011, **133**, 8458−8460.

(19) I. Robel, V. Subramanian, M. Kuno and P. V. Kamat, *J. Am. Chem. Soc.*, 2006, **128**, 2385−2393.

(20) Y. Wang, K. Lu, L. Han, Z. Liu, G. Shi, H. Fang, S. Chen, T. Wu, F. Yang, M. Gu, S. Zhou, X. Ling, X. Tang, J. Zheng, M. A. Loi and W. Ma, *Adv. Mater.*, 2018, **30**, 1704871.

(21) Y. Wu, C. Wadia, W. Ma, B. Sadtler and A. P. Alivisatos, *Nano Lett.*, 2008, **8**, 2551–2555.

 Part of this chapter has been published in **J. Power Sources 2019, 425, 204-216**.

(22) Y. C. Choi, D. U. Lee, J. H. Noh, E. K. Kim and S. I. Seok, *Adv. Funct. Mater.*, 2014, **24**, 3587−3592.

(23) L. Yu, R. S. Kokenyesi, D. A. Keszler and A. Zunger, *Adv. Energy Mater.*, 2013, **3**, 43−48.

(24) B. Yang, L. Wang, J. Han, Y. Zhou, H. Song, S. Chen, J. Zhong, L. Lv, D. Niu and J. Tang, *Chem. Mater.*, 2014, **26**, 3135–3143.

(25) Y. R. Lazcano, M. T. S. Nair and P. K. Nair, *J. Cryst. Growth*, 2001, **223**, 399–406.

(26) C. L. McCarthy, P. Cottingham, K. Abuyen, E. C. Schueller, S. P. Culver and R. L. Brutchey, *J. Mater. Chem. C*, 2016, **4**, 6230–6233.

(27) C. Garza, S. Shaji, A. Arato, E. P. Tijerina, G. A. Castillo, T. K. D. Roy and B. Krishnan, *Sol. Energy Mater. Sol. Cells*, 2011, **95**, 2001–2005.

(28) S. Moosakhani, A. A. S. Alvani, R. Mohammadpour, J. Sainio, Y. Ge and S. P. Hannula, *CrystEngComm*, 2018, **20**, 1527–1535.

(29) M. S. Ansari, A. Banik and M. Qureshi, *Carbon*, 2017, **121**, 90–105.

(30) K. A. Alim, V. A. Fonobarov, M. Shamsa and A. A. Balandin, *J. Appl. Phys.*, 2005, **97**, 124313.

(31) S. Kar and S. Chaudhuri, *J. Phys. Chem. B*, 2006, **110**, 4542–4547.

(32) Li. Zhang, Y. Li, X. Li, C. Li, R. Zhang, J. J. Delaunay and H. Zhu, *Nano Energy*, 2016, **28**, 135–142.

(33) S. Phadke, A. Du Pasquier and D. P. Birnie, *J. Phys. Chem. C*, 2011, **115**, 18342−18347

(34) V. D. Dao, L. L. Larina, Q. C. Tran, V. T. Bui, V. T. Nguyen, T. D. Pham, I. M. A. Mohamede, N. A. M. Barakate and B. T. Huyc, *Carbon*, 2017, **116**, 294–302.

(35) R. Kern, R. Sastrawan, J. Ferber, R. Stangl and J. Luther, *Electrochim. Acta*, 2002, **47**, 4213–4225.

# CHAPTER 5

## Enhanced Photovoltaic Performance Using Biomass Derived 3–D ZnO Hierarchical Superstructures and a D–A type $C_S$–Symmetric Triphenylamine Linked Bisthiazole

*This chapter demonstrates the synthesis of three dimensional (3−D) Zinc oxide (ZnO) hierarchical superstructures (HSs), assembled with compacted ZnO nanorods (NRs) using anionic polysaccharide "Polygalacturonic acid. We observe a substantial enhancement (~ 35 %) in efficiency (η) for 3−D ZnO HSs based device (η ~ 5.37 %) as compare to 1−D ZnO NRs (η ~ 3.48 %), attributed to better charge separation and collection, better light-scattering effect, higher BET surface area for sensitizer loading and efficient electron injection from dye D1 to the ZnO.*

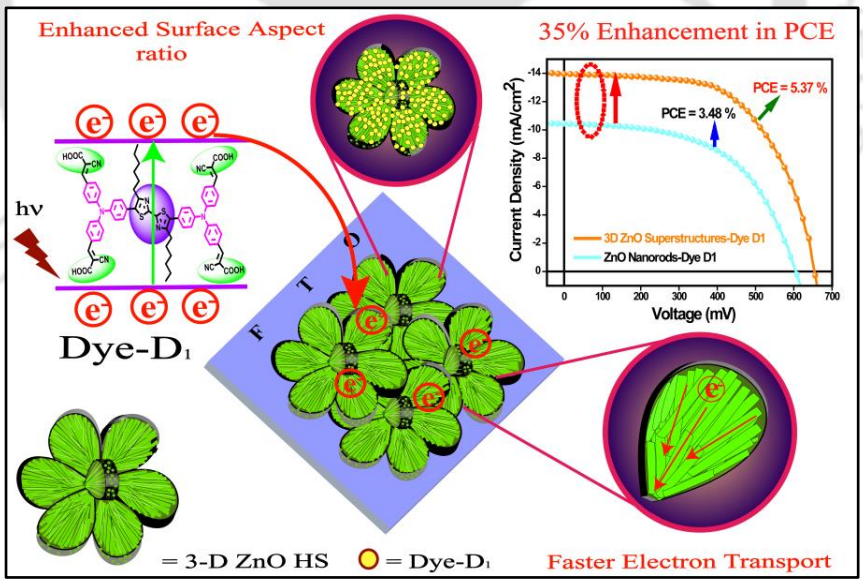


***Ansari, et al., Electrochim. Acta* 2018, *259*, 262–275.**

## 5.1 INTRODUCTION

Self-integration of one dimensional (1–D) and two dimensional (2–D) nanoscale building blocks into hierarchical structures (HSs) has been gain a consideration for the synthesis of micro/nanomaterials, specifically three dimensional (3–D) HSs.[1–3] These hierarchical architectures possess unique properties owing to combine features of both micro as well as nanoscale building blocks that are distinct from the features of single morphological structures[4], and utilized in various applications.[5–7] 3–D hierarchical superstructures are fabricated as a result of structure directing agent assisted self-assembling of nanoparticles, nanorods, nanotubes and nanosheets.[8] In general, templating agents used for assembling of basic building blocks have various disadvantages in terms of the high-cost, removal by chemical etching or by calcination at higher temperature and environmental unfriendly. Therefore, bio-inspired templating agents have been utilized to overcome these drawbacks for oriented growth of inorganic materials.[9] However, it is necessary to understand the growth mechanism for the development of new synthetic methodologies based on bio-templating route. It is believed that these superstructures are basically constructed through the nonclassical self-oriented attachment of basic building blocks,[10] in which high energy surfaces are eliminated by the epitaxial attachment of nanocrystals and considered to be a driving force for the crystal growth. In general, bioinspired templates consist of several functional groups such as hydroxyl, sulfonic and carboxyl groups which are capable to attach to the material surface with an ionic interaction and control the growth of nanoarchitechtures by assembling of building blocks in a definite direction. Fabrication of 3–D superstructure integrated with 1–D nanocrystal is very demanding because of its superior optoelectronic properties for photovoltaic applications.[11] Generally, 3–D superstructures possess large surface area for higher loading of light harvesting molecule, exceptional light scattering capability and direct pathway for faster transport of photogenerated electrons, owing to assembled 1–D nanocrystals. Moreover, porous nature of these structures is helpful for the better infiltration of redox couple in the photovoltaic devices. So far, there are very few reports for the fabrication of 3–D superstructures of zinc oxide (ZnO) yet it needs to be explored more for understanding the interaction between biotemplate and inorganic material.[12–15] In this chapter, we have reported a facile one step hydrothermal route for the controlled synthesis of 3–D ZnO HSs, integrated with compact ZnO nanorods (NRs). We have utilized a natural


Part of this chapter has been published in **Electrochim. Acta 2018, 259, 262–275**.

water soluble biopolymer "Polygalacturonic acid" as a crystal growth modifier which is easily take out from plant cell walls. It is considered to be an anionic polysaccharide and the chemical structure is shown in figure **5.1.1**. This biopolymer is responsible for specific integration of ZnO NRs to form hierarchically 3–D superstructures. We have discussed the probable reaction mechanism for the formation of these superstructures under the controlled reaction conditions. Photovoltaic properties of as-synthesized 3–D ZnO HSs as compared to its basic structural units i.e., ZnO NRs are investigated by sensitizing with a new bisthiazole linked metal free donor-acceptor dye; ((2E,2'E,2''E,2'''E)-3,3',3'',3'''-((((4,4'-dihexyl-[2,2'-bithiazole]-5,5'-diyl)bis(4,1 phenylene))bis(azanetriyl))Tetrakis (benzene-4,1-diyl))tetrakis (2-cyanoacrylic acid) (dye; D1).

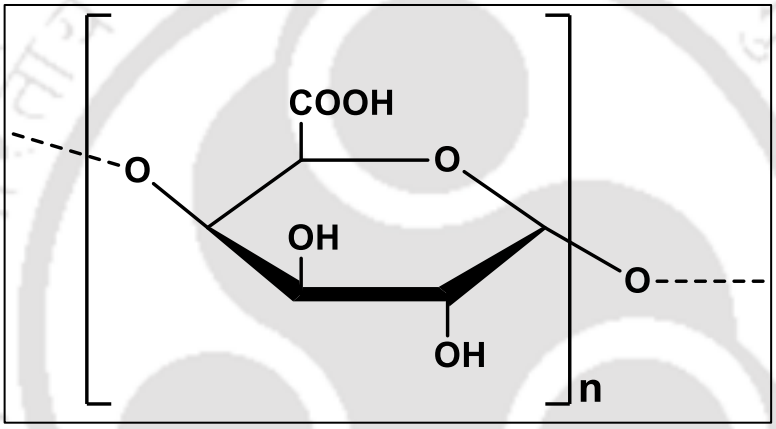


**Figure 5.1.1** Chemical structure of biomass derived templating agent "Polygalacturonic acid".

## 5.2 EXPERIMENTAL METHODS

### 5.2.1 SYNTHESIS OF 3–D ZnO HIERARCHICAL SUPERSTRUCTURES

3–D ZnO hierarchical superstructures were synthesised by dissolving the biopolymer polygalacturonic acid (1 mg/mL) in de-ionized water (25 mL) under vigorous stirring. Zinc nitrate hexahydrate (0.297 g, 1 mmol) was then added in same solution. Viscosity of the above solution increased due to interaction of biotemplate and inorganic salt and stirred continually for another 20 min at room temperature. Now, liquid ammonia, $NH_3 \bullet H_2O$ (25 %) was slowly added into the solution. Instantly, a white precipitate observed after the addition of $NH_3 \bullet H_2O$ in the solution. Continue addition of $NH_3 \bullet H_2O$ in the above solution until the white precipitate disappeared completely. Then, this clear solution was transferred into a Teflon autoclave, sealed tightly and kept at 125 $^oC$ for 2 h. After cooling, as-obtained precipitate was centrifuged, washed with distilled water and absolute ethanol to remove the unreacted ions and dried in a hot air oven

 Part of this chapter has been published in **Electrochim. Acta 2018, 259, 262–275**.

at 75 $^{o}$C. Control reaction in the absence of biotemplate was also carried out by following similar synthetic protocol and produced 1–D ZnO NRs.

### 5.2.2. SYNTHESIS OF DYE D1

The triphenylamine linked bisthiazole based donor–acceptor dye **D1** was synthesized by the Suzuki and Knoevenagel condensation reactions.[16] The precursor; 5,5′-dibromo-4,4′-dibutyl-2,2′-bisthiazole **(1)** was prepared by using previously reported protocol.[17] The 4,4'-((4-(4,4,5,5-tetramethyl-1,3,2-dioxaborolan-2-yl)phenyl)azanediyl)dibenzaldehyde **(a)** was synthesized from 4,4'-((4-iodophenyl)azanediyl)dibenzaldehyde by Suzuki coupling reaction. In detail, under argon atmosphere a solution of 4,4'-((4-iodophenyl)azanediyl)dibenzaldehyde (1.00 g, 2.34 mmol) and the 4,4,4',4',5,5,5',5'-octamethyl-2,2'-bi(1,3,2-dioxaborolane) (0.8 g, 3.1 mmol) in dry Toluene (20 ml), added KOAc (0.8 g, 8.1 mmol), $Pd(PPh_3)_4$ (0.095 g, 0.08 mmol), stirred for 16 h at 135 $^{o}$C, after completion of the reaction, the reaction mixture was concentrated under reduced pressure, the crude compound was purified by column chromatography on silica, using hexane/ DCM (35:65) to get **a** as a yellow solid (0.650 g, 65%). The compound **(1)** was reacted with 4,4'-((4-(4,4,5,5-tetramethyl-1,3,2-dioxaborolan-2-yl)phenyl)azanediyl)dibenzaldehyde boronic ester under the Suzuki coupling reaction condition to get dye **(2)** in 55% yield. The reaction of dye **(2)** with cyanoacetic acid in dry dichloromethane (DCM) (5 ml) and ammonium acetate stirred for 3 h at 65 °C in microwave resulted dye (2E,2'E,2"E,2'"E)-3,3',3",3'"-((((4,4'-dihexyl-[2,2'-bithiazole]-5,5'-diyl)bis(4,1-phenylene))bis(azanetriyl))tetrakis(benzene-4,1-diyl))tetrakis(2-cyanoacrylic acid) **D1** in 58% yield, as shown in scheme **5.2.1**.

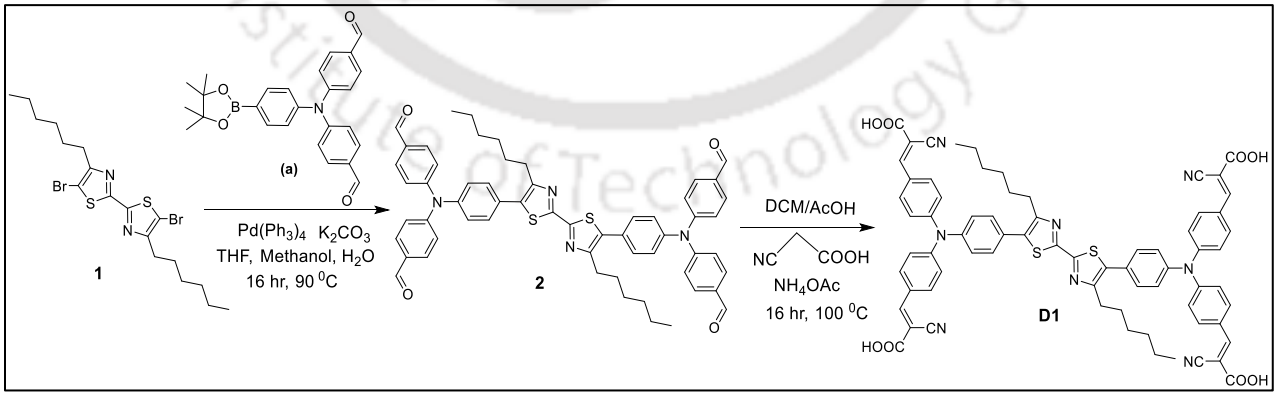


**Scheme 5.2.1.** Synthesis procedure for triphenylamine linked bisthiazole based donor–acceptor dye **D1**.


Part of this chapter has been published in **Electrochim. Acta 2018, 259, 262–275**.

As-synthesized dye **D1** was well characterized by $^{1}H$, $^{13}C$–NMR, and HRMS techniques. $^{1}H$ NMR (400 MHz, DMSO-$d_6$): δ = 8.29 (s, 4H), 8.04, (s, 4H), 7.97 (d, *J* = 8 Hz, 4H), 7.32 (d, *J* = 12 Hz, 4H), 7.22 (d, 8H), 2.86 (t, 4H), 1.73 (t, 4H), 1.31 (m, 12H), 0.85 (t, 6H) ppm. $^{13}C$ NMR (100 MHz, DMSO-$d_6$): δ = 172.56, 163.59, 157.75, 153.93, 148.50, 133.92, 131.57, 131.06, 128.75, 125.90, 123.95, 119.94, 31.33, 29.43, 29.33, 28.63, 22.44, 14.38 ppm. HRMS (ESI-TOF): m/z calculated for $C_{70}H_{58}N_8S_2O_8$ 1203. 3892; [M+H] found 1203.3897.

### 5.2.3 FABRICATION OF PHOTOANODES AND DEVICES

All photoanodes were fabricated by depositing a thin film of ZnO seed solution on precleaned FTO glass substrates. ZnO seed solution was prepared by dissolving 0.20 g of zinc acetate and 55 μL of ethanolamine in 3.0 mL of 2-methoxyethanol followed by overnight stirring. As-prepared ZnO seed solution was then filtered through PTFE membrane filter (0.2 μm). Filtered ZnO solution was spin coated on the FTO and then heated at ~ 200 °C for 15 min. A homogenous paste of both ZnO heterostructures were prepared and deposited it over the ZnO seeded FTO glass substrates. ZnO paste was prepared with terpineol and ethanolic solution of ethocel to get uniform paste. As prepared uniform paste was deposited on FTO substrates via doctor blade method and the films were dried in hot air at 90 °C for 20 min. After that as-deposited ZnO films were calcined at 450 °C for 40 min to remove the organic impurities. The measured thickness of the ZnO layer was in range of around ~ 9–12 μm. These substrates were then dipped into 0.3 mM dye; **D1** solution in Acetonitrile: ethanol (1:1) for 3 h at room temperature. Sensitized photoanodes were removed from dye solution, rinsed with same solvent and dried in hot air blow. Photovoltaic device was assembled by fitting the photoanode and counter electrode. Counter electrode was fabricated by spin coating of chloroplatinic acid (2mg/mL in isopropanol) solution on a FTO substrate and then calcined at 450 °C for 40 min in a furnace. The electrolyte solution was introduced between the sandwiched devices. The $I^-/I_3^-$ electrolyte solution was prepared by using previously reported protocol.[18] The active area for all fabricated devices was fixed and found to be 0.16 $cm^2$. Before the photovoltaic measurements, the fabricated devices were kept under dark condition for 24 h.


Part of this chapter has been published in **Electrochim. Acta 2018, 259, 262–275**.

## 5.3 RESULTS AND DISCUSSIONS

### 5.3.1 POWDER X-RAY DIFFRACTION ANALYSIS

Phase purity and crystal structure of both the synthesized materials are investigated by Powder X-ray diffraction (PXRD) analysis and the corresponding diffraction patterns are depicted in figure **5.3.1**. The diffractogram of both type of ZnO heterostructures show (10$\bar{1}$0), (0002), (10$\bar{1}$1), (10$\bar{1}$2), (11$\bar{2}$0), (10$\bar{1}$3), (20$\bar{2}$0), (11$\bar{2}$2), and (20$\bar{2}$1) crystal planes and defined to the formation of wurtzite type hexagonal phase with cell constants of a = 0.3249 nm and c = 0.5205 nm and the space group symmetry is $P6_3mc$ according to the JCPDS Card No. 36-1451.There is no extra diffraction peak from any type of impurity detected in both diffractogram which suggests that both material are pure and have good crystallinity. These diffraction patterns demonstrate the textural effect of the morphology and specific orientation of building blocks based on the relative intensity of the diffraction peaks. However, altering the surface energy of the crystal planes along c-axis should be an effective way to modulate the growth behaviour of ZnO nanostructures to obtain different morphological structures.

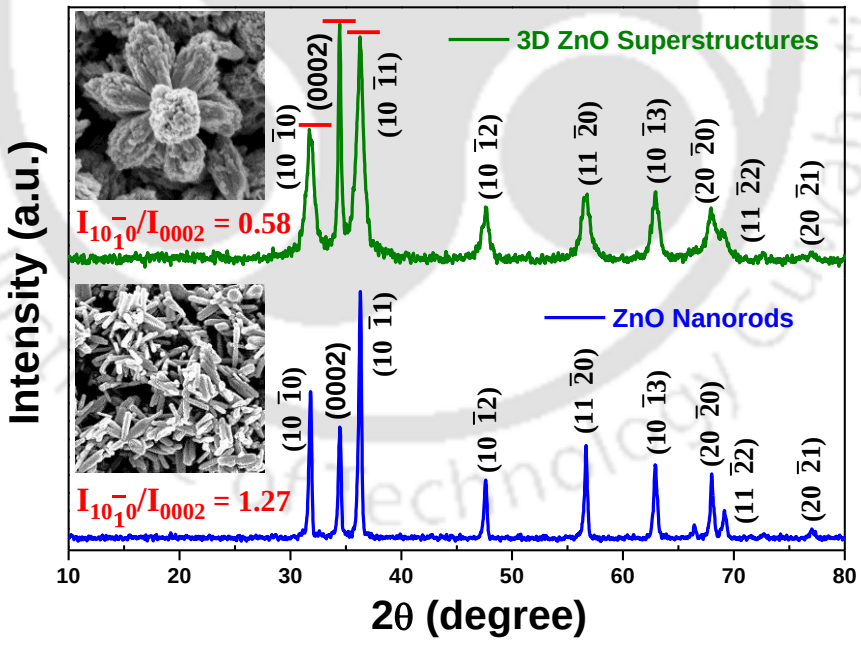


**Figure 5.3.1** Powder X-ray diffraction (PXRD) patterns of both ZnO materials**,** synthesized under different reaction conditions i.e., in presence of both polygalacturonic acid as well as $NH_3$•$H_2O$ (olive line) and only $NH_3$•$H_2O$ (blue line). Inset of this figure represents the relative intensity ratio of (10$\bar{1}$0) to (0002) crystal planes along with field emission scanning electron microscopy (FESEM) images of both type of ZnO heterostructures.


Part of this chapter has been published in **Electrochim. Acta 2018, 259, 262–275**.

Templating agent (Polygalacturonic acid in current synthesis) is utilised to decrease the surface energy of specific crystal planes through strong electrostatic interactions between the ions of the templating agent and the polar surfaces of ZnO. In the diffractogram, we have noticed the intensity variation of the diffraction peaks for crystal planes (1010), (0002) and (1011) in both the heterostructures, indicating a differential growth behaviour of ZnO crystals under different reaction conditions. Relative intensity ratios of (1010) to (0002) crystal planes are varied significantly for both types of ZnO structures. A smaller value of ratio of (1010)/(0002) planes suggest a preferential growth pattern along the c-axis while a higher value of intensity ratio specifies retarded growth along the c–axis.[19–20] We have obtained the lower value of (1010)/(0002) intensity ratio for the ZnO superstructure which is synthesized in presence of polygalacturonic acid and ammonium hydroxide and specifies the anisotropic crystal growth along longitudinal c-axis whereas larger value of intensity ratio in other ZnO structure (ZnO NRs), which is obtained in presence of only ammonium hydroxide, suggests the inhibited growth along c-axis. In this case, expected structures of ZnO should be nanoplatelets and other nanostructures due to presence of fewer number of (0001) crystal planes along c-axis but we have obtained the ZnO NRs. Subsequently, this consideration might be because of the random arrangement of ZnO NRs in the horizontal plane. However, 3–D ZnO superstructures are formed through hierarchically arrangement of several 1–D ZnO NRs, results in increment of the vertically aligned 1–D ZnO NRs which enhanced the intensity of (0002) crystal plane and support the directional growth of the constituent nanorods along the polar axis.

### 5.3.2 MATERIAL MORPHOLOGY

Surface morphologies and textural modification of as-synthesized ZnO heterostructures are investigated by performing Field emission scanning electron microscopy (FESEM) and Transmission electron microscopy (TEM) analysis. In figure **5.3.2**, FESEM images **(a-d)** demonstrate the morphological features of as-synthesized 3–D ZnO hierarchical superstructures at different magnifications. We have noticed that as-synthesized 3–D ZnO superstructures consist of multi- and connected-cage like superstructures, display in FESEM images. The average dimension of as fabricated multi-cage ZnO superstructure is observed in the micron range. Higher magnified FESEM image **(d)** is illustrated that the as-synthesized superstructure is composed of hierarchically arranged 1–D ZnO nanocrystals and these nanocrystals are well

 Part of this chapter has been published in **Electrochim. Acta 2018, 259, 262–275**.

oriented toward the same crystal axes in accordance to the oriented attachment mechanism. The highly directional integration of nanocrystals is determined by the hydroxyl and carboxylic groups, originating from the surface of polygalacturonic acid.

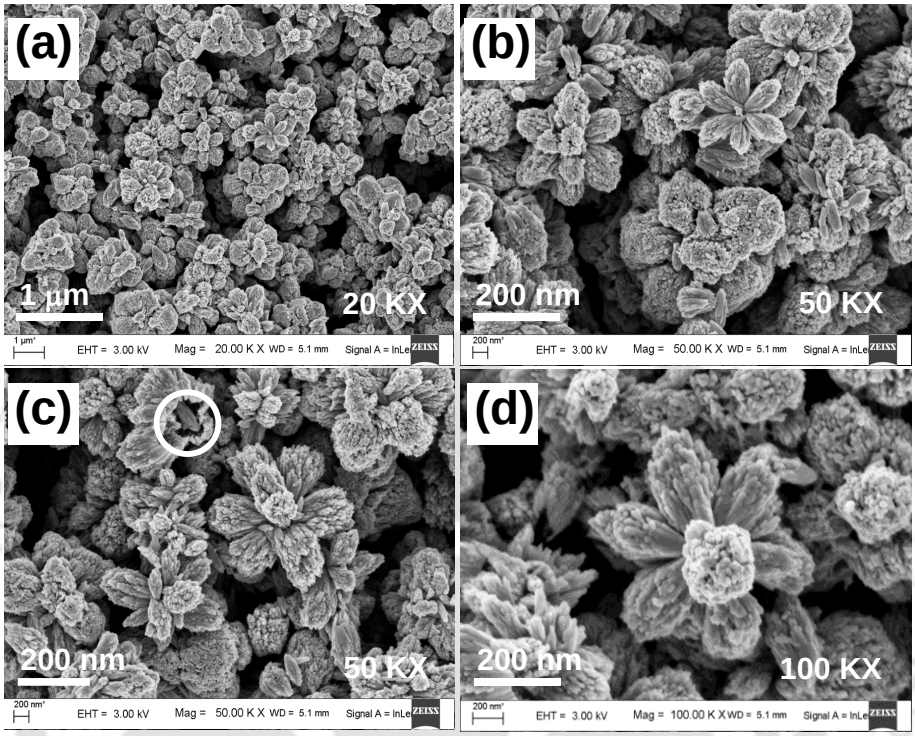


**Figure 5.3.2** Traces **(a-d)** represent the Field emission scanning electron microscopy **(**FESEM) images of as-synthesized 3–D ZnO hierarchical superstructures at different magnifications.

From FESEM image **(c)**, several broken superstructures are also observed, originating due to breakage of multi-cage superstructure at the adjoining points. Subsequently, a void is created due to the rupturing of cages and divulges the hollow nature of the material. These broken cages has been further supported that the ZnO superstructures are fabricated through the integration of the numerous 1–D ZnO NRs. During the attachment of the nanorods with different lengths, pores are formed in between the nanocrystals which infer the meso-porous characteristics of the superstructures. Moreover, we observed that the assembling units i.e., 1–D ZnO NRs of superstructure are fused well to each other and improved the inter-particle electrical connectivity. As a result, there is an enhancement in the current density ($J_{sc}$) value due to better transport of the photogenerated charge carriers in a solar device. We have also carried out TEM analysis to demonstrate the structural features of as-synthesized 3–D ZnO HSs. In figure **5.3.3**, TEM images **(a-c)** illustrate the as-synthesized connected and multi-cage like superstructures.


Part of this chapter has been published in **Electrochim. Acta 2018, 259, 262–275**.

The average dimensions of as fabricated multi-cage ZnO superstructures are observed to be in the range of ~ 1–4 μm, similar as in FESEM analysis. Image **(c)** depicts the lateral connection of two single caged structures which indicate the intimated interfacial contact to each other and helpful for better transport of the photogenerated electrons by minimizing the trap sites between these structures. From TEM images, it is confirmed that as-synthesized superstructure is formed by joining of the several single cages to each other to a single adjoin point.

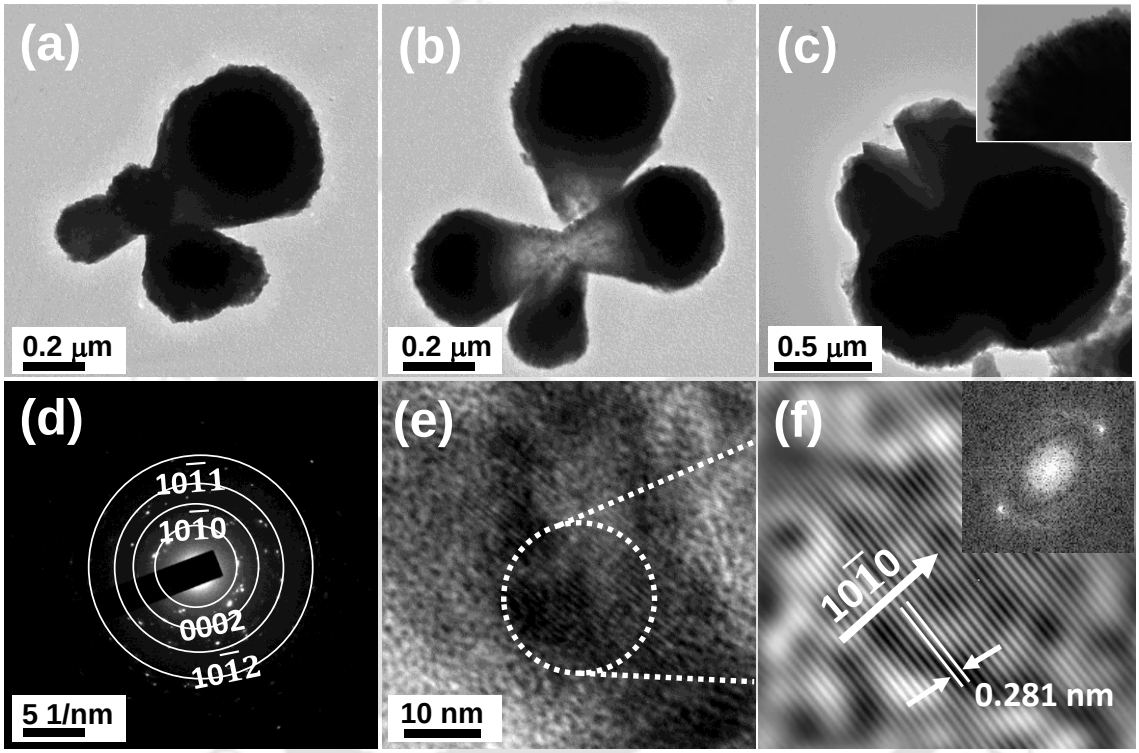


**Figure 5.3.3** Transmission electron microscopy (TEM) images **(a-c)** show the morphological features of as-synthesized 3–D ZnO hierarchical superstructure. Trace **(d)** depicts the selected area electron diffraction (SAED) pattern while trace **(e)** represents the High resolution transmission electron microscopy (HRTEM) image of the ZnO hierarchical superstructure. Trace **(f)** shows Inverse fast Fourier transform (IFFT) of selected portion for the image **(e)** with corresponding fast Fourier transform (FFT) in the inset.

In addition, as fabricated ZnO superstructure is formed by assembling of numerous tiny nanorods, shows in higher magnified TEM image [as inset of image **(c)**]. Image **(d)** represents the selected area electron diffraction (SAED) pattern for 3–D ZnO superstructure, showing the diffraction rings pattern which infers the polycrystalline nature of the ZnO Structure. SAED pattern is describing the wurtzite crystalline structure and crystal growth anisotropy of the ZnO which is consistent with the PXRD analysis. High resolution TEM (HRTEM) image **(e)** of 3–D ZnO superstructure shows the presence of well distinct lattice fringes. Inverse fast Fourier

transform (IFFT) analysis is performed for the circled part of image **(e)**, as shown in trace **(f)**. Lattice fringes with the interplanar distance of about ~ 0.281 nm, can be assigned for $(10\bar{1}0)$ crystal planes. The corresponding fast Fourier transform (FFT) pattern [inset of trace **(f)**] consists of highly symmetrical diffraction dots, revealing the single-crystalline nature of the 1-D nanocrystals (ZnO NRs).

Surface morphology and structural features of the ZnO material, synthesized in the absence of polygalacturonic acid are analyzed by FESEM and TEM analysis, depicted in the figure **5.3.4**.

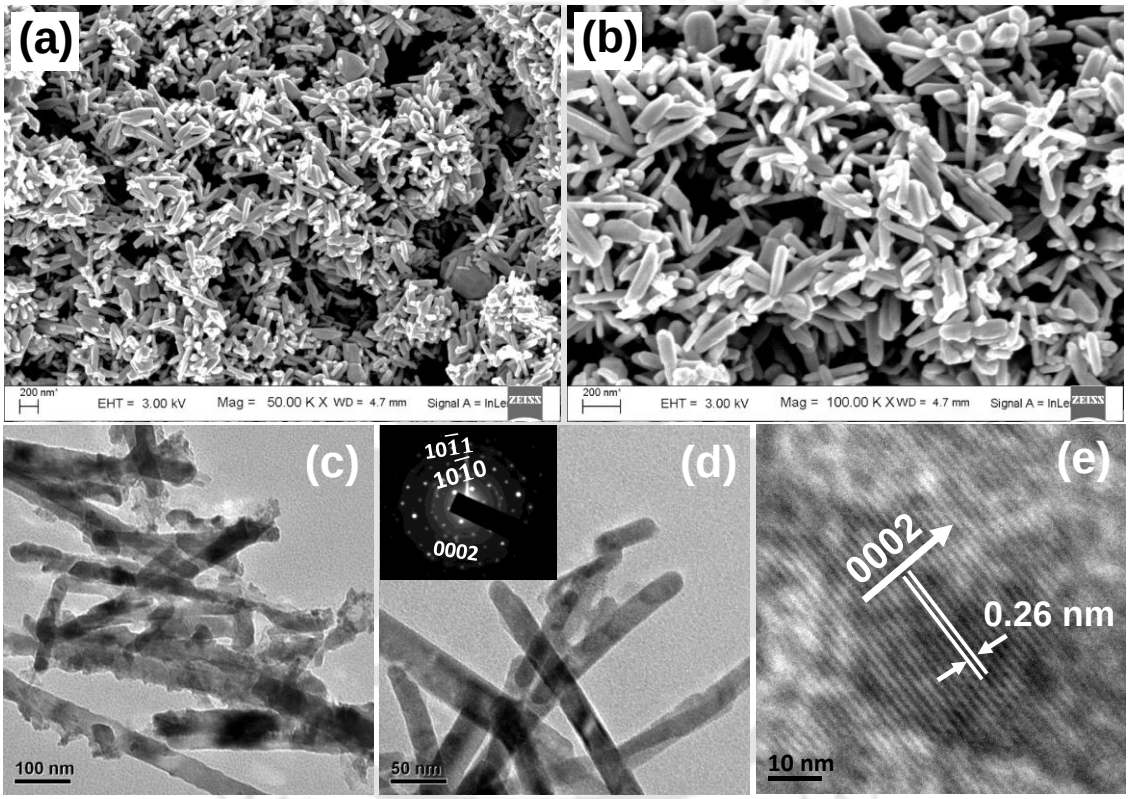


**Figure 5.3.4** Field emission scanning electron microscopy (FESEM) images **(a-b)** show morphological features of 1–D ZnO NRs at different magnifications. Transmission electron microscopy (TEM) images **(c-d)** display the structural features of 1–D ZnO NRs at different magnifications. Inset of TEM image **(d)** depicts the selected area electron diffraction (SAED) pattern while trace **(e)** represents the high resolution transmission electron microscopy (HRTEM) image of the 1-D ZnO NRs.

From the figure **5.3.4**, FESEM images **(a)** and **(b)** display the morphological features of as-synthesized ZnO sample at different magnifications. In absence of biotemplate, 1–D nanorods (NRs) of having different particle sizes are obtained. To investigate the structural features of as-synthesised ZnO in the absence of anionic polysaccharide, TEM analysis are carried out and


Part of this chapter has been published in **Electrochim. Acta 2018, 259, 262–275**.

presented in the figure **5.3.4**. TEM images **(c)** and **(d)** of figure **5.3.4** elucidate the formation of 1–D NRs at different magnifications, showing the non-uniform particles size distribution. The average dimensions of as-obtained 1–D ZnO NRs are in the range of about ~ 200–800 nm in length and ~ 30–60 nm in width respectively. Inset of TEM image **(d)** display the SAED pattern for 1–D ZnO NRs, exhibiting the diffraction dot ring patterns, suggests the polycrystalline nature of the sample. From the HRTEM analysis [image **(e)**], we have noticed the well distinct lattice fringes with the interplanar d-spacing value of about ~ 0.26 nm which is correspond to (0002) crystal planes of as-synthesised 1–D ZnO NRs.

### 5.3.3 GROWTH MECHANISM OF 3–D ZnO SUPERSTRUCTURES

As per the morphological analysis, the probable mechanism for the fabrication of 3–D ZnO hierarchical superstructures under controlled reaction conditions is illustrated in **Scheme 5.3.1**. In this synthetic protocol, we have used a biotemplate "**Polygalacturonic acid**" as an assembling agent of basic building blocks to fabricate the hierarchical superstructures. Polygalacturonic acid is a naturally occurring water soluble anionic polysaccharides, extracted from plant cell walls and the chemical structure of this homopolymer consists a backbone chain of 1,4–linked D–galacturonic acid units. It is well established that the growth process of the hierarchical superstructures can be controlled by two process viz. nucleation and the crystal growth at the assembling step. The growth mechanism for assembling of nanocrystals into microstructure is explained based on particle aggregation.[21–22] In this case; polygalacturonic acid is firstly dissolved in the aqueous medium and generates negative charged ions in the solution due to presence of hydroxyls and carboxylate groups. After that, Zn salt is added into above solution and releases the $Zn^{2+}$ ions in solution. Therefore, there is an electrostatic interaction between the negatively charged biotemplate and the inorganic ions (positively charged $Zn^{2+}$) and form an adduct ($Zn^{2+}$–Polygalacturonic acid) in the reaction mixture.[23] Addition of liquid ammonia ($NH_3 \bullet H_2O$) is responsible to change the pH of the reaction mixture and instantaneously generated a white precipitate, probably related to $Zn(OH)_2$. Liquid ammonia is further added into the reaction mixture until the white precipitate turns into colorless solution, attributed to the formation of water soluble $Zn(OH)_4^{2-}$ and $Zn(NH_3)_4^{2+}$ ions which are still attached to anionic polysaccharide chain in form of adduct 2.[24] $Zn(OH)_4^{2-}$ and $Zn(NH_3)_4^{2+}$ ions act as the crystal growth units for the formation of ZnO building blocks.

 Part of this chapter has been published in **Electrochim. Acta 2018, 259, 262–275**.

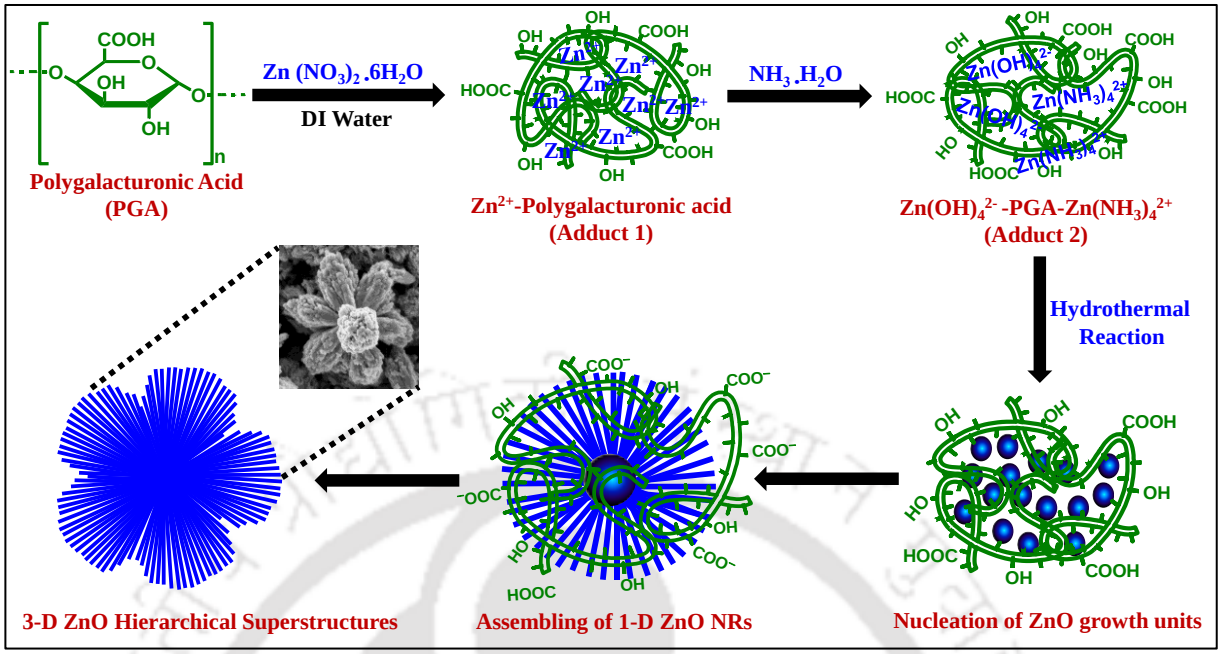


**Scheme 5.3.1** Schematic illustration of possible mechanism for biotemplate "Polygalacturonic acid" assisted synthesis of 3–D ZnO hierarchical superstructures.

Under the hydrothermal reaction, these growth units are transformed into the ZnO nuclei. Generally, the crystal growth units of ZnO have the tendency to grow along the c-axis by minimizing the surface energy. It is established that ZnO crystal possesses the (+0001) positive crystal surface and (–0001) negative crystal surface, attributed to the $Zn^{2+}$ populated and $O^{2-}$ populated high energy polar facets respectively. So, the crystal growth units i.e., zincate ions ($Zn(OH)_4^{2-}$) are favourably attached to the (+0001) positive surface of ZnO crystal, which encourage the formation of ZnO nanorods along the c-axis direction.[25] Therefore, the growth rate of ZnO crystal is considered to be faster in (+0001) positive crystal surface as compared to (–0001) negative crystal surface, indicative of $Zn(OH)_4^{2-}$ ions are major growth units for the ZnO crystal. In this growth mechanism, negatively charged biotemplate i.e., polygalacturonic acid is accountable for the suppressed growth of ZnO NRs along the c-axis, resulted in formation of non-uniform dimensions of nanocrystals. During the fabrication process, polygalacturonic acid not only acts as a template for the formation of ZnO nanorods, but also assists as an assembling agent to fabricate the hierarchical superstructures. After the complete nucleation of crystal from the precursor, the negatively charged biotemplate initiates the assembling of building blocks and arrange them in a three-dimensional array to form 3–D ZnO superstructures.


Part of this chapter has been published in **Electrochim. Acta 2018, 259, 262–275**.

As the reaction proceeds, multi-cage and connected cage like super-structures are formed and appear to be adjoined to a single point.

### 5.3.4 UV–VISIBLE DIFFUSE REFLECTANCE SPECTRA

Optical properties of as-synthesized heterostructures are investigated by analyzing the normalized UV–visible (UV–Vis) absorption spectra, recorded in the scan range of 200–800 nm as shown in figure **5.3.5 (A)**. Absorption onset of as-synthesized 3–D ZnO superstructures and 1–D ZnO NRs are noticed at ~ 381 nm and ~ 396 nm which correspond to the energy band gap of ~ 3.25 eV and ~ 3.13 eV respectively. We have noticed a reasonable blue shift (~ 15 nm) in the absorption profile of 3–D ZnO superstructures as compared to 1–D ZnO NRs. As observed hypsochromic shift in case of ZnO superstructures is mainly due to the assembling of discrete nano-sized 1–D ZnO NRs which are smaller as compared to other structure having particle size of about ~1–2 µm.

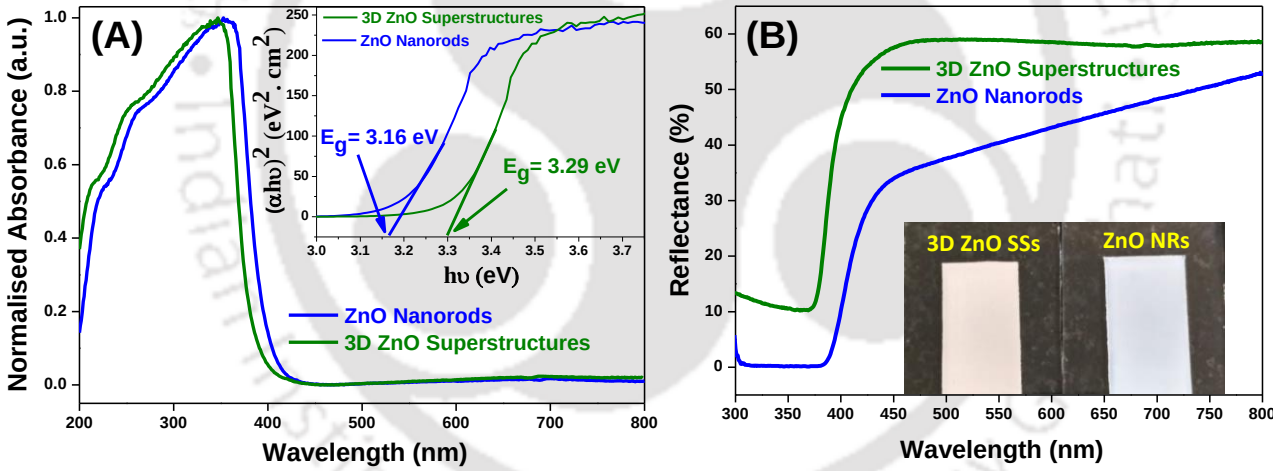


**Figure 5.3.5** Plot **(A)** represents the Normalized UV–visible absorption spectra of 3–D ZnO superstructures (olive line) and 1–D ZnO NRs (blue line) while inset of this figure depicts the corresponding Tauc's plots. Plot **(B)** shows Diffused reflectance spectra of both ZnO heterostructures (3–D ZnO HSs and 1–D ZnO NRs) based films with similar thickness while inset of same figure displays the digital photographs of both films.

Inset of figure **5.3.5 (A)** represents the corresponding Tauc's plots to estimate the optical band gap values for both the photoanodic materials, where $(\alpha h\upsilon)^2$ is plotted against the photon energy ($h\upsilon$) and band gap energies are calculated from the extrapolated lines to x-axis. From the Tauc's plots, calculated optical band gap energies for 3–D ZnO superstructures and 1–D ZnO NRs are found to be ~ 3.29 eV and ~ 3.16 eV respectively which are well consistent with the


Part of this chapter has been published in **Electrochim. Acta 2018, 259, 262–275**.

values observed from absorption spectra. As observed blue shift in the absorption profile of ZnO superstructures with respect to ZnO NRs is well supported with the shift in the estimated band gap energies. Despite of having inadequacy in terms of visible light absorption, 3–D ZnO superstructures based solar device will exhibit the better photovoltaic performance because of its high aspect ratio and excellent charge transport properties. To probe the light scattering effect in both types of ZnO heterostructures, reflectance measurements are carried out by fabricating the photoanodic films on FTO glass substrate of comparable thickness, depicted in figure **5.3.5 (B)**. We have noticed the higher reflectance value in case of 3–D ZnO superstructures as compare to 1–D ZnO NRs in the wavelength range of 450–700 nm, indicative of more utilization of incident photons and enhanced the repeated excitation process of sensitizer molecules on the photoanodic film of ZnO superstructures. Hollow nature (due to breakage of multicage superstructure) of 3–D ZnO superstructure is ascribed for the efficient light scattering which is not observed in other structure i.e., 1–D ZnO NRs. Better light harvesting ability of 3–D ZnO superstructure will establish a critical role in the enhanced photovoltaic performance of superstructures based solar device.

### 5.3.5 STEADY STATE AND TIME RESOLVED PHOTOLUMINESCENCE ANALYSES

Figure **5.3.6 (A)** shows the steady state photoluminescence (PL) spectra for both the morphological structures of ZnO, synthesized under control reaction conditions and recorded at an excitation wavelength of 325 nm. From steady state PL spectra, we can see a characteristics PL emission peak in UV region along with a strong peak at around ~ 466 nm and a weak intense peak at around ~ 564 nm for both the heterostructures. As observed emission peak in the UV range is mainly accredited to the radiative recombination of the excitons at near-band-edge of ZnO crystal.[26] There are several shoulder peaks in range of about ~ 410–450 nm along with a strong sharp peak at ~ 466 nm are related to the recombination of excitons at the interstitial sites of zinc vacancy ($Zn^{2+}$ interstitial sites) of the ZnO structures. The emission peak is noticed in the visible region (~ 564 nm), is associated to presence of intrinsic or extrinsic defects, generated by oxygen vacancies in the ZnO crystal structure.[27] It is known that ZnO is an intrinsic n-type semiconductor so several emission peaks are originated in visible region, attributed to the crystal defects in the ZnO crystal, such as zinc vacancy and oxygen interstitial sites.


Part of this chapter has been published in **Electrochim. Acta 2018, 259, 262–275**.

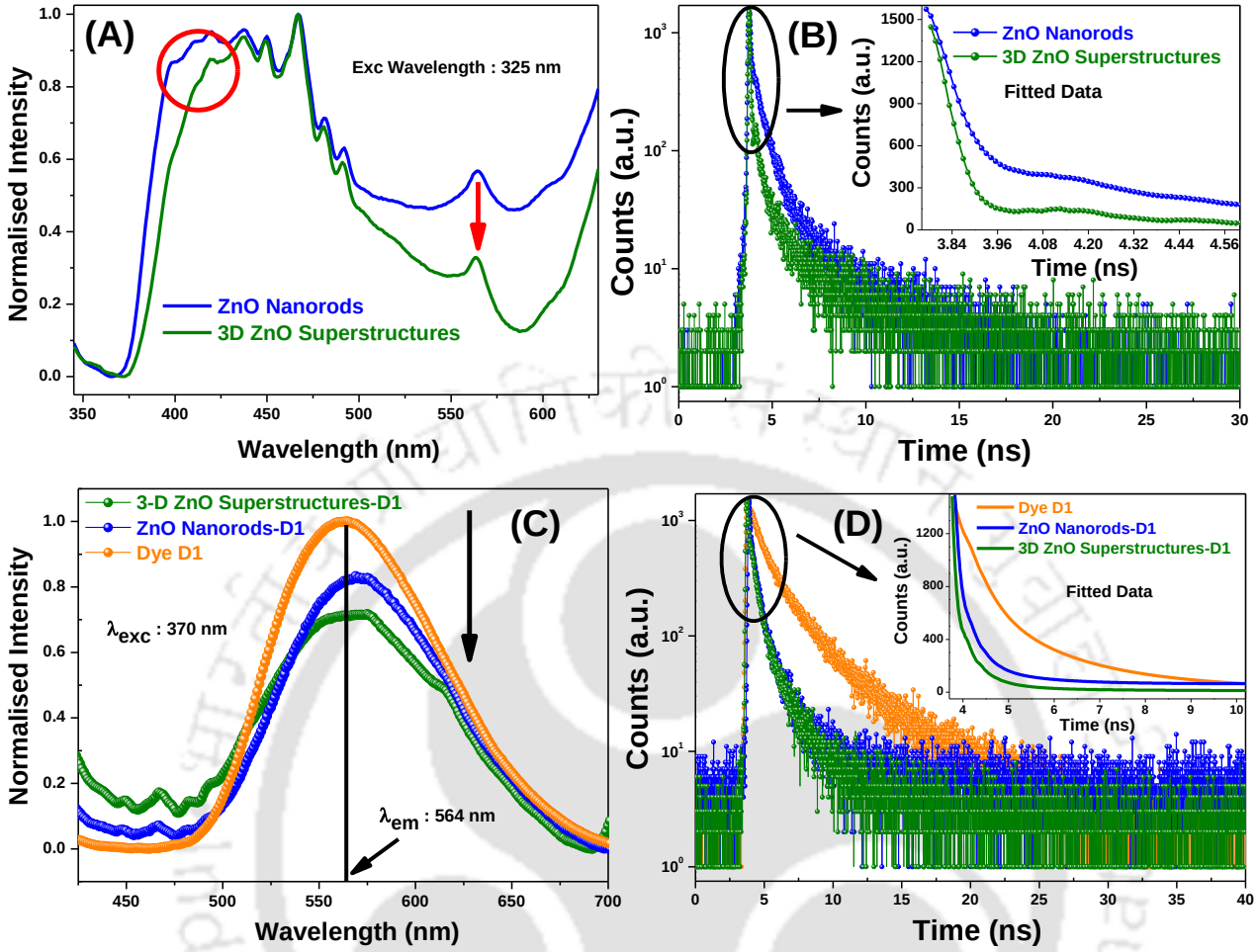


**Figure 5.3.6 (A)** Normalized Steady-state fluorescence spectra of both ZnO heterostructures [3–D ZnO HSs (olive line) and 1–D ZnO NRs (blue line)] at an excitation wavelength of 325 nm while figure **5.3.6 (B)** represents time-resolved photoluminescence (TRPL) spectra for same heterostructures at an excitation wavelength of 337 nm. **(C)** Normalized Steady-state fluorescence spectra of dye; D1 (orange line), 3–D ZnO HSs–Dye; D1 (olive line) and 1–D ZnO NRs–Dye; D1 (blue line) at an excitation wavelength of 370 nm. **(D)** Time-resolved photoluminescence (TRPL) spectra for the dye; D1 (orange line), 3–D ZnO HSs–Dye; D1 (olive line) and ZnO NRs–Dye; D1 (blue line) at an excitation wavelength of 375 nm.

Steady state PL spectra shows a gradual static quenching of PL intensity for 3–D ZnO superstructures as compared to 1–D ZnO NRs which indicates the inhibited electron–hole recombination and enhanced charge separation, later confirmed by TRPL study. Subsequently, the intensity of the emission peak due to oxygen defect sites is lower for ZnO superstructures relative to ZnO NRs which is a clear reflection of having lower population of defect sites in ZnO superstructures as compared to the ZnO NRs. Therefore, there is an improvement in the crystal quality of ZnO Superstructures due to lesser structural defects and oxygen vacancies, which is beneficial for the enhanced photovoltaic properties.


Part of this chapter has been published in **Electrochim. Acta 2018, 259, 262–275**.

To examine the further insights of excited state charge transport kinetics in both ZnO heterostructures, time resolved photoluminescence (TRPL) measurements are performed, fabricating thin films for both the samples on glass substrate and using a 337 nm diode excitation source, as shown in figure **5.3.6 (B)**. PL decay patterns are fitted with a tri-exponential function using fast software provided by Edinburgh instruments to calculate the value of average exciton lifetime. Observed multi-exponential decay patterns revealed various processes, which are involved during the decay of emissive excitons. The values of fitting parameter ($\chi^2$) and detailed spectroscopic results such as, exciton lifetimes ($\tau_1$, $\tau_2$, $\tau_3$), pre-exponential factors ($\alpha_1$, $\alpha_2$, $\alpha_3$), average exciton lifetimes ($<\tau>$) etc. are summarized in the table **5.3.1**. The average lifetime values are derived from **equation (1)**:[28]

$$<\tau>=\frac{\alpha_1 \tau_1^2+\alpha_2 \tau_2^2+\alpha_3 \tau_3^2}{\alpha_1 \tau_1+\alpha_2 \tau_2+\alpha_3 \tau_3} \qquad (1)$$

We have noted faster decay pattern for 3–D ZnO HSs with respect to 1–D ZnO NRs, suggesting the better charge transport dynamics in superstructures. Based on earlier explanation, crystal structure of 1–D ZnO NRs has more density of structural defect sites, act as trap sites for radiative recombination of photoexcited electrons and get the higher value of exciton lifetime. Thus, different photoluminescence behaviour of the 3–D ZnO HSs and 1–D ZnO NRs in visible region would be correlated to the atomic structure at the surface of the crystal.

To investigate the excited state electronic interactions between ZnO heterostructures and dye; **D1**, room temperature steady-state photoluminescence (PL) spectra of dye as well as composites are recorded at an excitation wavelength of 370 nm corresponds to dye; **D1**, as shown in figure **5.3.6 (C)**. From the Spectra, as-synthesised bisthiazole linked metal free donor–acceptor dye; **D1** exhibits the typical emission of around ~ 564 nm while a slight red shifts (~ 10–15 nm) is noticed in the PL emission profile of dye; **D1** after its deposition on the 3–D ZnO HSs and 1–D ZnO NRs, which is ascribed to the strong electronic interactions between dye D1 and ZnO heterostructures. We have observed a significant decrement in the PL intensity, corresponds to dye; D1 when it get adsorbed on the surface of ZnO heterostructures which confirmed the presence of excited-state electronic interactions between dye; **D1** and ZnO structures.


Part of this chapter has been published in **Electrochim. Acta 2018, 259, 262–275**.

**Table 5.3.1** Calculated parameters such as fitting parameter ($\chi^2$), exciton lifetimes ($\tau_1$, $\tau_2$, $\tau_3$) (ns), pre-exponential factors ($\alpha_1$, $\alpha_2$, $\alpha_3$) (%), average exciton lifetimes (<τ>) (ns) for dye; **D1**, 1–D ZnO NRs, 3–D ZnO HSs, 1–D ZnO NRs–dye **D1** and 3–D ZnO HSs–dye **D1** and electron injection rate constants (keinj) ($S^{-1}$) for 1–D ZnO NRs–dye **D1** and 3–D ZnO HSs–dye **D1**are summarized in the following table:

| **Samples** | $\chi^2$ | $\tau_1$ (ns) | $\tau_2$ (ns) | $\tau_3$ (ns) | $\alpha_1$ (%) | $\alpha_2$ (%) | $\alpha_3$ (%) | <τ> (ns) | $K_{einj}$ ($s^{-1}$) |
|---|---|---|---|---|---|---|---|---|---|
| **Dye (D1)** | 1.06 | 0.429 | 1.794 | 5.451 | 18.24 | 53.38 | 28.36 | 3.942 | ------ |
| **1–D ZnO NRs** | 0.99 | 0.111 | 0.657 | 3.697 | 41.30 | 42.87 | 15.82 | 2.645 | ------ |
| **3–D ZnO HSs** | 1.01 | 0.173 | 0.988 | 3.189 | 17.43 | 51.64 | 30.92 | 2.393 | ------ |
| **1–D ZnO NRs– dye (D1)** | 1.15 | 0.099 | 0.589 | 2.499 | 36.94 | 43.91 | 19.13 | **1.746** | **$3.18\times10^8$** |
| **3–D ZnO HSs–dye (D1)** | 1.10 | 0.083 | 0.448 | 1.563 | 36.05 | 34.71 | 29.23 | **1.224** | **$5.66\times10^8$** |

This statement is advocated the photogenerated charge injection from the dye; **D1** to ZnO structures and later will confirmed by electrochemical analysis. We have found the feasible photoexcited electron injection from dye; **D1** (CB edge ~ – 3.14 eV) to the ZnO (CB edge ~ – 4.24 eV). It is noteworthy that static quenching of the PL emission is more in case of 3–D ZnO superstructure as compared to 1–D ZnO NRs which confirmed the efficient charge separation and transport in 3–D ZnO HSs based photovoltaic device.

To investigate the kinetics of photoexcited electron and emission decay patterns of bare dye; **D1** and their composites, Time-resolved photoluminescence (TRPL) measurements are carried out by fabricating the thin films on glass substrate and recorded by using a 375 nm diode laser excitation as a source, as shown in figure **5.3.6 (D)**. All decay patterns are fitted with a tri-exponential function to calculate the average exciton lifetime values (summarised in Table **5.3.1**) using the **equation (1)**. Decay patterns for the composites (dye **D1** anchored on the ZnO structures) are found to be much faster as compared to bare dye; **D1**, indicative of the charge injection from conduction band (CB) of dye to CB of ZnO. From the Table **5.3.1**, calculated average exciton lifetime values for dye; **D1**, dye; **D1**–1–DZnO NRs and dye; **D1**–3–D ZnO HSs are found to be ~ 3.942 ns, ~ 1.746 ns and ~ 1.224 ns respectively. Subsequently, average exciton lifetime of dye; **D1**–3–D ZnO HSs is significantly decreases as compare to dye; **D1**–1–D ZnO NRs, suggesting the enhanced interfacial charge transfer in the 3–D ZnO superstructures based photoanodic film. It is believed to be charge transfer is the only pathway for the


Part of this chapter has been published in **Electrochim. Acta 2018, 259, 262–275**.

deactivation of excited dye; **D1**, so rate constant of electron injection ($k_{einj}$) from dye to ZnO structures is calculated from **equation (2)** and listed in table **5.3.1**:[28]

$$k_{einj} = \frac{1}{<\tau>_{composite}} - \frac{1}{<\tau>_{dye}} \qquad (2)$$

From table **5.3.1**, calculated $k_{einj}$ values for the composites i.e., dye; **D1**–1–D ZnO NRs and dye; **D1**–3–D ZnO HSs are found to be ~ $3.18 \times 10^8$ $s^{-1}$ and ~ $5.66 \times 10^8$ $s^{-1}$ respectively. As observed higher value of $k_{einj}$ for composite, dye; **D1**–3–D ZnO HSs advocated a faster charge injection dynamics in composite and leads to the reduced recombination processes which favour the enhanced photovoltaic performance of superstructures based solar devices.

### 5.3.6 BET SURFACE AREA ANALYSIS, CHEMISORPTION AND NORMALISED DIFFUSED REFLECTANCE UV–VISIBLE ABSORPTION SPECTRA OF PHOTOANODES

Figure **5.3.7 (A)** demonstrates the $N_2$ adsorption–desorption isotherms for ZnO heterostructures prepared under different reaction conditions and inset of this figure shows the corresponding Barrett-Joyner-Halenda (BJH) pore size distribution plot. High surface area and porosity of the photoanodic material are considered to be the significant features, used in the photoanodic segment to improve the performance of photovoltaic device. In the adsorption–desorption isotherm, both structures show the type IV isotherms with H3 hysteresis loops which demonstrate the mesoporous nature of as-synthesized materials. Observed BET surface area for 1–D ZnO NRs and 3–D ZnO HSs are found to be 16 $m^2g^{-1}$ and 42 $m^2g^{-1}$ respectively. As obtained higher BET surface area value of 3–D ZnO HSs is accountable to offer more adsorption sites for sensitizer loading, leading to a better light harvesting ability. From the pore-size distribution curves, we have noticed the broad pore size distribution for 3–D ZnO superstructures which is in the range of ~10–30 nm whereas there is no sign of pores in case of 1–D ZnO NRs. Broad pore size distribution is noticed for ZnO superstructure is possibly due to existence of inter void spaces in nanocrystals, assembled to each other to form hierarchical 3–D structure.


Part of this chapter has been published in **Electrochim. Acta 2018, 259, 262–275**.

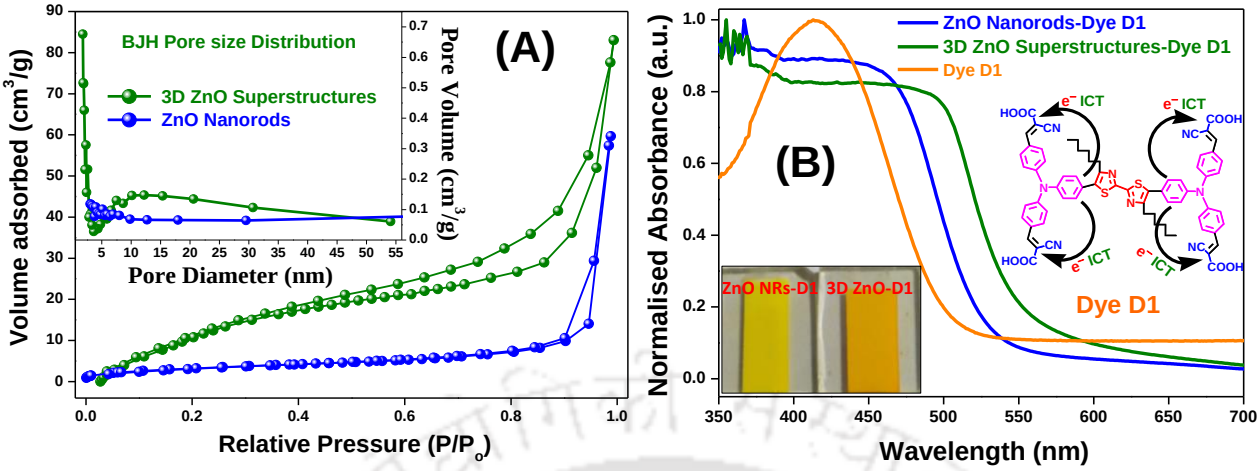


**Figure 5.3.7 (A)** Nitrogen adsorption–desorption isotherm and Barrett-Joyner-Halenda (BJH) pore size distribution plot (inset) for 3–D ZnO superstructures (olive line) and 1–D ZnO NRs (blue line) respectively. **(B)** Normalised diffused reflectance UV–Vis absorption spectra of bare dye **D1** (orange line), dye; D1 sensitized photoanodes based on both ZnO heterostructures [3–D ZnO HSs–Dye; **D1** (olive line) and 1–D ZnO NRs–Dye; **D1** (blue line)]. Inset of figure **5.3.7 (B)** shows the intramolecular charge transfer phenomenon in dye **D1** and digital photographs of dye sensitized photoanodes.

Chemisorption of dye molecules are accomplished for the quantitative estimation of adsorbed dye on the photoanodic materials. To calculate the amount of adsorbed dye, the dye sensitized photoanodic films with fixed area (1×1 $cm^2$) are rinsed in acetonitrile to remove residual dye and then immersed into 0.1 mM NaOH solution [Ethanol: Water, 1:1, v/v, (pH ~9)] for at least 4 h to completely removal of the dye.[29] After complete desorption of the dye, UV–Vis absorption spectra of same solution is recorded and calculated the concentration of the desorbed dye per $cm^2$ area by using Beer's law. It is observed that the photoanode based on 1–D ZnO NRs is showed the quantity of loaded dye of ~ $0.321 \times 10^{-7}$ mol $cm^{-2}$ while ~ $0.663 \times 10^{-7}$ mol $cm^{-2}$ for 3–D ZnO HSs. Higher dye loading is observed for the 3–D ZnO HSs relative to 1–D ZnO NRs, attributed to large BET surface area for ZnO hierarchical superstructure (~ 42 $m^2g^{-1}$) compared to ZnO NRs (~ 16 $m^2g^{-1}$).

Figure **5.3.7 (B)** depicts the diffused reflectance UV–Vis absorption profiles for bare dye; **D1** (orange line) and dye **D1** sensitized photoanodes which are fabricated with as-synthesized 3–D ZnO superstructures (olive line) and 1–D ZnO NRs (blue line), recorded in the scan range of 350–700 nm against blank FTO as a reference. Absorption onset of bare dye **D1** is found to be at ~ 524 nm which corresponds to the energy band gap of ~ 2.36 eV. Dye **D1** is exhibited a broad absorption bands in the visible region which is attributed to the intramolecular charge transfer


Part of this chapter has been published in **Electrochim. Acta 2018, 259, 262–275**.

from donor (triphenylamine) to acceptor moiety (cyanoacetic acid), as illustrated in inset of figure **5.3.7 (B).** Estimated value of molar extinction coefficient of dye **D1** (~ $1.02\times10^5$ $Lmol^{-1}$ $cm^{-1}$, at 439 nm) is higher than the conventional ruthenium based sensitizer i.e., N719 (e.g., ~ $1.39\times10^4$ $Lmol^{-1}$ $cm^{-1}$),[30] indicating that dye has good light-harvesting ability. Absorption range for dye sensitized photoanodes is noticed in the visible region of 350–550 nm which indicate the successful adsorption of dye **D1** onto the photoanodic scaffolds. Furthermore, we have noticed a significant red shift in the absorption onset of ZnO superstructure based photoanode in contrast to ZnO NRs based photoanode which may be due to the higher loading of sensitizer molecules in the photoanode. This observation confirms the statement of upsurge the sensitizer loading capability of a material with the higher surface area. Therefore, ZnO superstructures offer more adsorption sites for sensitizer loading so the observations are well consistent with surface area analysis. As deposition of more amount of dye, light harvesting ability of photoanode gets improved and the flux of photogenerated electrons will be higher which enhance the efficiency of photovoltaic device.

### 5.3.7 ELECTROCHEMICAL AND COMPUTATIONAL STUDY OF DYE D1

Electrochemical behaviour of the triphenylamine linked bisthiazole based donor–acceptor dye **D1** is demonstrated by performing the cyclic voltammetric analysis in dry dichloromethane (DCM) solution at room temperature, using tetrabutylammonium hexafluoro phosphate ($TBAPF_6$) as a supporting electrolyte and representative cyclic voltammogram is depicted in figure **5.3.8**. As obtained cyclic voltammogram of dye **D1** shows one reversible oxidation wave related to triphenylamine group and one reversible reduction wave correspond to bisthiazole group. From voltammogram, estimated values for oxidation potential and reduction potential are found to be ~ 0.68 V and ~ –1.66 V respectively. As obtained oxidation potential and reduction potential are converted to the corresponding highest occupied molecular orbital (HOMO) [using $E_{HOMO} = -(E_{onset,\ ox} - E_{1/2,\ Ferrocene} + 4.8)$ eV] and lowest unoccupied molecular orbital (LUMO) [using $E_{LUMO} = -(E_{onset,\ red} - E_{1/2,\ Ferrocene} + 4.8)$ eV] energy levels. The Calculated HOMO and LUMO energy levels of the dye D1 are found to be − 5.48 eV and − 3.14 eV respectively and estimated electrochemical band gap [$E_g$ (eV) = $E_{HOMO} - E_{LUMO}$] is around 2.34 eV. The HOMO energy level of dye **D1** (− 5.48 eV) is more negative as compared to $I^-/ I_3^-$ redox electrolyte ($E_{redox} \approx -4.90$ eV) which favours a faster regeneration of the dye while the LUMO energy level


Part of this chapter has been published in **Electrochim. Acta 2018, 259, 262–275**.

of dye **D1** (− 3.14 eV) is more positive than the conduction band of ZnO (− 4.24 eV), which facilitate the efficient photogenerated electron injection from LUMO of the dye to the CB of ZnO heterostructures, as shown in inset of figure **5.3.8**.

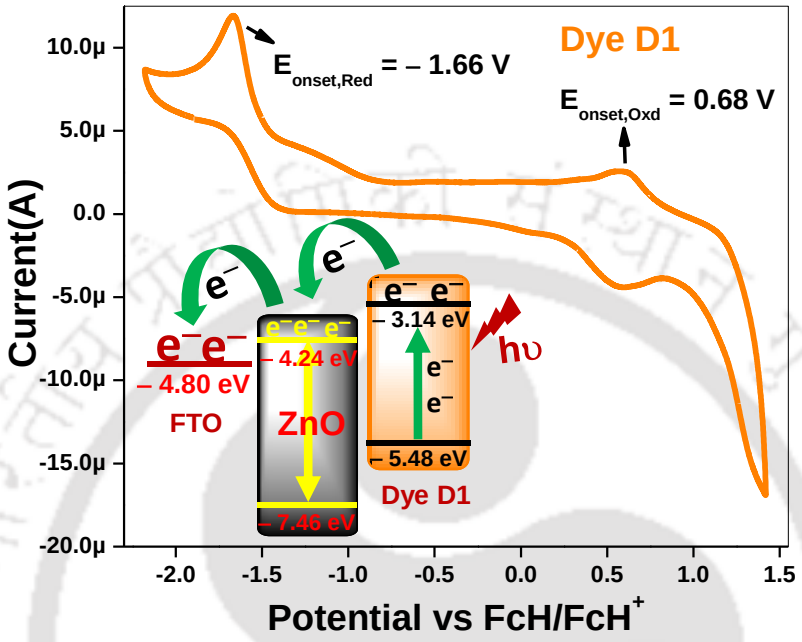


**Figure 5.3.8.** Cyclic voltammogram of dye **D1** ($1.0 \times 10^{-4}$ M) in DCM is recorded at a scan rate of 100 $mVs^{-1}$ while inset illustrate the feasible pathway for the photoexcited electron transfer from LUMO of dye **D1** to the CB of ZnO.

For better understanding of electronic structure, electrochemical and photophysical properties of the dye **D1**, the density functional theory (DFT) and time dependent density functional (TD–DFT) calculations are performed using the Gaussian 09 program. The optimization and solvent calculations are carried out in the dichloromethane (DCM) using the polarized continuum model (CPCM) of Gaussian 09 software and used 6-31G** basis set for C, N, H, O, S for all the calculations.[31–32] Vibrational frequency analyses are carried out to confirm the optimized structure of the dye. The ground state optimized structure along with the frontier molecular orbitals, namely, HOMO, HOMO−1, LUMO, and LUMO+1, are presented in figure **5.3.9 (A)** and **(B)** respectively. As we can see the electronic distributions at ground states (HOMO and HOMO−1 levels) are primarily localized on the triphenylamine and bisthiazole moieties, whereas the electronic distributions at excited states (LUMO and LUMO+1 levels) are on the acceptor moiety i.e., cyanoacrylic acids. As distinct electronic distribution from the HOMO to LUMO levels indicate the good separation of photoexcited electrons and holes in the


Part of this chapter has been published in **Electrochim. Acta 2018, 259, 262–275**.

dye which support the reduced electron–hole recombinations and obtain a better current output from the device.

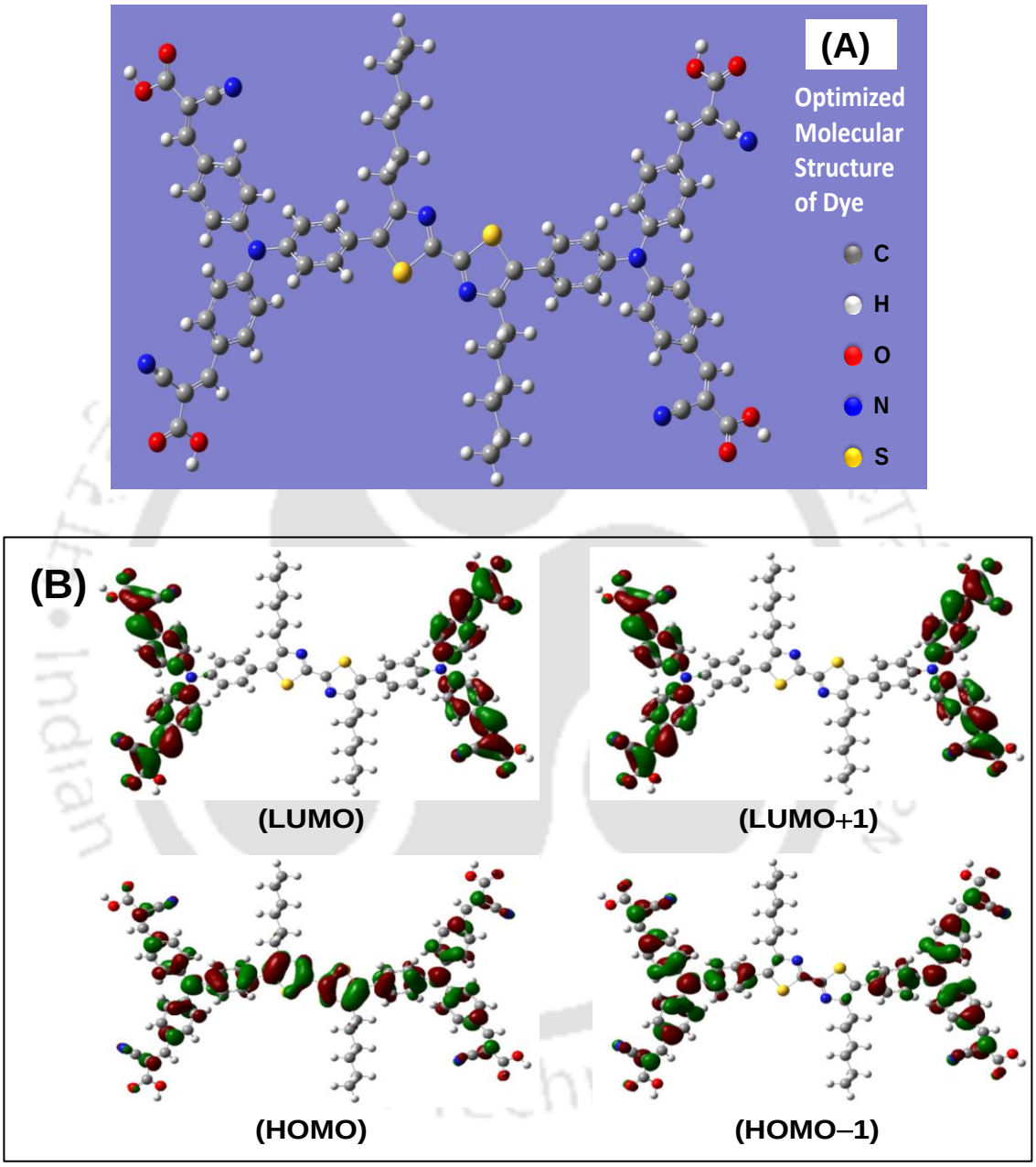


**Figure 5.3.9. (A)** Optimized molecular structure and **(B)** Frontier molecular orbitals (HOMO, HOMO−1, LUMO, and LUMO+1) of dye **D1**, as obtained from the DFT calculations.


Part of this chapter has been published in **Electrochim. Acta 2018, 259, 262–275**.

### 5.3.8 PHOTOVOLTAIC MEASUREMENTS OF SOLAR CELLS

To investigate the effects of different morphologies of ZnO in terms of light harvesting and charge transfer ability, we have fabricated the dye; **D1** sensitised photovoltaic devices and systematically evaluated the photovoltaic performance by using platinized FTO as a counter electrode and $I^-/I_3^-$ redox electrolyte under AM 1.5G irradiation with intensity of 100 mW $cm^{-2}$. Figure **5.3.10 (A)** display current density–voltage (*J*–V) curves for all devices. All photovoltaic parameters for both device such as, short circuit current density ($J_{sc}$), open circuit voltage ($V_{oc}$), fill factor (FF) and the overall power conversion efficiency (PCE, η) are summarized in table **5.3.2**. As obtained efficiency value for 3–D ZnO superstructures based device is higher as compared to 1–D ZnO NRs based device which confirm the supremacy of hierarchical superstructures by means of improved light harvesting as well as better charge transfer ability. Estimated values of all photovoltaic parameters such as $J_{sc}$ ($mAcm^{-2}$), $V_{oc}$ (mV), FF (%) and PCE, η (%) for 3–D ZnO HSs based device are higher as compare to 1–D ZnO NRs which are found to be ≈ 13.92, ≈ 653, ≈ 59.32, ≈ 5.37 while ≈ 10.57, ≈ 605, ≈ 54.29, ≈ 3.48 for ZnO NRs based device. Enhanced $J_{sc}$ value in the 3–D ZnO superstructures based device is ascribed to presence of more adsorption sites for sensitizer deposition which may lead to upsurge the flux of photoinduced electron injection.

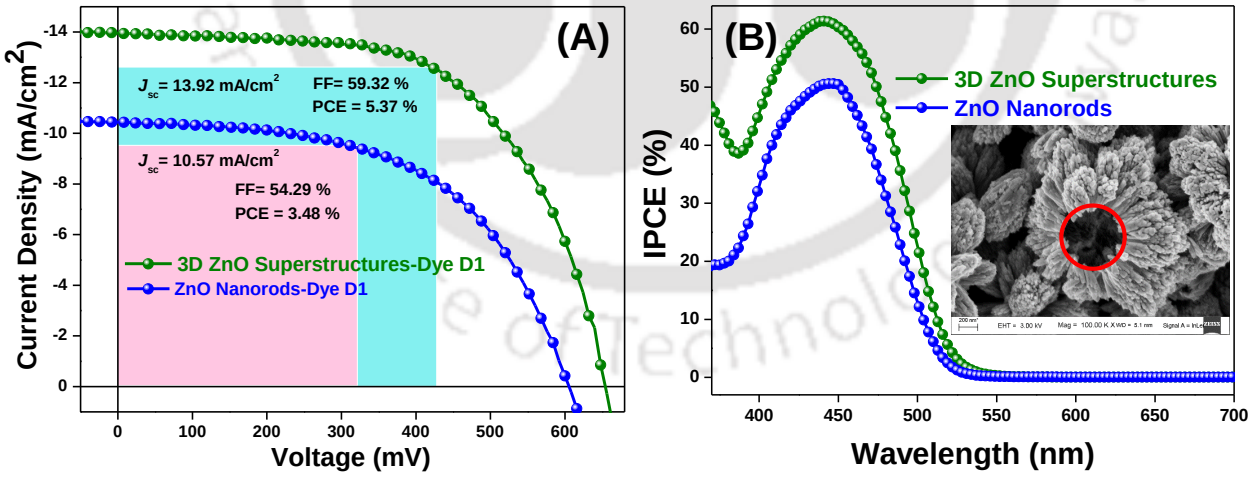


**Figure 5.3.10 (A)** Current density–Voltage (*J*–V) curve for as-fabricated photovoltaic devices based on both ZnO heterostructures. **(B)** Corresponding IPCE plot for the respective devices. Inset shows the porous and hollow nature of ZnO superstructures, helpful for the better infiltration of redox couple and efficient light scattering in the photovoltaic devices.


Part of this chapter has been published in **Electrochim. Acta 2018, 259, 262–275**.

**Table 5.3.2** Short-circuit current density ($J_{sc}$), open-circuit voltage ($V_{oc}$), fill factor (FF), power conversion efficiency (η) and incident photon-to-current conversion efficiency (IPCE) for as-fabricated photovoltaic devices based on both ZnO heterostructures.

| DSSC Photo-anode | $J_{sc}$ (mA cm$^{-2}$) | $V_{oc}$ (mV) | FF (%) | PCE (η, %)[a] | $IPCE_{max}$ (%) |
|---|---|---|---|---|---|
| **3–D ZnO Superstructures** | 13.92 | 653 | 59.32 | **5.37** | 61.33 |
| **1–D ZnO Nanorods** | 10.57 | 605 | 54.29 | **3.48** | 51.70 |

[a]PCE value for the best performed device out of 5 identical devices.

We also observed the larger $V_{oc}$ value (≈ 653 mV) for same device, indicative of better separation of photogenerated electron–hole pair and interfacial charge transfers. This observation reflects the minimum back transferring of photoinduced electron at the electrode/electrolyte interface, further discuss in electrochemical impedance spectroscopic analysis. Due to *meso*-porous nature of superstructures, sufficient pores are available in the photoanodic film for better functioning of electrolyte, responsible for effective regeneration of the sensitizer particles which infer the superiority of device. We have also noticed a significant enhancement in the fill factor value for 3–D ZnO HSs based device, owing to the better transport of photogenerated electron within the device and having the minimal recombination processes which is helpful to get the high efficiency of device.

Figure **5.3.10 (B)** exhibits corresponding incident photon-to-current conversion efficiency (IPCE) plots for both the device. 3–D ZnO superstructure based device showed better light harvesting ability as accordance with its $J_{sc}$ value, accredited to higher loading of sensitizer molecules and efficient interfacial charge transfer from dye to ZnO. Consequently, ZnO superstructure based device exhibits IPCE of about ~ 61.33 % whereas ZnO NRs based device showed of about ~ 51.70 % in the wavelength range of 360–540 nm. Observed lower IPCE value for ZnO NRs based device advocates the inadequate loading of sensitizer particles which limit the light harvesting ability as well as performance of device. As clear from the IPCE plot, we observed a red shift towards longer wavelength of 3–D ZnO superstructures based device (olive line), attributed to an efficient light scattering and repeated excitation of sensitizer molecules in the same photoanode. Efficient light confinement in the 3–D ZnO superstructures based photoanode is probably due to hollow nature of ZnO superstructures which is shown in the inset of figure **5.3.10 (B)**. Moreover, assembling units i.e., 1–D ZnO nanocrystals provide a better


Part of this chapter has been published in **Electrochim. Acta 2018, 259, 262–275**.

transport pathway for faster transport of photogenerated electrons to enhance the photovoltaic performance.

### 5.3.9 ELECTROCHEMCIAL IMPEDANCE SPECTROSCOPY ANALYSIS

To examine the electron transport and charge recombination kinetics of as-fabricated devices, electrochemical impedance spectroscopy (EIS) analysis is carried out under the dark conditions in a frequency range from 0.1 Hz to 100 kHz at an external bias equivalent to open circuit voltage, as shown in figure **5.3.11 (A)** & **(B)**. EIS analysis of a dye sensitized solar device mainly explain the charge transfer and recombination processes, taking place at various interfaces of device such as at counter electrode/electrolyte interface in the high-frequency region (1–100 kHz), at the ZnO/dye/electrolyte interface in the mid-frequency region (0.1–1 kHz), and the diffusion of electrolyte in the low frequency region (0.1–0.01 Hz).[33] Figure **5.3.11 (A)** represents the Nyquist plots, recorded under dark condition at the applied bias equivalent to the open-circuit voltages in the frequency range from 0.1 Hz to 100 kHz. Inset of same figure shows the equivalent circuit diagram, utilized to fit the EIS data. Both the Nyquist plot have two semicircles, one in the medium frequency region while another one in the higher frequency region. Diameter of the right semicircle ($R_k$), observed at medium frequency region mainly related to the charge transfer resistance ($R_{ct}$).[34] From figure **5.3.11 (A)**, as can be seen that diameter of semicircle ($R_k$) is considerably higher for 3–D ZnO superstructures based device (olive line) as compared to ZnO NRs based device (blue line). This observation assists our claim of faster and better charge transport in case of ZnO superstructures, resulting in a reduced recombination. From Table **5.3.3**, we have noted a lower series resistance ($R_s$) values for semiconductor sensitized 3–D ZnO superstructures based devices with respect to 1–D ZnO NRs, encouraging the collection efficiency of photogenerated electrons collection at the FTO substrate, helpful to improve the current outcome from the device. We have also found larger $R_{ct2}$ value for 3–D ZnO superstructures based device with respect to 1–D ZnO structures, exhibiting the better charge separation and transportation at working electrode/electrolyte interface. Enhanced $R_{ct}$ and $R_k$ for 3–D ZnO superstructures based device supports the larger $V_{oc}$ values from *J*–V measurements. So, enhanced $V_{oc}$ value is essentially due to better charge transport along 1–D path (1–D ZnO NRs as assembling units) and better interfacial electron

injection. Additionally, as obtained higher value of $V_{oc}$ may also a result of reduction in charge recombination processes, due to the presence of two long alkyl chains on a bisthiazole moiety which are considered to suppress the dark current.

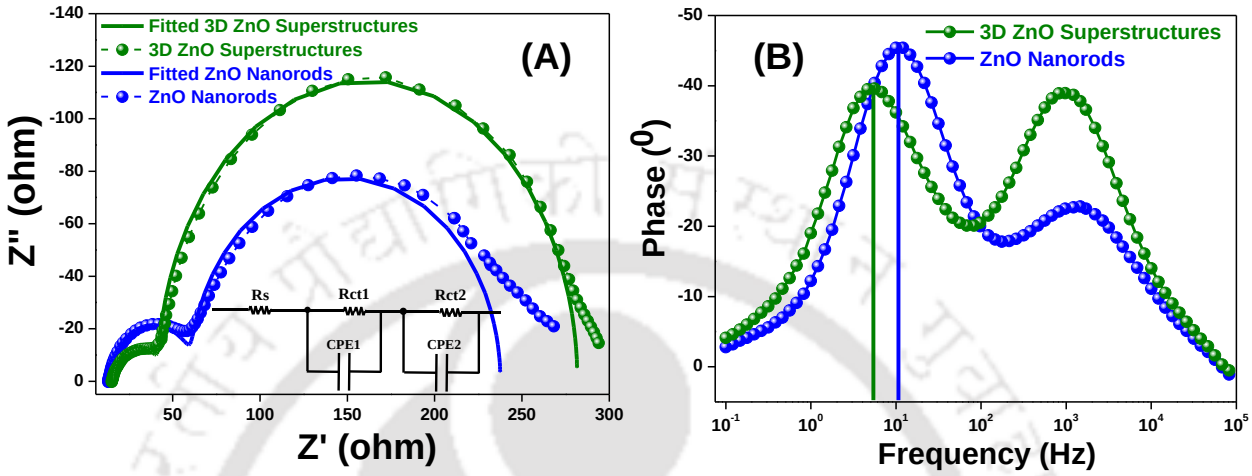


**Figure 5.3.11 (A)** Nyquist plot for as-fabricated photovoltaic devices. Inset of this plot depicts the equivalent circuit diagram and used abbreviations are as follow: $R_s$, sheet resistance; Rct1 & Rct2 , charge-transfer resistance of the counter electrode and working electrode ; CPE1 & CPE2, constant-phase element of the counter electrode and working electrode respectively. **(B)** Bode phase plot for the respective photovoltaic devices.

**Table 5.3.3** Fitted parameters such as series resistance (Rs), recombination resistance of the counter electrode and working electrode (Rct1 & Rct2), maximum peak frequency ($f_{max}$) and electron lifetime ($\tau_e$) for both devices based on different ZnO structures.

| **Photovoltaic Device** | **$R_s$ (ohm)** | **$R_{ct1}$ (ohm)** | **$R_{ct2}$ (ohm)** | **$f_{max}$ (Hz)** | **$\tau_e$ (ms)** |
|---|---|---|---|---|---|
| **1–D ZnO Nanorods** | 14.04 | 46.34 | 177.30 | 10.92 | 14.56 |
| **3–D ZnO Superstructures** | **13.42** | **40.46** | **240.10** | **5.41** | **29.38** |

Corresponding Bode phase plots for both the device are illustrated in figure **5.3.11 (B)**. In the Bode plots, two distinct peaks are observed which are corresponds to two diode interfaces of the device. Photoinduced electron lifetimes ($\tau_e$) can be calculated from characteristics maximum peak frequency ($f_{max}$) in the mid-frequency region. We have calculated the $\tau_e$ values for both devices by using the **equation (3)** and summarized in table **5.3.3**:[35]

$$\tau_e = \frac{1}{2\pi f_{max}} \qquad (3)$$


Part of this chapter has been published in **Electrochim. Acta 2018, 259, 262–275**.

From table **5.3.3**, maximum peak frequencies ($f_{max}$) for the 3–D ZnO superstructures and 1–D ZnO NRs based device are found to be present at ~ 5.42 Hz and ~ 10.71 Hz respectively and corresponding $\tau_e$ values for respective devices are calculated and found to be ~ 29.38 ms and ~ 14.56 ms. Enhanced ($\tau_e$) value for 3–D ZnO superstructures based device confirms the minimized recombination processes, occurred due to back transferring of photoinduced electrons to the electrolyte at the working electrode/electrolyte interfaces. This observation also suggested that photogenerated electrons stay more time in the photoanodic film, results increase the diffusion length of electrons in photoanodic film before getting collect at FTO. So, there is an enhancement of photoinduced electron density in CB of ZnO HSs which leads to improve the $J_{sc}$ value, contributed to get the higher efficiency of solar device.

### 5.3.10 STABILITY OF PHOTOVOLTAIC DEVICES

Photo-stability of solar device is a needed parameter for its actual practical application. All photovoltaic performance parameters such as $J_{sc}$, $V_{oc}$, FF, and η are studied with respect to time, under the solar irradiation (AM 1.5 G, 100 $mWcm^{-2}$) at ambient conditions without proper sealing of device. Values for all photovoltaic parameters of best performing device are recorded over a period of 48 h, as shown in figure **5.3.12**. Photo-current of the device increases substantially during the first few hours, attributed to the better penetration of iodide/triiodide redox electrolyte through the photoanodic film, after that $J_{sc}$ value decreases continually due to evaporation of electrolyte. Other parameters such as open circuit voltage and fill factor are constantly decreases as prolong irradiation. Thus, there is a ~ 38 % reduction in efficiency for ZnO superstructures based device after the 48 h duration. Based on the observations, we conclude that the device is quite stable initially but show a slow decrease in performance with increased time.


Part of this chapter has been published in **Electrochim. Acta 2018, 259, 262–275**.

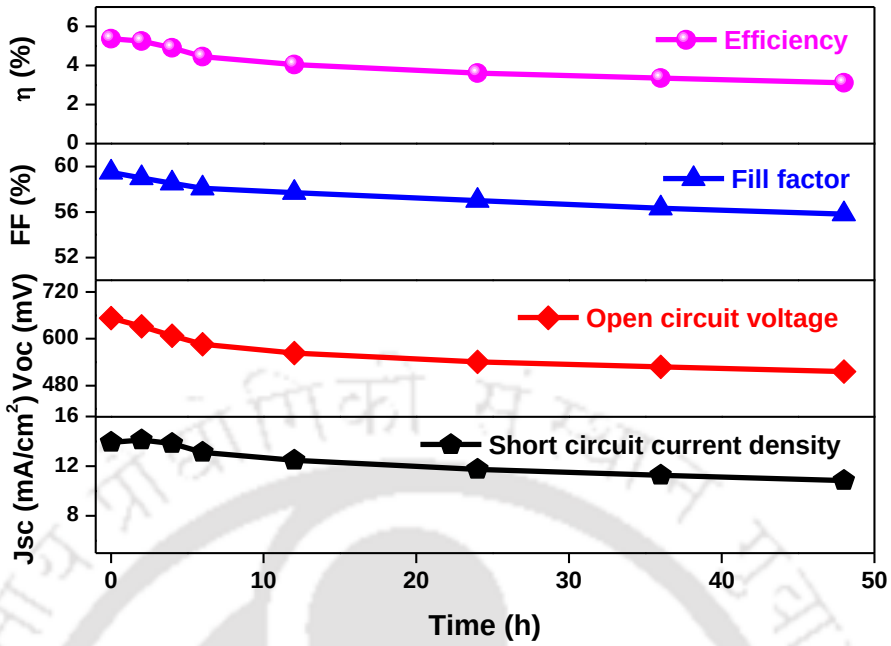


**Figure 5.3.12** Changing of different photovoltaic parameters such as current density (mA $cm^{-2}$), open circuit voltage (mV), fill factor (%) and efficiency value (%) with respect to time to evaluate the stability of the best performing photovoltaic device based on 3–D ZnO superstructures

## 5.4 CONCLUSIONS

In summary, we have reported the synthesis of three dimensional (3–D) Zinc oxide (ZnO) hierarchical superstructures (HSs), assembled with 1–D ZnO nanorods (NRs) under controlled hydrothermal route. Biotemplate "Polygalacturonic acid" is utilized as a crystal growth modifier for assembling the basic building blocks (ZnO NRs) in a specific orientation and generated the hierarchical superstructures. We have studied the probable reaction mechanism for the formation of these superstructures by means of the interaction between the polysaccharide and ZnO growth units. Surface morphology of as-synthesized 3D ZnO hierarchical superstructures (3D ZnO HSs) are investigated by field emission scanning electron microscopy (FESEM) and transmission electron microscopy (TEM) analysis. We studied the probable reaction mechanism for the formation of these superstructures by means of the interaction between the polysaccharide and ZnO growth units. Photovoltaic properties of as-synthesized 3–D ZnO HSs as compared to its basic structural units i.e., 1–D ZnO NRs are investigated by sensitizing with a new bisthiazole linked metal free donor–acceptor dye D1. We have observed a substantial enhancement (~ 35 %) in efficiency value (η) for 3–D ZnO HSs based device (η ≈ 5.37 %) as compare to 1–D ZnO NRs


Part of this chapter has been published in **Electrochim. Acta 2018, 259, 262–275**.

(η ≈ 3.48 %) which is mainly due to better charge separation and collection, owing to superior electron transport property of compacted ZnO NRs building blocks, better light-scattering effect, high BET surface area for sensitizer loading and efficient electron injection from $E_{LUMO}$ of dye D1 to the conduction band of ZnO. Further, electrochemical impedance spectroscopic (EIS) analysis is supported a slower photogenerated electron–hole recombination rate and better charge transports in the 3–D ZnO HSs based photovoltaic device by showing a higher charge recombination resistance and photoinduced electron lifetime. These observations have indicated that the hierarchical superstructures of ZnO are promising candidates for the enhancement in the efficiency of a photovoltaic device.

## 5.5 REFERENCES


(1) J. Y. Lao, I. G. Wen and Z. F. Ren, *Nano Lett.*, 2002, **2**, 1287–1291.

(2) P. Jiang, J. J. Zhou, H. F. Fang, C. Y. Wang, Z. L. Wang and S. S. Xie, *Adv. Funct. Mater.*, 2007, **17**, 1303–1310.

(3) X. F. Zhou, Z. L. Hu, Y. Q. Fan, S. Chen and W. P. Ding, *J. Phys. Chem. C*, 2008, **112**, 11722–11728.

(4) X. F. Gao and L. Jiang, *Nature*, 2004, **432**, 36.

(5) V. Bansal, H. Jani, J. Du Plessis, P. J. Coloe and S. K. Bhargava, *Adv. Mater.*, 2008, **20**, 717–723.

(6) A. Modi, N. Koratkar, E. Lass, B. Wei and P. M. Ajayan, *Nature*, 2003, **424**, 171–174.

(7) A. S. Arico, P. Bruce, B. Scrosati, J. M. Tarascon and W. V. Schalkwijk, *Nat. Mater.*, 2005, **4**, 366–377.

(8) Y. Zeng, T. Zhang, H. T. Fan, W. Y. Fu, G. Y. Lu, Y. M. Sui and H. B. Yang, *J. Phys. Chem. C*, 2009, **113**, 19000–19004.

(9) H. Zhou, T. Fan and D. Zhang, *Chem Sus Chem*, 2011, **4**, 1344–1387.

(10) S. Sotiropoulou, Y. Sierra-Sastre, S. S. Mark and C. A. Batt, *Chem. Mater.*, 2008, **20**, 821–834.

(11) H. C. Zeng, *J. Mater. Chem.*, 2006, **16**, 649–662.


 Part of this chapter has been published in **Electrochim. Acta 2018, 259, 262–275**.

(12) J.-J. Feng, Q.-C. Liao, A.-J. Wang and J.-R. Chen, *CrystEng-Comm*., 2011, **13**, 4202–4210.

(13) P. Hu, N. Han, X. Zhang, M. Yao, Y. Cao, A. Zuo, G. Yang and F. Yuan, *J. Mater. Chem.*, 2011, **21**, 14277–14284.

(14) B. Liu and H. C. Zeng, *Chem. Mater.*, 2007, **19**, 5824–5826.

(15) M. Mo, J. C. Yu, L. Zhang and S.-K. A. Li, *Adv. Mater.*, 2005, **17**, 756–760.

(16) R. Maragani, M.S. Ansari, A. Banik, R. Misra and M. Qureshi, *ACS Omega*, 2017, **2**, 5981–5991.

(17) J. H. Huang, C. M. Teng, Y. S. Hsiao, F. W. Yen, P. Chen, F. C. Chang and C. W. Chu, *J. Phys. Chem. C.*, 2011, **115**, 2398–2405.

(18) A. Banik, M. S. Ansari, T. K. Sahu and M. Qureshi, *Phys.Chem.Chem.Phys.*, 2016, **18**, 27818–27828.

(19) A. Mclaren, T. Valdes-Solis, G. Li, S. C. Tsang, *J. Am. Chem. Soc.*, 2009, **131**, 12540–12541.

(20) M. Huang, Y. Yan, W. Feng, S. Weng, Z. Zheng, X. Fu and P. Liu, *Cryst. Growth Des.*, 2014, **14**, 2179–2186.

(21) M. Mo, J. C. Yu, L. Zhang and S.-K. Li, *Adv. Mater.*, 2005, **17**, 756–760.

(22) H. Wang, C. Xie, D. Zeng and Z. Yang, *J. Colloid Interf. Sci.*, 2006, **297**, 570–577.

(23) X. Sun, J. Liu and Y. Li, *Chem.–Eur. J.*, 2006, **12**, 2039–2047.

(24) Z. Wang, X. F. Qian, J. Yin and Z. K. Zhu, *J. Solid State Chem.*, 2004, **177**, 2144–2149.

(25) X. M. Sun, X. Chen, Z. X. Deng and Y. D. Li, *Mater. Chem. Phys.*, 2002, **78**, 99–104.

(26) H. Zeng, G. Duan, Y. Li, S. Yang, X. Xu and W. Cai, *Adv. Funct. Mater.*, 2010, **20**, 561–572.

(27) X. L. Wu, G. G. Siu, C. L. Fu and H. C. Ong, *Appl. Phys. Lett.*, 2001, **78**, 2285–2287.

(28) A. Kongkanand, K. Tvrdy, K. Takechi, M. Kuno and P. V. Kamat, *J. Am. Chem. Soc.*, 2008, **130**, 4007–4015.

(29) K. Fan, M. Liu, T. Y. Peng, L. Ma and K. Dai, *Renewable Energy*, 2010, **35**, 555–561.

(30) P. Wang, C. Klein, R. Humphry-Baker, S. M. Zakeeruddin and M. Grätzel, *J. Am. Chem. Soc.*, 2005, **127**, 808–809.

(31) A. Pedone, *J. Chem. Theory Comput.*, 2013, **9**, 4087–561.

(32) D. G. Gusev, *Organometallics*, 2013, **32**, 4239–4243.

(33) S. Phadke, A. Du Pasquier and D. P. Birnie, *J. Phys. Chem. C*, 2011, **115**, 18342–18347.

(34) V. D. Dao, L. L. Larina, Q. C. Tran, V. T. Bui, V. T. Nguyen, T. D. Pham, I. M. A. Mohamede, N. A. M. Barakate and B. T. Huyc, *Carbon*, 2017, **116**, 294–302.

(35) R. Kern, R. Sastrawan, J. Ferber, R. Stangl and J. Luther, *Electrochim. Acta*, 2002, **47**, 4213–4225.

# CHAPTER 6

## Multifunctional Hierarchical 3–D ZnO Superstructures Directly Grown over FTO Glass Substrates: Enhanced Photovoltaic and Selective Sensing Applications

*This chapter describes biotemplate "k-carrageenan" assisted in-situ growth of hierarchical three-dimensional zinc oxide superstructures over a conductive glass substrate, i.e., fluorine-doped tin oxide, under a controlled hydrothermal route for low ohmic contact, allowing efficient charge injection. We have successfully demonstrated the applications of the as-characterized multifunctional 3−D ZnO hierarchical structures in photovoltaic and selective chemical vapor sensing. Improved photovoltaic and sensing applications in 3−D ZnO hierarchical structures are mainly related to larger surface to volume ratio for sensitizer loading; better light-scattering effect, efficient charge separation and collection.*

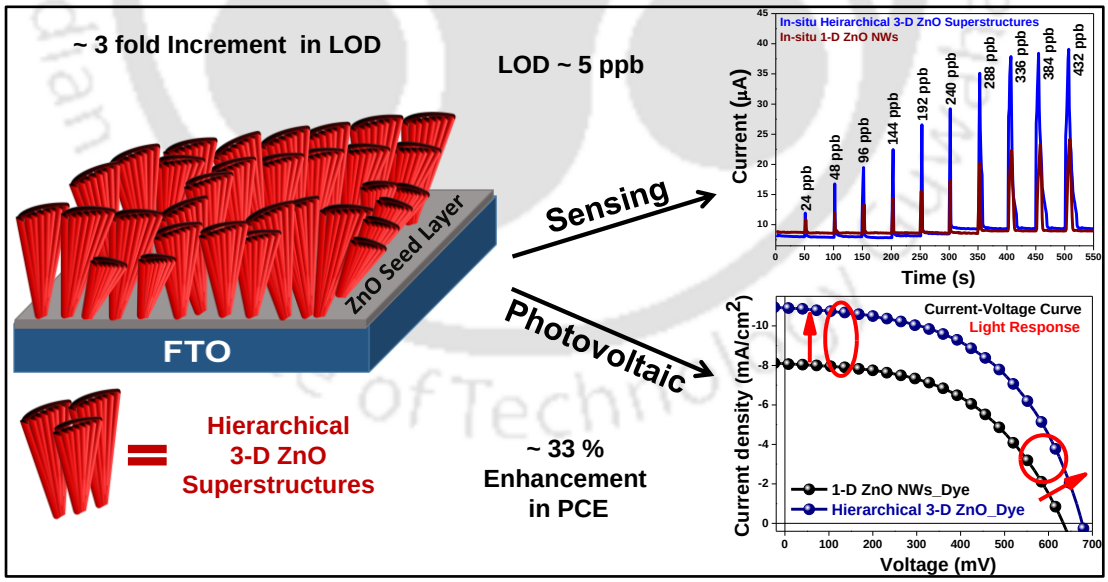


***Ansari, et al., J. Mater. Chem. A* 2018, *6*, 15868–15887.**

## 6.1 INTRODUCTION

Fabricating semiconductors having hierarchical morphologies based on one dimensional (1–D) nano-structures turns out to be a proficient way to improve the charge transfers and surface area significantly.[1] Multifunctional three dimensional (3–D) hierarchical nanoarchitechtures have the ability to vitalize the photoelectric conversion efficiency due to their favorable characteristics such as high sensitizer loading, strong light scattering effect and efficient electron transport through 1–D networks.[2–4] To assemble the 1–D nanostructures into a regular ordered array, several growth patterns have been utilized based on their crystal growth behavior similar to template derived homo-or hetero-epitaxial growth behavior.[5] Crystal growth mechanism is essential to comprehend the epitaxial attachment of 1–D nanocrystals to form the hierarchical structures via non-classical growth mechanism.[6–10] Growth patterns of different shapes are greatly affected by different reaction conditions and internal structure of a given crystal. Templating agents with various functionalities are responsible for modification of nanostructure morphologies by adsorbing at the surface of crystals and restrict the crystal growth in a specific crystal plane.[11] Relaxation energies related to various crystal planes are crucial for determining the equilibrium morphology of a crystal.[12–13] Hence, from the perspective of decreasing the total surface energy, a ZnO crystal will develop into 3–D morphology with distinct crystallographic facets.

Ammonia has extensively utilized in many applications such as agrochemicals, pharmaceuticals, organic dyes, synthetic fibers etc., due to which it can be diffused into the environment and cause severe effect on the human health as well as the environment.[14] Likewise, ammonium nitrate is usually found in many explosives which release the trace amount of ammonia on decomposition which is very crucial to be monitored in order to prevent the lethal accidents. Thus, it is necessity to develop a highly-sensitive and room-temperature-efficient $NH_3$ gas sensor. Gas sensors play an important role for the detection and monitoring of various toxic and harmful gases,[15] generated due to rapid industrialization, combustion of fuels and use of agro-chemicals. Therefore, ZnO heterostructures are utilized for the fabrication of highly sensitive $NH_3$ gas sensor devices in present study. Several sensing experiments are performed for supporting these sensor devices as simple, consistent, economical and effective in executing the $NH_3$ detection under practical conditions.


Part of this chapter has been published in **J. Mater. Chem. A 2018, 6, 15868–15887**.

In this chapter, we have grown hierarchical 3–D ZnO superstructures directly over conductive glass substrate i.e., FTO, utilizing biomass derived templating agent under controlled hydrothermal route for getting low Ohmic contact, thereby an efficient charge injection and collection. An anionic polysaccharide "k-carrageenan" is utilized for monitoring the hetero epitaxial aggregated growth of 1–D nanocrystals, display in figure **6.1.1**. We have successfully demonstrated the applications of as-characterized multifunctional 3–D ZnO hierarchical structures in photovoltaic and selective chemical vapor sensing.

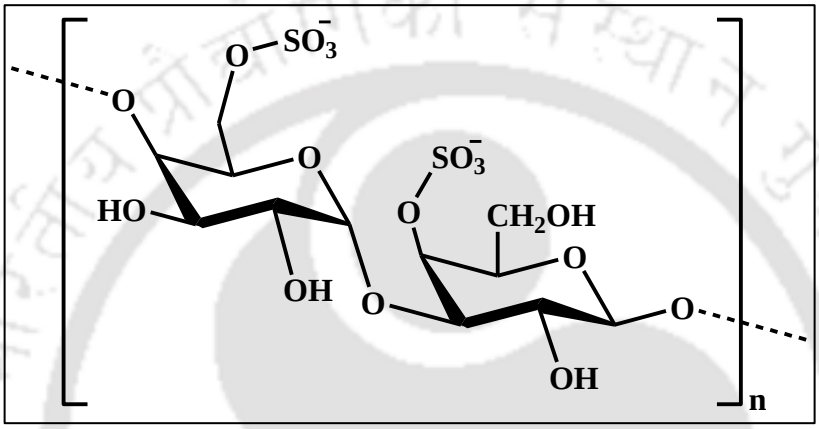


**Figure 6.1.1** Chemical structure of biomass derived templating agent "k-carrageenan".

## 6.2 EXPERIMENTAL METHODS

### 6.2.1 *IN–SITU* GROWTH OF ZnO HETEROSTRUCTURES

Firstly, ZnO seed layer solution was prepared by dissolving the zinc acetate (300 mM) and ethanolamine (300 mM) in 3 mL of 2-methoxyethanol with overnight stirring at room temperature, followed by filtration through a 0.2 μm PTFE syringe filter. Filtered seed solution was spin coated onto the ozonized FTO substrates and calcined at 200 °C for 15 min at room temperature. Same procedure was repeated for complete coverage of conductive substrate with seed layer, which acts as the template for uniform epitaxial growth of ZnO heterostructures. *In-situ* growth of ZnO heterostructures was carried out onto the ZnO seed layer coated FTO substrates under controlled hydrothermal reaction. At first, biopolymer, k-carrageenan (1 mg/mL) was dissolved in Milli-Q water (25 mL) under continuous stirring, followed by addition of Zn $(NO_3)_2$•$6H_2O$ (1 mmol) in the reaction mixture. Viscosity of this solution gets increased due to interaction of biomass derived template and metal salt. Now, liquid ammonia, $NH_3$•$H_2O$ (25 %) was dropwise added into the solution. Instantly, a white precipitate was observed in the

 Part of this chapter has been published in **J. Mater. Chem. A 2018, 6, 15868–15887**.

solution and on continual addition of $NH_3 \bullet H_2O$, precipitate got disappear and reaction solution become colorless. Then, this clear solution was transferred into a Teflon autoclave and ZnO seeded substrates were immersed (FTO side down) into this clear solutions. Teflon line stainless steel autoclave was closed tightly and kept at 125 $^oC$ for 4 h for the growth of ZnO heterostructures. Autoclave was allowed to cool down at room temperature, and the FTO substrates were taken out, and rinsed thoroughly with Milli-Q water and ethanol. The substrates were then calcined at 200 °C for 15 min and obtained hierarchical 3–D ZnO superstructures. In absence of templating agent (k-carrageenan), 1–D ZnO NWs were grown on the FTO glass under the same reaction condition. These ZnO heterostructures grown FTO substrates were further used for fabrication of photoanode via N719 dye-sensitization.

### 6.2.2 PHOTOVOLTAIC DEVICE FABRICATION

Photoanodes based on both *in-situ* grown ZnO structures were fabricated by dipping the FTO substrates having both *in-situ* structures into 0.3 mM dye (N719) solution [Acetonitrile: tert-butanol (1:1)] for 3 h at ambient condition. Sensitized photoanodes were taken out from the dye solution, washed with acetonitrile and dried in hot air blow. Photovoltaic device was constructed by integrating the photoanode and counter electrode. Counter electrode was prepared by spin coating of chloroplatinic acid (2mg/mL in isopropanol) solution onto the conductive glass substrate and then annealed at 450 °C for 30 min. Redox electrolyte was injected between the sandwiched devices.

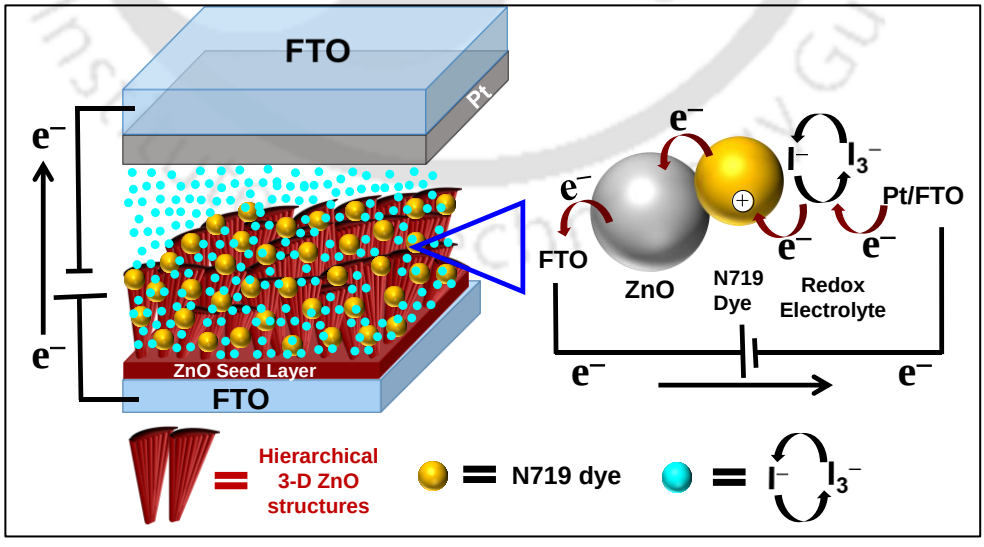


**Scheme 6.2.1** Schematic illustration of hierarchical 3–D ZnO superstructures based Photovoltaic device and electronic interaction of dye/electrolyte through electron transport mechanism.


Part of this chapter has been published in **J. Mater. Chem. A 2018, 6, 15868–15887**.

The $I^-/I_3^-$ redox electrolyte solution was prepared by using previously reported protocol.[16] Device area was fixed to the 0.16 $cm^2$. Schematic representation of hierarchical structures based photovoltaic device with the electronic interaction between dye/redox couple was shown in scheme **6.2.1**. In the DSSC, redox electrolyte mainly utilizes to regenerate the oxidized sensitizer (N719 dye) molecules and maintain electron flow within the solar cell to complete the circuit.

### 6.2.3 TWO-TERMINAL CHEMIRESISTOR DEVICE FABRICATION

Schematic representation of step by step fabrication of sensor device displayed in Scheme **6.2.2**. In the first step, FTO substrates were patterned by using zinc dust and conc. HCl to make the active sensing area (channel) of about 0.10 $cm^2$ [1 mm length (L) and 10 mm width (W)], for *in-situ* growth of ZnO heterostructures, acted as the active materials for gas sensing experiments. In the second step, similar synthetic procedure (as discussed in *in-situ* growth of ZnO heterostructures) was used for deposition of ZnO seed layer as well as growth of *in-situ* ZnO structures. After that FTO substrates were calcined at 200 °C for 15 min. In third step, devices having both *in-situ* ZnO structures were ready for all kinds of electrical measurements related to vapor phase sensing.

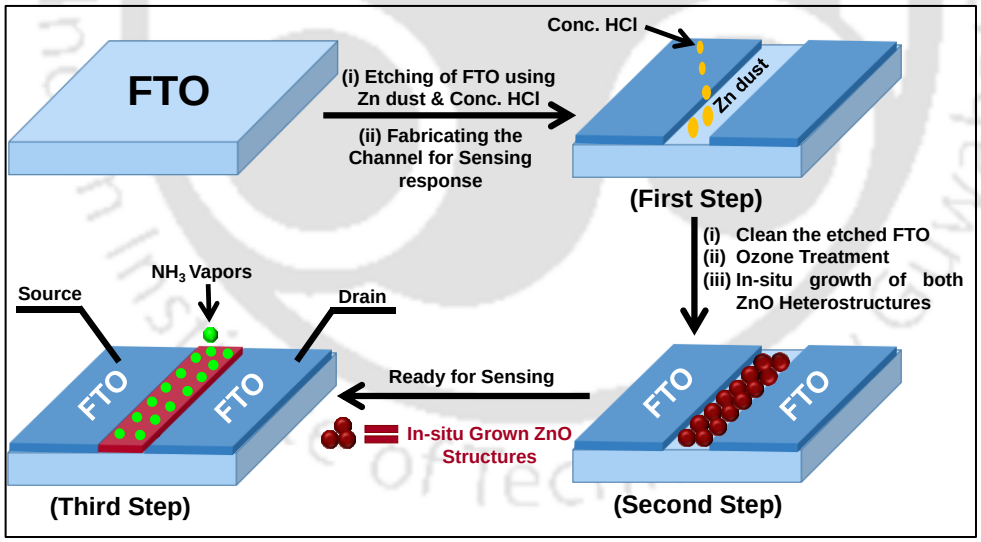


**Scheme 6.2.2** Schematic representation of step by step fabrication of two terminal chemiresistor devices for vapor phase sensing.

### 6.2.4 VAPOR PHASE DETECTION

For vapor phase detection, 7 mL of ammonia, common organic solvents (Hexane, Acetone, Ethyl acetate, Methanol, Tetrahydrofuran, Ethanol, Iso-propanol) and various amines (Ethanol amine, Methyl amine, Diethyl amine, Triethyl amine, Ethylene di-amine, Diethyl tri-

amine, Nitrobenzene) were kept for 24 h in 10 mL culture tube with proper sealing to ensure the complete saturation over the headspace area. Concentration of vapors in the headspace area were estimated by using the following expression,[17]

$$\textbf{Saturation Concentration of Analyte (ppm)} = \frac{\textbf{Vapour Pressure (mm Hg)}}{\textbf{760 (mm Hg)}} \times \mathbf{10^6}$$

We then converted the taken analyte volume into the concentration by using the following mathematical formula,

$$\mathbf{C_1V_1 = C_2V_2}$$

Where, $C_1$ is the saturated concentration of analyte and $V_1$ is volume of analyte taken while $C_2$ is the calculated concentration of analyte and $V_2$ is volume of culture tube.

## 6.3 RESULTS AND DISCUSSIONS

### 6.3.1 POWDER X-RAY DIFFRACTION ANALYSIS

Crystal phase purity of *in-situ* grown ZnO heterostructures are confirmed by taking Powder X-ray diffraction (PXRD) analysis and related diffractogram are presented in figure **6.3.1**. PXRD pattern of hierarchical 3–D ZnO superstructures with (10$\bar{1}$0), (0002), (10$\bar{1}$1), (10$\bar{1}$2), (11$\bar{2}$0), (10$\bar{1}$3), (20$\bar{2}$0), (11$\bar{2}$2), and (20$\bar{2}$1) crystal planes is stated to the formation of wurtzite type hexagonal crystal structure with space group symmetry $P6_3mc$ according to the JCPDS Card No. 36-1451. No impurity peak is identified in this diffractogram which infers that *in-situ* grown hierarchical superstructures are pure and have good crystallinity. In the absences of biotemplate, preferential crystal growth pattern of ZnO is observed along the c-axis having a strong diffraction peak of (0002) crystal plane at a 2θ of 35.35° which suggests the epitaxial growth of 1–D ZnO NWs on the multinuclear ZnO seed layer. These different crystal growth patterns validate the dissimilar morphological features and specific orientation of nano-crystals. Here, k-carrageenan is utilized as a templating agent, triggering the crystal growth behaviour by altering the relaxation energy of definite crystal planes via strong electrostatic interactions between the surface charges of the biotemplate and the polar facets of ZnO. Moreover, micro-structural features of as *in-situ* grown heterostructures are analyzed by FESEM and TEM analysis.


Part of this chapter has been published in **J. Mater. Chem. A 2018, 6, 15868–15887**.

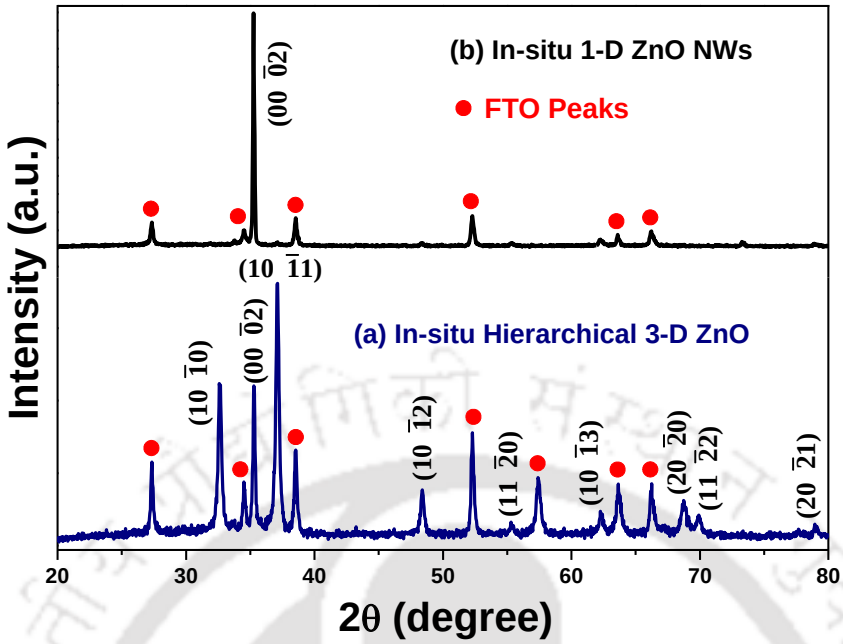


**Figure 6.3.1** Powder X-ray diffraction patterns of both the *in-situ* grown ZnO structures: **(a)** 3–D hierarchical ZnO superstructures (navy blue line) and **(b)** 1–D ZnO NWs (black line) while red circular marks are responsible for diffraction peaks related to conductive glass substrate ; FTO.

### 6.3.2 MATERIAL MORPHOLOGY

Morphological features of *in-situ* grown ZnO heterostructures are investigated by performing Field emission scanning electron microscopy (FESEM) and Transmission electron microscopy (TEM) analysis. Morphological features of different regions of *in-situ* grown hierarchical 3–D ZnO are displayed through FESEM images [figure **6.3.2 (a-c)**], carried out at different magnifications. It is noticed that most of the hierarchical superstructures are vertically aligned with uniform distribution on the entire surface of ZnO seeded FTO substrate. The size distribution of these *in-situ* grown hierarchical superstructures is observed in the micron range. Magnified FESEM image **(c)** is clearly advocated the hierarchical integration of 1–D nanocrystals to form 3–D ZnO superstructures. Surface functionalities of this templating agent are responsible for oriented assembling of building blocks, through interaction with polar surfaces of ZnO crystal. It is obvious from FESEM analysis that these superstructures seemed to be closely allied to each other which support the better inter-particles connectivity, resulting in efficient charge transfer and collection by minimizing the trap sites for electron–hole recombination. TEM analysis is performed for further corroboration of structural features of *in-situ* grown hierarchical superstructures at high magnification, as shown in figure **6.3.2**.


Part of this chapter has been published in **J. Mater. Chem. A 2018, 6, 15868–15887**.

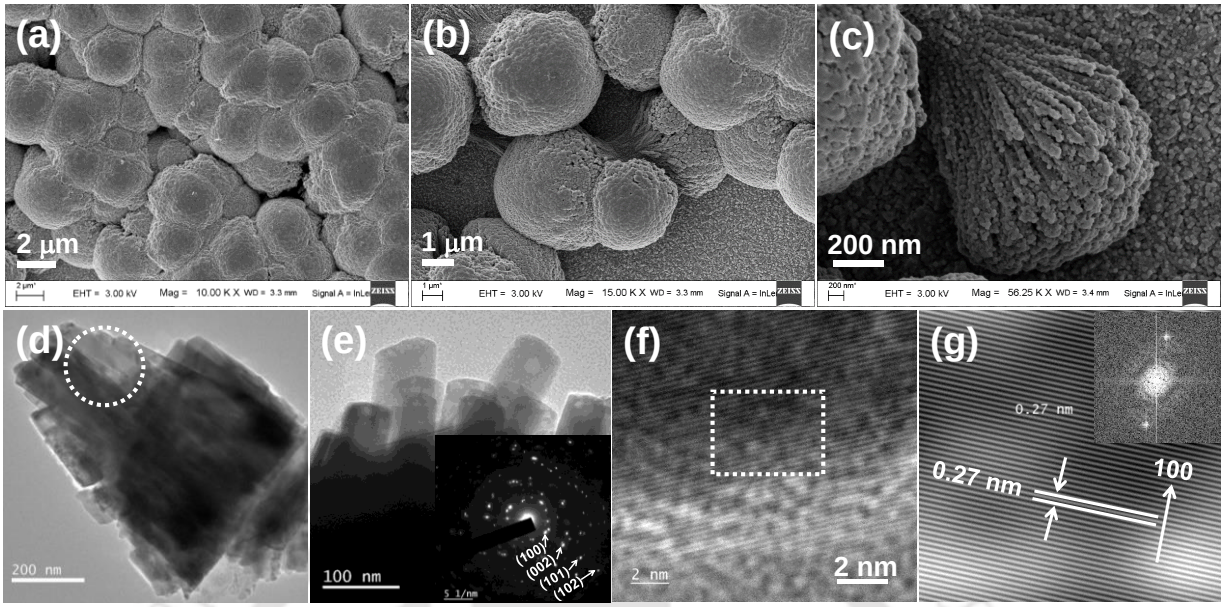


**Figure 6.3.2** Traces **(a-c)** represent the field emission scanning electron microscopy (FESEM) images of *in-situ* grown hierarchical 3–D ZnO superstructure of different regions at different magnifications. Transmission electron microscopy (TEM) images **(d & e)** show the structural features of *in-situ* grown hierarchical 3–D ZnO superstructure. Inset of image **(e)** shows the selected area electron diffraction (SAED) pattern with distinct crystal planes. Trace **(f)** displays the High resolution transmission electron microscopy (HRTEM) image of the hierarchical 3–D ZnO superstructure. Trace **(g)** represents Inverse fast Fourier transform (IFFT) analysis of selected portion for the image **(f)** with corresponding fast Fourier transform (FFT) image as inset of same image.

TEM image **(d)** of figure **6.3.2** elucidates the integration of 1–D nanocrystals in the homo as well as hetero-epitaxial manner to fabricate the hierarchical structure on conductive glass substrate. The average size of *in-situ* grown hierarchical ZnO superstructures is observed to be in the sub-micron ranges which are composed of 1–D NWs, having length in the range of 0.4–1 µm while the diameters appeared in the range of 40–80 nm. Trace **(e)** represents the higher magnification image of circled area of **6.3.2** trace **(d)**, supporting the claim of self-assembling of 1–D nanocrystals to form hierarchical superstructures. Inset of TEM image **6.3.2 (e)** depicts the selective area electron diffraction (SAED) pattern for hierarchical 3–D structures which depicts the diffraction rings pattern, revealing the polycrystalline nature of the hierarchical ZnO structure which is consistent with PXRD analysis. High resolution TEM (HRTEM) image for hierarchical ZnO structure exhibits the well-defined lattice fringes, as shown in trace **6.3.2 (f)**. Inverse fast Fourier transform (IFFT) analysis is performed for the selected portion of trace **6.3.2 (f)**, represented in trace **6.3.2 (g)**. Lattice fringes having interplanar distance of about ~ 0.27 nm can be ascribed for (100) crystal planes. Corresponding fast Fourier transform (FFT) pattern [inset of


Part of this chapter has been published in **J. Mater. Chem. A 2018, 6, 15868–15887**.

trace **6.3.2 (g)**] consist of very symmetrical dots, divulging the highly crystalline nature of the 1-D nanocrystals.

In absence of biotemplate, surface morphology of *in-situ* grown ZnO structures are also investigated, represented in figure **6.3.3**. From FESEM images **(a & b)** of figure **6.3.3**, epitaxial growth of 1–D ZnO NWs over the ZnO seeded FTO substrate is divulged the preferential crystal growth behaviour along c-axis with the minimal surface energy. Moreover, TEM analysis is also performed for further confirming the structural features of *in-situ* grown 1–D ZnO structures. TEM image **(c)** of figure **6.3.3** exhibits the *in-situ* growth of 1–D ZnO nanocrystals, having average dimensions; length in the range of 2–4 μm while diameter appears in the range of 50–80 nm.

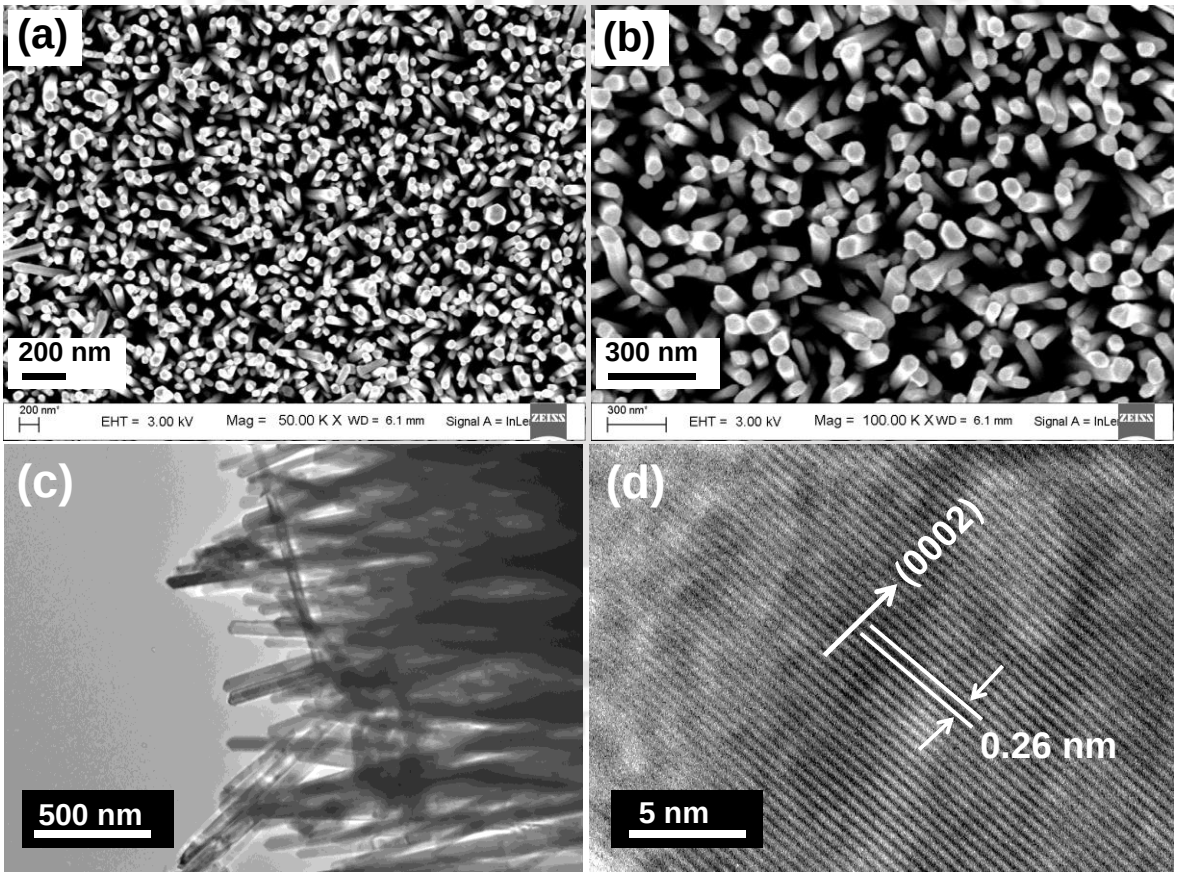


**Figure 6.3.3** Traces **(a & b)** represent the field emission scanning electron microscopy (FESEM) images of *in-situ* grown 1–D ZnO nanostructures at different magnifications. Transmission electron microscopy (TEM) image **(c)** shows the structural features of *in-situ* grown 1–D ZnO structure while trace **(d)** displays the High resolution transmission electron microscopy (HRTEM) image of 1–D ZnO structure.


Part of this chapter has been published in **J. Mater. Chem. A 2018, 6, 15868–15887**.

Trace **(d)** of figure **6.3.3** represents the high resolution TEM (HRTEM) image for 1–D ZnO structure, showing the well-defined lattice fringes with interplanar distance of about ~ 0.26 nm can be ascribed for (0002) crystal planes.

### 6.3.3 GROWTH MECHANISM FOR *IN–SITU* HIERARCHICAL 3–D ZnO SUPERSTRUCTURES

In accordance to morphological analysis, the plausible growth mechanism for the *in-situ* deposition of hierarchical 3–D ZnO superstructures over FTO substrate, under controlled hydrothermal reaction conditions is presented in scheme **6.3.1**. In general, growth process of the hierarchical 3–D superstructures can be triggered via two processes i.e., generation of primary structures and the crystal growth by means of secondary nucleation. It is anticipated that hierarchical 3–D superstructures are fabricated via assembling of primary ZnO structures i.e., 1–D ZnO NWs. Herein, water soluble and sulfate group containing an anionic polysaccharide "**k-carrageenan**" is utilized for monitoring the hetero epitaxial aggregated growth of 1–D nanocrystal. Natural hydrocolloid carrageenan is derived from red edible seaweed, having the repeating units of galactose and 3,6 anhydrogalactose (3,6-AG) and these repeating units are joined by alternating α-1,3 and β-1,4 glycosidic linkages, as shown in figure **6.1.1**.

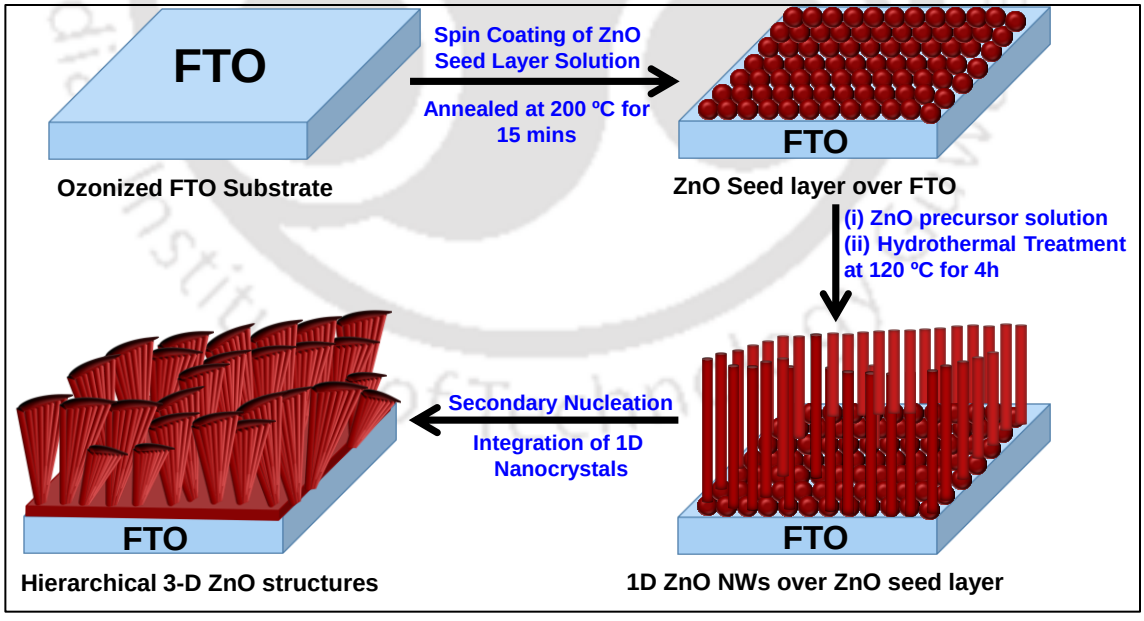


**Scheme 6.3.1** Schematic illustration of bio-mass derived template "k-Carrageenan" assisted *in-situ* growth of hierarchical 3–D ZnO structures.


Part of this chapter has been published in **J. Mater. Chem. A 2018, 6, 15868–15887**.

For direct deposition of hierarchical superstructures over conductive substrate, multinuclear ZnO seed layer is firstly deposited over cleaned and ozonized FTO. This seed layer provides the specific growth sites for the epitaxial growth of 1–D ZnO nanocrystals. ZnO seeded FTO substrate (down side) is then immersed into the ZnO precursor solution and kept for hydrothermal reaction at 125 $^{o}$C for 4 h for the growth of ZnO structures. ZnO precursor solution is prepared by dissolving the biotemplate (1mg/mL) in the Milli-Q water, producing negative charged ions in solution because of hydroxyls and sulfate groups. After that, zinc nitrate is added into the reaction mixture and generated the positively charged $Zn^{2+}$ ions in the solution. Thus, there is an electrostatic interaction between the negatively charged ($OH^{-}$/$SO_3^{-}$) and positively charged ($Zn^{2+}$) ions and generates adduct into the reaction mixture.[18] Liquid ammonia ($NH_3$•$H_2O$) is then added into the reaction mixture which instantly produce a white precipitate of $Zn(OH)_2$. On continual addition of $NH_3$•$H_2O$, white precipitate turns into clear solution, associated to the formation of $Zn(OH)_4^{2-}$ and $Zn(NH_3)_4^{2+}$ ions which act as the crystal growth units for the formation of 1–D nanocrystals.[19] In this growth mechanism, negatively charged k-carrageenan is utilized for the suppressing the crystal growth of 1–D ZnO along the c-axis, resulting in the generation of non-uniform nanocrystals.[20] During the secondary nucleation process, negatively charged biotemplate initiates the assembling of 1–D nanocrystals into a 3–D array to form hierarchical ZnO superstructures. After the complete nucleation of crystals, FTO substrate uniformly covers with the hierarchical 3–D ZnO superstructures.

### 6.3.4 DIFFUSE REFLECTANCE UV–VISIBLE ABSORPTION SPECTRA ANALYSES

Optical behaviour of both *in-situ* grown ZnO heterostructures are examined by recording the UV–Vis diffuse reflectance spectra in the wavelength range of 300–800 nm and depicted in figure **6.3.4 (A)**. Absorption edge of *in-situ* grown 1–D ZnO NWs and 3–D hierarchical ZnO superstructures are observed at ~ 397 nm and ~ 378 nm, relate to the optical band gap of ~ 3.12 eV and ~ 3.28 eV respectively. Hence, there is a hypsochromic shift in the absorption onset of hierarchical 3–D ZnO structures with respect to 1–D ZnO NWs which is mainly due to the integration of smaller size dimension of 1–D building blocks to form hierarchical structures. ZnO NWs accomplish in absence of templating agent have larger particle size with respect to 1–D nanocrystals which are to be self-assembled. Moreover, this hypsochromic shift is further verified by estimating the energy band gap ($E_g$) of both heterostructures by using Tauc's plots, as

 Part of this chapter has been published in **J. Mater. Chem. A 2018, 6, 15868–15887**.

represented in inset of figure **6.3.4 (A)**. For Tauc plot, $(\alpha h\upsilon)^2$ is plotted against the photon energy ($h\upsilon$) and a line is extrapolated to x-axis to calculate the optical energy band gap. As estimated optical band gap energies for *in-situ* grown 1–D ZnO NWs and 3–D hierarchical ZnO superstructures are observed to be ~ 3.231 eV and ~ 3.294 eV respectively which are in accordance with the values noticed from absorption spectra.

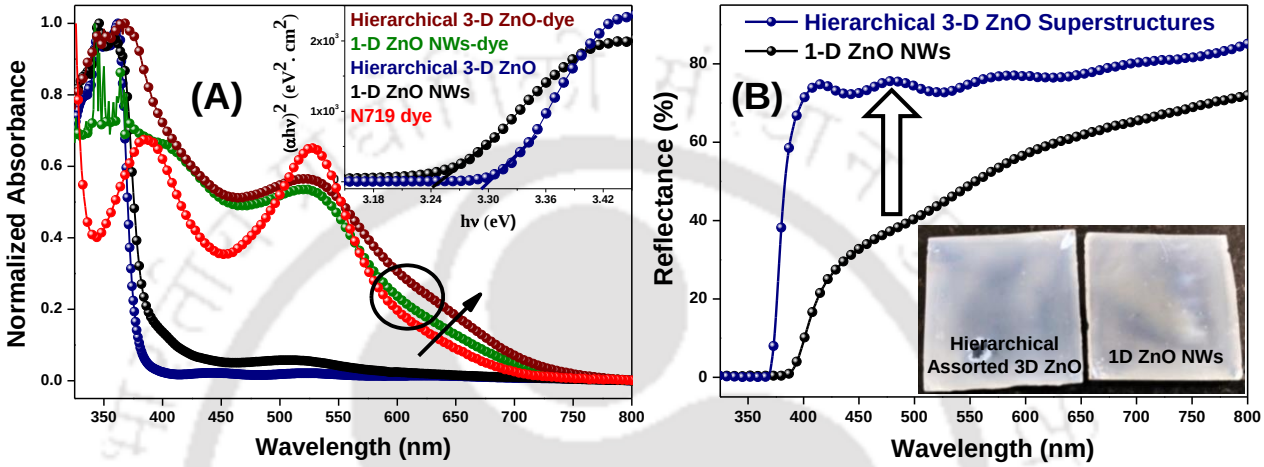


**Figure 6.3.4 (A)** Normalized UV–Visible absorption spectra of *in-situ* grown ZnO heterostructures i.e., hierarchical 3–D ZnO superstructure (navy blue line), 1–D ZnO NWs (black line), N719 dye (red line), dye sensitized hierarchical 3–D ZnO superstructures film (wine red line) and dye sensitized 1–D ZnO NWs film (olive line) while inset of this figure depicts the Tauc's plot of both ZnO heterostructures. Trace **(B)** represents the Diffused reflectance spectra of *in-situ* grown heterostructures (hierarchical 3–D ZnO superstructure and 1–D ZnO NWs), grown on FTO coated glass substrate and inset of this plot shows the digital photographs of both ZnO heterostructures.

Subsequently, this clear shift in energy band gap estimation is further advocating the hypsochromic shift in the absorption profile of hierarchical structures as compared to 1–D ZO NWs. Optical behaviour of N719 dye sensitized *in-situ* grown ZnO heterostructures along with bare dye are also studied, depicted in figure **6.3.4 (A)**. It is well established that N719 dye shows a broad absorption profile in the visible region (400–650 nm) with absorption onset of about 700 nm. Dye sensitized photoanodes show the characteristic absorption profile for both the constituents i.e., ZnO as well as N719 dye, indicative of successful loading of N719 dye onto the thin films. Moreover, a hyperchromic shift is observed in the absorption edge of hierarchical structure based photoanode contrary to ZnO NWs based photoanode because of effective anchoring of sensitizer molecule, revealing higher sensitizer loading with better surface aspect ratio. Therefore, light harnessing capability of hierarchical superstructures based photoanode gets enriched with more loading of dye and generated the large flux of photoexcited electrons which


Part of this chapter has been published in **J. Mater. Chem. A 2018, 6, 15868–15887**.

encouraged the upsurging in the population of charge injection and collection to enhance the photovoltaic performance of device.

Diffuse reflectance measurements are performed to examine the light scattering effect in both type of *in-situ* grown ZnO heterostructures having similar thickness, depicted in figure **6.3.4 (B)**. Large reflectance value is noticed for hierarchical structure in contrast to 1–D ZnO NWs in the wavelength range of 420–800 nm, suggesting the more consumption of incident light by means of increased optical path length through multiple internal reflections which is helpful in repetitive excitation of sensitizer molecules. Therefore, improved light harnessing capability of hierarchical 3–D ZnO structure will ascertain a crucial role to improve the photon conversion efficiency of hierarchical superstructures based photovoltaic device.

### 6.3.5 STEADY STATE AND TIME RESOLVED PHOTOLUMINESCENCE ANALYSES

Room temperature steady-state and dynamic photoluminescence (PL) analyses are carried out to investigate the surface defect states and excited state charge transfer processes of in situ grown ZnO heterostructures, measured at an excitation wavelength of 325 nm and represented in figure **6.3.5 (A)** and **(B)**. A regular static quenching in the PL intensity is noticed in the steady-state PL spectra of hierarchical superstructures with respect to 1–D ZnO NWs, indicative of having lesser trap sites for electron–hole recombination. For both *in-situ* structures, we have observed a characteristic emission peak in the UV region along with a strong peak at around ~ 467 nm and a weak intense peak at around ~ 563 nm. The emission peak in the UV range is mainly associated with the radiative recombination of the photogenerated electron–hole pair at the near band-edge of the ZnO crystal.[21] Various emission peaks in the range of ~ 410–490 nm along with a sharp peak at ~ 467 nm are ascribed to the structural defects associated with the zinc vacancies of the ZnO structures. An emission peak at around ~ 563 nm is also observed which is mainly related to the inherent defects of the crystal structure caused by oxygen vacancies.[22] Moreover, the PL emission intensity due to oxygen defects gets quenched in case of hierarchical structures, as compared to ZnO NWs, indicating the occurrence of less oxygen defect sites in hierarchical structures contrary to ZnO NWs. This observation supports the better charge transport in 3–D ZnO hierarchical superstructures and also suggests the reduced population of trap sites due to the close proximity of integrated 1–D nanocrystals.


Part of this chapter has been published in **J. Mater. Chem. A 2018, 6, 15868–15887**.

Time-resolved photoluminescence (TRPL) measurements are performed to further monitor the kinetics of the excited state charge transport for both the in situ grown heterostructures. Measurements are carried out using the as-fabricated *in-situ* thin films and a 375 nm laser excitation source, as depicted in figure **6.3.5 (B)**.

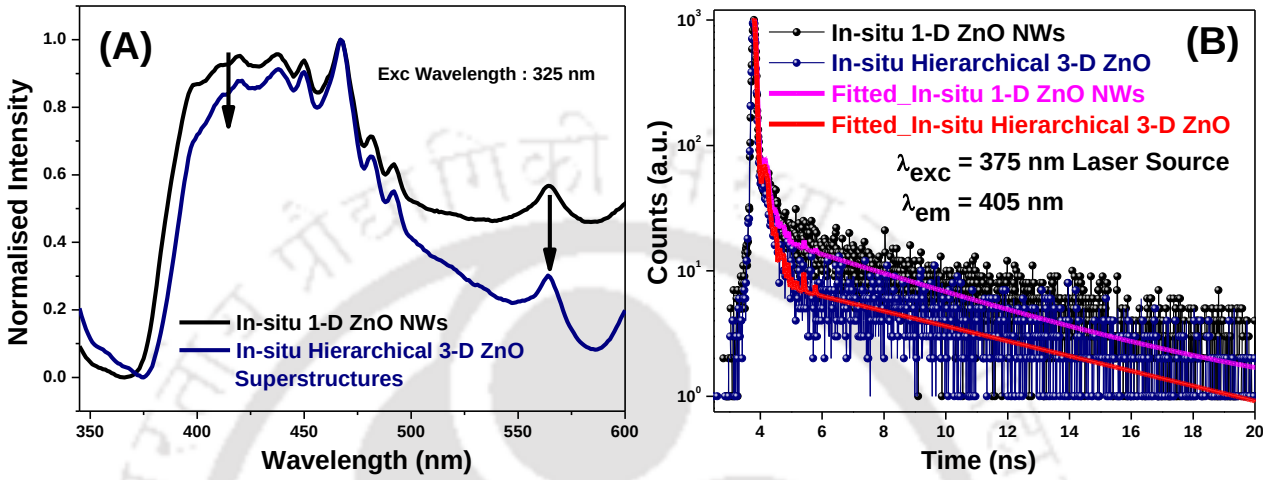


**Figure 6.3.5 (A)** Normalized Steady-state photoluminescence spectra of *in-situ* grown ZnO structures i.e., hierarchical 3–D ZnO superstructure (navy blue line), 1–D ZnO NWs (black line)] at the excitation wavelength of 325 nm while **6.3.5 (B)** shows Time-resolved photoluminescence (TRPL) spectra for both *in-situ* structures at an excitation wavelength of 375 nm.

Both the decay patterns are fitted with a tri-exponential function, using fast software provided by Edinburgh instruments to estimate the average exciton lifetime. Several processes are involved in the decay of emissive excitons in the multi-exponential decay patterns. Values of several fitting parameters such as ($\chi^2$) and exciton lifetimes ($\tau_1$, $\tau_2$, $\tau_3$), pre-exponential factors ($\alpha_1$, $\alpha_2$, $\alpha_3$), average exciton lifetimes ($<\tau>$) etc. are briefed in Table **6.3.1**. Average lifetime values are derived from **equation (1)**:[23]

$$<\tau>=\frac{\sum_i \alpha_i \tau_i^2}{\sum_i \alpha_i \tau_i} \qquad (1)$$

In figure **6.3.5 (B)**, decay pattern for hierarchical ZnO superstructures is faster with respect to 1–D ZnO NWs, revealing the better charge transfers due to the presence of fewer recombination sites in the hierarchical superstructures. From Table **6.3.1**, the estimated average exciton lifetime values for ZnO NWs and hierarchical ZnO structures are found to be ~ 6.526 ns and ~ 5.302 ns, respectively. Moreover, a gradual decrement in the average exciton lifetime is observed in the


Part of this chapter has been published in **J. Mater. Chem. A 2018, 6, 15868–15887**.

case of hierarchical structures with respect to NWs, which implies the enhanced charge transfer in the photoanodic segment. Larger value of the exciton lifetime for ZnO NWs is mainly associated with the presence of a greater population of structural defects that act as trap sites for the recombination of photoexcited electron–hole pairs.

**Table 6.3.1** Estimated fitting parameters such as ($\chi^2$), exciton lifetimes ($\tau_1$, $\tau_2$, $\tau_3$), pre-exponential factors ($\alpha_1$, $\alpha_2$, $\alpha_3$), average exciton lifetimes ($<\tau>$) for 1–D ZnO NWs and hierarchical 3–D ZnO superstructure are summarized in the following table:

| **Samples** | **$\chi^2$** | **$\tau_1$ (ns)** | **$\tau_2$ (ns)** | **$\tau_3$ (ns)** | **$\alpha_1$ (%)** | **$\alpha_2$ (%)** | **$\alpha_3$ (%)** | **$<\tau>$ (ns)** |
|---|---|---|---|---|---|---|---|---|
| **1–D ZnO NWs** | 1.005 | 0.021 | 0.754 | 6.879 | 73.85 | 7.86 | 18.27 | 6.526 |
| **Hierarchical 3–D ZnO structures** | 0.998 | 0.024 | 0.048 | 5.358 | 67.96 | 1.64 | 30.08 | **5.302** |

Excited state charge interactions and injection kinetics between N719 dye and *in-situ* structures are monitored by recording the static PL spectra of the bare dye and dye sensitized heterostructures at an excitation wavelength of 505 nm with respect to the dye, as shown in figure **6.3.6 (A)**. From this plot, the N719 dye exhibits the emission peak at around 756 nm. The PL intensity of the dye was gradually quenched when it became anchored to the surface of *in-situ* grown ZnO structures, validating the occurrence of excited-state electronic interactions between dye and ZnO. This observation supports the probability of photogenerated charge injection from the dye to the ZnO structures. Based on the energy band positions of the dye (CB edge ~ – 3.64 eV) and ZnO (CB edge ~ – 4.24 eV), a photocurrent is generated due to the feasible photogenerated electron injection from the lower unoccupied molecular orbital (LUMO) of the dye to the conduction band (CB) of ZnO. It is obvious from the spectrum that there is a gradual decrement in the PL intensity of the composite materials with respect to the pristine dye, suggesting the improved charge kinetics with lesser trap sites. Furthermore, the emission intensity of the 3–D ZnO hierarchical structure is more quenched with respect to ZnO NWs, indicative of effective charge separation and transport in the hierarchical structure based photovoltaic device. TRPL analysis is carried out to gain insight about the kinetics of photoexcited electron injection with the corresponding decay patterns, measured by using a 475 nm laser excitation source, displayed in figure **6.3.6 (B)**.


Part of this chapter has been published in **J. Mater. Chem. A 2018, 6, 15868–15887**.

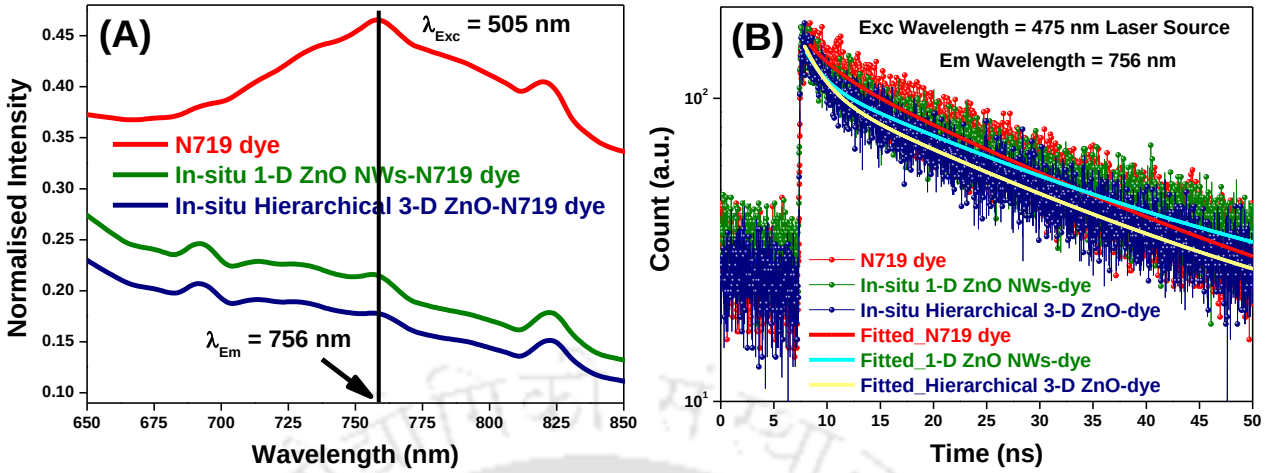


**Figure 6.3.6 (A)** Normalized Steady-state photoluminescence spectra of N719 dye (red line), *in-situ* hierarchical 3–D ZnO superstructure–dye (olive line) and *in-situ* 1–D ZnO NWs–dye (navy blue line) at an excitation wavelength of 505 nm while figure **6.3.6 (B)** depicts the Time-resolved photoluminescence spectra for the bare N719 dye and dye sensitized ZnO structures at an excitation wavelength of 475 nm.

**Table 6.3.2** Calculated parameters such as fitting parameter ($\chi^2$), exciton lifetimes ($\tau_1$, $\tau_2$) (ns), pre-exponential factors ($\alpha_1$, $\alpha_2$) (%), average exciton lifetimes (<τ>) (ns) for N719 dye, 1–D ZnO NWs–dye as well as hierarchical 3–D ZnO superstructure-dye and electron injection rate constants ($k_{einj}$) ($S^{-1}$) for 1–D ZnO NWs–dye and hierarchical 3–D ZnO superstructure–dye are mentioned in the following table:

| **Samples** | $\chi^2$ | $\tau_1$ (ns) | $\tau_2$ (ns) | $\alpha_1$ (%) | $\alpha_2$ (%) | <τ> (ns) | $K_{einj}$ ($s^{-1}$) |
|---|---|---|---|---|---|---|---|
| **N719 Dye** | 1.018 | 1.728 | 24.447 | 3.143 | 96.857 | 24.395 | ------ |
| **1–D ZnO NWs–dye** | 1.048 | 2.082 | 24.055 | 5.270 | 94.730 | 23.949 | $\mathbf{0.76\times10^6}$ |
| **Hierarchical 3–D ZnO–dye** | 1.060 | 2.633 | 23.486 | 2.783 | 97.217 | 23.410 | $\mathbf{1.72\times10^6}$ |

The bi-exponential function is used for fitting the decay patterns, and the average exciton lifetime values are calculated using **equation (1),** as mentioned in Table **6.3.2**. From figure **6.3.6 (B)**, we notice that both decay patterns related to dye-sensitized ZnO structures are faster as compared to the pristine N719 dye, enlightening the photo-excited electron injection from the LUMO of the dye to the CB of ZnO. From Table **6.3.2**, the as-estimated average exciton lifetime values for the N719 dye, dye–1–D ZnO NWs and dye–3–D hierarchical ZnO are found to be ~ 24.395 ns, ~ 23.949 ns and ~ 23.410 ns, respectively. Accordingly, (<τ>) of the hierarchical superstructure-based composite is considerably decreased as compared to the 1–D NWs-based composite and this observation reflects better charge transfer in the hierarchical structure based photoanodic film. Charge injection from the dye to ZnO should be the only pathway for the


Part of this chapter has been published in **J. Mater. Chem. A 2018, 6, 15868–15887**.

deactivation of excited dye molecules, so the rate of electron injection ($k_{einj}$) was calculated from **equation (2)** and is listed in Table **6.3.2**:[23]

$$k_{einj} = \frac{1}{<\tau>_{dye-ZnO}} - \frac{1}{<\tau>_{dye}} \qquad (2)$$

From Table **6.3.2**, the as-calculated keinj values for the 1–D ZnO NWs–dye and hierarchical 3–D ZnO–dye are found to be ~ 0.76 × $10^6$ $s^{-1}$ and ~ 1.72 × $10^6$ $s^{-1}$, respectively. The as-obtained higher value of $k_{einj}$ for the hierarchical 3–D ZnO based composite encourages the faster charge injection dynamics, indicative of lesser recombination processes and support to meet the better device efficiency.

### 6.3.6 RAMAN SPECTRA

Raman spectroscopy is an essential technique to explain the several characteristics of materials such as their crystallization, structural disorder and optical properties. Figure **6.3.7** shows the typical room temperature Raman spectra of *in-situ* grown ZnO heterostructures [hierarchical 3–D ZnO superstructure (navy blue line) and 1–D ZnO NWs (black line)] on FTO substrates, carried out at an excitation of 514 nm.

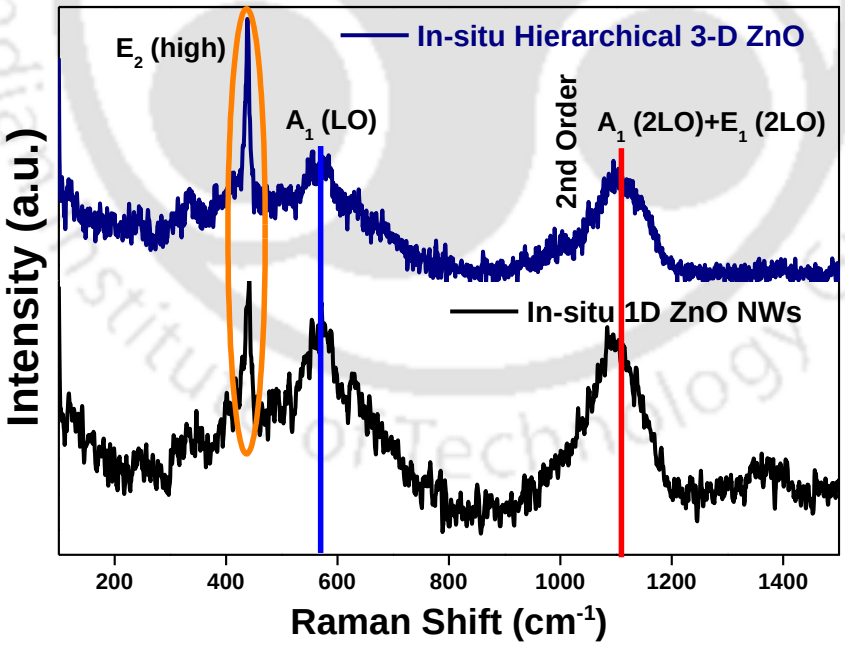


**Figure 6.3.7** Room temperature micro Raman spectra of *in-situ* grown ZnO heterostructures thin films [hierarchical 3–D ZnO superstructures (navy blue line) and 1–D ZnO NWs (black line)] fabricated on FTO coated glass substrates at an excitation of 514 nm.

For both the structures, a sharp and dominant peak is observed at 438 $cm^{-1}$, assigned to the E2 (high) mode of wurtzite hexagonal ZnO lattice which is mainly due to the vibration of oxygen sub-lattices in the non-polar modes.[24] This mode is likely to be considered as a fingerprint for the crystallinity of wurtzite ZnO which reflects the purity of crystal structure for both *in-situ* grown structures. Subsequently, it is noticed that there is no shift in the peak positions of the wurtzite hexagonal ZnO lattice, confirming the purity of crystal phase of both structures. The E2 (high) peak of hierarchical structure is found to be more sharp and intense as compared to 1–D NWs, associated with the higher oxygen content which may lead to reduce the structural defect related to oxygen vacancy. The suppressed peak at 571 $cm^{-1}$ is associated to A1 (LO) mode, which may appear due to c-axis growth pattern of wurtzite ZnO. In the figure **6.3.7**, a broad Raman peak is noticed at 1106 $cm^{-1}$, attributed to multi-phonon modes having combination of single phonon mode i.e., A1+ E2.[24] This multi-phonon scattering modes of 1–D ZnO NWs exhibit a blue Raman shift with respect to 3–D hierarchical superstructures, due to the optical phonon confinement, presence of more structural defects or impurities in the 1–D ZnO NWs.

### 6.3.7 PHOTOVOLTAIC MEASUREMENTS OF THE SOLAR CELLS

To validate the supremacy of 3–D hierarchical superstructures over the 1–D NWs in terms of better light harvesting and charge transport ability, photovoltaic measurements are performed by fabricating the dye (N719) sensitized photovoltaic devices based on both the *in-situ* grown structures, under solar light irradiation of 100 mW $cm^{-2}$ with AM 1.5 G. Figure **6.3.8 (A)** represents the current density–voltage (*J*–V) curves for both devices. As-calculated values of all performance parameters such as, short circuit current density ($J_{sc}$), open circuit voltage ($V_{oc}$), fill factor (FF) and the overall power conversion efficiency (PCE, η) are given in table **6.3.3**. Based on the calculated photovoltaic parameters, PCE of hierarchical 3–D ZnO superstructures based device is found to be higher in contrast to 1–D ZnO NWs based device which supported the advancement of hierarchical superstructures over NWs. In the earlier observations, it is clear that the hierarchical superstructures have large surface to volume ratio for higher loading of the light responsive material, resulting in enhanced light harvesting capability of solar device. Moreover, hierarchical superstructures also reveal the better separation and transportation of photogenerated electron–hole pair, accredited to lesser surface defects for recombination

 Part of this chapter has been published in **J. Mater. Chem. A 2018, 6, 15868–15887**.

processes which facilitate the improved interfacial charge transfer, as confirmed from TRPL analysis.

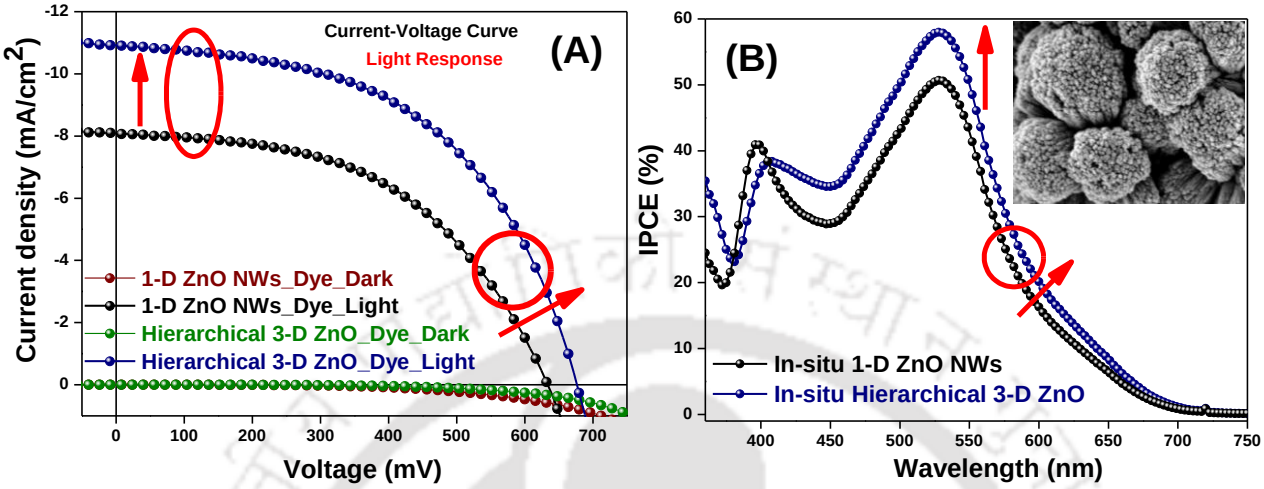


**Figure 6.3.8 (A)** Current density–Voltage (*J*–V) curve for both *in-situ* grown ZnO heterostructures based devices. **(B)** Incident photon to current conversion efficiency plot for the respective devices. Inset of figure **6.3.8 (B)** shows the *in-situ* grown hierarchical 3–D ZnO superstructures, helpful for the effective light utilization owing to provide higher loading sites for sensitizer adsorption.

**Table 6.3.3** Photovoltaic performance parameters such as short-circuit current density ($J_{sc}$), open-circuit voltage ($V_{oc}$), fill factor (FF) and power conversion efficiency (η) along with dye adsorption (mol $cm^{-2}$) for as-fabricated photovoltaic devices based on both ZnO heterostructures are mentioned in the following table:

| **Photovoltaic Device (N719 dye)** | **Dye Loading (mol $cm^{-2}$ )** | **$J_{sc}$ (mA $cm^{-2}$)** | **$V_{oc}$ (mV)** | **FF (%)** | **PCE (η, %)[a]** | **$IPCE_{max}$ (%)** |
|---|---|---|---|---|---|---|
| ***In-situ* 1–D ZnO NWs** | **~ 0.47 × $10^{-8}$** | ~ 8.18 | ~ 633 | ~ 49.78 | **~ 2.57** | ~ 50.61 |
| ***In-situ* hierarchical 3–D ZnO structure** | **~ 1.18 × $10^{-8}$** | **~ 10.89** | **~ 676** | **~ 52.12** | **~ 3.83** | **~ 58.02** |

[a]PCE value for the best performed device out of 5 identical devices.

Therefore, the as-calculated values of all photovoltaic parameters such as $J_{sc}$ ($mAcm^{-2}$), $V_{oc}$ (mV), FF (%) and PCE, η (%) for hierarchical 3–D ZnO superstructures based devices are found to be higher with respect to 1–D NWs based device which are observed to be ≈ 10.89, ≈ 676, ≈ 52.12 and ≈ 3.83 while ≈ 8.18, ≈ 633, ≈ 49.78, ≈ 2.57 for NWs based device. As obtained, higher $J_{sc}$ value in the 3–D ZnO hierarchical superstructures based device is ascribed to the presence of more exposed surface area for sensitizer loading, resulting in improved light harvesting which is accounted for increasing the flux of photoinduced electron injection. Furthermore, based on the

quantitative estimation of chemisorbed dye molecules on the surface of metal oxide heterostructures, it is found that the 3–D hierarchical structures based photoanode exhibited the higher loading of dye molecules viz. ~ $1.18 \times 10^{-8}$ mol $cm^{-2}$ while ~ $0.470 \times 10^{-7}$ mol $cm^{-2}$ for 1–D ZnO NWs based photoanode. This observation further confirmed the statement of upsurge in the generation of photogenerated electrons and improved charge injection as well as collection which is attributed to enhance the current density of the solar device. Moreover, *in-situ* growth of hierarchical superstructures over multinucleated ZnO seed layer offers better electrical connectivity with low Ohmic resistance between the ZnO structures and FTO substrate which encouraged the collection of photoexcited electrons with minimum obstacles. As-observed, higher $V_{oc}$ (≈ 676 mV) and FF (≈ 52.12 %) values for the 3–D ZnO hierarchical superstructures based device is likely to reflect the efficient separation of photoexcited electron–hole pair which encouraged the better interfacial charge transfers. This statement infers the reduced recombinations at electrode/electrolyte interface. Basically, 3–D ZnO structures are fabricated by integration of 1–D NWs in a very close manner due to which inter-particle electrical connectivity gets improved, facilitating the transport of the photogenerated electrons by minimizing the recombination sites. Improvement in the fill factor value for 3–D hierarchical ZnO based device is mainly associated to the improved photogenerated electron transport in the device and presence of lesser recombination sites, helpful to attain the high PCE value of device.

Incident photon-to-current conversion efficiency (IPCE) analysis is carried out for enhanced interpretation of photocurrent behavior of the as-fabricated solar devices, measured in the wavelength range of 360–750 nm as shown in figure **6.3.8 (B)**. Basically, IPCE of a solar device depends on (i) the light harvesting efficiency, (ii) the electron injection efficiency, and (iii) the injected electrons collection efficiency. From the figure **6.3.8 (B)**, both the IPCE plots follow the similar increasing trend as observed for $J_{sc}$ in current voltage (*J*–V) curve of solar devices. As-obtained higher $J_{sc}$ value due to the higher loading of sensitizer molecules, inhibited back transferring of photoexcited electrons and facilitated charge collection are also explicit in the IPCE value of hierarchical superstructures based device which is of about ~ 58.02 %. As-observed lower IPCE value (~ 50.61 %) for 1–D NWs based device reveals the lesser deposition of sensitizer molecules as having the lower surface area, which impede the light harvesting ability as well as performance of device. In the IPCE plot, a significant red shift is noticed at


Part of this chapter has been published in **J. Mater. Chem. A 2018, 6, 15868–15887**.

longer wavelength in case of hierarchical 3–D superstructures based device (navy blue line), occurring due to scattering of the incident light which is utilized for repetitive excitation of sensitizer molecules. Efficient light scattering ability of hierarchical ZnO superstructures based photoanode is probably due to large size of 3–D ZnO structures, as shown in the inset of figure **6.3.8 (B)**. Moreover, 3–D ZnO superstructures assembled with the 1–D ZnO nanocrystals encourage better transport pathway for faster interfacial transfers of photogenerated electrons to enhance the photovoltaic performance. Hence, better photovoltaic performance of hierarchical superstructures based solar device is confirmed with enhanced light harvesting and better charge transporting properties

### 6.3.8 ELECTROCHEMCIAL IMPEDANCE SPECTROSCOPY ANALYSIS

Electrochemical impedance spectroscopy (EIS) is considered to be a crucial technique for explaining the kinetics of interfacial charge transfers along with the numerous recombination processes, arise due to the electrochemical reactions occurring at various interfaces of solar device. EIS analysis are recorded in dark condition within the frequency range of 0.1 Hz to 100 kHz by employing a bias equivalent to open circuit voltage ($V_{oc}$), depicted in figure **6.3.9 (A)** & **(B)**. Usually, EIS of a dye sensitized solar device exhibits three different electrochemical behaviour, taking place at the various interfaces of device such as at counter electrode/electrolyte interface in the high-frequency region, at the ZnO/dye/electrolyte interface in the mid-frequency region (0.1 Hz to 1 kHz), and the diffusion of electrolyte in the low frequency region (0.1 Hz to 0.01 Hz). [26, 27] Figure **6.3.9 (A)** characterizes the Nyquist plots for both solar devices, measured at bias equivalent to $V_{oc}$ under dark condition in a frequency range of 0.1 Hz to 100 kHz. Both the Nyquist plots have two distinct semicircles, one in the medium frequency region (0.1 Hz to 1 kHz) whereas one in the higher frequency region (1–100 kHz). As-observed smaller semicircle is ascribed to the charge transfers and recombination processes, occurred at platinum and redox electrolyte interface while bigger semicircle is attributed to electrochemical processes taking place at photoanode and redox electrolyte interface. Interpretation of EIS measurements is basically carried out by fitting the impedance data into an equivalent electrical circuit which represents the different electrochemical processes occur at several interfaces of device. Inset of figure **6.3.9 (A)** displayed the equivalent circuit model used to fit the Nyquist plot and the parameters obtained from the fitted Nyquist plots are summarized in table **6.3.4**.

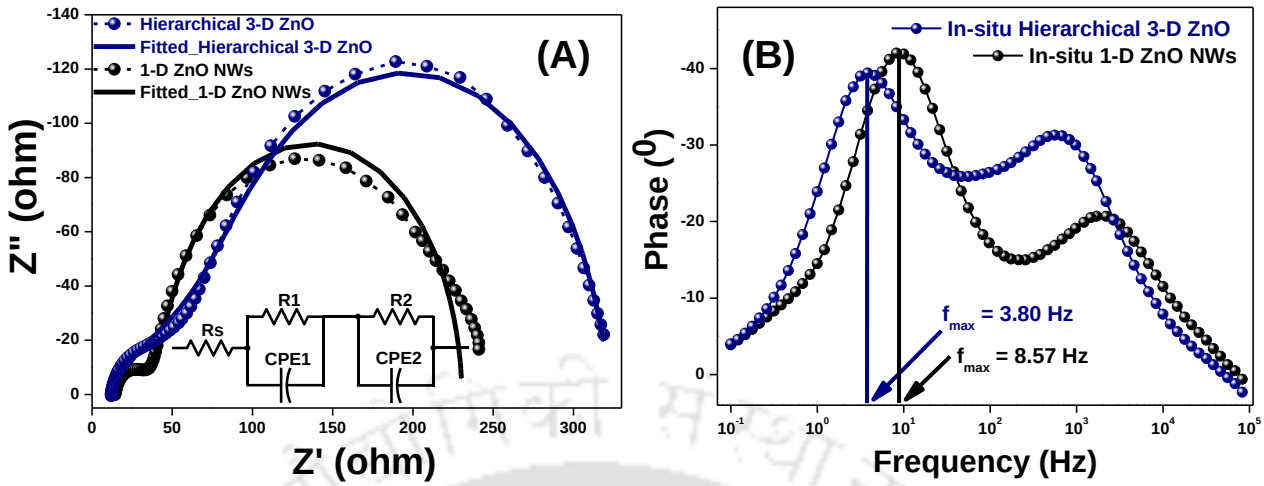


**Figure 6.3.9 (A)** Nyquist plot for as-fabricated photovoltaic devices based on both *in-situ* grown ZnO heterostructures. Inset of this plot depicts an equivalent circuit diagram with abbreviations: $R_s$, sheet resistance; R1 & R2 , charge-transfer resistance of the counter electrode and working electrode ; CPE1 & CPE2, constant-phase element of the counter electrode and working electrode respectively. **(B)** Bode phase plot for the respective photovoltaic devices.

It is established that the series resistance ($R_s$) mainly accounts for the transport resistance, occurring at the interface of transparent conductive oxide (TCO) substrate and ZnO film. From the table **6.3.4**, lower Rs value (~ 9.60 Ω) for hierarchical superstructures based photoanode is found as compared to 1–D NWs based photoanode (~ 11.91 Ω), advocating the close packing of 1–D nanocrystals in hierarchical structures and encouraging the better collection of photogenerated electrons at FTO substrate which contributes to enhance the current density of solar device. Fitting of the first semicircle yields $R_1$ and CPE–1 (a component of chemical capacitor), associated to the recombination resistance and capacitance offered at surface of Pt and electrolyte. Basically, the counter electrode (CE) of a DSSC is responsible to collect the electrons from the external circuit and reducing the oxidized form of the iodide/triiodide redox couple. The charge transfer between the CE and the electrolyte emerges as a voltage loss at the CE which contributes to substantiate the series resistance of the solar device. So, a CE must possess high recombination resistance for better separation of electron–hole, suggesting the better electrocatalytic activity and chemical stability. Subsequently, this observation is further supported with the as-obtained higher $R_1$ value (~ 110.30 Ω) in case of hierarchical superstructures based device with respect to 1–D NWs (~ 39.23 Ω) based device. In the Nyquist plot, the shifting of high-frequency peak for hierarchical structures based device is also observed, inferring faster electron transfer at the counter electrode-electrolyte interface that leads to reduce


Part of this chapter has been published in **J. Mater. Chem. A 2018, 6, 15868–15887**.

the recombination processes and advocating to the improved fill factor in same photovoltaic device. Bigger semicircle observed at medium frequency region is also fitted in a similar way as smaller circuit and generated the $R_2$ and CPE-2, attributed to recombination resistance and capacitance offered at interface of working electrode-electrolyte.

**Table 6.3.4** Fitted parameters such as sheet resistance ($R_s$), recombination resistance of the counter electrode and working electrode (R1 & R2), constant-phase element of the counter electrode and working electrode (CPE1 & CPE2), maximum peak frequency ($f_{max}$) and electron lifetime ($\tau_e$) for both devices based on *in-situ* grown ZnO heterostructures, are given in the following table.:

| **Photovoltaic Device (N719 dye)** | **Rs (Ω)** | **$R_1$ (Ω)** | **$R_2$ (Ω)** | **CPE1 (μF)** | **CPE2 (μF)** | **$f_{max}$ (Hz)** | **$\tau_e$ (ms)** |
|---|---|---|---|---|---|---|---|
| ***In-situ* 1–D ZnO NWs** | **~ 11.91** | ~ 39.23 | ~ 179.70 | ~ 593 | ~ 271 | ~ 8.57 | ~ **18.58** |
| ***In-situ* hierarchical 3–D ZnO structure** | **~ 9.60** | ~ 110.30 | ~ 203 | ~ 909 | ~ 532 | ~ 3.80 | ~ **41.90** |

From table **6.3.4**, it is found that the hierarchical superstructures based device showed higher $R_2$ value viz. ~ 203 Ω as compared to 1–D NWs based device having $R_2$ value of about ~ 179.70 Ω. Moreover, as-observed higher recombination resistance assists the statement of faster and better charge transport in case of hierarchical superstructures, reducing recombination process at the electrode/electrolyte interfaces. Enhanced $R_2$ value for hierarchical 3–D ZnO based device supports to large $V_{oc}$ value, obtained from *J*–V measurements. Hence, enhanced $V_{oc}$ value is mainly attributed to the better charge transport along one dimensional path (1–D ZnO NWs as the integrating building blocks) and better interfacial electron transfer. From table **6.3.4**, nearly two fold increment in capacitance value for hierarchical structure device (~ 532 μF) is observed as contrast to (~ 271 μF) of 1–D NWs based device, symptomatic of the higher population of photogenerated electrons in the conduction band. Therefore, the resistivity of 3–D ZnO device gets decreased which may be accounted for improving the photogenerated electrons density in the metal oxide. This observation enhances the collection efficiency of photo-excited electrons and contributes to enrich the efficiency of solar device.

Figure **6.3.9 (B)** represents the Bode phase plots for both the devices. Two different peaks correspond to two diode interfaces of the device are observed. Photoinduced electron lifetimes ($\tau_e$) can be estimated from maximum peak frequency ($f_{max}$) in the mid-frequency

 Part of this chapter has been published in **J. Mater. Chem. A 2018, 6, 15868–15887**.

region. The $\tau_e$ values for both devices are calculated by using the **equation (3)** [28] and mentioned in table **6.3.4**:

$$\boldsymbol{\tau_e = \frac{1}{2\pi f_{max}}} \qquad (3)$$

From table **6.3.4**, maximum peak frequencies for the hierarchical 3–D ZnO superstructures and 1–D ZnO NWs based devices are observed at ~ 3.80 Hz and ~ 8.57 Hz respectively and the corresponding $\tau_e$ value for both devices are estimated and found to be ~ 41.90 ms and ~ 18.58 ms respectively. Enhanced '$\tau_e$' value for hierarchical structures based device validates the minimized recombination processes, occurred due to back transferring of photoinduced electrons to the electrolyte at the working electrode/electrolyte interfaces. Subsequently, higher '$\tau_e$' value has also inferred that the photoinjected electrons spend more time in the photoanodic film before collecting at FTO substrate. Therefore, there is an enrichment of photoinduced electron density in CB of hierarchical 3–D ZnO which enhanced the $J_{sc}$ value and contributed to get the higher efficiency of solar device.

### 6.3.9 OPEN CIRCUIT VOLTAGE DECAY (OCVD) AND TAFEL POLARIZATION CURVE

To further corroborate the observations occurring in EIS analysis, open circuit voltage measurement is carried out by using a CHI680D electrochemical workstation. Charge transport and recombination kinetics processes of a DSSC are demonstrated by monitoring the nature of $V_{oc}$ decay pattern as a function of time. OCVD measurement is performed by illuminating the simulated solar light on the device to get the steady-state voltage, after which the illumination is turned off and the $V_{oc}$ decay pattern recorded as a function of time, depicts in figure **6.3.10 (A)**.[29] However, we observe the sharp $V_{oc}$ decay patterns for both the photovoltaic devices which are mainly due to recombinations occurring at the electrode/electrolyte interface. It is clear from the $V_{oc}$ decay patterns; the hierarchical 3–D ZnO superstructures based photoanode has a slower decay as compared to 1–D ZnO NWs based photoanode, symptomatic of the slower recombination kinetics in the earlier device. As observed, slower $V_{oc}$ decay in hierarchical superstructures based photoanode advocates the better charge transport by effectively impeding the back transfer of photoexcited electrons to the electrolyte and this statement is well supported to the supremacy of hierarchical structures, as claimed in the earlier discussion.


Part of this chapter has been published in **J. Mater. Chem. A 2018, 6, 15868–15887**.

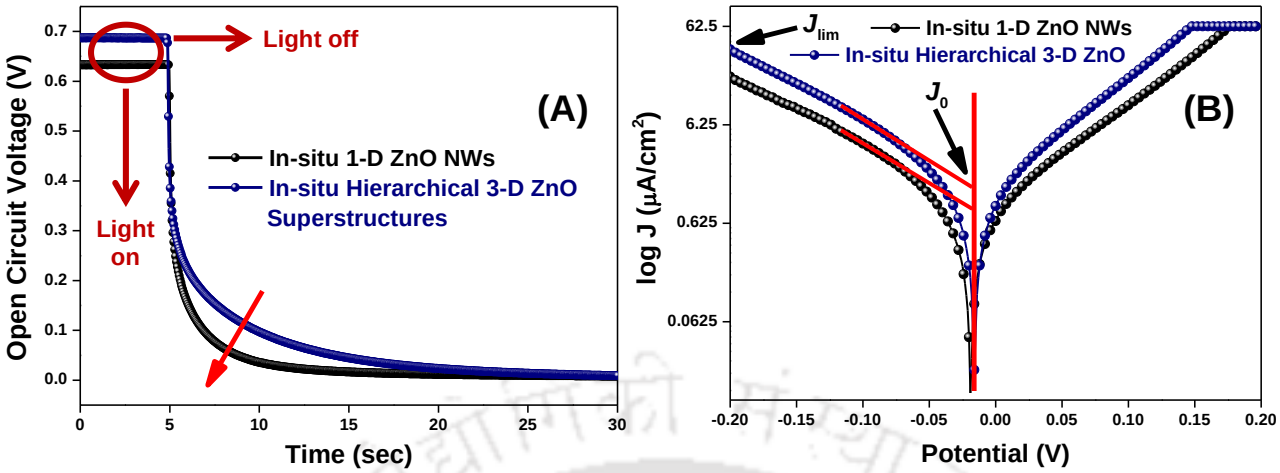


**Figure 6.3.10 (A)** Open-circuit voltage decay spectra of as-fabricated devices based on both *in-situ* grown ZnO heterostructures. Both decay curves are recorded after switching off the illumination. **(B)** Tafel polarization curves for both devices under dark condition.

In case of 1–D NWs based device, faster $V_{oc}$ decay pattern is noticed, attributed to presence of more structural defects which are responsible for the recombination of photoexcited electrons, resulting in lower PCE value.

Tafel polarization measurements are performed to analyze the kinetics of the interfacial charge transfer reactions, occurred at the electrode/electrolyte interfaces of the dye sensitized solar cell, recorded by using a CHI680D electrochemical workstation under the dark condition. Both the devices are swept with a bias potential range from –0.2 to +0.2 V at a scan rate of 10 mV/s, corresponding plots are depicted in figure **6.3.10 (B)**. The kinetics of the interfacial charge transfer reactions occurring at the electrolyte and ZnO photoanode interface can be represented using the Buttler–Volmer **equation (4)**;[30]

$$j = -j_o \left( \exp \frac{\alpha_c nF}{RT}(E - Eeq) - \exp \frac{\alpha_a nF}{RT}(E - Eeq) \right) \quad (4)$$

Where $j_0$ is the exchange current density; $\alpha_c$ and $\alpha_a$ are the anodic and cathodic transfer coefficients; E is the applied voltage and *Eeq* is the equilibrium potential of the iodide/triiodide redox system. It is evident from this equation that $j = -j_o$ as E = Eeq in the dark condition. Intersection point of the Tafel curves gives '$j_o$' which is directly correlated to the recombination reactions happening in the photovoltaic device. From the figure **6.3.10 (B)**, the behaviour of Tafel plot for both the device look very similar, signifying the smooth interfacial charge transfers at the electrode/electrolyte interface. Exchange current density values for both devices are

estimated by fitting the Tafel curves which are found to be ~ 1.46 μA/cm$^2$ for hierarchical superstructures based device and ~ 0.85 μA/cm$^2$ for 1-D NWs based device respectively. As observed '$j_o$' values for both heterostructures based solar devices are supporting the trend of recombination resistance ($R_1$ and $R_2$), obtained in EIS analysis and larger '$j_o$' value of hierarchical superstructures based device verified the enhanced photovoltaic performance over the 1–D NWs based device.

### 6.3.10 PHOTO-STABILITY OF SOLAR DEVICE

Operational photo-stability of solar devices is essential for actual practical application. Figure **6.3.11** depicts the photostability test for the best performing photovoltaic device based on hierarchical 3–D superstructures. Variation in values of all photovoltaic parameters, such as short circuit current density ($J_{sc}$), open circuit voltage ($V_{oc}$), Fill factor (FF) and the power conversion efficiency (η) are recorded over a period of more than 100 h under the solar irradiation (AM 1.5 G, 100 mWcm$^{-2}$) at ambient conditions without sealing.

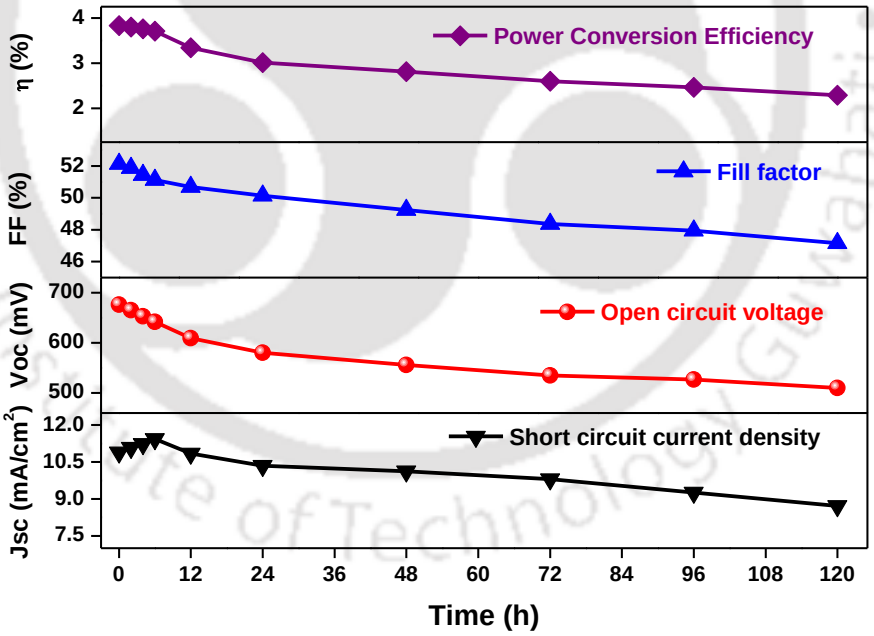


**Figure 6.3.11** Dependency of all photovoltaic parameters such as current density (mA/cm$^2$), open circuit voltage (mV), fill factor (%) and efficiency value (%) with respect to time under the solar irradiation (AM 1.5 G, 100 mWcm$^{-2}$) at ambient conditions to evaluate the photo-stability of the best performing photovoltaic devices.

Initially, Photo-current density of the device increases considerably upto first few hours, accredited to the better penetration of iodide/triiodide redox electrolyte through the photoanodic


Part of this chapter has been published in **J. Mater. Chem. A 2018, 6, 15868–15887**.

film, after that photo-current value decreases continually due to leakage and evaporation of electrolyte, results in reduced hole recovery rate of the electrolyte. Other parameters such as open circuit voltage, fill factor and power conversion efficiency are slightly decreases in the beginning hours and then constantly decreases as prolonged irradiation. Thus, there is ~ 32 % reduction in power conversion efficiency for hierarchical 3–D ZnO superstructures based photovoltaic device after 120 h duration. Based on the observations, we conclude that the photovoltaic device are quite stable initially but show a gradual drop in performance with increased time.

### 6.3.11 SENSING STUDIES OF CHEMIRESISITOR DEVICES

Two terminal chemiresistor devices based on both *in-situ* grown ZnO structures are fabricated and employed for the sensitive and selective detection of ammonia ($NH_3$) vapors by observing the changes in current intensity. All the measurements are performed using Keithley 4200–SCS, at room temperature under ambient conditions. To examine the conducting behaviour of both chemiresistor devices, current-voltage (*I*−V) measurement is performed by sweeping the voltage from −10 V to +10 V at room temperature with relative humidity (RH) 53 %, as presented in figure **6.3.12 (A)**. As-observed *I*−V curves of both sensing devices exhibit the good conducting nature through the establishment of Ohmic contact between the *in-situ* grown ZnO structures and FTO substrate. Before performing the sensing experiments, we have calibrated both sensor devices at the ambient conditions with RH 52 %. For calibrating the sensor before measurement, it is essential to install the sensor in such a position where the calibration can be performed easily and also possible to observe how fine the sensor can adjusted in any type of environment. Gas sensing calibration measurements are performed by sequentially measuring the current response as a function of time under ambient condition at relative humidity of RH 52 % without presence of any analyte vapors, as shown in figure **6.3.12 (B)**. In the blank stage, we have passed the voltage into the device without any analyte equivalent to 500 measurement cycles, and let the device current to be saturated, so that the contribution of the factors surrounding it will be minimized in the calibration. As shown in the calibration curves, initially, we observe a decrement in current response for both sensor devices with respect to time but after some time there is no significant change in current values over the time. After calibrating the sensor device, we have injected a calculated amount of various analyte vapors

onto the sensing device to check the selectivity of sensor devices. Selectivity of the metal oxide based gas sensing device is considered to be one of the major challenges. To demonstrate the selectivity of sensor devices, sensing experiments are carried out at room temperature with relative humidity of RH 49 %, by exposing the vapor of definite concentration (960 ppb) of common volatile organic solvents such as hexane, ethyl acetate, acetone, methanol, ethanol, isopropanol, tetrahydrofuran (THF) along with the much lesser concentration (96 ppb) of $NH_3$ vapors. Observations related to this experiment are displayed in figure **6.3.12 (C)**. From the observed trend, it is evident that the sensing response for both the devices is negligible towards the vapors of common organic volatile solvents while exhibiting the significant sensing response for the comparatively lower concentration of $NH_3$ vapors. Interestingly, with such notable selectivity and sensitivity towards $NH_3$ vapors, these sensor devices are considered to be rare example with respect to reported literature. After the selective sensing experiment, further sensing response of both the chemiresistor devices are evaluated at room temperature with relative humidity range of about RH 48 % by varying the concentration of $NH_3$ vapors from 24 ppb to 432 ppb based on the steady state measurements. Changes in the current intensity on varying the concentration of $NH_3$ vapors are observed for both the devices, presented in figure **6.3.12 (D)**. Steady state response of both sensor devices for $NH_3$ vapors sensing is essential for getting an idea about the saturation concentration of analyte vapors. From the figure **6.3.12 (D)**, there is not much changes in current intensity response beyond 336 ppb concentration of $NH_3$ vapors which may be due to complete coverage of all binding sites available for solid-gas interaction in metal oxides films. As far as concern of the sensing response, both sensing devices have shown the good sensitivity at very low concentration of $NH_3$ vapors which may be crucial for the detection of traces amount of $NH_3$ vapors during the explosive accidents. However, continual increment in the current intensity is noticed for both the devices with increase in the concentration of $NH_3$ vapors from 24 ppb to 432 ppb. For the hierarchical superstructures based sensing device, sharp increment of the current intensity is noticed at higher concentration of $NH_3$ vapors which is mainly due to the uniform distribution of vapor molecules on large exposed surface area of these nanostructured film.[31] Accordingly, as-observed high current response for hierarchical superstructures based device is reflective of large specific surface area and high electron mobility. 1–D NWs based sensing device showed lesser changes in the current with increased concentration of $NH_3$ vapors, due to lesser surface area for gas molecules adsorption.


Part of this chapter has been published in **J. Mater. Chem. A 2018, 6, 15868–15887**.

Additionally, multilayers of ammonia vapors may also be formed because of small exposed surface area for adsorption of high $NH_3$ vapors.

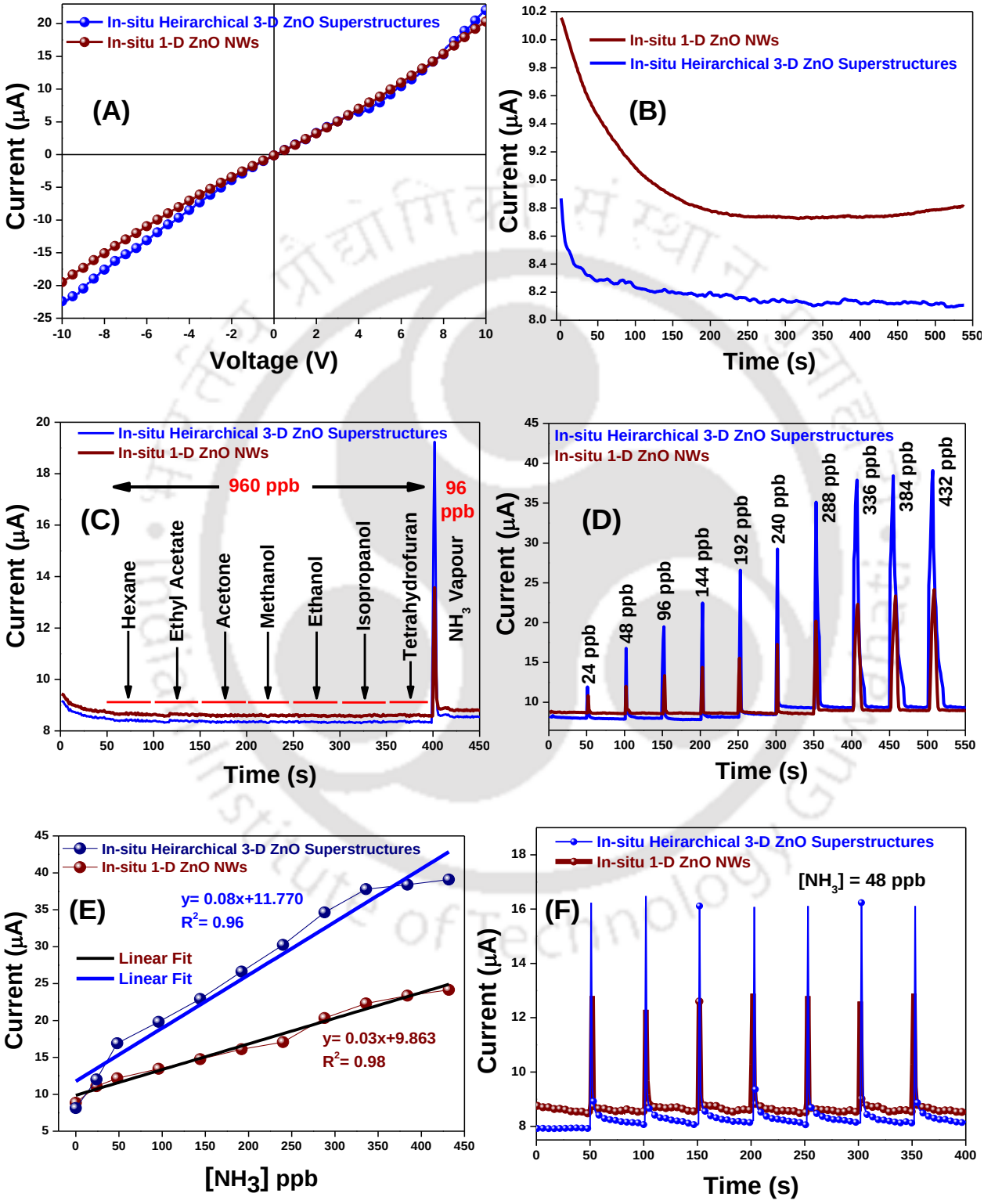


 Part of this chapter has been published in **J. Mater. Chem. A 2018, 6, 15868–15887**.

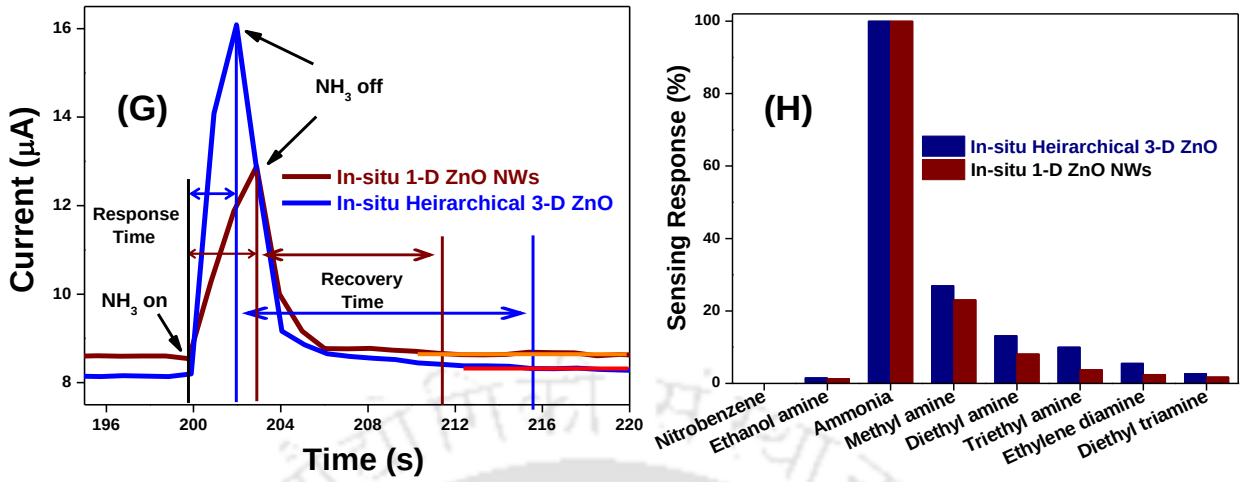


**Figure 6.3.12 (A)** *I*–V curve for as-fabricated vapor phase sensing devices based on in-situ grown ZnO structures, recorded at relative humidity of RH 53 %. **(B)** Gas sensing calibration curves for both in-situ grown heterostructures based sensor devices, measuring the current response as a function of time without injection of any analyte vapors under ambient condition at relative humidity of RH 52 %. **(C)** Sensing response of the as-fabricated chemiresistor devices based on both *in-situ* grown ZnO heterostructures with vapors of various common organic solvents as well as $NH_3$ at relative humidity of RH 49 %. **(D)** Sensing response for both devices towards various concentrations of $NH_3$ vapors (RH 48 %). **(E)** Calibration curve for calculating the limit of detection (LOD) of both chemiresistor devices as a function of $NH_3$ concentration. **(F)** Recyclability test of both chemiresistor devices with 48 ppb concentration of $NH_3$ vapors (RH 48 %). **(G)** Response and recovery time of the $NH_3$ sensing based on both devices. **(H)** Sensing response of the both chemiresistor devices with vapors of different amines, nitrobenzene as well as $NH_3$ (RH 47 %). All sensing measurements are carried out at room temperature.

As-decreased active sites present in the 1–D NWs film restrict the further interaction of $NH_3$ vapors with ZnO structures. Hence, current intensity response is not much changed at higher concentrations of $NH_3$ vapors. For the quantitative estimation as the limit of detection (LOD), calibration curve is plotted as the maximum current intensity response as a function of different concentration of $NH_3$ vapors, depicted in figure **6.3.12 (E)**. Subsequently, this curve is fitted linearly and calculates the slope (S) for each device with considerable correlation coefficients ($R^2$) values. LOD is calculated by using the mathematical expression viz., LOD = 3σ/S, where 'σ' is the relative standard deviation of the current response of sensor device in the absence of $NH_3$ vapors and 'S' is the slope of the calibration curve.[17] It is observed that LOD of hierarchical superstructures based device is found to be ~ 5 ppb while ~ 17 ppb for 1–D NWs based sensor device. Based on these lower LOD values, both sensor devices are reflected to be highly sensitive with respect to the minimum permissible limit for $NH_3$ in the working environment i.e. 25 ppm. Moreover, hierarchical 3–D superstructures based sensor device shows the higher sensitivity with lower LOD value which is mainly associated to the large surface area for better

adsorption of gas molecules and efficient electron transport for improved current response. To check the feasibility of these gas phase sensing device for practical application, reusability or recyclability test for both devices are carried out by exposing specific concentration (48 ppb) of $NH_3$ vapors after definite interval of time with RH 48%, represented in figure **6.3.12 (F)**. Consequently, it is found that both the devices exhibited approximately similar trend of change in current intensity. Hence, this observations support the viability of these sensing devices for realistic application. Response and recovery time is considered to be the essential parameter for determining the efficient usability of a vapor phase sensor device. Response time of a sensing device is the time required to change the 90 % of the current response after exposing the analyte vapor on the device while recovery time is the time elapsed in changing the 90 % of the current response to reach the original position after the turning off the analyte vapor. As-obtained trends of response and recovery times for both sensing devices are shown in in figure **6.3.12 (G)**. However, the calculated response/recovery time for hierarchical superstructures based sensing device is found to be 3s/13s whereas for 1–D NWs based sensing device it is 4s/9s, revealing the high sensitivity of both devices for the $NH_3$ vapors. Recovery time for hierarchical structure based device is more as compared to 1–D NWs based device, due to diffusion of $NH_3$ vapors into hierarchical superstructures which requires more time for its complete removal. To the extent of reported articles, such highly sensitive/selective $NH_3$ vapors sensing devices have not been reported yet and also showing remarkable response/recovery times for $NH_3$ vapors detection. Based on these observations, both sensing devices are highly suitable for the rapid detection of $NH_3$ vapors. Selectivity of both devices is further checked by exposing the vapors of nitrogen containing different organic solvent such as nitrobenzene, ethanolamine and several amines like methylamine, diethyl amine, triethyl amine, ethylene diamine, diethyl triamine along with $NH_3$ vapors with relative humidity of RH 47 %. From the in figure **6.3.12 (H)**, it can be seen that the sensitivity of both sensor devices is very less and insignificant towards the nitrogen containing different groups with respect to $NH_3$ vapors, even at much higher concentrations.

In general, sensing mechanism of metal oxide semiconductor based chemiresistor device comprises the binding of analytes on the surface of sensing device through the diffusion or dissociation and form a possible charge transfer complex, ultimately leading to improve the mobility of charge carriers on the surface of device, resulting in increment in the current of device.[32] Moreover, lesser trap sites in the crystal structure of ZnO also encourages the efficient

charge transport and this observation is more prominent in the hierarchical structures based sensing device. Based on chemical nature of device film and analyte, the binding may be weak or strong, and depends on the chemical interactions such as covalent bonding, hydrogen bonding, dipole–dipole interactions etc. As exposing the $NH_3$ vapors on the surface of ZnO based sensor devices, current intensity response shows significant change with a very low response time. This observation can be elucidated through the schematic of probable sensing mechanism, displayed in figure **6.3.13**. As-noticed change in current intensity may be explained by forming donor-acceptor complex between the $NH_3$ (electron donor) and n-type metal oxide i.e., ZnO (electron acceptor). Wurtzite crystal structure of ZnO consist alternative staking of $O^{2-}$ and $Zn^{2+}$ ions along the c-axis, reflecting the Zn–terminated (0001) and O–terminated (000$\bar{1}$) planes with higher surface energy. Therefore, ZnO has affinity to bind with $NH_3$ via an acid-base interaction and generated Zn–$NH_3$ complex ion pairs as the binding of $NH_3$ vapors on the surface of ZnO, due to which ionic conductivity of sensing device substantially improved and consequently current response of the device.

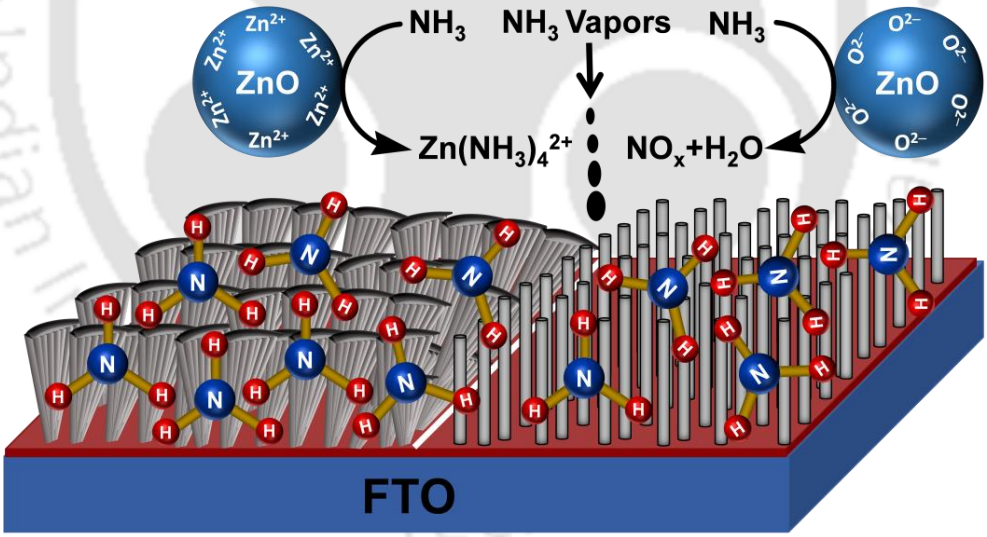


**Figure 6.3.13** Schematic illustration represents the probable sensing mechanism.

Additionally, sensing mechanism can also be explained on the basis of chemical interaction between $NH_3$ and oxygen species of ZnO, ascribed to release the electrons at the surface of ZnO, which leads to upsurge the charge carriers population and electrical conductivity of ZnO.


Part of this chapter has been published in **J. Mater. Chem. A 2018, 6, 15868–15887**.

For further confirming $NH_3$ adsorption and diffusion on ZnO based sensor device, Fourier Transform Infrared (FT–IR) analysis is performed as before and after exposure to $NH_3$ vapors and corresponding IR spectrum is depicted in figure **6.3.14**. In the absence of $NH_3$ vapors (trace a), we observe a sharp IR peak at 551 $cm^{-1}$, related to –Zn–O stretching vibration mode while IR peak at 3426 $cm^{-1}$ assigned to –O–H stretching vibration mode which may be observed due to moisture. After exposing the $NH_3$ vapors on sensing device trace **(b)**, a broad IR peak in the range of 3200–3600 $cm^{-1}$ is observed which corresponds to –N–H stretching vibration mode, advocating the adsorption/diffusion of $NH_3$ vapors onto device surface through an electronic interaction (acid–base interaction) between $NH_3$ and ZnO and consequently enhanced the electrical conductivity of the film. Additionally, after some time (30s), we again recorded the IR spectra to demonstrate the recovery of sensing device.

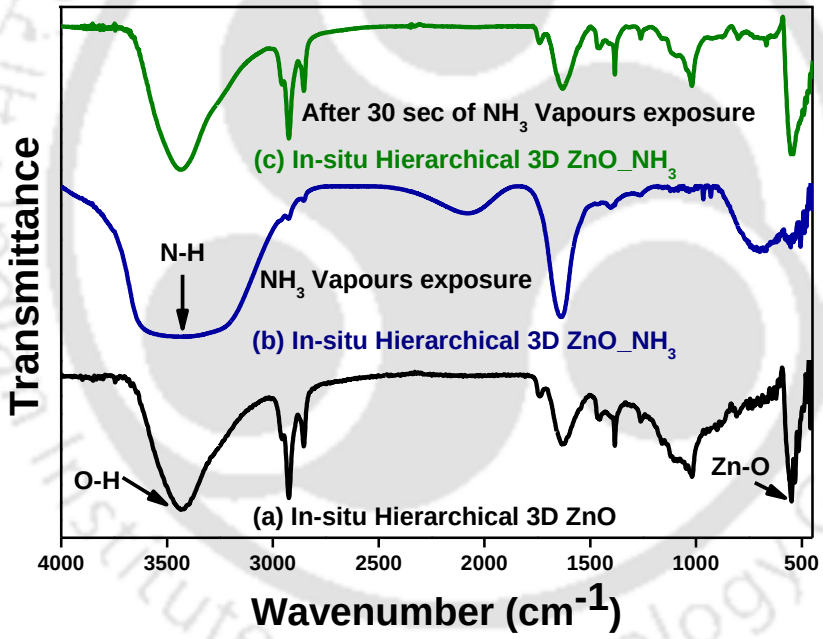


**Figure 6.3.14** FT–IR spectra of hierarchical structures based sensing device before [trace **(a)**] and after exposure of $NH_3$ vapors [trace **(b)**]. Trace c represents the FT-IR spectrum recorded after 30 s of $NH_3$ exposure.

From the IR spectrum [trace **(c)**], it is clear that there is no peak found as related to N–H stretching vibration mode which reflects the complete evacuation of $NH_3$ vapors from the surface of device, confirming the low recovery time of sensor device.

Additionally, the efficient adsorption of $NH_3$ vapors on the exposed surfaces of wurtzite ZnO structure is well explained in a schematic illustration, mentioned in figure **6.3.15**. Figure

**6.3.15** shows the three dimensional stacking model of Wurtzite ZnO showing Zn–terminated (0001) and O–terminated (000$\bar{1}$) polar planes. The exposed (0001) facets are polar surfaces and consist of a positive Zn-terminated $Zn^{2+}$–ZnO surface or $Zn^{2+}$ (0001) and a negative O–terminated $O^{2-}$–ZnO surface or $O^{2-}$ (000$\bar{1}$). In Wurtzite crystal structure, each layer contains all positive $Zn^{2+}$ions or all negative $O^{2-}$ions in the (0001) direction. Due to different atomic charges on Zn and O atoms, an internal electric field is generated between $Zn^{2+}$–ZnO (0001) and $O^{2-}$–ZnO (000$\bar{1}$) planes. Under the internal electric field, ZnO heterostructures with exposed (0001) polar facets efficiently separate electrons to positive polar $Zn^{2+}$–ZnO (0001) planes and holes to negative polar $O^{2-}$–ZnO (000$\bar{1}$) planes. Efficient charge separation between exposed polar (0001) surfaces can effectively reduce the probability of recombination of electrons and holes, thereby improving the charge transport leading to a better gas sensing response. Rapid charge separation occurs at the interface of the heterostructure and the body of sensing material, where in, electrons can efficiently react with analyte vapour during the sensing process and gets better sensitivity along with short response/ recovery times.[33]

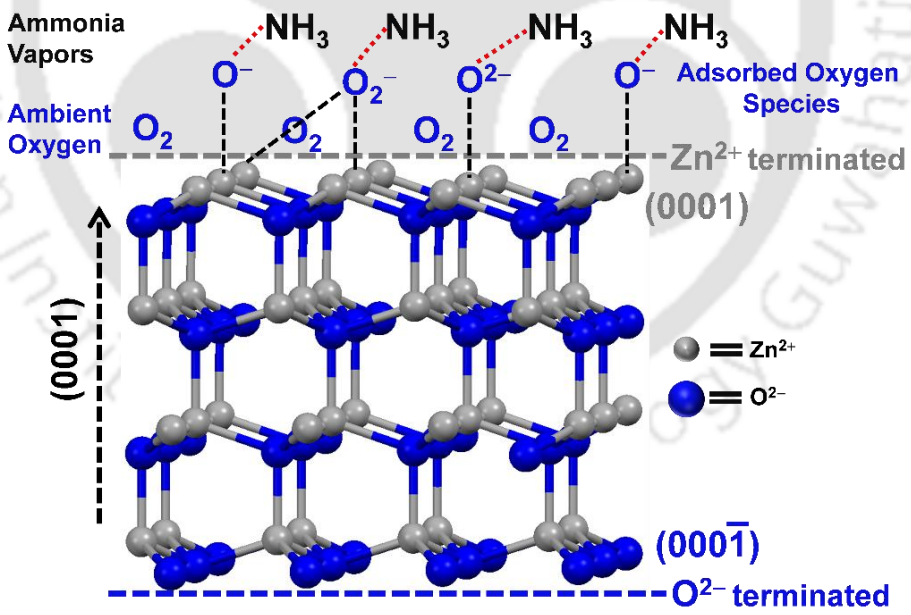


**Figure 6.3.15** Schematic illustration for the interaction of $NH_3$ vapors with chemisorbed oxygen species on $Zn^{2+}$ terminated sites of wurtzite ZnO structures.

The exposed surface of ZnO heterostructures adsorb oxygen molecules from the ambient gas components, which capture electrons from the conduction band of metal oxide and generate ion-

 Part of this chapter has been published in **J. Mater. Chem. A 2018, 6, 15868–15887**.

adsorbed oxygen species ($O^{2-}$, $O^{-}$ and $O_2^{-}$) on the surface of the sensing layer, as depicts in following **equations**.[34, 35]

$$O_2\,(g) \rightarrow O_2\,(ads) \quad (5)$$

$$O_2\,(ads) + e^{-} \rightarrow O_2^{-}\,(ads) \quad (6)$$

$$O_2^{-}\,(ads) + e^{-} \rightarrow 2O^{-}\,(ads) \quad (7)$$

$$2O^{-}\,(ads) + e^{-} \rightarrow O^{2-}\,(ads) \quad (8)$$

Reaction with the adsorbed oxygen ions can modify the intrinsic conductivity of a metal oxide by changing the carrier concentration. Hence, oxygen adsorption plays an important role in electrical transport properties of ZnO. Moreover, chemisorbed oxygen species are likely to reduce the grain boundaries of ZnO thin film and trapped free electrons from the conduction band, encouraging the efficient charge transfer processes at interface of analyte Vapors and sensing material. Consequently, due to high reactivity of these chemisorbed oxygen species, sensing surface of ZnO films becomes more sensitive for the interaction with reducing analyte species, $NH_3$ Vapors, in our case.[36] Therefore, $NH_3$ sensing response in both the sensing devices can be explained based on the efficient adsorption of $NH_3$ molecules at the surface of sensing material. Furthermore, inducing a change in the oxygen content on the surface of ZnO, a surface reaction or adsorption of another species, induces a broad, intense IR band with discrete weak bands superimposed on it.[37] In our case, we observe a broad IR band in the range of 3200–3600 $cm^{-1}$ after exposing the reducing species i.e., $NH_3$ Vapors on ZnO surface, as discussed earlier in FT–IR analysis. This broadness of IR spectrum is assigned to the electronic transition from a native donor level, the oxygen vacancy in the bulk of the domain, to the conduction band of the ZnO.

### 6.3.12 STABILITY OF CHEMIRESISTOR DEVICE

We have also checked the stability of hierarchical superstructures based chemiresistor devices to justify the claim of practical usability of the sensor device. After storage of these devices for 2 weeks initially and then 8 weeks at ambient conditions, sensitivity of the devices are tested by exposing the different concentration of $NH_3$ vapors at room temperature with relative humidity, RH 48 %. In figure **6.3.16**, it is observed that after analyte vapors exposure, current intensity responses of the stored device exhibited no significant changes in current response, advocating the stability of this sensor device under prolonged storage at ambient

conditions with no significant loss in sensitivity. Hence, sensing device is considered to be a stable and proficient for $NH_3$ vapors detection under practical conditions. Based on several sensing experiments like selectivity, sensitivity, LOD, recyclability, response/recovery time and stability, both sensing devices are demonstrated as cost-effective, stable and proficient for $NH_3$ vapors detection under practical conditions.

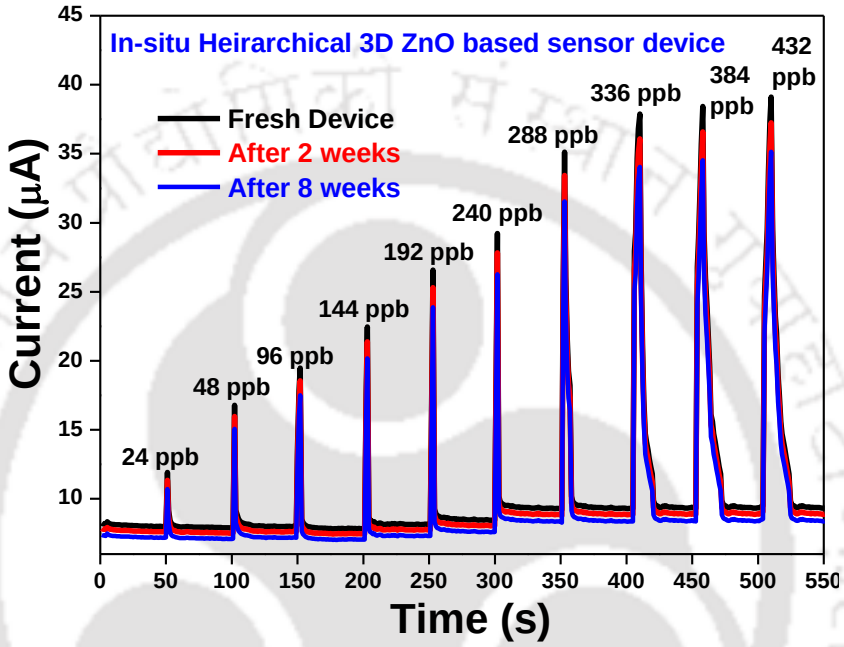


**Figure 6.3.16** Sensing response of the hierarchical structures based sensing devices (fresh, 2 weeks and 8 weeks old device, stored at ambient conditions) with different concentration of $NH_3$ vapors, obtained at room temperature with relative humidity range of about RH 48 %.

## 6.4 CONCLUSIONS

In summary, we have reported a biomass assisted *in-situ* growth of multifunctional hierarchical three dimensional (3–D) zinc oxide (ZnO) superstructures directly over FTO substrate using controlled hydrothermal synthetic route. Sulfate group containing an anionic polysaccharide "k-carrageenan" is employed for regulating the hetero epitaxial aggregated growth of 1–D nanocrystal. Non-classical growth mechanism is accounted for the fabrication of hierarchical 3–D superstructures. These superstructures are seemed to be formed by assembling the 1–D in a very compact manner due to which inter-particle electrical connectivity gets improved. As a result, good contact with low Ohmic resistance has played a very crucial role in the transport and collection of photogenerated charge carriers. Both ZnO heterostructures are utilized in photovoltaic as well as in selective chemical vapor sensing. A significant enrichment


Part of this chapter has been published in **J. Mater. Chem. A 2018, 6, 15868–15887**.

(~ 33 %) in power conversion efficiency (η) has been observed for hierarchical 3–D ZnO superstructures based photovoltaic device (η = ~ 3.83 %) as compared to 1–D ZnO NWs (η = ~ 2.57 %), mainly attributed to the larger surface to volume ratio for sensitizer loading, better light-scattering effect, better charge separation and collection. Two terminal sensor devices displayed high sensitivity and selectivity for $NH_3$ vapors with the LOD value of ~ 5 ppb for 3–D ZnO hierarchical superstructures while ~ 17 ppb for 1–D ZnO NWs, which is very less as compared to maximum permissible limit i.e., 25 ppm. As-observed high sensitivity of hierarchical superstructures based device for $NH_3$ vapors sensing is reflective of creating a good Ohmic contact in the 3–D hierarchical superstructures and FTO substrate with respect to 1–D structures. Additionally, large surface area and high electron mobility of 3–D structures also played a crucial role for better sensing ability to $NH_3$ vapors. We have also performed the other experiments such as selectivity, sensitivity, recyclability, response/recovery time and sensitivity for various amines, advocated these sensor devices as simple, consistent, economical and effective in the $NH_3$ detection under practical conditions.

## 6.5 REFERENCES


(1) Q. Zhanga and G. Cao, *J. Mater. Chem.*, 2011, **21**, 6769–6774.

(2) S. H. Ko, D. Lee, H. W. Kang, K. H. Nam, J. Y. Yeo, S. J. Hong, C. P. Grigoropoulos and H. J. Sung, *Nano Lett.*, 2011, **11**, 666–671.

(3) N. Memarian, I. Concina, A. Braga, S.M. Rozati, A. Vomiero and G. Sberveglieri, *Angew. Chem. Int. Ed.*, 2011, **50**, 12321–12325.

(4) M. S. Ansari, R. Maragani, A. Banik, R. Misra and M. Qureshi, *Electrochim. Acta.*, 2018, **259**, 262–275.

(5) S. Xu, Y. Ding, Y. Wei, H. Fang, Y. Shen, A. K. Sood, D. L. Polla and Z. L. Wang, *J. Am. Chem. Soc.*, 2009, **131**, 6670–6671.

(6) S. Sotiropoulou, Y. Sierra-Sastre, S. S. Mark and C. A. Batt, *Chem. Mater.*, 2008, **20**, 821–834.

(7) V. M. Guérin and T. Pauporté, *Energy Environ. Sci.*, 2011, **4**, 2971–2979.

(8) J. Qiu, M. Guo and X. Wang, *ACS Appl. Mater. Interfaces*, 2011, **3**, 2358–2367.

(9) T. L. Sounart, J. Liu, J. A. Voigt, M. Huo, E. D. Spoerke and B. McKenzie, *J. Am. Chem. Soc.*, 2007, **129**, 15786–15793.

(10) T. Zhang, W. Dong, M. K. Brewer, S. Konar, R. N. Njabon and Z. R. Tian, *J. Am. Chem. Soc.*, 2006, **128**, 10960–10968.

(11) T. R. Chetia, M. S. Ansari and M. Qureshi, *ACS Appl. Mater. Interfaces*, 2015, **7**, 13266–13279.

(12) Z. L. Wang, *Mater. Sci. Eng. R*, 2009, **64**, 33–71.

(13) C. Tang, M. J. S. Spencer and A. S. Barnard, *Phys. Chem. Chem. Phys.*, 2014, **16**, 22139–22144.

(14) A. Kalita, S. Hussain, A. H. Malik, N. V. V. Subbarao and P. K. Iyer, *J. Mater. Chem. C*, 2015, **3**, 10767–10774.

(15) R. Kumar, O. Al-Dossary, G. Kumar and A. Umar, *Nano-Micro Lett.*, 2015, **7**, 97–120.

(16) T. R. Chetia, M. S. Ansari and M. Qureshi, *Phys. Chem. Chem. Phys.*, 2016, **18**, 5344–5357.

(17) A. H. Malik, S. Hussain, A. Kalita and P. K. Iyer, *ACS Appl. Mater. Interfaces*, 2015, **7**, 26968–26976.

(18) X. Sun, J. Liu and Y. Li, *Chem.–Eur. J.*, 2006, **12**, 2039–2047.

(19) Z. Wang, X. F. Qian, J. Yin and Z. K. Zhu, *J. Solid State Chem.*, 2004, **177**, 2144–2149.

(20) X. M. Sun, X. Chen, Z. X. Deng and Y. D. Li, *Mater. Chem. Phys.*, 2002, **78**, 99–104.

(21) H. Zeng, G. Duan, Y. Li, S. Yang, X. Xu and W. Cai, *Adv. Funct. Mater.*, 2010, **20**, 561–572.

(22) X. L. Wu, G. G. Siu, C. L. Fu and H. C. Ong, *Appl. Phys. Lett.*, 2001, **78**, 2285–2287.

(23) A. Kongkanand, K. Tvrdy, K. Takechi, M. Kuno and P. V. Kamat, *J. Am. Chem. Soc.*, 2008, **130**, 4007–4015.

(24) K. A. Alim, V. A. Fonobarov, M. Shamsa and A. A. Balandin, *J. Appl. Phys.*, 2005, **97**, 124313-1–5.

(25) P. Wang, G. Xu and P. Jin, *Phys. Rev. B*, 2004, **69**, 113303.

(26) S. Phadke, A. D. Pasquier and D. P. Birnie, *J. Phys. Chem. C*, 2011, **115**, 18342–18347.

(27) M. S. Ansari, A. Banik and M. Qureshi, *Carbon*, 2017, **121**, 90–105.

(28) R. Kern, R. Sastrawan, J. Ferber, R. Stangl and J. Luther, *Electrochim. Acta*, 2002, **47**, 4213–4225.

(29) N. Memarian, I. Concina, A. Braga, S. M. Rozati, A. Vomiero and G. Sberveglieri, *Angew. Chem. Int. Ed.*, 2011, **123**, 12529–12533.

(30) J. N. Soderberg, A. C. Co, A. H. C. Sirk and V. I. Birss, *J. Phys. Chem. B*, 2006, **110**, 10401–10410.

(31) S. Hussain, T. Liu, M. S. Javed, N. Aslam and W. Zeng, *Sens Actuators B Chem.*, 2017, **239**, 1243–1250.

(32) M. Z. Dai, Y. L. Lin, H. C. Lin, H. W. Zan, K. T. Chang, H. F. Meng, J. W. Liao, M. J. Tsai and H. Cheng, *Anal. Chem.*, 2013, **85**, 3110–3117.

(33) Y. Yang, C. Tian, J. Wang, L. Sun, K. Shi, W. Zhou and H. Fu, *Nanoscale*, 2014, **6**, 7369–7378.

(34) T. J. Hsueh, C. L. Hsu, S. J. Chang and I. C. Chen, *Sens Actuators B Chem.*, 2017, **126**, 473–477.

(35) N. Yamazoe, J. Fuchigami, M. Kishikawa and T. eiyama, *Surf. Sci.*, 1979, **86**, 335–344.

(36) I. Paulowicz, V. Postica, O. Lupan, N. Wolff, S. Shree, A. Cojocaru, M. Deng, Y. K. Mishra, I. Tiginyanu, L. Kienle and R. Adelung, *Sens. Actuators B Chem.*, 2018, **262**, 425–435.

(37) S. Lenaerts, J. Roggen and G. Maes, *Spectrochim. Acta*, 1995, **51A**, 883–894.

# THESIS SUMMARY & FUTURE SUGGESTIONS

## Thesis overview :

*The work presented in this thesis revolves around the utilization of several photoanodic architechtures to improve the performance of 3rd generation photovoltaic systems i.e., dye-/quantum dots sensitized solar cells. Several efforts have been made to enhnace the solar light harvesting efficiency of sensitized solar cells, exploring the different morphologies of metal oxide and sensitizer materials. Naurally occuring biomass derived templating agents are used for tuning the morphologies of metal oxide. Chemiresistor devices based on different morphologies of metal oxide are fabricated for highly selective and ultrasensitive gas sensing application. Significant observations and improvements related to fabrication of hybrid photoanodes have been achieved during my PhD work. The summary and conclusions of each chapter are summarized as follows:*

- *In **Chapter 3**, we have demonstarted the beneficial effects of nanotubular structures of photo-booster g–$C_3N_4$ to improve the efficiency of a quantum dots sensitized solar cell (QDSSC). g–$C_3N_4$ nanotubes (NTs) are synthesized through morphological transformation of as-exfoliated g–$C_3N_4$ nanoflakes (NFs). Low temperature medium i.e., cold water is mainly used for morphological transformation of g–$C_3N_4$ NFs by means of a thermal gradient. Photo-booster effect of g–$C_3N_4$ NTs have investigated using the composites having ZnO Nanorods (ZnO NRs), sensitized by CdS quantum dots. We have observed a **~ 32 %** enhancement in power conversion efficiency (PCE, η) for the devices fabricated with composite ZnO NR–g–$C_3N_4$ NTs [**$\eta \approx 2.90$ %**, for an optimized weight ratio of 1:0.5] as compared to composite ZnO NR–g–$C_3N_4$ NFs based device [**$\eta \approx 2.0$ %**, for same weight ratio (1:0.5)].*
- *In **Chapter 4**, we have used porous two dimensional (2–D) zinc ZnO disk structures as photoanodic material to fabricate semiconductor sensitized solar cells. Biomass derived templating agent i.e., Xanthan gum is mainly accountable to control the growth kinetics of high energy facets of wurtzite ZnO crystal structure and likely to obtain these disk structures. A comparative photovoltaic study of as-synthesized 2–D porous ZnO disk structures with respect to 1–D ZnO structures (obtained in absence of xanthan gum) is carried out by co-sensitizing with in-situ grown 1–D CdS nanowires array and ternary*

*metal chalcogenide viz. copper antimony sulfide ($CuSbS_2$). Superior photovoltaic performance (~ **45 %** enhancement in efficiency) is obtained for CdS-$CuSbS_2$ co-sensitized with 2–D porous ZnO disks (**$\eta \approx 2.64$ %**) as compared to 1–D ZnO structures (**$\eta \approx 1.82$ %**).*

- *In **Chapter 5**, we have utilized three dimensional (3–D) ZnO hierarchical superstructures to fabricate hybrid photoanode. An anionic polysaccharide "Polygalacturonic acid" is utilized as a crystal growth modifier for assembling the basic building blocks (ZnO NRs) in a specific orientation and generated the hierarchical superstructures. We studied the probable reaction mechanism for the formation of these superstructures by means of the interaction between the polysaccharide and ZnO growth units. Photovoltaic properties of as-synthesized 3–D ZnO HSs as compared to its basic structural units i.e., ZnO NRs are investigated by sensitizing with a new bisthiazole linked metal free donor-acceptor dye **D1**. We have observed a substantial enhancement (~ **35 %**) in efficiency value ($\eta$) for 3–D ZnO HSs based device (**$\eta \approx 5.37$ %**) as compare to ZnO NRs (**$\eta \approx 3.48$ %**).*
- *In **Chapter 6**, we have reported the biomass assisted in-situ growth of multifunctional hierarchical 3–D ZnO superstructures directly grown over FTO substrates. An anionic polysaccharide, "k-carrageenan" has employed for monitoring the heteroepitaxial aggregated growth of 1–D nanocrystals. Low ohmic resistance offred by these structures with FTO, helpful for transport and collection of photogenerated charge carriers. We have utilized the in-situ grown 3–D ZnO hierarchical structures in photovoltaic as well as selective chemical vapor sensing. A significant enrichment (~ **33 %**) in the power conversion efficiency ($\eta$) has observed for the hierarchical 3–D ZnO structure-based photovoltaic device (**$\eta \approx 3.83$ %**) as compared to the 1–D ZnO NWs (**$\eta \approx 2.57$ %**), which is mainly attributed to the larger surface to volume ratio for sensitizer loading, better light-scattering effects, better charge separation and collection. Two terminal sensor devices have displayed high sensitivity and selectivity for $NH_3$ vapor with the LOD value of ~ **5 ppb** for 3–D ZnO hierarchical superstructures, and ~ **17 ppb** for 1–D ZnO NWs, which are very small as compared to the maximum permissible limit, i.e., 25 ppm.*

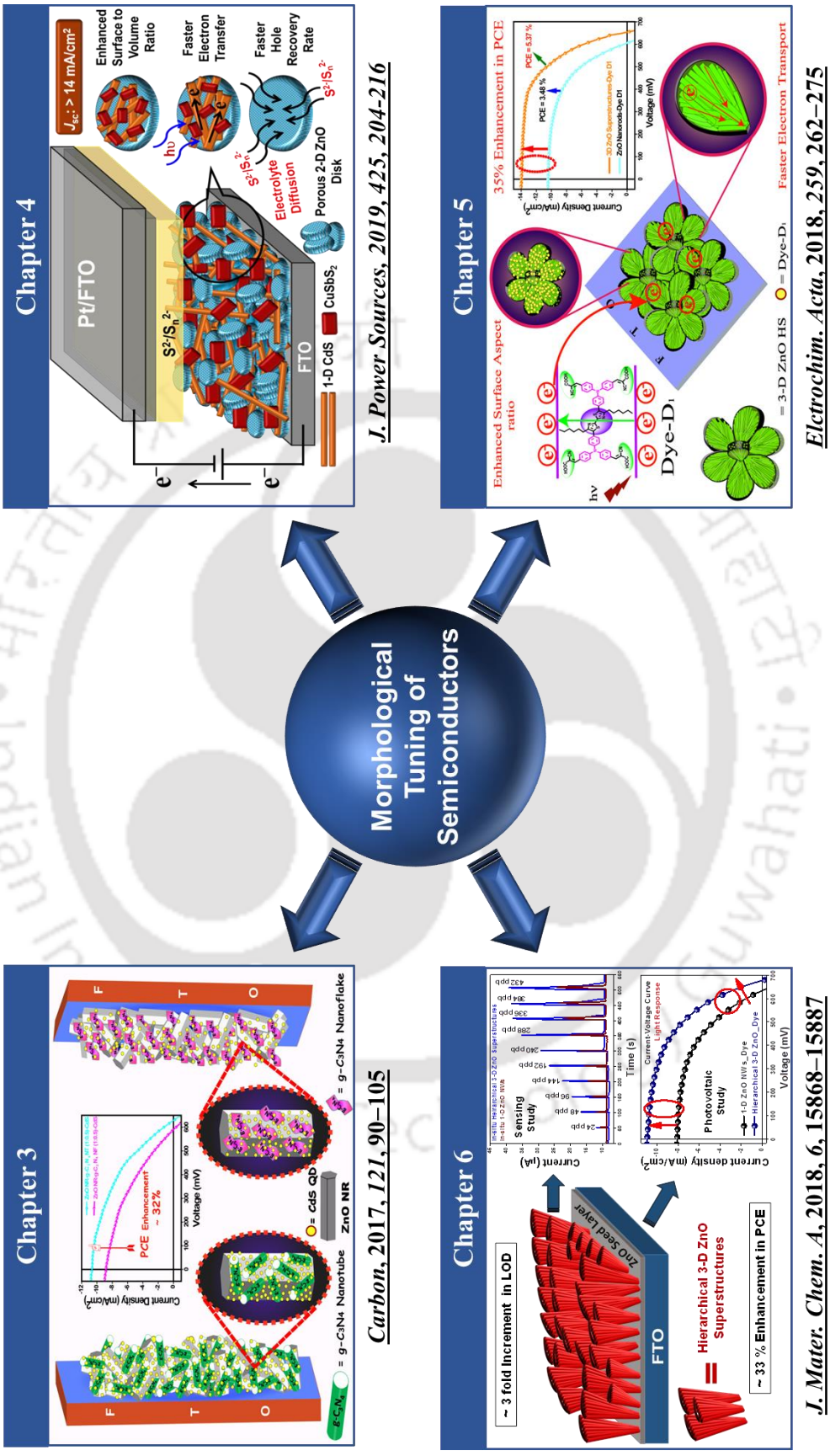

**Table 1. Comparison of photovoltaic performance of ZnO based dye-sensitized solar cells by our approaches to the available literatures reports as mentioned in Chapter 1.**

| **ZnO Structures** | **Sensitizer** | **$J_{sc}$ (mA.cm$^{-2}$)** | **$V_{oc}$ (mV)** | **FF (%)** | **η (%)** | **Ref. (Chapter 1)** |
|---|---|---|---|---|---|---|
| Nanorods like structures | N719 | 23.2 | 620 | 57 | 8.2 | 60 |
| Hierarchical aggregates | N719 | 19.8 | 640 | 59 | 7.5 | 74 |
| Nanowires (NWs) arrays assembly | N719 | 15.3 | 780 | 59 | 7.0 | 61 |
| ZnO tetrapods/$SnO_2$ nanoparticles | N719 | 16.3 | 656 | 59 | 6.3 | 76 |
| ZnO aggregates/$TiO_2$ shell | N3 | 15.8 | 709 | 56 | 6.3 | 77 |
| ZnO nanosheet | D149 | 18.0 | 530 | 63 | 6.1 | 59 |
| Oriented porous films | D149 | 12.2 | 690 | 65 | 5.6 | 79 |
| Nanoparticles/Hollow cavities | N719 | 15.7 | 563 | 62 | 5.5 | 80 |
| **3-D ZnO Superstructures** | **Dye D1** | **13.9** | **653** | **59** | **5.4** | **Chapter 5** |
| Nanoparticles | D102 | 17.4 | 630 | 48 | 5.4 | 62 |
| Hierarchical aggregates | D205 | 12.2 | 653 | 67 | 5.3 | 83 |
| Caterpillar like ZnO Array | N719 | 15.2 | 690 | 50 | 5.2 | 63 |
| ZnO Nanoparticles/Buffer layer | N719 | 11.8 | 670 | 64 | 5.0 | 85 |
| Tetrapod-like ZnO nanopowder | D149 | 12.4 | 607 | 65 | 4.9 | 64 |
| Nanosheet/Nanowires | N719 | 10.9 | 680 | 65 | 4.8 | 86 |
| Self-assembled nanostructures | N719 | 10.7 | 710 | 62 | 4.7 | 65 |
| Nanocones | N719 | 15 | 640 | 45 | 4.3 | 66 |
| ZnO Nanowires/Nanoparticles | N3 | 15.2 | 610 | 46 | 4.2 | 87 |
| Mesoporous film | N719 | 11.8 | 650 | 52 | 4.0 | 89 |
| **In-situ 3-D ZnO structures** | **N719** | **10.8** | **676** | **52** | **3.8** | **Chapter 6** |
| Rectangular Prism | N719 | 8.9 | 730 | 51 | 3.3 | 67 |
| Hierarchical Nanowires | N719 | 8.8 | 680 | 53 | 2.6 | 90 |
| Nanoflower | N719 | 5.5 | 650 | 53 | 1.9 | 68 |
| Nanotubes | N719 | 3.3 | 739 | 64 | 1.6 | 69 |

**Table 2. Comparison of photovoltaic performance of ZnO based semiconductor-sensitized solar cells by our approaches to the available literatures reports as mentioned in Chapter 1.**

| **Photoanodic Architecture** | **$J_{sc}$ (mA.cm$^{-2}$)** | **$V_{oc}$ (mV)** | **FF (%)** | **η (%)** | **Ref. (Chapter 1)** |
|---|---|---|---|---|---|
| ZnO tetrapods/CdSe/ZnSe | 17.3 | 760 | 47 | 6.2 | 113 |
| ZnO nanorods/CdS/CdSe | 16.5 | 700 | 45 | 5.2 | 115 |
| ZnO microsphere/CdS/CdSe | 17.1 | 560 | 53 | 5.1 | 116 |
| ZnO nanoparticles/CdS/CdSe | 10.4 | 683 | 62 | 4.4 | 117 |
| ZnO nanowire array/CdS/CdSe | 17.3 | 627 | 38 | 4.1 | 118 |
| ZnO nanorods/nanosheets/CdS/CdSe | 10.7 | 610 | 50 | 3.2 | 114 |
| ZnO nanoparticles/CdS/$CuSbS_2$ | 15.6 | 470 | 43 | 3.2 | 119 |
| ZnO nanoparticles/CdS/$CuSbS_2$ | 14.7 | 490 | 44 | 3.1 | 120 |
| **ZnO nanorods/$C_3N_4$ nanotubes/CdS** | **10.9** | **628** | **43** | **2.9** | **Chapter 3** |
| ZnO nanoparticles/CdS nanorods | 7.3 | 703 | 54 | 2.8 | 121 |
| **2-D ZnO nanodisks/CdS/$CuSbS_2$** | **14.2** | **428** | **42** | **2.6** | **Chapter 4** |
| ZnO nanosheets/CdS/CdSe | 19.3 | 490 | 28 | 2.6 | 122 |
| ZnO nanorods/g-$C_3N_4$/CdS | 11.1 | 650 | 34 | 2.4 | 123 |
| ZnO nanowires/mesospheres/CdS | 9.0 | 511 | 51 | 2.4 | 124 |
| ZnO hierarchical nanowires array/CdS | 7.3 | 700 | 31 | 1.6 | 125 |
| ZnO nanowires/$CuSbS_2$ | 5.9 | 491 | 56 | 1.6 | 41 |
| ZnO nanowires/CdS | 5.4 | 580 | 34 | 1.1 | 126 |
| ZnO nanoparticles/CdS/$CuSbS_2$ | 8.9 | 309 | 31 | 0.9 | 40 |

**Table 3. Comparison of sensing performance of ZnO heterostructure-based $NH_3$ sensing devices with different reported materials as discussed in Chapter 1.**

| Sensing Material Composition | Limit of detection (LOD) | Response Time (s) | Recovery Time (s) | Ref. (Chapter 1) |
|---|---|---|---|---|
| Au doped ZnO nanorods | 100 ppm | 22 | 57 | 139 |
| Reduced GO/ZnO NWs | 50 ppm | 50 | 250 | 140 |
| ZnO spherical nanostructures | 25 ppm | 20 | 25 | 141 |
| Ce doped ZnO | 25 ppm | 18 | 12 | 142 |
| Mn doped ZnO microspheres | 20 ppm | 4 | 10 | 143 |
| ZnO nanorod arrays | 20 ppm | 200 | 800 | 144 |
| Cu-doped ZnO nanorods | 10 ppm | 13 | 15 | 145 |
| Ag doped ZnO nanorod flower | 10 ppm | 13 | 20 | 146 |
| Ni-doped ZnO micro-discs | 10 ppm | 18 | 50 | 147 |
| Carbon nanotubes/ ZnO NWs | 4 ppm | 25 | 18 | 148 |
| ZnO hierarchical 3D-flower | 2 ppm | 45 | 17 | 149 |
| Au doped ZnO nanowires (NWs) | 0.5 ppm | 20 | 22 | 150 |
| Graphene oxide (GO)/ZnO NWs | 0.5 ppm | 2 | 36 | 151 |
| $Fe_2O_3$–ZnO nanocomposite | 0.4 ppm | 20 | 20 | 152 |
| Carbon nanotubes/ ZnO tetrapods | 0.2 ppm | 18 | 35 | 153 |
| **1-D ZnO Nanowires** | **17 ppb** | **4** | **9** | **Chapter 6** |
| **Hierarchical 3-D ZnO Superstructures** | **5 ppb** | **3** | **13** | **Chapter 6** |

## Future Scope:

We have noticed several significant outcomes of as-conducted research work related to design and development of photoanodic architectures of sensitized photovoltaic system. Various dimensional nanostructured utilized as photoanodic scaffold, have gained considerable attention due to their unique optoelectronic properties. Subsequently, we also observed some important findings of these nanomaterials for selective gas sensing applications. Development of the presented work in this thesis can be extended in many directions, given the diverse nature of the investigation. Indeed, there are so many other possibilities that can be explored for further improving the light harvesting efficiency of these photovoltaic devices, and sensitivity of the chemiresistor devices. An assessments of the conducted research work presented in this thesis has some key future investigations that have been proposed below.

- Improving the charge transfer kinetics and stability of photovoltiac devices by using the two semiconductor metal oxide with well-matched band positions.
- Broadening the light absorption of hybrid photoanode by tuning the molecular archietecture of organic dyes.
- Focusing on high-quality alloy QDs are worthwhile for further studies as their optoelectronic performance can be controlled by adjusting the proportions of the constituent elements rather than by changing the QD size.
- For the environmental safety concern, low toxic QDs should be employed in the QDSCs.
- Less volatile and noncorrosive electrolytes e.g., ionic liquids or solid-state electrolytes will be used for improving the durability of the QDSCs.
- Designing the chemiresistor device based on heterojunction systems for the development of highly selective and ultrasensitive gas sensor, attributed to low interfacial resistance with improved electronics at hetero-junction and greater stability of the sensor devices.

# LIST OF PUBLICATIONS AND CONFERENCES/WORKSHOPS ATTENDED

## Journal Articles:

### *Included in Thesis:*

1. ***Mohammad Shaad Ansari**, Avishek Banik, Suhaib Alam, Mohammad Qureshi, Combined effect of in–situ grown p–type $CuSbS_2$ / n–type CdS coupled with hierarchical ZnO nano-disks for improved photovoltaic light harvesting efficiency. **J. Power Sources**, 2019, 425, 204.*
2. ***Mohammad Shaad Ansari**, Avishek Banik, Anamika Kalita, Parameswar Krishnan Iyer, Mohammad Qureshi, Multifunctional hierarchical 3–D ZnO superstructures directly grown over FTO glass substrates: enhanced photovoltaic and selective sensing applications. **J. Mater. Chem. A**, 2018, 6, 15868.*
3. ***Mohammad Shaad Ansari**, Ramesh Maragani, Avishek Banik, Rajneesh Misra, Mohammad Qureshi, Enhanced photovoltaic performance using biomass derived nano 3–D ZnO hierarchical superstructures and a D–A type $C_S$–Symmetric triphenylamine linked bisthiazole. **Electrochim. Acta**, 2018, 259, 262.*
4. *Ramesh Maragani*, **Mohammad Shaad Ansari***, Avishek Banik, Rajneesh Misra, Mohammad Qureshi, $C_S$–Symmetric triphenylamine-linked bisthiazole-based metal-free donor-acceptor organic dye for efficient ZnO nanoparticles-based dye-sensitized solar cells: synthesis, theoretical studies, and photovoltaic properties. **ACS Omega**, 2017, 9, 5981.*
5. ***Mohammad Shaad Ansari**, Avishek Banik, Mohammad Qureshi, Morphological tuning of photobooster g–$C_3N_4$ with higher surface area and better charge transfers for enhanced power conversion efficiency of quantum dot sensitized solar cells. **Carbon**, 2017, 121, 90.*

### *Not Included in Thesis:*

1. *Avishek Banik, **Mohammad Shad Ansari**, Mohammad Qureshi, Superior light harnessing and charge injection kinetics utilizing mirror-like nano cuboidal ceria coupled with reduced graphene oxide in zinc oxide nanoparticle based photovoltaics. **Solar Energy**, 2019, 185, 89.*
2. *Avishek Banik, **Mohammad Shaad Ansari**, Suhaib Alam, Mohammad Qureshi, Thermodynamic barrier and light scattering effects of nanocube assembled $SrTiO_3$ in enhancing the photovoltaic properties of zinc oxide based dye sensitized solar cells. **J. Phys. Chem. C**, 2018, 122, 16550.*
3. *Avishek Banik, **Mohammad Shaad Ansari**, Mohammad Qureshi, Efficient energy harvesting in $SnO_2$–based dye sensitized solar cells utilizing nano-amassed mesoporous zinc oxide hollow microspheres as synergy boosters. **ACS Omega**, 2018, 3, 14482.*

4. *Tushar Kanta Sahu, Adit Kumar Shah, Gaurangi Gogoi, Anindya Sundar Patra,* ***Mohammad Shaad Ansari****, Mohammad Qureshi, Effect of surface overlayer in enhancing the photoelectrochemical water oxidation of in–situ grown one-dimensional spinel zinc ferrite nanorods directly onto the substrate.* ***Chem. Commun.,*** *2018, 54, 10483.*
5. *Avishek Banik,* ***Mohammad Shaad Ansari****, Tushar Kanta Sahu, Mohammad Qureshi, Understanding the role of silica nanospheres with their light scattering and energy barrier properties in enhancing the photovoltaic performance of ZnO based solar cells.* ***Phys. Chem. Chem. Phys.****, 2016, 18, 27818.*
6. *Tridip Ranjan Chetia,* ***Mohammad Shaad Ansari****, Mohammad Qureshi, Graphitic Carbon Nitride as a photovoltaic booster in quantum dot sensitized solar cells: a synergistic approach for enhanced charge separation and injection.* ***J. Mater. Chem. A****, 2016, 4, 5528.*
7. *Tridip Ranjan Chetia,* ***Mohammad Shaad Ansari****, Mohammad Qureshi, Rational design of hierarchical ZnO superstructures for efficient charge transfer: mechanistic and photovoltaic studies of hollow, mesoporous, cage-like nanostructures with compacted 1−D building blocks.* ***Phys. Chem. Chem. Phys.****, 2016, 18, 5344.*
8. *Tridip Ranjan Chetia,* ***Mohammad Shaad Ansari****, Mohammad Qureshi, Ethyl cellulose and cetrimonium bromide assisted synthesis of mesoporous, hexagon shaped ZnO nanodisks with exposed ± {0001} polar facets for enhanced photovoltaic performance in quantum dot sensitized solar cells.* ***ACS Applied Mater. Interfaces****, 2015, 7, 13266.*
9. *Mohammad Qureshi, Tridip Ranjan Chetia,* ***Mohammad Shaad Ansari****, Saurabh S. Soni, Enhanced photovoltaic performance of mesoporous $SnO_2$ based solar cells utilizing 2−D MgO nanosheets sensitized by a metal-free carbazole derivative.* ***J. Mater. Chem. A****, 2015, 3, 4291.*

## Conferences and Workshops Attended

1. *International Conference on Frontiers in Chemical Sciences (FICS), 2018, Indian Institute of Technology Guwahati, Guwahati, India (**Poster presentation**).*
2. *Research Conclave' 18, Students' Academic Board (SAB), Indian Institute of Technology Guwahati, Guwahati, India (**Poster presentation**).*
3. *Annual Chemical Engineering Festival (Reflux 2018), Department of Chemical Engineering, Indian Institute of Technology Guwahati, Guwahati, India (**Oral presentation**).*
4. *5$^{th}$ International Conference on Advanced Nanomaterials and Nanotechnology (ICANN), 2017, Indian Institute of Technology Guwahati, Guwahati, India (**Poster presentation)***
5. *International conference Nanotechnology: Ideas, Innovations & Initiatives (ICN:3I) 2017, Indian Institute of Technology Roorkee, Uttarakhand, India (**Oral presentation**).*
6. *International Conference on Sophisticated Instruments in Modern Research (ICSIMR), 2017, Indian Institute of Technology Guwahati, Guwahati, India (**Poster presentation**).*
7. *20$^{th}$ CRSI national symposium in chemistry, 2017, Department of Chemistry, Gauhati University, Guwahati, India (**Poster presentation)**.*
8. *3$^{rd}$ National Workshop on NEMS/MEMS and Theranostics Devices-2017, Department of Nanotechnology, Indian Institute of Technology Guwahati, Guwahati, India (**Attended**).*
9. *National Conference on Frontiers in Chemical Sciences (FICS), 2016, Indian Institute of Technology Guwahati, Guwahati, India (**Oral presentation**).*
10. *4$^{th}$ International Conference on Advanced Nanomaterials and Nanotechnology (ICANN), 2015 at Indian Institute of Technology Guwahati, Guwahati, Assam, India (**Attended**).*